The Prediction of Unsteady Three-Dimensional Aerodynamics on Wind Turbine Blades

Xabier Munduate, M.Eng.

Thesis submitted to the Faculty of Engineering,
University of Glasgow, for the Degree of Doctor of Philosophy
August 2002

University of Glasgow
Department of Aerospace Engineering

Declaration

The author hereby declares that this thesis is a record of work carried out in the Department of Aerospace Engineering at the University of Glasgow during the period from October 1997 to December 2000. The thesis is original in content except where otherwise indicated.

August 2002

Xabier Munduate

Acknowledgements

It has been a pleasure and a real inspiring experience to have Dr. Frank N. Coton as both my mentor and supervisor. I express my immense gratitude for his generous advice, guidance and encouragement during the course of this work.

I would like to gratefully acknowledge the Aerospace department for the provision of the research position and their financial support.

I would also like to thank the many departmental researchers and personnel, for their support and shared burden in this study.

Finally, I have long derived pleasure from the prosecution of this work abroad, with the enthusiastic support of my family, especially my parents, Mila and Luis and the care and strength of my fiancée Esther. My debt and thanks to them are infinite.

Abstract

Experience with operational wind turbines over the last few years, has triggered much interest in three-dimensional effects and the unsteady aerodynamics of Horizontal Axis Wind Turbines (HAWTs). Currently these effects are not commonly incorporated into blade design routines. This has led to conservatively over-designed turbines and in some cases, has even compromised the structural integrity of some machines. With this is mind, the work carried out in this thesis is aimed at developing simple unsteady aerodynamic models, that can, at an early stage of the design, be used to both identify and predict unsteady aerodynamic phenomena affecting wind turbines.

After introducing the main features of the aerodynamics of wind turbines, a review of key theoretical studies and aerodynamic modelling methods provides the opportunity to focus on predictive methods and the main technical challenges associated with the aerodynamics of HAWTs. The basic aerodynamic method adopted in this study, a classic Blade Element Momentum theory model, BEM, is described next and its extension to yawed flow is detailed for completeness. Analysis then focuses on how stall delay due to three-dimensional effects can be predicted on a HAWT. Implementation of a semi-empirical stall delay model shows sensitivity to blade geometry but no dependency on wind velocity or rotational speed. This seems to be physically incorrect and suggests that a deeper understanding of 3–D effects is still needed if better algorithms are to be developed.

The work then examines the onset of dynamic stall. A 2–D semi-empirical correlation of vortex stall onset, developed previously at Glasgow University, is implemented and validated through available field data from the NREL turbine Phases II and IV. The comparison of measured and predicted locations of dynamic stall onset highlights some interesting features of the three-dimensionality of the process; after the local inception, earlier dynamic stall appears to be triggered in adjacent stations. An attempt to study how 3–D stall delay interacts with the onset of dynamic stall, shows that stall delay appears not to influence the inception of dynamic stall in the way it does static stall. Moreover, the firsts signs of dynamic stall onset are generally best characterised by the correlation when it assumes locally 2–D flow. This is a significant result, as it demonstrates that the earliest signs of dynamic stall onset on wind turbines can be correctly predicted using 2–D tools. A closer examination of the discrepancies between the predictions and measurements has highlighted the particular aerodynamic characteristics of the S809 aerofoil, utilised as the blade section of the NREL turbines. The unusual stalling characteristics of this aerofoil bring into question the significance of the static stall angle in relation to dynamic stall. It is show that other features of the static behaviour may provide a more appropriate link to dynamic stall for some aerofoils.

Finally, the phenomenon of tower shadow on a downwind turbine is studied. Unaveraged pressure measurements and integrated normal force coefficients from tests conducted at Glasgow University are analysed. The analysis highlights many interesting features of the tower shadow response. In particular, as the blade enters the tower shadow region, there is a rapid reduction in normal force due to the tower wake velocity deficit. As the blade leaves the tower shadow, the recovery is consistently slower and more progressive and apparently extends further than the edge of the velocity deficit region. These observations are then used in a examination of tower shadow modelling. A steady model, based on a cosine shaped velocity deficit

is evaluated by comparison with the wind tunnel measurements. Unfortunately neither the phase nor the intensity of the response is adequately captured. This leads to the implementation of a new model, based on classic unsteady thin aerofoil theory that accounts for the aerofoil wake induced velocities. The unsteady model captures, in a satisfactory manner, the global response of the blade through the tower shadow region, with a negligible computational cost.

Contents

Nomenclature xv

1 Introduction 1

1.1 Theoretical Studies of Rotor Performance 3

1.2 Aerodynamic Challenges for Predictive Codes 9

1.2.1 Basic Flow States 9

1.2.2 Yaw Misalignment 13

1.2.3 Dynamic Inflow 14

1.2.4 3–D Effects 14

1.2.5 Dynamic Stall 16

1.2.6 Tower Shadow 17

1.3 Scope of the Study 20

2 Basic Aerodynamic Model 23

2.1 Model Description: BEM Formulation 23

2.1.1 Blade Element/Momentum Theory 24

2.2 Yawed Flow Model 33

2.3 Results and Discussion 35

3 Three-Dimensional Stall Delay Modelling 37

3.1 Three-Dimensional Effects in Stall 37

3.2 Modelling Tools Background 41
3.3 3–D Stall Delay Model 44
3.3.1 The 3–D Boundary Layer Equations 44
3.3.2 Formulation of the Separation Model 47
3.4 Implementation of the 3–D Stall Delay Model 49
3.4.1 Sensitivity of the Correlation to the Coefficients 49
3.4.2 Sensitivity of the Correlation to the Speed Ratio 49
3.5 Results and Discussion 51
3.5.1 Results: Regions Of Stall Delay 51
3.5.2 Effect of Changes in Wind Velocity 52
3.5.3 Effect of Changes in Yaw 53
3.5.4 Discussion 55
3.6 Conclusions 59

4 Dynamic Stall Onset Prediction **60**
4.1 Introduction 60
4.2 Brief Overview: Experimental and Modelling Dynamic Stall 63
4.3 Dynamic Stall Onset 66
4.4 2–D Dynamic Stall Onset Predictor 71
4.4.1 The Method 72
4.4.2 Results 77
4.4.3 Regions of Dynamic Stall: NREL UAE Phase II 77
4.4.4 Regions of Dynamic Stall: NREL UAE Phase IV 85
4.4.5 Discussion 108
4.4.6 2–D Conclusions 118
4.5 3–D Dynamic Stall Onset Predictor 119
4.5.1 Three Dimensional Unsteady Stall Model 119

4.5.2 Results and Discussion 124
4.5.3 3–D Conclusions 139

5 Tower Shadow **140**

5.1 Tower Shadow Effects 140
5.2 Tower Shadow Experiments and Modelling 143
5.3 Wind Tunnel Experiment 146
5.3.1 Description of the Wind Tunnel Experiment 146
5.3.2 Pre and Post-Processing of Data 148
5.3.3 Results of the Wind Tunnel Experiment 148
5.3.4 Discussion 168
5.3.5 Conclusions 180
5.4 Modelling of Tower Shadow Effects 181
5.4.1 Formulation and Implementation of the Steady Model 181
5.4.2 Results and Discussion 184
5.4.3 Enhancement of the Tower Shadow Modelling 185
5.4.4 The Küssner Function 186
5.4.5 Implementation of the Unsteady Tower Shadow Model 189
5.4.6 Results and Discussion 189
5.4.7 Conclusions 194

6 Conclusions and Recommendations **197**

6.1 Final Conclusions 197
6.2 Further Work 200

Bibliography **204**

List of Figures

1.1 *Thrust coefficient for basic flow states, (source: Eggleston et al. 1987)* 10

1.2 *Comparison of normal force from field data to 2–D wind tunnel measurements, (source Hansen 1993)* 16

1.3 *Dynamic stall process and lift force and pitching moment variations, (source: Ekaterinaris and Platzer 1997)* 17

2.1 *Schematic One-dimensional Actuator disc flow* 25

2.2 *Schematic inflow velocity and aerodynamic forces at the blade element* 30

2.3 *Schematic yawed inflow configuration for a downwind wind turbine* . . 34

2.4 *Comparison of BEM and Prescribed Wake predicted incidence, yaw*=0° 36

3.1 *Schematic of 3–D Separation coordinate system on the blade* 45

3.2 *Correlation and Numerical results for the 3–D Separation factor ks* . 50

3.3 *Influence of C_1, C_2, C_3 values on the separation factor ks* 50

3.4 *Effect of λ_m in the separation factor ks* 51

3.5 *Influence of wind velocity on 3–D effects for NREL UAE Phase II* . . 54

3.6 *Influence of yawed flow on 3–D effects for NREL UAE Phase II* . . . 55

4.1 *Correlation of C_p deviation incidences, (source: Gracey et al. 1986)* 76

4.2 *Dynamic Stall, wind velocity=18.96 m/s, NREL Phase II* 81

4.3 *Effect of wind velocity at yaw*=+30°, *NREL Phase II* 82

4.4 *Angle of Attack for Fig 4.3, NREL Phase II* 83

4.5 *Dynamic Stall prediction compared to measurements, NREL Phase II* 84
4.6 *Twist angle distribution for NREL Phase IV wind turbine* 85
4.7 *Effect of Twist distribution on incidence, NREL Phase IV* 90
4.8 *Effect of yaw at wind velocity=14 m/s, NREL Phase IV* 91
4.9 *Effect of wind velocity at yaw=+30° , NREL Phase IV* 92
4.10 *Effect of wind velocity at yaw=+15°, NREL Phase IV* 93
4.11 *Effect of wind velocity at yaw=+5° , NREL Phase IV* 93
4.12 *Effect of pitch angle, NREL Phase IV* 94
4.13 *Dynamic Stall prediction compared to NREL Phase IV measurements* 101
4.14 *Dynamic Stall prediction compared to NREL Phase IV measurements* 102
4.15 *Dynamic Stall prediction compared to NREL Phase IV measurements* 103
4.16 *Dynamic Stall prediction compared to NREL Phase IV measurements* 104
4.17 *BEM and PWake Dynamic Stall prediction compared to Phase IV* . . 105
4.18 *BEM and PWake Dynamic Stall prediction compared to Phase IV* . . 106
4.19 *BEM and PWake Dynamic Stall prediction compared to Phase IV* . . 107
4.20 *Azimuthal step size influence on PWake and BEM angle of attack* . . 114
4.21 *Radial Step size influence on BEM Dynamic Stall prediction* 115
4.22 *Effect of local averaged inflow values in BEM, NREL Phase IV* . . . 116
4.23 *Effect of history of the reduced pitch rate, NREL Phase IV* 117
4.24 *Calculated lift coefficient incorporating 3–D stall delay* 122
4.25 *Calculated flow separation incorporating 3–D stall delay* 123
4.26 *Dynamic Stall prediction, α_{ss} fixed from 2–D static test, NREL Phase II* 128
4.27 *3–D Dynamic Stall prediction, compared to NREL Phase II* 129
4.28 *Dynamic Stall prediction compared to NREL Phase II measurements* 129
4.29 *3–D Dynamic Stall prediction compared to NREL Phase II* 130
4.30 *3–D Dynamic Stall prediction compared to NREL Phase II* 130

4.31 *3-D Dynamic Stall prediction compared to NREL Phase II* 131

4.32 *Dynamic Stall prediction with α_{ss} variable at f=0.38 and S_2 fixed from the 2-D static test* 138

5.1 *Sketch of tower shadow velocity deficit, plant view* 141

5.2 *Schematic of the wind turbine model for tower shadow experiment* . . 150

5.3 *Pressure distribution on the aerofoil for one cycle, no tower, wind velocity=11 m/s, yaw=0°* 152

5.4 *Comparison of measured pressure (diamonds) and calculated via panel method (triangles), no tower, wind velocity=11 m/s, yaw=0°* 153

5.5 *Upper and lower surface pressure measurements, normal force and pitching moment coefficients, smooth tower, yaw=0°, wind velocity=9 m/s* 158

5.6 *Upper and lower surface pressure measurements, normal force and pitching moment coefficients, smooth tower, yaw=0°, wind velocity=11 m/s* 159

5.7 *Upper and lower surface pressure measurements, normal force and pitching moment coefficients, rough tower, yaw=0°, wind velocity=11 m/s* 160

5.8 *Upper and lower surface pressure measurements, normal force and pitching moment coefficients, no tower, yaw=0°, wind velocity=11 m/s* 161

5.9 *Upper and lower surface pressure measurements, normal force and pitching moment coefficients, smooth tower, yaw=0°, wind velocity=11.7 m/s* 162

5.10 *Upper and lower surface pressure measurements, normal force and pitching moment coefficients, smooth tower, yaw=+20°, wind velocity=9 m/s* 163

5.11 *Upper and lower surface pressure measurements, normal force and pitching moment coefficients, smooth tower, yaw=+20°, wind velocity=11 m/s* 164

5.12 *Upper and lower surface pressure measurements, normal force and pitching moment coefficients, rough tower, yaw=+20°, wind velocity=11 m/s* 165

5.13 *Upper and lower surface pressure measurements, normal force and pitching moment coefficients, no tower, yaw=+20°, wind velocity=11 m/s* 166

5.14 *Upper and lower surface pressure measurements, normal force and pitching moment coefficients, smooth tower, yaw=+20°, wind velocity=11.7 m/s* 167

5.15 *Detail of Upper surface -Cp measurements near the L.E., yaw=0* . . . 169

5.16 *Comparison of Upper surface -Cp measurements near the L.E. at three wind velocities, yaw=0°* 171

5.17 *Comparison of Upper surface -Cp measurements near the L.E. at three wind velocities, yaw=+20°* 172

5.18 *Effect of tower shadow at two wind velocities, 11 m/s and 11.7 m/s, yaw=0°* 176

5.19 *Effect of tower shadow at two wind velocities, 11 m/s and 11.7 m/s, yaw=+20°* 177

5.20 *Effect of tower roughness on Cn, Cm, wind velocity=11 m/s, yaw=0°* 178

5.21 *Effect of tower roughness on Cn, Cm, wind velocity=11 m/s, yaw=+20°* 178

5.22 *Experimental comparison of two consecutive cycles, yaw=0° at wind velocity=11 m/s* 179

5.23 *Experimental comparison of two consecutive cycles, yaw=0° at wind velocity=11.7 m/s* 179

5.24 *Definition of the tower shadow modelling parameters* 183

5.25 *Steady prediction ($D_V = 0.30, B_t = 2.75$) compared to measurements, yaw=0°, wind velocity=9 m/s* 184

5.26 *Tower shadow prediction ($D_V = 0.30, B_t = 2.75$) and measurement at yaw=0°, wind velocity=9 m/s* 190

5.27 *Tower shadow prediction ($D_V = 0.30, B_t = 2.75$) and measurement at yaw=0°, wind velocity=11 m/s* 191

5.28 *Tower shadow prediction ($D_V = 0.30, B_t = 2.75$) and measurement at yaw=0°, wind velocity=11.7 m/s* 192

5.29 *Effects of tower shadow geometry, D_V and B_t on the unsteady prediction at yaw=0°, wind velocity=11.7 m/s* 193

Nomenclature

Roman Notation

$(-)$	denoting non-dimensional quantity
A	area of the rotor disc
A_w	cross sectional area of the wake far downstream
A_∞	cross sectional area of the freestream
A_1, A_2	constants used in indicial response functions
a	axial induced velocity factor at blade element
a'	tangential induced velocity factor at blade element
B	number of blades
B_t	width of tower shadow
b_1, b_2	constants used in indicial response functions
C_d	drag coefficient
C_l	lift coefficient
C_{lp}	theoretical potential lift coefficient
$C_{l\alpha}$	lift curve slope
C_m	pitching moment coefficient
C_n	normal force coefficient
$C_{n\,\alpha}$	normal force (lift) curve slope
C_P	power coefficient
C_Q	torque coefficient
C_T	thrust coefficient
C_t	tangential (chordwise) force coefficient
C_x	force coefficient normal to the rotor disc
C_y	force coefficient circumferential to the rotor disc
C_1, C_2, C_3	correction factors in stall delay model
c	blade aerofoil chord
C_p	pressure coefficient
D	tower diameter
D_V	maximum velocity deficit
f	non-dimensional separation point $f = x/c$
f_d, f_l	drag and lift 3–D correction factors

f_{max}, f_{min}	coefficients representing separation point curve fit
K_1, K_2	coefficients representing separation point curve fit
k	constant representing velocity gradient (Chapter 3);
	reduced frequency $k = \omega c/2W$ (Chapter 4)
L	lift
M_∞	Mach number
n	coefficient in Corrigan and Schillings (1994) stall delay formula (Chapter 3)
P	rotor power
p	pressure
Q	rotor torque
R	rotor radius
R_0	radius at the blade root
$\overline{R}_0$	non-dimensional $R_0 = R_0/R$
Re	Reynolds number
R_t	root radius or extension
r	radial distance;
	polar coordinate (Section 3.3.1);
	reduced pitch rate only in (Figure 4.1)
$\overline{r}$	non-dimensional $r = r/R$
S	non-dimensional distance travelled by aerofoil in semi-chords
S_1, S_2	coefficients representing separation point curve fit
s	laminar separation point;
	arc length measured from leading edge up to the separation point
T	rotor thrust
t	time
V	velocity;
	axial velocity through the rotor disc, (Chapter 2)
V	uniform wind velocity;
	wind velocity at hub height
V_c	cross-flow component of the freestream velocity under yawed flow
V_n	normal component of the freestream velocity under yawed flow
V_r	radial component of the velocity on the blade (Section 3.3.1)
V_t	tangential velocity of the rotor under yawed flow
V_w	axial velocity in the wake far downstream
V_z	normal component of the velocity on the blade (Section 3.3.1)
V_θ	tangential component of the velocity on the blade (Section 3.3.1)
V_∞	freestream velocity
W	resultant relative inflow velocity at blade element
$\overline{W}$	non-dimensional $W = W/V_\infty$
$w_{ge}(S)$	velocity deficit obtained from the Küssner model
w_g	prescribed velocity deficit introduced into the Küssner model
$w_g(0)$	initial value of the velocity deficit

X_2	constant in the dynamic stall correlation (Figure 4.1)
$X(S), Y(S)$	deficiency functions for the Küssner model
x	chordwise distance
z	cartesian coordinate normal to the blade
Z_t	distance from yawing axis to rotor rotation plane

Greek Notation

α	angle of attack
α_0	zero-lift angle of attack
α_1	angle of attack at break point of separation point fit curve
α_{ds}	angle of attack for dynamic stall onset
α_{ss}	angle of attack for static stall
α^+	reduced pitch rate, $\alpha^+ = \frac{\mathrm{d}\alpha}{\mathrm{d}t} c/2W$
γ	yaw angle
Δ	denoting increment or decrement
θ	blade pitch angle;
	polar coordinate (Section 3.3.1)
Λ	modified tip speed ratio
λ	tip speed ratio
λ_m	modified local tip speed ratio
λ_r	local tip speed ratio
ϱ	air density
σ	local solidity of rotor;
	time variable (Section 5.4.4)
ϕ	inflow angle
ψ	azimuth
	indicial response function (Section 5.4.4)
ψ_t	azimuthal angle of tower shadow
ψ_0	half angle of tower shadow
ψ_1	azimuthal angle at which blade enters tower shadow
ψ_2	azimuthal angle at which blade leaves tower shadow
Ω	angular velocity of rotor
ω	angular velocity of the wake just behind the rotor disc
ω_w	angular velocity of the wake far downstream
ω_∞	angular velocity of the freestream

Subscript

$2D$	denoting two-dimensional quantity
$3D$	denoting three-dimensional quantity

Chapter 1

Introduction

After describing the main features of the aerodynamics of wind turbines this chapter continues with a brief review of key theoretical studies and aerodynamic modelling methods. This provides the opportunity to focus in the following section on the aerodynamic challenges that face predictive methods for horizontal axis wind turbines. The chapter then concludes by identifying the aspects of the unsteady three-dimensional flow environment that will be addressed in the following chapters.

Wind turbine aerodynamics deals with the interaction between the turbine structure and the surrounding air flow. This interaction of the air flow with the tower, nacelle and rotor blades determines the loads on the turbine and its energy performance. Obviously, the aerodynamic loads must be well understood before the structural response can be accurately determined. Wind turbine blade performance is concerned with the amount of energy extracted from the air flow and the dynamic loads caused by the wind interacting with the turbine structure. From the point of view of the wind flow, the turbine extracts the energy at the cost of the dynamic loading. Therefore, a mathematical representation describing the air flow, which aims to accurately predict power output and blade loads, seems the first requirement towards success of a rotor blade design. The Navier–Stokes equations, known

since 1821-1845, provide a complete mathematical description of the physics of the fluid motion. However, analytical solutions are known for very few limited cases, and full solutions for the flow conditions and geometries of interest for wind turbines have not, as yet, been obtained numerically. Some further remarks regarding Navier–Stokes methods will be made later within this section. Thus, theoretical approximation studies of the relevant physics involved in rotor aerodynamics have been carried out for more than a 100 years. Depending on the approach and the assumptions made when representing the flow field, the resulting model can offer a different spectrum of applications and purpose.

There are different ways of classifying the types of flow relevant to rotor blade aerodynamics. If spatial and time scale classifications are used, the global flow field can be distinguished from the local blade field, despite the fact that both are intimately related. The flow in the global region extends from far upstream of the turbine to far downstream. The spatial scale in the global field is the rotor diameter $2R$, and the time scale is $2R/V_\infty$, where V_∞ is the wind velocity. The local blade field, refers to the local flow in the proximity of the rotor and around the blade surface. Here, the spatial scale is the blade chord c, and the time scale is $c/\Omega r$, where Ω is the rotational speed and r represents the blade local radius. Both flow fields have a strong interaction with different time and spatial scales. The overall flow around the rotor determines the inflow conditions for the local blade flow, and vice versa, the forces on the blade affect the global flow field.

In the following section a review of aerodynamic studies of rotor performance is presented, in which both global and local flow theories are merged into unified modelling approaches. A review of separated global and local flow theories can be found in other sources such as Snel (1998).

1.1 Theoretical Studies of Rotor Performance

Modelling of the rotor performance of a wind turbine has been attempted using a rich diversity of methods which solve the global and local flow fields based on different levels of approximation; from simple blade element momentum theory, through simplified or full potential flow models and more sophisticated viscous–inviscid interactive codes, vortex wake methods and Reynolds averaged or full Navier-Stokes solvers. These studies are summarised below starting with the earliest approaches and progressing towards more complex and time demanding performance models.

BEM

Modelling of the global flow field around wind turbines has its origins in marine and aeroplane propeller theory. The first published paper on lifting propellers was due to Rankine (1865), where one-dimensional momentum theory was applied to analyse the global flow behaviour on a propeller disc. Later, Froude (1889) incorporated the local flow of the rotor as a disc at which there is a sudden change in pressure without any discontinuity of velocity, into what is generally known as one-dimensional actuator disc theory. One-dimensional or axial momentum theory for global flow was extended to a two-dimensional level for concentric annuli by Glauert (1935). He added the angular momentum balance which incorporates the tangential velocity of the rotating blade; this is known as general momentum theory. For the local flow, Glauert applied blade element theory. Here it is assumed that the aerodynamic forces at independent elements of the blade are equal to the forces on the same aerodynamic profile taken from two-dimensional wind tunnel aerofoil tests. This approach is based on Prandtl's slender wing, lifting line approximation; the forces on a wing element are taken equal to the two-dimensional forces for an equivalent angle of attack, which is formed by the mean flow plus the velocities induced by the

three-dimensional trailing system. On a wind turbine blade the induction is due to the helical trailing vortex in the rotor wake. This induction is assumed equal to the axial and tangential induction velocity factors of momentum theory. Blade element theory is usually employed to analyse the local blade flow when the Momentum theory is used for the global flow region. Together, they form what is commonly known as Blade Element/Momentum theory, (BEM). Most of the contemporary predictive and design codes for wind turbine rotor blade aerodynamics are based on the analytical work of Wilson and Lissaman (1974) using the BEM method.

The validity and limitations of the BEM theory are still under discussion. Sorensen and Mikkelsen (2001) analysed some of the basic assumptions behind this theory. Comparison of BEM results with an unsteady model of the axisymmetric inviscid form of the Navier–Stokes equations, showed the worst case to produce a maximum error of up to 3% in the axial induced velocity on the rotor. They concluded that "In general, the results demonstrate that inherent inconsistencies of the BEM model result in negligible errors".

Potential Flow

Two-dimensional potential flow has been used by some of the earliest aerofoil design methods such as the *Eppler* code. The major application of potential flow is found in panel methods were the local blade flow and the global flow including the wake, are covered with panels that induce a velocity of infinite extension. Therefore, the panels on the blade and on the wake have to be resolved simultaneously or by iteration if the geometry of the wake is modified. This may take significant computational time. Full potential methods were ignored by wind turbine researchers due to difficulties in modelling the rotor wake, despite the fact that they have been widely used in helicopter aerodynamic research. If an inadequate grid size is used, the methods suffer from the fact that vorticity diffuses at a much faster rate than would be

expected in real flows under the influence of viscosity. This may lead to errors in the calculation of blade aerodynamic characteristics (Conlisk 1997).

Recently, some wind turbine researchers, however paid renewed attention to simplified potential methods. One such method is the asymptotic acceleration potential model (Bussel 1996). Under the assumption that the pressure field acts as an acceleration potential, there is no need to model the wake and only the blades are represented by means of pressure distributions. This method has been used in the Delft University design code *Predichat.*

Viscous-Inviscid Interaction

Viscous–inviscid interactive codes introduce viscosity by separating the flow domain into an outer region of potential flow and a thin viscous boundary layer on the surface of the blade. The popular *XFOIL* code for aerofoil design makes use of this technique. One of the first applications to predicting 3–D stall on a wind turbine by a viscous-inviscid interaction model can be found in Sorensen (1986). The main advantage of such methods is that they demand less computing resource than Navier–Stokes solvers. A major drawback, however, is that they are not reliable when a large part of the boundary layer is separated. These models were developed specifically to simulate attached steady flow, and so are generally unable to simulate unsteady behaviour such as dynamic stall or vortex shedding due to separation.

Vortex Wake

In a vortex wake model, the incoming wind flow is vorticity free and only the evolution of vorticity contained in the wake, which was generated at the blades, is calculated in time. This method is unsteady in nature and it is therefore applicable to time-varying flow. There are three approaches to modelling the rotor wake: rigid wake, prescribed wake and free wake techniques.

In the rigid wake technique (Miller *et al.* 1978, Rawlinson-Smith and Hales 1990), the vortex system position is specified as a function of tip speed ratio and thrust. The expansion of the wake is not taken into account and thus the blade load calculations tend not to be very accurate. However, the level of precision of the wake geometry has proved to have only a small influence on gross power and thrust; Gould and Fiddes (1992) concluded that, for one example rotor, the power output and thrust loading were insensitive to the shape of wake. For that case, a prescribed wake expansion of 35% compared to a cylindrical wake produced a change in power prediction of approximately 4% and 1% in the thrust.

Prescribed wake methods tend to be more complex and make use of experimental data or numerical results to locate the wake position. The vortex system is assumed to move initially, near the disc, with the fluid velocity and then, at a certain distance downstream, is assumed to roll into root and tip vortices. Normally the prescribed wake technique is used for the global flow region with lifting line or lifting surface formulations applied to the local blade flow. When using lift coefficients obtained from wind tunnel measurements, the lifting line method is equivalent to the 2–D blade element method as far as local blade flow analysis is concerned. Over the last eight years, Glasgow University has developed (Robison *et al.* 1995, Coton and Wang 1999, Coton *et al.* 2002) a prescribed wake model for the prediction of the aerodynamic performance of HAWTs. Here the wake is divided into a near wake and a far wake. The geometry of the near wake is prescribed by simple functions based on momentum theory, while the latter is modelled as a semi-infinite cylinder. The prescribed wake method offers an balance of computational time and accuracy that could be appealing for future design applications. A prescribed wake code still, however needs to incorporate effects such as 3–D stall delay, dynamic stall onset and tower shadow by some corrective scheme in the same way as the blade element momentum technique does.

Hybrid methods have been also developed in which the near wake (e.g. one rotor diameter downstream) is considered as a free wake and the rest of the wake treated as a prescribed wake. One of these methods appears to give a 75% reduction in computational time whilst only introducing a 5% error compared to free wake computations (Bareiß*et al.* 1996).

In free wake methods, the wake is allowed to develop in time avoiding the difficulty of prescribing the wake geometry. This strategy is suitable for detailed calculations of the complex flow field that HAWTs normally encounter but at the cost of introducing large amounts of computational time, making them somewhat impractical as a design tool. (Simoes and Graham 2001) combined a vortex lattice representation of the local flow over the blade with a free vortex near wake. Beyond this region the near wake was merged with a simplified axisymmetric far wake. Their comparison of the free wake with a BEM method, produced generally good agreement for the axial and tangential induced factors, except at the root and tip, with little differences in the predicted power output of the rotor for both attached and separate flows.

Navier–Stokes

The global and local flow field of a wind turbine can be studied in more detail by methods based on solution of the Navier–Stokes equations. The full set of equations is non-linear in the velocity components and, therefore, analytical solutions are restricted. On the other hand, direct numerical solution of the equations at high Reynolds numbers has proved difficult. The flow over a wind turbine encompasses a Reynolds number range of 10^4 for the global flow to 5 x 10^6 at the blade local flow for megaWatt sized turbines. This variety can create instabilities in time and space on such small scales that current computational capability cannot deal with. Consequently, solutions have just started to appear in the literature using

the Reynolds averaged Navier–Stokes, RANS, equations. These methods require, a suitable turbulence model to be chosen from the many existing models. This may introduce some uncertainty and precaution should be taken when interpreting the results. Voutsinas (1995) points out that Navier–Stokes methods for calculating the viscous flow around wind turbine blades, are highly sensitive to the choice of turbulence models.

The Navier–Stokes method is not often applied to model the global flow. However, Madsen (1996) and Sorensen *et al.* (1998) used the axisymmetric inviscid form of the Navier–Stokes equations for the global flow together with an actuator disc to represent the local flow of the rotor. This approach can be of help in correcting the momentum theory method for yawed flow or high rotor loading (low wind velocities), were wake states can be analysed in severe reversed flow conditions.

Another hybrid approach is that of Xu and Sankar (2000) who used a Navier–Stokes / potential flow solver. The local flow at the blade was provided by the Navier–Stokes equations but the variations of circulation on the blade were captured using vortex filaments freely convected by the local flow. The global flowfield was modelled using potential flow theory.

The work of Duque *et al.* (1999) presented the first Navier–Stokes computation of a wind turbine rotor, tower and nacelle. The computed results are still not quite satisfactory, mainly due to grid density mismatches in the analysis and dependence on the turbulence modelling. In his own words, (Duque 2001): " the computations were very expensive and really not too practical".

With the improvements in the speed and memory of computers and with the advances in computational fluid dynamics techniques, the Navier–Stokes solvers are becoming a promising method for analysis of wind turbine aerodynamics. The state of the art of these techniques in Europe, for studying the aerodynamics of wind turbine blades can be found in Sorensen (1999).

1.2 Aerodynamic Challenges for Predictive Codes

The application of predictive codes to augment reliability and reduce the costs of wind generated energy has a recent history of about 30 years. In most of the actual design codes, the aerodynamics are treated with Glauert's blade element momentum theory, due to its simplicity, reduced computational requirements, and reliability. Over this period BEM models have been used in blade design, performance prediction and in the determination of dynamic loads and aeroelastic applications. (Griffiths 1977, Viterna and Janetzke 1982, Tangler 1983, Hansen *et al.* 1990, Riziotis *et al.* 1996, Giguere *et al.* 1999). A recent comparison of the aerodynamics of several BEM wind turbine design codes conducted at the National Renewable Energy Laboratory, NREL, (Buhl *et al.* 1997) showed that, although the produced results are not identical, the agreement between them is quite reasonable.

BEM theory, however, is not able to predict all flow conditions and so cannot accurately represent some of the flow states encountered by the wind turbine in real situations. Some attempts to overcome its limitations are summarized in this section. Before this, however, the basic flow states are described with reference to one-dimensional momentum theory. A full description of this theory is provided in Chapter 2.

1.2.1 Basic Flow States

The gross flow behaviour of propellers and rotors (Stoddard 1977, Eggleston and Stoddard 1987) can be described by reference to the different flow states of the air stream through the rotor disc:

- Propeller state, when $a \leq 0$
- Windmill brake state, when $0 < a \leq 0.5$

- Turbulent wake state, when $0.5 \leq a \leq 1$
- Vortex ring state, when $a = 1$
- Propeller brake state, when $a > 1$

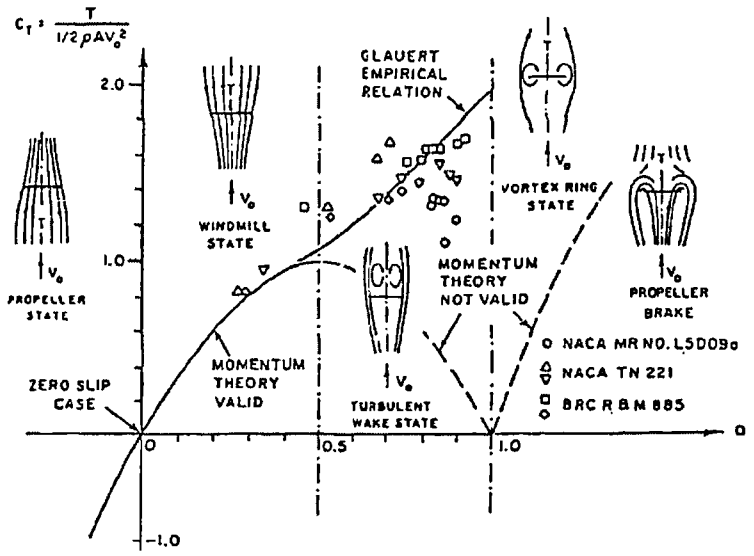

Figure 1.1: *Thrust coefficient for basic flow states, (source: Eggleston et al. 1987)*

where a is the axial interference factor indicative of the extent to which the flow is slowed down by the rotor disc. This term is discussed fully in the following chapter. The main features of these states are illustrated in Figure 1.1. In the figure the thrust coefficient, C_T, is shown as a function of the axial interference factor, a, for various flow states. For $a \leq 0$ the rotor works in the propeller state and for $0 < a \leq 0.5$ it is operating in the so called windmill brake state, which is the usual operating condition for a wind turbine. For a values greater than 0.5, one-dimensional momentum theory is no longer valid because the far wake velocity $V_w = (1 - 2a)V_\infty$ becomes negative, violating the one-dimensional flow assumption. The turbulent wake state appears for $0.5 \leq a \leq 1$, where recirculation of the flow takes place downstream of the rotor. In this range the usual equation for thrust

coefficient, $C_T = 4a(1-a)$, is normally replaced by an empirical relation. Several correlations have been proposed on a experimental basis:

- Glauert (1948): $C_T = 0.89 - 0.44a + 1.56a^2$, for $a > 0.4$
- Wilson (1981): $C_T = 0.578 + 0.96a$, for $a > 0.38$
- de Vries and den Blanken (1981): $C_T = 0.53 + 1.07a$, for $a > 0.4$
- Anderson *et al.* (1982): $C_T = 0.425 + 1.39a$, for $a > 0.326$

For $a = 1$ the velocity of the air at the disc $V = (1-a)V_\infty$ becomes zero. The flow through the rotor is completely blocked, and the rotor is in its vortex ring state. This is the transition phase between energy being extracted from the flow and energy being put into the flow. For $a > 1$ the rotor acts as a propeller brake such that energy is added to the flow, and a forward flow is induced and a downwind thrust created. Wilson and Lissaman (1974) introduced the absolute sign to the thrust and power coefficient equations in order to cope with this situation i.e.

$$C_T = 4a|1-a| \tag{1.1}$$

$$C_P = 4a(1-a)|1-a| \tag{1.2}$$

A wind turbine is operating as a energy extraction device when $C_P \geq 0$ for $0 < a \leq 1$, that is in the windmill brake, turbulent wake and vortex ring states. For most normal operating conditions $a \leq 0.5$, however, "for off design conditions spurious solutions with $0.5 \leq a \leq 1$ might occur", (Wilson and Lissaman 1974).

Windmill Brake State

In momentum theory a velocity discontinuity line divides the flow into two regions at the rotor radius, $r < R$ and $r > R$, each with a constant velocity. In Sorensen

et al. (1998) the tip vortex is seen to alter the flow field near the tip region, where a peak in a, is seen to occur for C_T values greater that 0.5 . This effect becomes more pronounced as C_T is increased, indicating that the basic assumption that the induced velocity factor in the rotor plane, a is half the value far downstream, is violated for highly loaded rotors. This peak in a can be explained by the expansion of the wake. Navier–Stokes calculations, Sorensen *et al.* (1998), show good agreement with momentum theory up to $a = 1/3$ after which, in accordance with experimental observations from Gessow and Myers (1952), they start to deviate. At $a = 0.5$ momentum theory gives $C_T = 1$, but, from calculations (Sorensen *et al.* 1998), $C_T = 1$ is reached at $a = 0.39$. This result is in good agreement with the computations of (Madsen 1996), which also include turbulent mixing.

Turbulent Wake and Vortex Ring

For very highly loaded rotors, $a \geq 0.4$, the rotor flow can transition from the windmill brake state to the turbulent or vortex ring state. For a wind turbine this state is reached at high tip speed ratios (i.e. small wind velocities) or by adjusting the pitch setting (i.e. negative pitch).

In the turbulent wake state, an important amount of kinetic energy is converted into turbulent recirculation. The flow is seen first to create a recirculation bubble downstream the rotor. Next, a large recirculation bubble encloses the rotor. The flow becomes unsteady and goes through a complicated transient phase, after which it settles to a steady state when the large bubble shrinks and a slender recirculation bubble is formed upstream of the rotor. The resulting flow field settles to a steady state corresponding to the propeller brake state, as predicted by momentum theory. Although a BEM technique may be able to provide an estimate of the final steady state conditions, it will not be able to predict the transient loads experienced by the turbine during the transition to this state.

Increasing C_T further results in the vortex ring state. Recirculation bubbles are now formed in the rotor plane and owing to self induction they move upstream in the opposite direction to the incoming wind. The induced flow goes through a periodic transient and, in its final state, the flow becomes steady and similar to that of the propeller brake state as in the turbulent wake case.

The wind turbine entrance into the turbulent wake state brings flow reversal, high turbulence, vibration along the blades and a decrease in shaft torque (Stoddard 1977). It is rare that a wind turbine will operate in the turbulent wake state, except as a transient, since it most probably will stall and lose induced velocity. For a constant rotational speed wind turbine, it occurs at winds much lower that the rated wind velocity. As the phenomenon takes place at low wind speed, where energy generation and blade loads are low, the problem has not been a priority for the wind turbine community; "Although for a fixed speed wind turbine it can be estimated that 15%-20% of the yearly energy generation takes place in this condition" (Snel 1998). For a variable speed wind turbine it might not occur at all during normal operation (Molenaar and Dijkstra 1999).

1.2.2 Yaw Misalignment

Non axial flow is beyond the capabilities of a pure classic BEM model, and so it cannot be used to predict the flow arising from yaw misalignments. For practical use it is necessary to extend the capability of the model to include yawed flows. This is important since wind turbines normally operate in some degree of yawed flow, where cyclic variations in incidence may result in dynamic stall.

At high yaw angles, the wake is skewed and the induced velocities may be prone to error. Attempts to alleviate this problem have been made and prescribed empirical distributions of azimuthal induction have been proposed (Hansen 1992, Snel 2001), some of them taken from an early model by Glauert (1935).

1.2.3 Dynamic Inflow

The BEM method is time independent and therefore assumes that the induced velocities react instantaneously to a change in blade loading. Wind fluctuations and blade movements produce continuous variations of the load on the blade. The mass of air in the wake makes the change in induced velocity lag the blade response. This is well known from helicopters, and it is these that have resulted in the first dynamic inflow models. This engineering approach involves introducing differential momentum equations in time that allow a new steady state to be reached after some time lag (Snel 2001). A major Joule project study on dynamic inflow (Snel and Schepers 1994) concluded that wind turbine blade pitching movements have more effect on dynamic inflow than wind fluctuations. This is important for control techniques, aimed at reducing dynamic loading effects, such as fatigue, and improving the rotor efficiency.

1.2.4 3–D Effects

Blade element momentum theory assumes that there is no aerodynamic interference between one blade element and another. Therefore, blade geometry and end effects have been only partially incorporated in BEM models via some form of tip-loss, traditionally due to Prandtl or Goldstein (Wilson and Lissaman 1974), that accounts for the finite number of blades, but not for the finite length of the blades. Thus, for example, tip and root vortex effects are not considered and there is no aerodynamic model to account for the aspect ratio of the blade within the BEM. In addition the radial, or spanwise, flow is not taken into account. This assumption may be acceptable in attached head-on flow but under stall conditions produces a severe deviation between the predicted and measured normal force coefficients and power levels. This is commonly known as 3–D stall delay (sometimes referred to as 3–D

rotational effects) and has recently been a major focus of attention for wind turbine blades. Constant operation in stalled conditions is unique to stall regulated wind turbines compared, for example, to helicopter rotors. The massive flow separation on a rotor blade in three-dimensional conditions where rotational effects are present has been the focus of several studies (de Vries 1979, Viterna and Janetzke 1982, Milborrow 1985, Rasmussen *et al.* 1988, Madsen and Rasmussen 1988). It has been established, for example, that measured pressure distributions on inboard blade sections differ considerably from their 2–D counterparts (Butterfield 1989*b*, Musial *et al.* 1990, Madsen 1991, Acker and Hand 1999). This has been primarily associated with a delay in the forward movement of separation with increasing incidence that leads ultimately to a delayed stall. As a result, very high maximum lift coefficients have been recorded on the inboard sections of some wind turbines.

Prediction of load distributions near the blade root by BEM or other conventional techniques, which utilise two dimensional blade sectional data is, therefore, problematic. In the case of separated flow, the characteristics of a stalling aerofoil are different to those of a rotating blade. For example, Figure 1.2 illustrates the extent to which such a prediction may differ from measured data on a typical wind turbine. It can be seen that at all four span locations, the normal force coefficient, C_n is higher than the wind tunnel 2–D aerofoil value, and has different stalling characteristics. At 30% blade span, a severe increase in C_n values is observed on the rotating blade with no sign of a drop in C_n at high angles of attack.

Amongst others, Snel *et al.* (1993) and Tangler and Selig (1997) relate the increment in lift due to stall delay to the local blade solidity, c/r. The recent work of Du and Selig (1998) presents a correction formula based on two key parameters (the ratio of local chord to local radius c/r, and the ratio of rotational speed to inflow velocity Λ) and three empirical factors. These techniques have been applied with varying degrees of success.

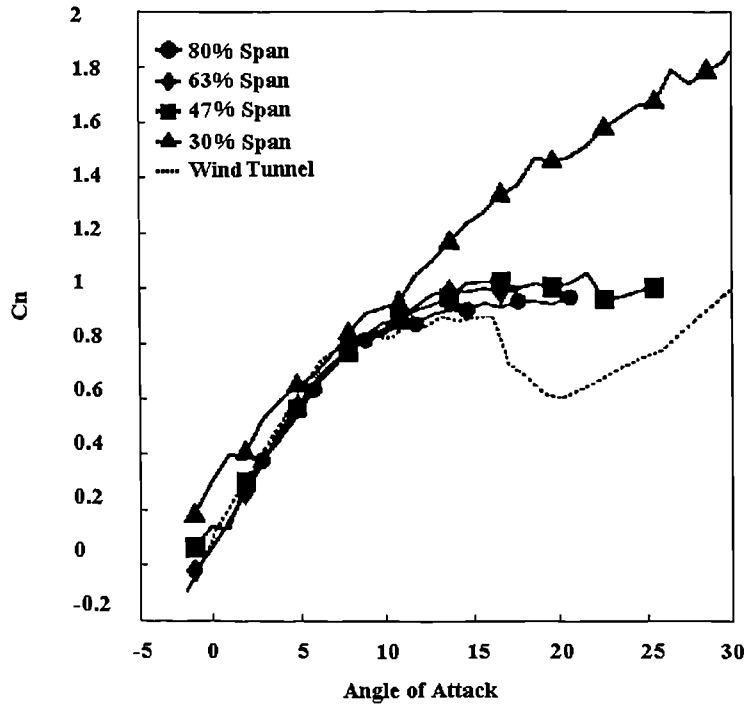

Figure 1.2: *Comparison of normal force from field data to 2-D wind tunnel measurements, (source Hansen 1993)*

1.2.5 Dynamic Stall

The BEM theory is steady in nature, with time not being explicitly included in its formulation. There are many unsteady factors such as atmospheric turbulence, wind shear and skewed flow that result in a typical turbine operating almost continuously in some degree of yawed flow. Under yawed conditions the blades experience cyclic variations in incidence which can, if severe enough, result in dynamic stall (Shipley *et al.* 1995*a*). The severe load fluctuations associated with this phenomenon can play an important role in both the aerodynamic performance of the turbine and the fatigue life of its structure.

Figure 1.3 shows the difference between the lift force and pitching moment variations during dynamic stall compared to the static case (bottom plots). The figure

also shows (top plots) the evolution of the aerofoil dynamic stall vortex process.

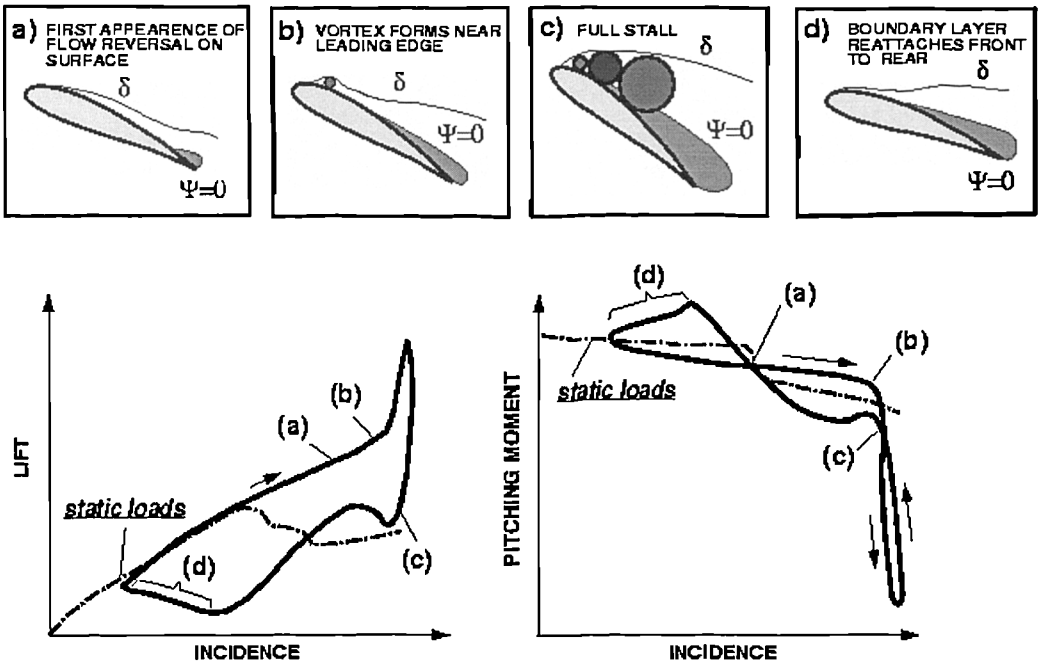

Figure 1.3: *Dynamic stall process and lift force and pitching moment variations, (source: Ekaterinaris and Platzer 1997)*

Studies have been initiated to examine wind turbine dynamic stall (Bjorck 1995) and the results from these studies have fuelled the development of new predictive methods.

1.2.6 Tower Shadow

In BEM theory the inflow velocity at the blade element is uniform. On downwind wind turbines, the presence of the tower reduces the local velocity encountered by the blade as it passes the tower. Tower shadow is a factor of concern for new conceptual downwind designs. The influence of the turbine tower on the blades (Powles 1983), contributes to the wind turbine unsteady aerodynamic envelope. It has the potential to trigger dynamic stall and also introduces unsteadiness even under attached conditions, once every cycle.

It has become clear that blade element momentum theory has some specific deficiencies that limit the useful information, that can be generated by BEM techniques. In recent years, much effort has been made towards improving modelling strategies by understanding the physical rotor flow field. Although contemporary aerodynamic prediction models reflect more of the flow physics than was previously possible, a key aerodynamic issue remaining to be addressed is the manner in which unsteady three-dimensional flow develops and subsequently influences the loading distribution on the blades. Robinson *et al.* (1995) concluded that unsteady aerodynamic effects "must be considered in the design of future turbines if there is to be a significant decrease in the cost of energy production by such devices". The ability to characterise three-dimensional unsteady separated flow could dramatically improve both the performance and life span of a wind turbine; hence the interest in design tools that can predict these effects in the preliminary stages of blade design.

General Trends for Solution

The BEM theory has been extended by engineering methods to overcome some of its deficiencies, but these tools are still under development since the understanding of the physics behind the problems and appropriate implementation of reliable solutions still remains a challenge. There is a need to gain more knowledge from experimental studies such as field and wind tunnel measurements, in order to clearly understand the aerodynamics of rotating blades and aerofoils specifically designed for wind turbines. The International Energy Agency, IEA, through Annex XIV and Annex XVIII (Schepers *et al.* 1997) has published a comprehensive experimental dataset on field tested wind turbines. On the other hand, the NREL Unsteady Aerodynamics Experiment has produced an important database of field measurements (Simms *et al.* 1999, Hand *et al.* 2001*a*), a small subset of which has been included in the IEA collaboration. The field environment is influenced by complex

atmospheric conditions that prevent researchers from isolating the complex inflow from the benign steady state. A serious attempt has just been made to address this problem; the NREL wind turbine was tested in the NASA Ames full-scale 24.4 m by 36.6 m wind tunnel on the 17th May, 2000 (Hand *et al.* 2001*b*). This has provided the wind turbine community with quality data from steady tests, which are virtually free of wind tunnel constraint effects, that should provide a basis for the evaluation and improvement of predictive codes (Simms *et al.* 2001).

At this stage, it seems clear that both, experimental and modelling efforts are still needed to help to incorporate engineering corrections into the prediction methods and design codes used for wind turbine aerodynamics.

1.3 Scope of the Study

The aim of this study is to develop tools to aid in the prediction of the three-dimensional unsteady aerodynamics of HAWTs for design applications. The particular aspects covered in this investigation are the three-dimensional rotating response, the onset of dynamic stall and the tower shadow. In all cases, the developed tools will be embedded in a classic BEM, Blade Element Momentum theory scheme. The intention is not to provide a comprehensive modelling tool but rather a method that allows the designer to identify potential problem areas at the conceptual design stage in advance of detailed performance calculations.

HAWTs operate all times under unsteady aerodynamic conditions. In addition to the ground boundary layer and atmospheric turbulence, which are not addressed here, field operating conditions such yawed flows and the tower shadow cause cyclic and impulsive variations of the blade loads. Under these circumstances, the blade can stall dynamically generating transient forces that can be up to five times the steady predicted values (Robinson *et al.* 1995). These unsteady loads can produce power output fluctuations, and can have a serious impact on the fatigue stress levels, increasing maintenance requirements and reducing the life of the wind turbine machine components.

In head-on flow, three-dimensional rotating effects are responsible for the delay of the flow separation process over the blade surface. This delay in stall could increase, by up to twice, the steady aerodynamic forces (Hansen and Butterfield 1993), especially near the root of the blade span. This makes it difficult to accurately predict the structural loads and the peak power performance.

If advances in rotor blade design are to be achieved, then modelling and prediction of three-dimensional unsteady aerodynamics seems a necessary step to take in the preliminary stage of any wind turbine design. To provide a fast and reli-

able aerodynamic prediction is still desirable for the designer and a challenge for the aerodynamicist. Limitations, exist in every modelling strategy. Computational Fluid Dynamics, CFD, and free wake vortex methods have recently started to show some degree of promise. Unfortunately, these highly computationally demanding methods are still inappropriate for day to day engineering purposes, although they can be useful tools to enhance engineering methods.

Less time consuming, is the prescribed wake strategy which can also give detailed information on the blade loads. However, the accuracy of this method is compromised because of the necessity to incorporate empirical formulations (to represent the wake) and, to an extent, its capacity is limited by the accuracy of the BEM theory that forms part of the prescribed wake calculations. If accurate representation of the wake can be achieved, then the prescribed wake method has considerable potential to improve modelling strategies.

Blade element momentum theory, with its inherent limitation of steady flow, is intensively used as part of present design methods for blade tailoring because it produces rapid and acceptable results for some of the flow states considered in the wind turbine design process. However, without the ability to model three-dimensional unsteady aerodynamics BEM modelling performance is severely limited. A relevant part of the research community has been occupied over the past few years in a effort to incorporate the unsteady aerodynamics of wind turbines into simple schemes. If constructed appropriately, a BEM scheme offers the opportunity to focus on and study features of the unsteady three-dimensional effects. For this reason, basic BEM theory has been adopted in this study and extended to include yawed flow, three-dimensional stall delay, the onset of dynamic stall and a tower shadow model.

The methodology and results of this investigation are documented in this thesis, covering

1. A brief introduction to wind turbine aerodynamics.

2. The basic BEM aerodynamic model extended to incorporate yawed flow.

3. A study of 3–D stall delay effects.

4. Prediction of the onset of dynamic stall on HAWTs, its severity and a study of the effect of three-dimensionality on the dynamic stall onset process.

5. Enhancement of tower shadow modelling and preliminary validation via wind tunnel experimental data analysis.

6. Concluding remarks and suggested further work.

With the exception of the opening and concluding chapters, every chapter has an identical structure; a basic introduction describing the phenomenon, a literature review concerning experimental and modelling efforts, the methodology, results and discussion, and finally, conclusions based on the content of the chapter.

Chapter 2

Basic Aerodynamic Model

2.1 Model Description: BEM Formulation

The modelling technique adopted in the present study is the classical combination of blade element strip theory with one-dimensional momentum theory. This approach, often described as a blade element momentum theory BEM, provides a simple and fast solution for steady one-dimensional head on flow. As mentioned in the Introduction, despite several limitations, at moderate and high wind velocities Glauert's BEM method demonstrates accurate agreement with, for instance, experimental data (Stoddard 1977) and numerical analysis (Sorensen *et al.* 1998). It also has the advantage of being computationally efficient.

For the range of flow states considered in the present study, a pure BEM model would not be sufficient. For this reason, the engineering tool described below, based on BEM theory, has been extended to cope with yawed flow, tower shadow and three dimensional flow effects. The method also includes a correlation used to identify the possibility of dynamic stall.

2.1.1 Blade Element/Momentum Theory

In this section, axial momentum theory is introduced, and then the blade element momentum theory formulation is considered.

Momentum Theory: Rankine-Froude

Rankine-Froude axial momentum theory considers one-dimensional flow past a rotor in which the blades have been replaced by an actuator disc enclosed in a streamtube. The assumptions for the flow are:

- steady: time independent flow.
- incompressible flow.
- uniform flow.
- axial flow:there is no radial flow component, and so radial forces are ignored.
- irrotational flow: there is no rotational motion in the fluid, i.e. turbine wake does not rotate.
- no energy losses: no turbulence, no dissipation.
- inviscid: no viscous interaction, i.e. drag assumed to be zero.

The analysis applies conservation of mass, linear momentum theory and the energy equation in order to determine the thrust T on the actuator disc and the work done by this force: i.e. the power P extracted from the air. In this analysis,the actuator disc device, of area $A = \pi R^2$, accounts only for the extraction of kinetic energy. It does not explain what happens to that energy in terms of work and energy losses. Before the wind interacts with actuator disc, Figure 2.1,it has a velocity V_∞. The cross sectional area of the fluid that will ultimately interact with the disc can,

at this stage, be expressed as A_∞. The flow gradually slows down as it gets close to the rotor disc area A, reaching a velocity V at the disc itself. As the air proceeds downstream, a further slowing down of the wind continues until it reaches the steady far wake velocity V_w at which point it has a cross sectional area A_w. Application of continuity of the mass flow rate through the streamtube gives

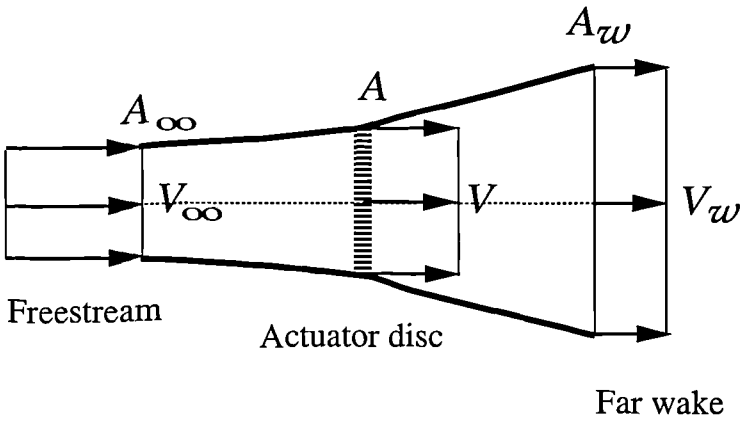

Figure 2.1: *Schematic One-dimensional Actuator disc flow*

$$\varrho A_\infty V_\infty = \varrho A V = \varrho A_w V_w \tag{2.1}$$

where ϱ is the density of the air,i.e. the mass flow rate is the same at any section within the streamtube.

Considering the rate of change of momentum of the air passing through the disc, the thrust can be expressed as

$$T = \varrho\, \pi R^2\, V\, (V_\infty - V_w) \tag{2.2}$$

The thrust due to the pressure difference Δp across the actuator disc can also be formulated as

$$T = \Delta pA = \frac{1}{2}\varrho({V_\infty}^2 - {V_w}^2)\pi R^2 \tag{2.3}$$

where the pressure drop Δp is calculated by applying Bernoulli's equation to both the upstream and downstream regions of the rotor disc. Equating Eq. (2.2) and Eq. (2.3) then gives

$$V = \frac{V_\infty + V_w}{2} \tag{2.4}$$

This equation states that, the air velocity at the disc is half of the sum of the air velocities far upstream and far downstream. It is practical to consider that the disc interferes with the free stream and that the magnitude of this interference follows from

$$a = \frac{V_\infty - V}{V_\infty} = 1 - \frac{V}{V_\infty} \tag{2.5}$$

which, in terms of the velocity at the disc is simply

$$V = (1 - a)V_\infty \tag{2.6}$$

where the term a is called the axial interference factor or axial induced velocity factor. So from Eq. (2.4) and Eq. (2.6) the velocity of the far wake is given by

$$V_w = (1 - 2a)V_\infty \tag{2.7}$$

Comparing Eq. (2.6) and Eq. (2.7) it may be observed the axial induced velocity factor in the far wake, $2a$, is twice that across the disc.

The force coefficient is defined as

$$C_T = \frac{T}{\frac{1}{2}\varrho {V_\infty}^2 \pi R^2} = 4a(1-a) \tag{2.8}$$

and represents the efficiency of the rotor disc, which is maximum for $a = 1/2$.

Assuming that the pressure of the wake far downstream is atmospheric, the work done by the thrust force is $P = TV$. Thus the power coefficient is defined as

$$C_P = \frac{P}{\frac{1}{2}\varrho {V_\infty}^3 \pi R^2} = 4a(1-a)^2 \tag{2.9}$$

where the numerator is the power output extracted by the disc and the denominator represents the power available in the air, which is the kinetic energy of the air contained in an area equal to that of the rotor. The maximum value of C_P in Eq. (2.9) occurs when $a = 1/3$, hence the maximum power coefficient

$$C_{Pmax} = \frac{16}{27} \tag{2.10}$$

this is widely known as the Betz limit.

BEM: Blade Element/Momentum Theory

One-dimensional momentum theory does not account for either the geometry or the rotation of the blades. Glauert's BEM method, combines 2–D Momentum Theory with Blade Element Theory to address these deficiencies.

The analysis begins by applying 2–D, axial and angular momentum to concentric annular elements of the disc to determine the thrust T and the torque Q. Next, the two expressions, containing the induction velocities of momentum theory, are

equated to the thrust and torque obtained by blade element theory, based on 2–D geometry, aerofoil section wind tunnel tests. From here, a set of non-linear equations can be solved numerically in an iterative fashion to obtain the axial thrust and torque of the rotor, as well as the power.

2–D Momentum Theory

The actuator disc is divided into concentric circular streamtubes, which are assumed to work independently of each other. By applying the axial momentum equation to an annular ring at radius r with width $\mathrm{d}r$, the local thrust is given by

$$\mathrm{d}T = \varrho\, 2\pi r \mathrm{d}r\, V\,(V_\infty - V_w)$$

or combining, with Eq. (2.6) and Eq. (2.7)

$$\mathrm{d}T = \frac{1}{2}\varrho V_\infty^2 2\pi r\, 4a(1-a)\mathrm{d}r \tag{2.11}$$

From angular momentum conservation, the local torque Q produced by the tangential force on a circular element at radius r is given by

$$\mathrm{d}Q = \varrho\, 2\pi r \mathrm{d}r\, V\,(\omega_w r - \omega_\infty r)\, r \tag{2.12}$$

where ω_w is the angular velocity of the wake far downstream, and ω_∞ is the angular velocity of the wind far upstream.

Considering a' as the tangential interference factor or tangential induced velocity factor, the rotation of the wake and the rotor is introduced as

$$a' = \frac{\omega}{\Omega} \tag{2.13}$$

where ω is the angular velocity of the wake just behind the disc, and Ω is the angular velocity of the rotor disc. Assuming then that $\omega_w = 2a'.\Omega$ and that the wind far upstream is irrotational, $\omega_\infty = 0$, then rewriting Eq. (2.12) gives the torque

$$dQ = \varrho \cdot 2\pi r dr \cdot V_\infty(1-a) \cdot 2a'\Omega r \cdot r \tag{2.14}$$

Blade Element Theory

From blade element considerations it is assumed that the blade element acts like a two dimensional aerofoil. Applying the velocities obtained from 2–D momentum analysis to a blade element at radius r, the non-dimensional normal and tangential forces on the rotor disc, C_x and C_y acting on the blade element can be calculated.

From Figure 2.2 the following trigonometric relations are obtained. The local relative inflow velocity W at the blade element is

$$W = \sqrt{V_\infty^2\,(1-a)^2 + \Omega^2 r^2\,(1+a')^2} \tag{2.15}$$

acting at an inflow angle ϕ to the plane of rotation, which can be determined by

$$\tan\phi = \frac{V_\infty(1-a)}{\Omega r(1+a')} = \frac{1-a}{\lambda_r(1+a')} \tag{2.16}$$

where $\lambda_r = \lambda\overline{r}$ is the *local tip speed ratio*, $\lambda = \Omega R/V_\infty$ the *tip speed ratio*, and $\overline{r} = r/R$. The angle of incidence or angle of attack, α, is then given by

$$\alpha = \phi - \theta \tag{2.17}$$

where, ϕ is the inflow angle and θ the blade pitch angle.

Knowing the two dimensional aerofoil lift and drag coefficients, C_l and C_d, respectively, as a function of the angle of attack, α, it is now possible to determine the normal and tangential force coefficients at the rotor disc, C_x and C_y

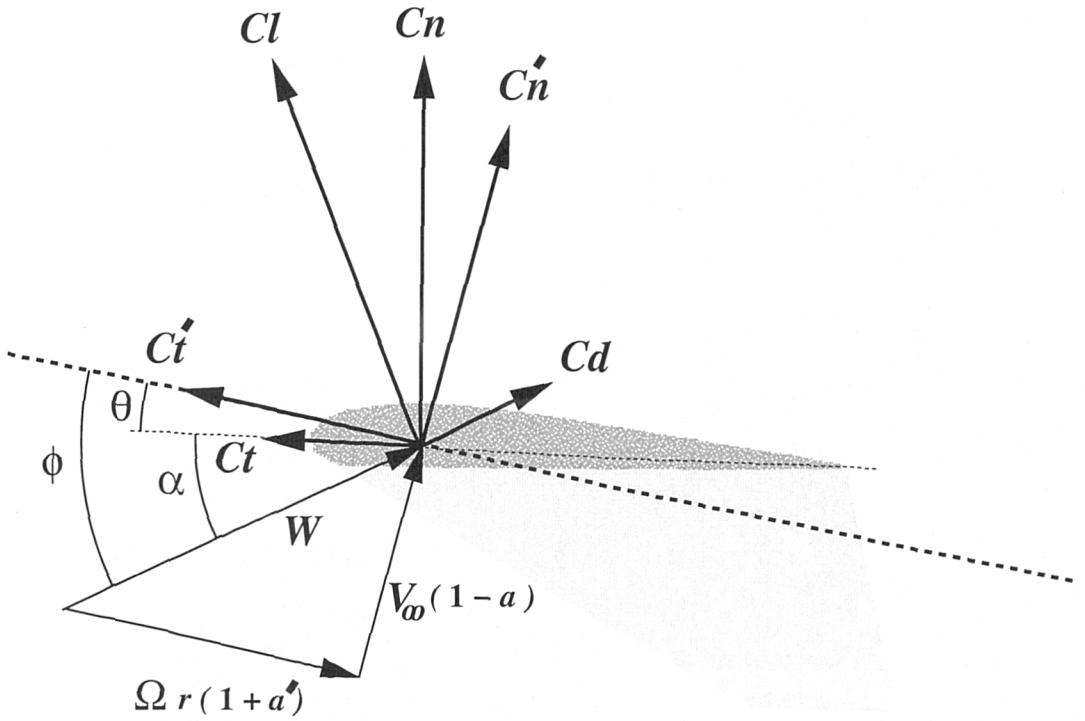

Figure 2.2: *Schematic inflow velocity and aerodynamic forces at the blade element*

$$C_x = C_l \cos\phi + C_d \sin\phi \tag{2.18}$$

$$C_y = C_l \sin\phi - C_d \cos\phi \tag{2.19}$$

where C_x is the force coefficient normal to the rotor disc and C_y the force coefficient tangential to the rotor disc. This nomenclature is used here to distinguish between these terms and the *normal force coefficient* of an aerofoil, C_n, and *tangential force coefficient* or *chordwise force coefficient* of an aerofoil, C_t, which will appear in the following chapters

$$C_n = C_l \cos\alpha + C_d \sin\alpha \tag{2.20}$$

$$C_t = C_l \sin\alpha - C_d \cos\alpha \tag{2.21}$$

From the normal and tangential force coefficients at the rotor disc, C_x and C_y, the elemental thrust and torque can be calculated

$$\mathrm{d}T = \frac{1}{2}\varrho W^2 B c C_x \,\mathrm{d}r \tag{2.22}$$

$$\mathrm{d}Q = \frac{1}{2}\varrho W^2 B c C_y r \,\mathrm{d}r \tag{2.23}$$

where W is the relative velocity, B is the number of blades, and c the chord of the blade element.

Equating the elemental thrust obtained via momentum theory Eq. (2.11) to the expression given by blade element theory Eq. (2.22), results in

$$\frac{a}{1-a} = \frac{\sigma C_x}{8\sin^2\phi} \tag{2.24}$$

where $\sigma = Bc/(\pi r)$ is the local solidity.

Similarly, equating the expressions for torque, Eq. 2.14 and Eq. 2.23, we obtain

$$\frac{a'}{1+a'} = \frac{\sigma C_y}{8\sin\phi\cos\phi} \tag{2.25}$$

For each blade station , the axial, a, and tangential, a', interference factors can determined by the following procedure. For a given rotor configuration and operating conditions and knowing how the two-dimensional aerofoil lift and drag coefficients vary with the angle of incidence and assuming c and θ at a given r, B, Ω, V_∞, C_l and C_d are known then the set of non-linear equations can be solved numerically in a iterative fashion:

1. Assume initial values of a and a' ($a = a' = 0$ is a reasonable starting point)

2. Calculate ϕ from Eq. (2.16)

3. Calculate α from Eq. (2.17)

4. Calculate C_l and C_d

5. Calculate C_x and C_y from Eqs. (2.18) and (2.19)

6. Calculate a from Eq. (2.24)

7. Calculate a' from Eq. (2.25)

8. Go to step 2 and repeat until a and a' converge.

Once the spanwise variations of a and a' are determined, the rotor thrust, torque and power coefficients, C_T, C_Q and C_P can now be calculated from blade element considerations. By integration of Eqs. (2.22) and Eqs. (2.23), respectively,

$$C_T = \frac{T}{\frac{1}{2}\varrho V_\infty^2 \pi R^2} = \int_{\overline{R}_0}^{1} \frac{Bc}{\pi R} \overline{W}^2 C_x \, \mathrm{d}\overline{r} \tag{2.26}$$

$$C_Q = \frac{Q}{\frac{1}{2}\varrho V_\infty^2 \pi R^3} = \int_{\overline{R}_0}^{1} \frac{Bc}{\pi R} \overline{W}^2 C_y \, \overline{r} \, \mathrm{d}\overline{r} \tag{2.27}$$

where the non-dimensional relative velocity $\overline{W}$ is given by

$$\overline{W} = \frac{W}{V_\infty} = \sqrt{(1-a)^2 + \lambda_r^2 (1+a')^2} \tag{2.28}$$

and $\overline{R}_0 = R_0/R$, R_0 the radius at the blade root, and R the radius at the blade tip. The power coefficient can then be obtained from

$$C_P = \lambda C_Q \tag{2.29}$$

2.2 Yawed Flow Model

Yaw misalignment, occurs when the direction of the incoming wind velocity and the rotor axis are not parallel, forming an angle $\gamma \neq 0°$, in a manner that the flow can not be considered axial anymore. The non axial state is beyond the theory of a pure classic BEM model, which is unable to predict yaw misalignments. To allow the model to address the phenomena examined in the remainder of this thesis, it is first necessary to extend the capability of the model to include yawed flows.

Real wind turbines operate at all times in an unsteady aerodynamic environment. Factors such as atmospheric turbulence, wind shear, skewed flow, and the influence of the turbine tower on the blades, etc., all have significant effects on turbine blade inflow conditions. In addition to these factors, the disparity between the time scales associated with changes in wind direction and the yawing speed of a typical turbine inevitably results in the turbine operating almost continuously in some degree of yawed flow. Under yawed conditions the blades experience cyclic variations in incidence which can, if severe enough, result in dynamic stall (Shipley *et al.* 1995*a*). The severe load fluctuations associated with this phenomenon can play an important role in both the aerodynamic performance of the turbine and the fatigue life of its structure. Obviously, the aerodynamic loads must be well understood before the structural response can be accurately determined. Studies have been initiated to examine dynamic stall, tower shadow on downwind machines and dynamic inflow and the results from these studies have fuelled the development of new predictive methods. The impact of this work on the aeroelastic tailoring of future blade designs should not be underestimated.

The way in which the onset flow conditions for such a flow are modelled are described here. The sign convention and reference systems for yaw γ, and blade azimuth angle ψ, follow those used in the IEA Annex XIV Field Rotor Aerodynamics (Schepers *et*

al. 1997). The configuration for yawed flow is showed in Figure 2.3.

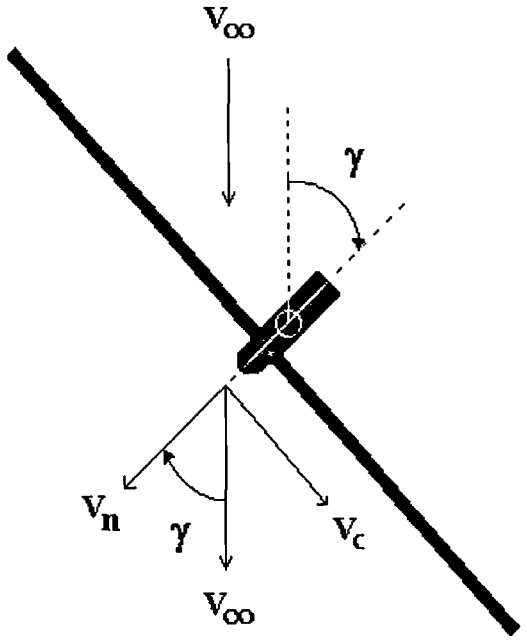

Figure 2.3: *Schematic yawed inflow configuration for a downwind wind turbine*

For non-zero yaw the incoming wind speed, V_∞ can be reduced to normal and cross-flow components relative to the rotor disc

$$V_n = V_\infty \cos\gamma \tag{2.30}$$

$$V_c = -V_\infty \sin\gamma \tag{2.31}$$

Then, the tangential velocity to the rotor is given by

$$V_t = \Omega r + V_c \cos\psi \tag{2.32}$$

Where Ωr is the rotational velocity at the blade radius under consideration, and ψ is the blade azimuth angle measured from the upward vertical position. Thus, the

local tip speed ratio at a given radial location and azimuth angle in yawed flow can be expressed as

$$\lambda_r = \frac{Vt}{Vn} = \frac{\Omega r - V_\infty \sin\gamma \cos\psi}{V_\infty \cos\gamma} \tag{2.33}$$

From Eq. (2.33), the dependence of λ_r on azimuthal position implies that the angle of attack of the blade will vary with time in yawed flow.

As stated above, the angle of attack at the blade is therefore no longer constant around the azimuthal angle, ψ. This cyclic variation in incidence results in a effective pitching of the turbine blade. If the reduced frequency of this pitching is high enough, unsteady effects are manifest, deviating the loading from the steady values. If unsteady effects become severe they may result in dynamic stall.

2.3 Results and Discussion

As mentioned previously in Chapter 1, the basic model will still exhibit the classical limitations of a BEM model at low wind speed or high yaw angles; i.e. the predicted blade incidence will be prone to error. Although the predicted unsteadiness, i.e. locations of dynamic stall will be sensitive to this effect, it is likely that the gross distribution will still be correctly characterised. Nevertheless, the general level of prediction obtained from the scheme is suitable for preliminary investigations. This is illustrated in Figure 2.4 where the BEM predicted spanwise variation in blade incidence on the NREL Unsteady Aerodynamics Experiment, UAE Phase IV turbine is compared with predictions from the more sophisticated Prescribed Wake scheme of Coton and Wang (1999) over a range of wind velocities. The general level of agreement shown in this figure gives confidence that the BEM model provides a suitable platform for the following investigation of three-dimensional unsteady effects.

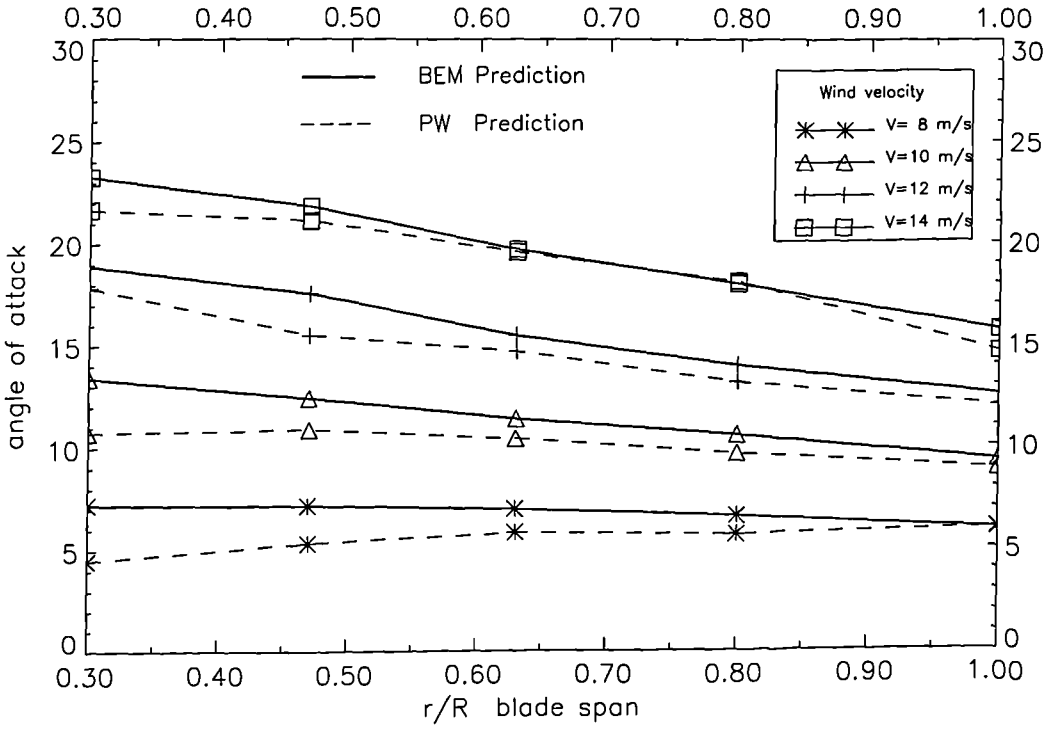

Figure 2.4: *Comparison of BEM and Prescribed Wake predicted incidence, yaw=0°*

Chapter 3

Three-Dimensional Stall Delay Modelling

3.1 Three-Dimensional Effects in Stall

With the appearance on the horizon of new rotor technologies such as megaWatt wind turbines, tiltrotor helicopters, microflight machines and space rotary wing devices, and the increased tendency for more aerodynamically efficient blades, interest has grown in understanding the physics of rotating blades. Specifically, the way in which non-linear additional lift is generated when compared to the classical aerodynamics of a wing section in a steady airflow, has received considerable interest.

In real conditions rotor blades operate facing an unsteady 3–D flow (axial, tangential and radial to the rotor plane), which includes aerodynamic transients in time bound together through the rotational movement of finite blades with a 3–D geometry.

For attached flow on rotating blades, the radial or spanwise flow is not effective compared to chordwise flow and hence the flow might be considered 2–D (Fogarty 1951). Thus, application of lift and drag coefficients, C_l and C_d obtained from 2–

D wind tunnel measurements to predict the aerodynamic forces on rotating blade sections shows a good degree of accuracy, provided the sections are operating well below stall.

In contrast, for separated flow, rotating blades exhibit a sensitivity to chordwise flow which changes the stall mechanism. At high wind speeds, when the rotor blade is close to stall, the measured power curve and C_n values on a stall regulated wind turbine exceed the values predicted by steady 2–D aerofoil data. More generally, through experiments (Milborrow 1985, Butterfield 1989*b*, Madsen 1991, Butterfield *et al.* 1992*a*, Butterfield *et al.* 1992*b*), it has been established that, especially on inboard sections of the blade, stall is delayed to angles of attack well above those measured in two dimensional wind tunnel tests. This is due to a rotating blade stalling differently. In steady head on flow, this has been related to how the boundary layer on a rotating blade delays stall beyond the non-rotating static stall angle measured in a wind tunnel. Moreover, this stall delay gives rise to larger lift coefficients, which can be close to twice those obtained in 2–D wind tunnel tests. Figure 1.2, showed the extent to which such a wind tunnel prediction may differ from field measured C_n data on a typical wind turbine.

In reality, as discussed above, there exists a spanwise flow along the rotating blade, resulting in strong 3–D flow effects (McCroskey and Yaggy 1968, Young and Williams 1972). Thus, BEM prediction methods, based on traditional 2–D aerofoil data, under-predict aerodynamic forces particularly at high wind speeds when the blades are operating at or above the 2–D stalling incidence. Peak power is under predicted by 10% to 30% in these conditions, (Tangler and Selig 1997).

Within a BEM model, it is assumed that there is no aerodynamic interference between one blade element and another and that steady 2–D aerofoil lift and drag coefficients obtained from wind tunnel experiments can be used on each element. At each element, one-dimensional momentum theory is applied in the axial direction

and radial dependency is exclusively included kinematically, through local incidence and rotational speed.

In steady flow, significant 3–D considerations are i) non rotational, tip and root, end effects, and ii) three-dimensionality arising from the blade geometry and rotation. The former has traditionally been incorporated in BEM models via some form of tip-loss correction. The latter, which is the primary contributor to the stall delay phenomenon, is not usually represented in a BEM model. Nevertheless, it is possible to include the effects of 3–D stall delay within such a model by adjustment of the sectional aerodynamic data used to drive the calculation. The extent to which this can be done successfully is considered in the remainder of this chapter. Both steady and unsteady inflow conditions can contribute to the 3–D effect but, only time averaged head on flow, is considered. Later, in Chapter 4 an attempt is made to model the impact of unsteady 3–D effects on the stalling process.

3–D Rotating Stall Delay

Stall delay due to rotation is by no means new, and can be found throughout the whole spectrum of the rotor aerodynamic community. An extensive experimental stall delay related bibliography covering tests on helicopter rotors in hover and forward flight, wind turbines, tiltrotor experiments, and propellers operating within a duct or in a free stream, can be founded in Corrigan and Schillings (1994). The experimental work from the authors cited in this paper concluded that a rotating blade section behaves differently from an aerofoil section isolated in a free stream. As discussed above, the rotating blade section generates much higher lift than the aerofoil, through some stall delaying mechanism.

Three-dimensional stall delay due to rotation has been attributed to a radial flow which is initiated by centrifugal viscous pumping and the radial pressure gradient, resulting in an outboard spanwise flow from root to tip, Snel *et al.* (1993). The

spanwise flow is then influenced by Coriolis forces on the rotating blade. These Coriolis forces will produce (positive) favourable pressure gradients in the chordwise direction, significantly increasing suction in the separated region. As a result, the separation is shifted to a higher angle of attack by the favourable pressure gradient, generating higher $C_{l\max}$ than on a non-rotating blade (Schlichting 1979).

Himmelskamp (1947) was the first to measure an increment in the amount of lift on a rotating blade system when compared with 2–D data. For his experiments he used a two-bladed propeller, where one of the blades was instrumented with pressure taps along circular arcs at various radial blade stations. A lift enhancement was obtained from the rotating blade sections compared with a stationary aerofoil measured in the wind tunnel. Further, the stall delay became more severe on the inner blade sections towards the center of rotation. He ascribed the effect to a the radial flow created by centrifugal and Coriolis forces with the most important mechanism being the resulting thinning of the boundary layer, delaying stall.

Milborrow (1985), studied the development of spanwise flows on wind turbine blades and a fan, where a critical evaluation of experimental data from different sources is made and a theoretical basis for radial flow is developed.

A more recent experiment on a rotating and a non-rotating wind turbine blade was conducted by Ronsten (1992). The author indicates that the strongest 3–D effects appear to be confined to regions of separated flow on the blades.

Stall delay due to rotation has been modelled with sophisticated CFD methods by for example (Sorensen 1986, Narramore and Vermeland 1992, Chaviaropoulos 1996, Duque *et al.* 1999). Nevertheless, as previously mentioned, these Navier–Stokes codes have some specific drawbacks including extensive computational time. Additionally, as a participant on the Joule II Project, Dynamic Stall and 3–D Effects, Voutsinas (1995) noted that Navier–Stokes methods for calculating the viscous flow around wind turbine blades, were highly sensitive to the choice of turbulence models.

Despite these problems, systematic use of such codes may help to develop new simple and practical engineering tools.

For design purposes, simplified methods need to be implemented in prediction codes that capture the first order effects of rotation. Progress has been made in developing such engineering tools. A useful review can be found in the next section, before the engineering method adopted here to model three-dimensional steady stall due to rotation is described.

3.2 Modelling Tools Background

Over the past five decades theoretical research has been carried out on the solution of the boundary layer on a rotating blade. Fogarty and Sears were among the first researchers to publish work on the rotation of laminar boundary layers (Sears 1950, Fogarty and Sears 1950). The assumptions made by these researchers, consisted of the chordwise and radial momentum equations being decoupled. The chordwise velocity at radial stations was independent of the spanwise velocity due to rotation, thus the separation was unaffected by rotation. Therefore, their results for the rotating environment were similar to those of the boundary layer behaviour on a fixed wing. This work provided no insight into why a rotating blade section performs differently from a static aerofoil.

Subsequently, other researchers took a different approach. Without making the same assumptions, Banks and Gadd (1963) established a set of equations coupled through the Coriolis and centrifugal forces. In addition, they assumed an external flow having a linear adverse velocity gradient, acting in the chordwise direction on the blade's suction surface. Banks and Gadd (1963) concluded: "rotation is found to delay laminar separation and sometimes to prevent it entirely". Following a more detailed analysis, by means of a straightforward integration technique, Dwyer

and McCroskey (1970) confirmed Banks and Gadd's results and concluded that the turbulent regions of the boundary layer are the key to understanding the effect that rotation has on the stall delay process. Almost 20 years later, Narramore and Vermeland (1992) conducted computations using a Navier–Stokes solver with an algebraic turbulence model, and showed that laminar boundary layer separation was postponed by rotation and particularly at inboard sections the delay on separation was extremely pronounced on a blade similar to the V-22 tilt rotor system. They also concluded that Banks and Gadd's results are also manifest in a turbulent flow.

As a result of the theoretical modelling efforts, engineering methods have emerged. Methods of this type, based on experimental observation and simplified theoretical analysis of centrifugal and Coriolis terms, have been proposed for rotating wind turbine blades (Viterna and Corrigan 1981, Eggers and Digumarthi 1992, Snel *et al.* 1993, Corrigan and Schillings 1994, Tangler and Selig 1997, Du and Selig 1998).

Viterna and Corrigan (1981) proposed a method based on the modification of 2–D lift coefficients via field test measurements of the power in stall. Because of the empirical nature of the method, it may give good results once the experimental data are known, but it cannot be used to model different blade configurations under various flow conditions, especially when dealing with novel designs.

Eggers and Digumarthi (1992) presented a scaling model based on approximate power series solutions of the Navier–Stokes equations in which the centrifugal and Coriolis effects on spanwise pressure distributions and flows are considered to be of first order while the effects of these on chordwise quantities are neglected, and assumed to be of second order. The rotational effects can then be calculated by adding scaling factors to the wind tunnel aerofoil data. Therefore, pressure data from the corresponding blade are required to calculate the scale factors, suffering from the same limitation as the previous method regarding new blade platforms. The predicted mean power and pressure distributions from using this approach compare

well with the NREL Phase II test data for a no taper, no twist blade.

In Snel *et al.* (1993) a 3–D boundary layer formulation for a rotating system is simplified to obtain a 2–D procedure using the incompressibility assumption for a high aspect ratio blade. The effects of centrifugal and Coriolis forces are retained. This method relates the increment in lift due to stall delay to the local blade solidity, c/r. The proposed formula is $f = \tanh 3(c/r)^2 \simeq 3(c/r)^2$. The success of the analysis is only qualitative. It was observed by Corrigan and Schillings (1994) that the results from this correction, although qualitatively correct, appear to overpredict the effects of rotation on $C_{l\,\max}$ by a considerable amount. Snel *et al.* (1994) also noted this and recommended, on the basis of the comparison of computed results against experimental wind turbine data, that f required reduction by a factor of 2/3.

Corrigan and Schillings (1994) empirical model modifies 2–D aerofoil data to account for stall delay effects due to rotation. Based on Bell helicopter experience and correlation, the model relies heavily on the data published by Banks and Gadd (1963). The model assumes an external chordwise flow with an adverse velocity gradient which provides a parameter to represent the stall delay in the form $k(c/r)^n$, where k, the velocity gradient is a function of the local solidity (c/r). The term n determines the strength of the rotation, and after correlating against some of the available test data, Corrigan and Schillings indicate that this varies from 0.8 to 1.6, and recommend the use of $n = 1$ for a wide range of cases.

Tangler and Selig (1997) presented an evaluation of Corrigan and Schillings (1994) stall delay model applied to two HAWT blades; one with a constant chord and a second with taper, but both with twist. The stall delay model was implemented in the BEM code named *PROP* (Wilson and Lissaman 1974), and compared against NREL test data. They concluded that Corrigan and Schillings (1994)'s model appears to quantify the first-order effects of rotation and that empirical terms used in

the method required further evaluation.

Recently a engineering stall delay model, for wind turbine blades has been proposed by Du and Selig (1998). This model is described below and has been adopted for the purposes of the present work.

3.3 3–D Stall Delay Model

The method of Du and Selig (1998) was chosen for the current work because it represents the latest generation of engineering methods for 3–D stall delay. More especially, the new correlation is the first, to the author's knowledge, that accounts in an explicit form for both, blade shape and rotational speed. By implementation into the BEM code, described in Chapter 2, an evaluation of its ability to quantify the influence of 3–D rotational effects over the rotor blade has been conducted and presented below.

The model is based on the analysis of laminar boundary layer development under the influence of rotational effects, and, in this way, simulates a delay in the movement of the separation point for the rotating blade.

3.3.1 The 3–D Boundary Layer Equations

3–D Terms

The equations of motion for the 3–D incompressible steady boundary layer in cylindrical coordinates, Figure 3.1, are given by

$$V_r\frac{\partial V_r}{\partial r}+V_\theta\frac{\partial V_r}{r\partial\theta}+V_z\frac{\partial V_r}{\partial z}=-\frac{1}{\varrho}\frac{\partial p}{\partial r}+\frac{1}{\varrho}\frac{\partial \tau_r}{\partial z}+\frac{(V_\theta-\Omega r)^2}{r} \tag{3.1}$$

$$V_r\frac{\partial V_\theta}{\partial r}+V_\theta\frac{\partial V_\theta}{r\partial\theta}+V_z\frac{\partial V_\theta}{\partial z}=-\frac{1}{\varrho}\frac{\partial p}{r\partial\theta}+\frac{1}{\varrho}\frac{\partial \tau_\theta}{\partial z}+2\Omega V_r-\frac{V_rV_\theta}{r} \tag{3.2}$$

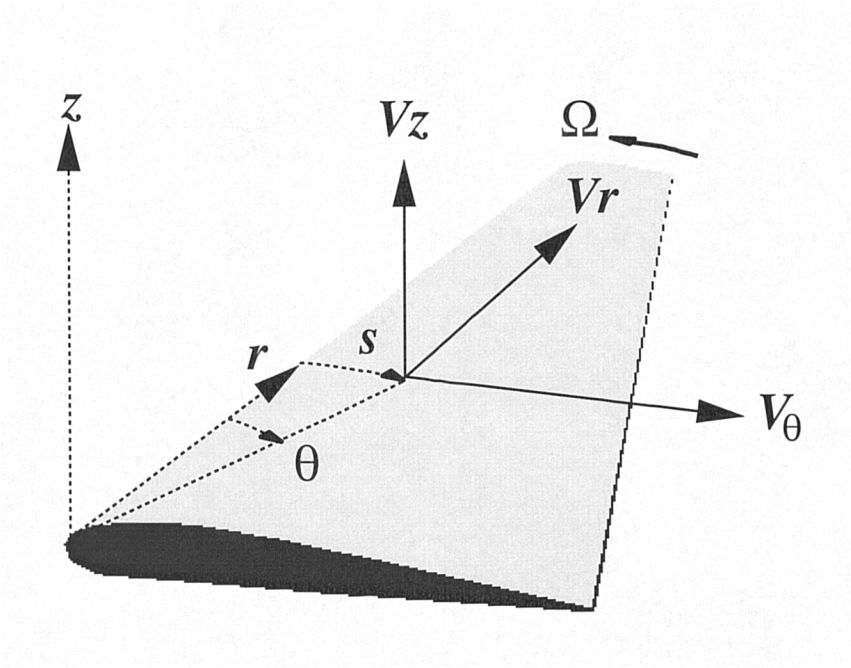

Figure 3.1: *Schematic of 3–D Separation coordinate system on the blade*

$$\frac{V_r}{r} + \frac{\partial V_r}{\partial r} + \frac{\partial V_\theta}{r\partial\theta} + \frac{\partial V_z}{\partial z} = 0 \tag{3.3}$$

They are the r-momentum, θ-momentum, and continuity equations, respectively. It has been assumed that the surface on which the boundary layer develops is in the plane of rotation $z = 0$. τ_r and τ_θ are the shear stresses in the r- and θ- directions, respectively.

From the momentum equations, the 3–D terms can be clearly identified. The

θ-momentum equation (Eq. 3.2) contains the Coriolis-force term ($2\Omega V_r$) and coordinate curvature term ($V_r V_\theta / r$). The r-momentum equation (Eq. 3.1) contains the centrifugal-force term that consists of a coordinate curvature term (V_θ^2 / r), a Coriolis-force component ($-2V_\theta \Omega r$) and the formal centrifugal force ($\Omega^2 r$) resulting from the rotation of the coordinate system.

Numerical Solution of Integral Boundary Layer Equations

The technique used to integrate the above boundary layer equations by Du and Selig (1998) is based on that of Snel *et al.* (1994). The full 3–D integral boundary layer equations are simplified into a 2–D form, where the 3–D terms for centrifugal and Coriolis forces are retained. The solution is further simplified by assuming laminar boundary-layer velocity profiles in the chordwise, θ direction, and in the spanwise or radial direction, r. Moreover, the boundary conditions for radial, tangential and normal velocities are expressed as:

- at z=0 on the blade surface, $V_r = V_\theta = V_z = 0$
- at z=∞ outside the boundary layer, $V_\theta = \sqrt{(V_\infty)^2 + (\Omega R)^2}\,(1 - ks)$ and $V_r = V_z = 0$

where k is a constant, which represents the velocity gradient and s is the arc distance from the leading edge along the surface of the blade section r.

An external flow with a linear adverse velocity similar to that of Banks and Gadd (1963) is assumed in order to solve the laminar case. The result of integrating the boundary layer equations from the leading edge up to the laminar separation point, s, gives an equation where the separation factor ks is expressed in the form

$$ks = f\,(\lambda_m, s/r) \tag{3.4}$$

where ks is a function of a modified local tip speed ratio $\lambda_m = \Omega r/\sqrt{(V_\infty)^2 + (\Omega r)^2}$, the point of laminar separation s and the radial position r, Figure 3.1. The separation factor is numerically calculated by means of Eq. 3.4 for different values of λ_m and s/r. The numerical results from Du and Selig at λ_m=1 are presented in Figure 3.2. In this figure, for a fixed value of λ_m, the separation factor ks increases with increasing s/r. Therefore, stall delay will increase on the inboard sections of the blade, and for a fixed radial position with s the arc length along the aerofoil surface. The assumptions inherent in the numerical model can, thus, be summarised as:

- The full 3–D integral boundary layer equations are not used, instead 2–D equations are enriched with some preserved 3–D terms.
- Surface curvature of the blade in the chorwise direction has been neglected, as if the flat sector of a circle is rotating in its own plane.
- An external flow with a linear adverse velocity gradient is imposed on the blade.
- Only laminar boundary layer separation is considered.

3.3.2 Formulation of the Separation Model

A simple correlation that simulates the numerical results of Eq. 3.4 is required, if an engineering tool based on the above method is to be employed in a design code. Following the work of Du and Selig (1998) a simple semi-empirical relation allows the notional position of the boundary layer separation point to be related to the ratio of local chord to local radius, (c/r), and the rotational speed of the rotor Ω. In particular, the forward movement of the separation point, with increasing incidence, is delayed as these two parameters increase in magnitude. The non-dimensional

parameter, ks, is then an indicator of the severity of the three-dimensional stall delay.

Du and Selig propose a correlation to simulate 3–D rotating separation as follows

$$ks = 1.6\,(s/r).\frac{C_1 - (s/r)^{\frac{C_3}{\lambda_m}}}{C_2 + (s/r)^{\frac{C_3}{\lambda_m}}} \tag{3.5}$$

In general, the greater the difference between the two-dimensional value of ks and its value at some point on the rotating blade, the more severe the stall delay is likely to be. This difference, termed $\Delta(ks)$, is given by the expression

$$\Delta(ks) = \frac{1.6(s/r)}{0.1267}.\frac{C_1 - (s/r)^{\frac{C_3}{\lambda_m}}}{C_2 + (s/r)^{\frac{C_3}{\lambda_m}}} - 1 \tag{3.6}$$

In light of the empirical and approximate nature of the correction, the ratio s/r is replaced by the blade local solidity parameter c/r. Also λ_m is replaced by a modified tip speed ratio Λ and Eq. 3.6 is then re-expressed as

$$\Delta(ks) = \frac{1.6(c/r)}{0.1267}.\frac{C_1 - (c/r)^{\frac{C_3}{\Lambda}\frac{R}{r}}}{C_2 + (c/r)^{\frac{C_3}{\Lambda}\frac{R}{r}}} - 1 \tag{3.7}$$

where

$$\Lambda = \frac{\Omega R}{\sqrt{(V_\infty)^2 + (\Omega R)^2}} = \frac{\lambda}{\sqrt{1+\lambda^2}} \tag{3.8}$$

The ratio of local chord to local radius (c/r), which accounts for the geometry of the blade, appears directly in the above expression, whereas, the modified tip speed ratio Λ, is used to account for the effect of rotation. The coefficient 0.1267 is the two-dimensional value of ks for a 2–D flow without rotation. The factors C_1, C_2, and C_3 are empirical constants and, following the recommendation of Du and Selig (1998), are set to unity. In this form, Eq. (3.7), can be used to identify regions of the rotor liable to experience three-dimensional stall delay.

3.4 Implementation of the 3–D Stall Delay Model

3.4.1 Sensitivity of the Correlation to the Coefficients

Initially, in order to implement Eq. (3.7) into the BEM model, the coefficients C_1, C_2, and C_3 need to be selected. Based on their full numerical model, Du and Selig found them to vary from approximately 0.8 to 1.2 for C_1, C_2 and from 0.4 to 1.0 for C_3. They recommended that the three coefficients be set to unity, but this does not result in a very accurate fitting of the correlation expressed in Eq. (3.5) to the numerical solution represented by Eq. (3.4) as can be observed in Figure 3.2.

The Figure 3.2 shows the variation of the separation factor with the local blade solidity parameter c/r, for a fixed value of the modified local tip speed equal to unity. It can be clearly seen how the correlation differs consistently from the numerical solution, especially at the inboard positions of the blade.

Thus, prior to the implementation of the model, the sensitivity of the calculation to the three coefficients from Eq. (3.5) was evaluated. This sensitivity is highlighted in Figure 3.3 were the values of the coefficients have been varied in the ranges suggested by Du and Selig to produce the entire range of possible numerical solutions.

3.4.2 Sensitivity of the Correlation to the Speed Ratio

To evaluate how the separation point is affected by changes in the λ_m speed ratio, the coefficients were set to $C_1 = C_2 = C_3 = 1$, as recommended by Du and Selig (1998). According to their numerical model ks should increase when augmenting λ_m for every value of c/r. Contrary to this, as can be seen from the calculations of Eq. 3.5 in Figure 3.4, ks decreases when λ_m is increased from 0.6 to 1 for any value of c/r.

As a preliminary conclusion, it can be established that in order to reproduce,

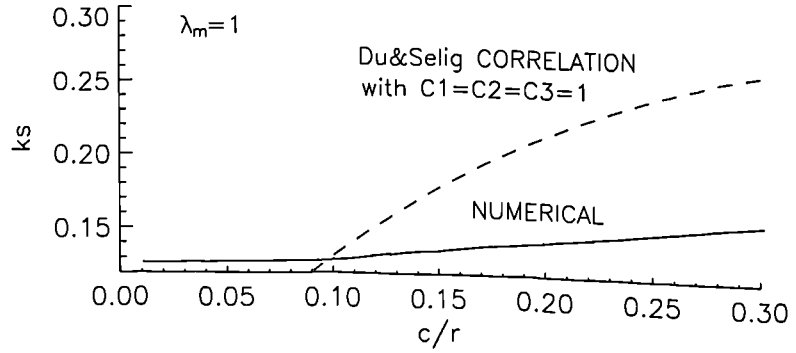

Figure 3.2: *Correlation and Numerical results for the 3–D Separation factor ks*

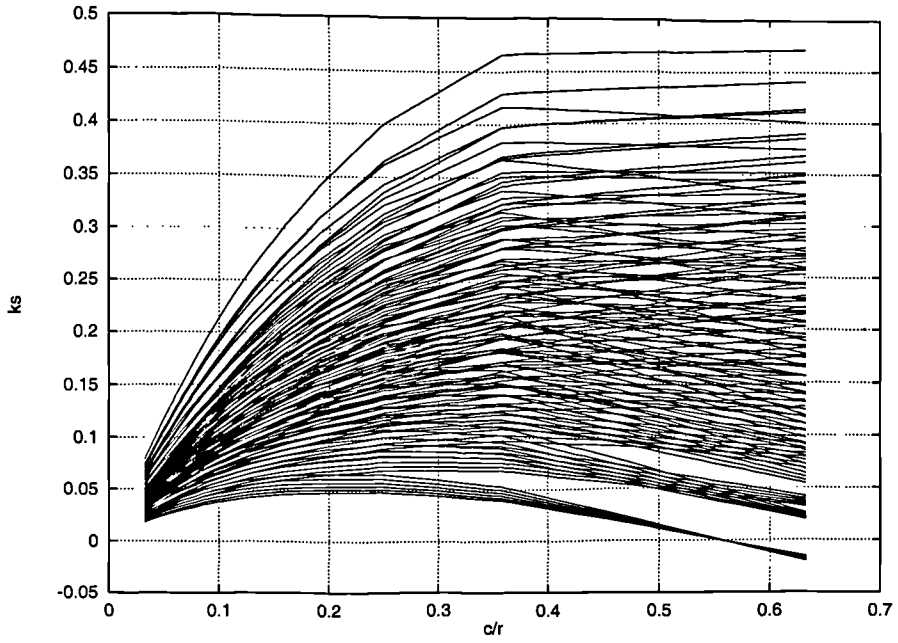

Figure 3.3: *Influence of C_1, C_2, C_3 values on the separation factor ks*

with fidelity, the numerical results of Du and Selig (1998) using their suggested correlation

- From Figure 3.2 and Figure 3.3 the coefficients C_1, C_2, C_3 should change at

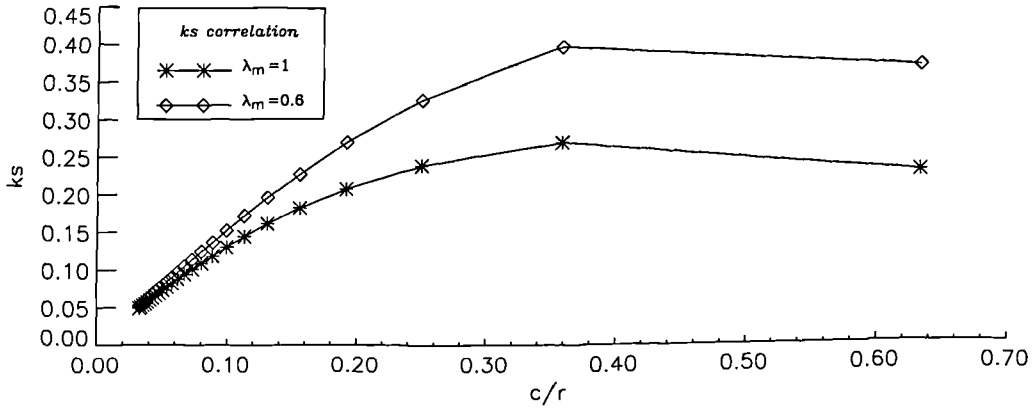

Figure 3.4: *Effect of λ_m in the separation factor ks*

each radial station considered on the blade to simulate the numerical results.

- From Figure 3.4 the coefficients C_1, C_2, C_3 should further vary with the speed ratio λ_m for a fixed radial position, whenever there is a change in wind velocity or rotational speed.

As can be seen from the previous comparison of numerical results against the correlation, the values of the coefficients might need some refinement. Because of the lack of available experimental data to validate any new set of these parameters, it was decided to set $C_1 = C_2 = C_3 = 1$, on the basis of the advice of Selig (1998). Once these coefficients have been set, Eq. (3.7) is implemented into the BEM model, to assess the onset and severity of the three-dimensional stall delay phenomenon.

3.5 Results and Discussion

3.5.1 Results: Regions Of Stall Delay

NREL's Unsteady Aerodynamics Experiment, UAE wind turbine was chosen as the basis for examination of three-dimensional stall delay. This machine was chosen because of the wealth of field data which it has been used to collect and because

it is now the focus of experiments to assess the impact of unsteady aerodynamics on wind turbines. It is a 10.058 metre diameter, three-bladed downwind machine that rotates clockwise (viewed from downwind) at a constant 72 r.p.m. The turbine is supported on a 0.406 metre cylindrical tower. The data used in this study came from NREL's UAE Phase II of the experiment (Butterfield *et al.* 1992*b*, Schepers *et al.* 1997) which utilised untwisted rectangular planform blades of chord 0.457m. These blades, whose cross-section was the NREL S809 aerofoil, were set at a constant $+12°$ pitch angle.

The results presented here are computed for Eq. (3.7) with C_1=C_2=C_3=1, and serve to identify regions of the rotor liable to experience three-dimensional stall delay. It is known that three-dimensional stall delay is, generally, manifest on inboard regions of wind turbine blades. In Figure 3.5(a), contours of the parameter $\Delta(ks)$ are presented for the baseline case of a 18.9 m/s onset flow at zero yaw. As discussed previously, higher values of $\Delta(ks)$ indicate that stall delay due to rotation is likely to be more severe. Values of $\Delta(ks)$ below unity indicate regions of the rotor where such effects are likely to be almost negligible. As the figure shows, the severity of the three-dimensional stall delay increases significantly towards the rotor hub. This is entirely consistent with NREL Phase II field measurements (Butterfield *et al.* 1992*b*) and computational studies (Sorensen 1986, Narramore and Vermeland 1992).

3.5.2 Effect of Changes in Wind Velocity

Increasing the wind speed has remarkably little effect on the result as can be observed in Figure 3.5(b). In this figure, the wind speed has been increased to 37.9 m/s which corresponds to a tip speed ratio of unity. Despite this significant change in velocity, there is only a very small outboard movement of the contours. The reason why the change is so small relates to the use of the modified tip speed ratio parameter, Λ, in the Eq. (3.8). The modified tip speed ratio parameter changes very little despite

the large change in velocity. As a result, it is questionable whether this parameter is an appropriate medium to represent changes in onset flow speed. Decreasing the wind speed to 10 m/s in Figure 3.5(c) has a negligible effect producing nearly the same contours as for higher wind speeds.

3.5.3 Effect of Changes in Yaw

Another factor which may influence three-dimensional stall delay is any variation in the onset flow angle. In fact, as shown in Figure 3.6, even a yaw angle of $\pm 30°$ has almost no effect on the extent of the stall delay region.

One small effect which can be identified by careful comparison of Figure 3.5 and Figure 3.6 is the flattening of the contours as they pass through tower shadow, at 180° azimuth, in the zero yaw case. The tower shadow effect is not so apparent in the yawed case but does appear in Figure 3.6(a) and (b) as a slight disturbance in the $\Delta(ks)$=1 contour at approximately 170° and 190° azimuth, respectively. Tower wake effects will be fully addressed on Chapter 5, Tower Shadow, where the blade interaction with the tower wake is examined by means of modelling and experimental results.

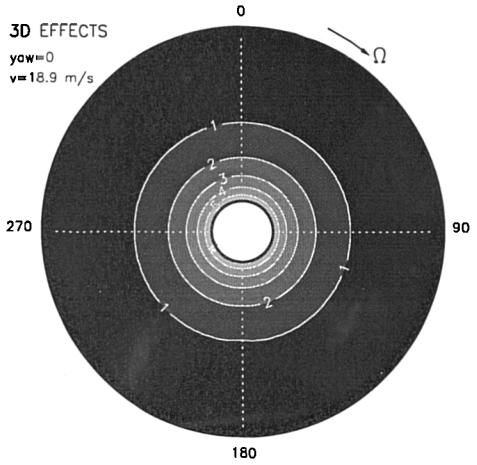

(a) $\Delta(ks)$ for yaw=0°, wind velocity=18.9 m/s

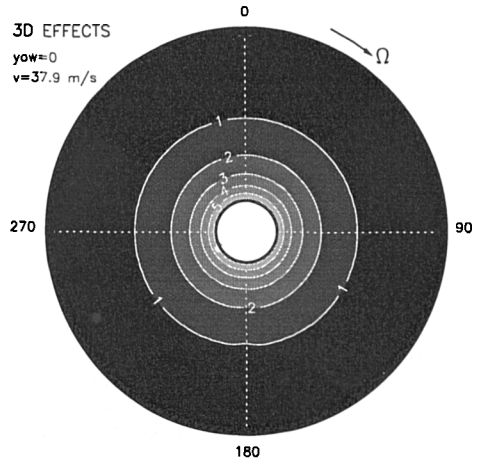

(b) $\Delta(ks)$ for yaw=0°, wind velocity=37.9 m/s

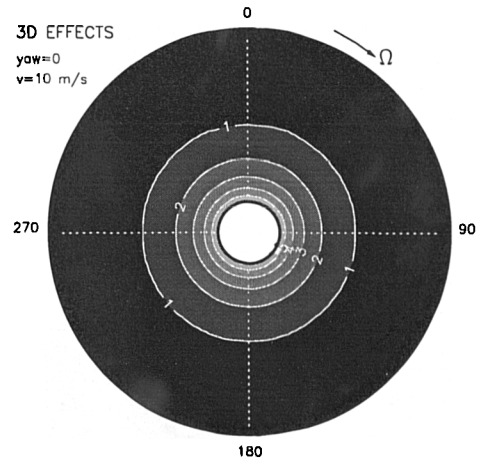

(c) $\Delta(ks)$ for yaw=0°, wind velocity=10 m/s

Figure 3.5: *Influence of wind velocity on 3-D effects for NREL UAE Phase II*

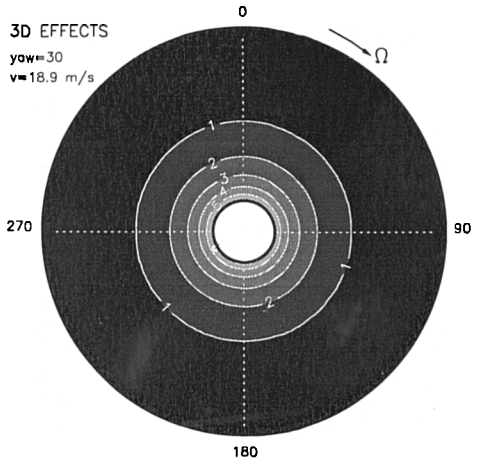

(a) $\Delta(ks)$ for yaw= $+30°$, wind velocity=18.9 m/s

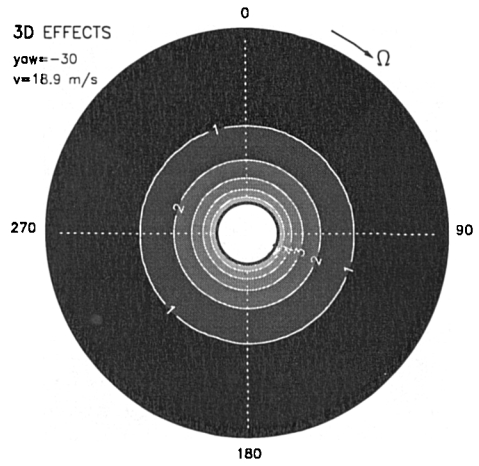

(b) $\Delta(ks)$ for yaw= $-30°$, wind velocity=18.9 m/s

Figure 3.6: *Influence of yawed flow on 3–D effects for NREL UAE Phase II*

3.5.4 Discussion

The characteristics of the model evaluated in this study exhibit some limitations when reproducing the effects of 3–D flow on wind turbine blades. This is discussed further below.

The Stall Delay Model

From the results presented above it appears that the 3–D correlation correctly represents the sensitivity to the blade shape term c/r. Use of the model confirms c/r as the main parameter of influence. It also, however, exhibits a heavy dependency on C_1, C_2, C_3, which is problematic as these coefficients are not uniquely defined. It is suggested that a better fit could be achieved by varying the value of the coefficients at each radial station; although the manner in which this should be done is unclear. Finally, the model appears to have low sensitivity to changes in wind velocity and rotational speed for the normal operational conditions of the NREL Phase II wind turbine.

It is noted above that the model is based on a laminar separation analysis, not taking into consideration the turbulent boundary layer. The movement of the separation point of the laminar boundary layer is a very significant factor in the 3–D stalling process but it is not the only factor. Flow visualisation, e.g. McCroskey (1971), has provided insight into the way in which spanwise flows develop on wind turbine blades and has indicated that the strongest effects appear to be confined to turbulent regions of separated flow on the blades. This modifies the pressure distribution in the separated region and, consequently, 3–D chordwise pressure distributions often bear little resemblance to their 2–D counterparts, (Ronsten 1992). Consideration of a turbulent radial flow thus appears to be appropriate.

There are contradictory opinions about the movement of the separation point on a rotating blade when compared to the 2–D case. Snel *et al.* in his study of Sectional Prediction states: "the real separation line is the same as 2–D". McCroskey (1971), based on measurements and flow visualization, also notes no change in the separation location on the rotating blade. Depending on the nature of the experiment there are different observations: Savino and Nyland (1983) in a wind turbine flow visualization experiment, found radial flow downstream of the separation line on the suction side of the blade. Besides this, the location of the separation line was found to be 10%

to 20% of chord downstream when compared to a 2–D non-rotating blade.

Another feature of the Du and Selig model is that it does not account for Reynolds number, therefore omitting variations in the boundary layer thickness. The radial flow on the blade increases the Reynolds number thus reducing the boundary layer thickness over the suction surface of the blade (Tangler and Selig 1997). In the head-on situation, the outward radial flow is stronger on inboard sections where the larger Reynolds number, thins the boundary layer, promoting a more attached flow. This might play an important role in the stall delay mechanism.

A further potential limitation of the model of Du and Selig is that it neglects radial flow generated by yaw angle. In the yawed case, a cross-flow is manifest, as seen in Eq. (2.31) from Chapter 2. This cross-flow will have a radial flow component, V_r, which will change direction depending on the azimuthal position of the blade ψ, since $V_r = V_c \sin\psi$. If the blade tip is pointing towards the cross flow, the radial flow will go from tip to root. On the other side of the rotor disk, the radial flow will be from root to tip. Therefore the thinning of the boundary layer changes in a cyclic fashion with azimuth and can be more severe either towards the root or towards the tip. As shown in Figure 3.6, yawed flow has almost no effect on the results produced by the correlation assessing the severity of the three-dimensional stall delay.

One further consideration in the Du and Selig model is that the blade shape contribution to the stall delay is only expressed by the ratio of local chord to local radius, c/r. As a result, other parameters such as the twist angle, are not considered. In a recent study from Chaviaropoulos and Hansen (2000), 3–D and rotational viscous effects were investigated by means of a quasi 3–D Navier–Stokes solver for both laminar and turbulent flow. The work suggested that "the two most important parameters that trigger three-dimensional effects are the chord by radii ratio and the twist angle of the considered blade section". It is also added that those effects do not influence the attached flow regime significantly, while they play an

important role where the flow is massively separated.

Other Models

Most authors (Milborrow 1985, Snel *et al.* 1993, Corrigan and Schillings 1994, Tangler and Selig 1997, Du and Selig 1998), use the c/r blade shape function as an integral part of the empirical model, based on *the analysis of centrifugal and Coriolis forces* within the laminar boundary layer or both laminar and turbulent boundary layers (Chaviaropoulos and Hansen 2000). There are only a few examples were 3–D rotational effects are considered in an alternative way.

Wentz and Calhoun (1981) looked to r/R, the ratio of local radius to tip radius of the blade to provide a correlation. The results from this method appeared to overpredict the measurements.

Eggleston (1990) suggested on the basis of flow visualization that a possible cause for the increase in lift coefficients near the blade root may be a trapped vortex.

Wood (1991), regarded 3–D flow *differently than the centrifugal and Coriolis force* approach. He hypothesized that 3–D effects are related to the inviscid, external flow. Wood assumed that the main cause of the stall delay was the influence of trailing edge vorticity, and as a consequence that stall delay depends mainly on the local blade solidity and local tip speed ratio. His results are obtained by means of a 3–D panel method, with a helical vortex formulation for the trailing edge vorticity. Apparently the results indicated that increasing local blade solidity c/r and decreasing the local tip speed ratio, λ_r, increased thc 3–D effects. The chordwise pressure distributions for the blade (3–D) and the aerofoil (2–D) presented sharper differences near the root sections and for higher wind velocities. Increasing λ_r, Wood showed a closer agreement between the blade and the aerofoil pressure distributions. He also added that three-dimensionality affects both, the structure of turbulence and transition, and that these effects would have to be considered when,

eventually, boundary layer calculations were performed along with the external flow calculation.

3.6 Conclusions

In line with previous work, it has been shown that three-dimensional stall delay is restricted to inboard blade sections regardless of the onset flow condition. The results showed an acceptable sensitivity to the blade shape c/r parameter, but almost no dependency to changes in wind velocity and rotational speed for the normal operational conditions of the NREL Phase II wind turbine.

In order to improve 3–D calculations a better physical understanding of the flow under rotational conditions is needed. Full numerical calculations together with experimental flow measurements and visualization may throw some new light onto the physics of 3–D stall delay. This, in turn, may provide the basis for new simple and practical empirical models that capture and embody the physics of turbulence and separated flows around rotating wind turbine blades.

Chapter 4

Dynamic Stall Onset Prediction

4.1 Introduction

Wind turbines operate in a complex three-dimensional aerodynamic environment within which they experience rapidly changing unsteady aerodynamics. A wide range of operational parameters contribute to the unsteady flow over a wind turbine blade including atmospheric turbulence, wind speed variations, wind shear, skewed flow, yawed flow, control inputs, the influence of the turbine tower on the blades, blade and aerofoil shape and deformation, roughness sensitivity and the disturbance created by other turbines in close proximity. In addition, unsteady aerodynamics are of major importance in predicting performance, dynamic loads and fatigue limits. Aspects of unsteady aerodynamics have been documented by Leishman (2002), Robinson *et al.* (1995), Hansen and Butterfield (1993), Madsen (1991) and Galbraith *et al.* (1990).

There are no theories or models for wind turbines which can properly account for all of the unsteady factors listed above. One particular unsteady effect, which has recently attracted the attention of wind turbine researchers, is the dynamic stall event.

The term dynamic stall refers to unsteady flow separation occurring on aerodynamic bodies which execute an unsteady motion. Dynamic stall phenomena are often observed during the operation of wind turbines, the forward or manoeuvering flight of helicopters, insect wings, on propeller and turbomachinery blades and on the wings of rapidly manoeuvering aircraft. The physics of the dynamic stall process are detailed by McCroskey *et al.* (1976), Carr (1977), McCroskey (1981), Carr (1988) and Carr and Chandrasekhara (1996).

On stall regulated wind turbines, large portions of the blades suffer from separated flow at high wind velocities during normal operating conditions. In addition, under yawed conditions, the blade section will experience a cyclic variation in incidence which produces an effective blade pitching motion relative to the onset flow. In the case of pitch regulated machines, this same effect may be originated from both the delay in activating the mechanism and the sudden pitching motion of the blade. Regardless of the type of control employed to regulate the power output, the pitching motion, means that the blade sections operate in unsteady conditions.

When the flow separates from the blade surface, the aerodynamic characteristics become progressively non-linear and stall hysteresis can occur for a periodically varying incidence. This non-reversible effect occurs due to the differences in separation and reattachment for an increment or decrement in angle of attack. During stalled operation, if the cyclic variations in incidence are such that the hysteresis is severe enough, then highly non-linear effects will *dynamically* affect the *stall* process.

It has been generally accepted that dynamic stall is manifest when the static stall angle has been dynamically exceeded due to severe pitching, or translational motions as plunging or flapping. A characteristic feature of the dynamic stall process is a delay in the forward movement of separation and the formation and shedding of a discrete vortex near the leading edge, whose convection over the upper surface of the aerofoil induces a highly unsteady pressure field. As a result, a delay in the onset of

stall to a higher angle of attack than the static stall angle is produced together with hysteresis loops in the unsteady lift, drag, and pitching moment coefficients when plotted as a function of incidence.

The sequence of events during dynamic stall have been studied by many researchers in wind tunnel experiments on aerofoils. These can be summarised briefly as observed by Carr (1977) or Niven (1988) as follows

- flow reversal from the trailing edge prior to flow separation at the leading edge,
- subsequent shedding of a vortical structure from the leading edge,
- vortex convection downstream over the chord,
- as the vortex leaves the trailing edge, the flow over the aerofoil becomes fully separated,
- when the angle of attack is reduced the flow reattaches, leading edge to trailing edge.

The evolution of this process is shown in Figure 1.3 in Chapter 1.

The loads produced under these circumstances can be much higher than the equivalent steady-state loads and may have important life cycle implications for a wind turbine. Under certain conditions lift coefficients as great as five times their maximum static counterparts are produced during formation of the dynamic stall vortex, (Robinson *et al.* 1995).

As a result of the severity of the dynamic stall events, it has become clear that a preliminary aerodynamic design method for wind turbines must be capable of detecting the onset of the dynamic stall process. Modelling of the whole dynamic stall process is beyond the scope of this work, but the prediction of its inception is considered here.

The objective has been to develop an engineering method, to detect the onset of dynamic stall suitable for routine design work on wind turbine blade planforms. The work here has focussed on both the detection of the dynamic stall phenomenon and the prediction of its likely severity.

In this section a modified Blade Element/Momentum, BEM method is presented which tracks temporal changes in blade incidence to identify regions of the rotor disc which are susceptible to dynamic stall. It does this via a previously developed dynamic stall onset correlation, Gracey *et al.* (1996), which is used for the detection of dynamic stall onset. The results from the method are compared with experimental data from two wind turbine configurations. In general, the method is shown to give good predictions over a wide range of operating conditions and inflow angles.

4.2 Brief Overview: Experimental and Modelling Dynamic Stall

A brief overview of previous studies of dynamic stall on wind turbines will now be presented to put the present work in context.

Experimental Efforts Review

In 1989 Butterfield (1989*a*) presented results that quantified both the existence of dynamic stall and its effect on rotor loads by measuring pressure distributions on a 10 m HAWT. Dynamic stall was shown to occur as a consequence of several factors, including turbulence, tower shadow, and yawed flow. Also, the existence of dynamic hysteresis was found to significantly increase yaw loads. In a further study by Hansen *et al.* (1990), it was again found that stall hysteresis has a large influence on rotor yawing moments. Instantaneous pressure distributions measured on the rotor provided conclusive evidence that stall hysteresis was present and calculations

showed that the hysteresis increased the mean yaw moment dramatically (typically over 100%) and the cyclic yaw moments to a lesser extent. In 1991 Madsen (1991) published the results of a four year project on the experimental aerodynamics of a 100 kW HAWT in natural (field) conditions conducted by the Risø National Laboratory. In particular, the measurements were designed to quantify the importance of both 3–D flow on a rotating wing and unsteady effects. From the unsteady aerodynamics analysis it was concluded "that clear stall hysteresis loops can occur when the yaw error is big". Results from the Combined Experiment, conducted by the National Renewable Energy Laboratory, NREL, have shown that unsteady aerodynamics are present to some extent in all operating conditions and that dynamic stall can occur for high yaw angle operation while stall hysteresis can be detected at even small yaw angles (Butterfield *et al.* 1992*a*, Shipley *et al.* 1995*a*, Huyer *et al.* 1996). Continuation of the Combined Experiment, under the name of the Unsteady Aerodynamics Experiment, UAE by NREL (Simms *et al.* 1999), has provided the opportunity to comprehend and characterise the three-dimensional, unsteady, vortical flows that dominate the wind turbine blade aerodynamics (Schreck *et al.* 2000).

Historically, most of this research has been inspired by observations from dynamic stall studies on nominally two-dimensional aerofoils. More recent wind tunnel experimental studies on three-dimensional blade geometries show interesting blade planform effects on the three-dimensionality of the dynamic stall process, (Moir and Coton 1995, Coton and Galbraith 1999, Coton *et al.* 2001, Tan and Carr 1996).

Recently a remarkable experiment has been carried out by NREL in the NASA Ames wind tunnel (Hand *et al.* 2001*b*). This unique effort involved the wind tunnel testing of a well instrumented full size wind turbine and produced aerodynamic measurements of high quality, which were free of the environmental disturbances that compromise field data. These new measurements may help to improve the future knowledge base of wind turbine rotor aerodynamics, (Schreck *et al.* 2001) and

with it, predictive and modelling methods (Simms *et al.* 2001).

Numerical and Semi-empirical Modelling

One of the first to consider dynamic stall effects on wind turbine performance was Cardona (1984) in 1984, who simulated it using a free vortex model of a VAWT. The study of HAWT unsteady aerodynamics with engineering or numerical models for dynamic stall has progressed well (Thresher *et al.* 1986, Hansen 1995, Pierce and Hansen 1995, Voutsinas and Riziotis 1996, Riziotis *et al.* 1996, Ekaterinaris *et al.* 1998, Johansen 1999). The results from these studies have fuelled the development of new predictive methods. Semi-empirical methods attempt to use static aerofoil test data with corrections based on experimental tests to model dynamic stall events. They are not based on the conservation of mass and momentum, but are the result of the physical understanding between the forces on the aerofoil and its motion. The semi-empirical approaches are not computationally intensive and so are suitable for routine aeroelastic analysis. A good review of semi-empirical models of dynamic stall can be found in Leishman (2002). Examples of engineering tools applied to wind turbines with different degrees of success are a version of the *Onera* model as suggested by Peters (1985), the Oye (1991) model, and the Risø *fgh* model in Rasmussen (1995). Results from these three models can be found in the Final report for the Joule II Project, Dynamic Stall and 3–D Effects, Bjorck (1995). The agreement they achieved with 2–D tests on three different aerofoils was generally good when the model constants were appropriately tuned. Their simulation of field measurements on wind turbine blade sections reflected a reasonable representation of the main dynamic stall characteristics, but with less accuracy than for the 2–D wind tunnel measurements.

The work of other researchers, has also been directed towards the application of helicopter models to wind turbines. Gormont (1973) developed a dynamic stall

model derived from the so-called gamma function method (Harris *et al.* 1970), where the gamma function is an empirical function, which depends on aerofoil geometry and Mach number and is different for lift and moment stall. The *Gormont* method has been applied to the analysis of the yaw dynamics of HAWTs (Hansen *et al.* 1990). Application of the *Beddoes-Leishman* (Leishman and Beddoes 1989) model to wind turbines has demonstrated good agreement, in general, with measured data (Coton *et al.* 1994, Pierce and Hansen 1995, Bjorck 1995) and CFD calculations (Johansen 1999).

The inclusion of dynamic stall effects in wind turbine performance prediction codes has generally involved coupling a basic prediction method with some form of unsteady aerofoil predictor. This type of scheme, for example the unsteady prescribed wake model of Coton and Wang (1999), can provide very detailed information on the instantaneous loadings experienced by the blades. It does this, however, at a cost in terms of computation time and, because of the empirical nature of such models, may be prone to error. In the present work, the emphasis is not on predicting the effects of dynamic stall but, rather, on identifying where on the rotor dynamic stall is likely to occur. To do this, a correlation developed by Gracey *et al.* (1996) which indicates incipient dynamic stall onset is used. The correlation relates the dynamic stall onset incidence of an aerofoil to its stall characteristics in steady conditions and its reduced pitch rate.

4.3 Dynamic Stall Onset

Aerofoil Static Stall Onset

The study of flow separation from a solid surface, such as an aerofoil, and the way in which this separation affects the flow field, is one of the most fundamental and difficult problems of fluid mechanics. A separated flow when compared with a the-

oretical attached flow exhibits major differences, not only in terms of the trajectory, but also in terms of the aerodynamic forces produced on a body. It is well known that, normally, separation induces lost of lift, a sharp increase in drag and changes in the pressure distribution. Prandtl (1904) was the first to explain the physical mechanism of separation as being associated with a thin viscous region of particles that is always present near the solid surface, and which he called the boundary layer. Thus, the behaviour of the boundary layer in immediate contact with the surface was the agent provocateur for the air particles not to follow the contour of the surface and to separate from it. The mechanism for separation was explained by Prandtl as follows (Prandtl and Tietjens 1957). The boundary layer consists of fluid particles whose velocity/kinetic energy, decreases towards the surface. As we move away from the surface their velocity increases, until a point were they reach a constant velocity equal to the free particles of the stream; this being, the edge of the boundary layer. Because the velocity/kinetic energy of the particles inside the boundary layer appears to be less than at its outer edge, an increase in the pressure in the flow may cause the particles inside the boundary layer not to have the enough velocity/kinetic energy to keep moving. This causes the particles near the surface to stop and turn back into a reverse flow region, which characterises separated flows.

Despite progress in this field, Schlichting (1979), many aspects of boundary layer separation remain unresolved. Most notably, the theory remains predominantly restricted to incipient or small scale separations. Little is still known about three dimensional boundary layer separation and unsteady separation, for instance.

The flow over aerofoil sections has been studied and measured many times in wind tunnel experiments, as reported for example in Abbott and von Doenhoff's Theory of Wing Sections. Augmenting the angle of attack of an aerofoil in attached flow results in a linear increase in the lifting force. This progresses until the onset of flow separation, after which the increase of lift becomes non-linear. Static stall is

defined as the critical phenomenon that takes place when the extent of separation is such that the lift reaches a maximum value and begins to decrease with subsequent increases in incidence. An interesting work which describes the manner in which aerofoil sections stall was conducted by McCullough and Gault (1951). In their study, wind tunnel measurements were presented for a series of five aerofoil sections. The stalling characteristics of these aerofoil sections at low speeds are of three types:

- "Trailing-edge stall (preceded by movement of the turbulent separation point forward from the trailing edge with increasing angle of attack)". This appears primarily on thick aerofoils

- "Leading-edge stall (abrupt flow separation near the leading edge generally without subsequent reattachment)". This appears primarily on moderate thickness aerofoils

- "Thin-airfoil stall (preceded by flow separation at the leading edge with reattachment at a point which moves progressively rearward with increasing angle of attack)". This appears primarily on sharp edged aerofoils or, on rounded edge thin aerofoils.

The effect that flow separation has on the aerodynamic loads on an aerofoil can be estimated using quite simple models such as the Kirchhoff model which, for the case of 1–D steady flow, provides an estimated effect of the variation of the separation point along the chord at a given angle of attack. Modifications to the Kirchhoff separation model, in order to introduce 2–D geometry (chordal variation) have been attempted by Kuchemann in 1950, (Kuchemann 1978), and later by Beddoes (1991) for 2–D steady flow. These studies were concerned with static stall, where the stall is nominally steady, repeatable, and, in addition, the flow and geometry of the body is considered to be two dimensional.

Unsteadiness, and a 3–D geometry obviously introduces variations from 2–D steady flow conditions, and the process of separation can be significantly different. Under dynamic conditions, the two-dimensional flow separation process behaves differently from the one-dimensional case, and may be significantly different to dynamic stall on a three-dimensional body, Coton *et al.* (2001).

Aerofoil Dynamic Stall Onset

The exact nature of the mechanism which triggers the formation of the 2–D dynamic stall vortex is still unclear although, at low Mach numbers and for aerofoils which display a smooth static trailing edge stall, there are indications that dynamic stall onset is related to the steady trailing edge flow. The dominant nature of the vortex formed near the leading edge has ,however, focussed research efforts on the determination of its initiation mechanism.

Through experimentation, McCroskey *et al.* (1976) identified four different boundary layer phenomena as possible sources of vortex inception and therefore of dynamic stall onset. These dynamic stall triggers were separated into two categories: the first pair were termed leading edge mechanisms, whilst the last two were termed abrupt trailing edge and trailing edge respectively, these are

- the bursting of the laminar separation bubble.
- the appearance of transonic flow at the leading edge (M_∞ >0.2).
- the abrupt breakdown of the turbulent flow over the forward portion of the aerofoil, commonly known as reseparation.
- the arrival, at the leading edge region, of a thin stratum of reversed flow traveling upstream from the trailing edge.

These mechanisms have been reviewed in detail by Young (1984). Several meth-

ods have been employed in order to asses the moment of dynamic stall onset. Carta (1974) employed pressure coefficient histories as a technique to asses the incipient dynamic stall. Scruggs *et al.* (1974) defined dynamic stall onset as the incidence at which there is a sudden deviation in the gradient of the lift curve. Beddoes (1976) studied its inception from the examination of airloads, i.e. C_n, whereas Wilby (1980) determined a critical angle, which if exceeded meant that dynamic stall was unavoidable, based on the break in pitching moment under oscillatory tests. Wilby (1984) later suggested that the dynamic stall incidence could be taken as the angle of attack at which the pressure coefficient at 0.5% chord was at a minimum since this was easier to define than a pitching moment break. Lorber and Carta (1987), monitored the vortex by means of a variation in the unaveraged pressure readings, over the aerofoil.

Gracey *et al.* (1989), in a consideration of low speed dynamic stall onset, presented a review of the various studies. They decided that dynamic stall onset could be detected by examination of the pressure response at discrete chordwise locations. This was based on a previous analysis by Seto and Galbraith (1985), who established a criterion for indicating that the dynamic stall process had been initiated. At low pitch rates they observed that the form of the pressure profile history was largely unaltered, although significant lift and moment overshoots were evident. They labelled this response "quasi-static" and observed the limit of this regime as being at a reduced pitch rate of 0.01. For higher reduced pitch rates, prior to the suction peak collapse, they observed evidence of a vortex and the dynamic overshoot of C_n and C_m, associated with dynamic stall. As in the manner of Carta (1974), the first indication that the dynamic stall vortex had been initiated was found to be when a sudden and abrupt deviation in one of the C_p traces was observed, normally on the upper surface in the vicinity of 25% chord. The incidence at which this C_p deviation occurred was defined as being at the intersection of two straight lines through data

points immediately before and after the onset. They remark that this incidence is the earliest indication of dynamic stall onset that can be observed from experimental data but is not the stall trigger. This indicator, C_p deviation was used by Gracey *et al.* (1996), to develop the correlation described later in this chapter.

4.4 2–D Dynamic Stall Onset Predictor

Dynamic stall is a term used to describe the complex series of events, which occur when a rapidly pitching aerofoil, or blade, stalls. The phenomena which are manifest in such cases are quite different from those associated with nominally steady flow and, as previously mentioned, have a significant impact on the loads produced and in the power quality generated by the turbine. The aerofoil incidence is the major determinant of aerodynamic response. Instantaneous incidence generally is a function of the axial and tangential induction factors, the inlet flow V_∞ , blade rotational velocity $\Omega \times r$, and turbine yaw,γ. Rapid changes in these variables alter the incidence dynamically and may induce dynamic stall. This will occur if the blade is effectively pitched up through stall from below the incidence of static stall at a sufficiently high pitch rate. If this happens, the stall will be delayed well beyond the incidence of static stall and the blade loads will continue to rise Robinson *et al.* (1995). As stall develops, large fluctuations in lift, drag and pitching moment, which are potentially detrimental to the structural integrity of the turbine, will be experienced by the blades.

When HAWTs operate in yawed inflow they are subject to a cross wind which produces a velocity component tangential to the rotor that varies with ψ, the blade's azimuthal position. As seen in Eq. (2.32) in the yawed Flow Model section of Chapter 2, this velocity, $V_t = \Omega r + V_c \cos\psi$, implies that the angle of attack of the blade section will vary in a cycle. The angle of attack at the blade is therefore no

longer constant around the azimuth. This cyclic variation in incidence results in an effective pitching of the turbine blade. If the reduced frequency of this pitching is high enough, unsteady effects are manifest, deviating the loading from the steady values. If unsteady effects become severe they may result in dynamic stall.

The present work focuses on the detection of regions of dynamic stall on the rotor disc. The occurrence of dynamic stall depends primarily on the rate at which the blade is pitched and the incidence that it achieves during the pitching motion. In the present predictive scheme, these parameters are used, via a correlation developed by Gracey *et al.* (1996), to identify the likely onset of dynamic stall. The manner in which this relationship is used in the present scheme, both as an indicator and predictor of dynamic stall is fully described in next section.

4.4.1 The Method

The correlation attempts to relate the dynamic stall onset incidence of an aerofoil to its stall characteristics in steady conditions and its reduced pitch rate. The parameters in this correlation, which can be derived from experiment or predictive algorithm, are the incidence of steady stall and a term related to the trailing edge separation characteristics.

Progressive trailing edge separation appears to be involved in most types of stall Beddoes (1983). Wilby (1984) from experimental tests suggested that trailing edge separation may play a significant role in the onset of dynamic stall. In HAWT experiments Huyer *et al.* (1996) observed this movement of the trailing edge separation point, which produces a loss of circulation and introduces non-linearities in the force coefficients.

Calculation of the movement of the separation point can be performed using a coupled boundary layer/separation calculation. Alternatively, an approximation to the location of boundary layer separation at any angle of attack for an aerofoil

experiencing trailing edge separation in steady flow has been described by Beddoes (1983) based on Kirchhoff flow theory.

Kirchhoff Flow Theory

Kirchhoff theory models (uniform, inviscid) separated flow regions on 2–D bodies, (Thwaites 1960). A specific case, with $C_p = 0$ in the wake, has been derived by Kirchhoff for separated flow past a 2–D flat plate in which the normal force (lift) C_n is related to the separation point $f = x/c$ by

$$C_n = C_{n_\alpha} \left(\frac{1 + \sqrt{f}}{2} \right)^2 (\alpha - \alpha_0) \tag{4.1}$$

where C_{n_α} is the normal force (lift) curve slope, f is the non dimensional separation point in terms of x/c measured along the chord from the leading edge to the trailing edge, α is the angle of attack, and α_0 the angle of attack corresponding to zero force. Thus, if the separation point is determined then the normal force can be calculated directly from the above Eq. (4.1), or vice versa.

Physically f is related to the divergence point of the separated streamline but, for the steady case, this approximates to the boundary layer separation point. The relationship between the separation point f and the angle of attack α, which depends on the shape of the aerofoil, can be calculated by inserting C_n data obtained from aerofoil wind tunnel tests into Eq. (4.1) rearranged as

$$f = 4 \left[\sqrt{\frac{C_n}{C_{n_\alpha} (\alpha - \alpha_0)}} - \frac{1}{2} \right]^2 \tag{4.2}$$

The variation of the separation point with angle of attack can be modelled as

described in Beddoes (1983) by two exponential equations that are matched at the 70% chord location. These equations generalise into the form

$$f = \begin{cases} f_{max} + K_1 \exp\left[\dfrac{\alpha - \alpha_1}{S_1}\right] & \text{for } \alpha \leq \alpha_1 \\ f_{min} + K_2 \exp\left[\dfrac{\alpha_1 - \alpha}{S_2}\right] & \text{for } \alpha > \alpha_1 \end{cases} \tag{4.3}$$

where α represents the angle of attack and f is the separation point in the non-dimensional form x/c. The seven terms, $f_{max}, f_{min}, K_1, K_2, S_1, S_2$ and α_1 are constants for a particular aerofoil and Reynolds number under steady conditions.

The constant f_{max} represents the maximum value that the separation point reaches at very small incidence α, $f_{max} = 1$. The constant f_{min} represents the location of bluff body separation, at high incidence and is approximately equal for each aerofoil, $0 < f_{min} < 0.0025$. K_1 and K_2 are constants for each aerofoil obtained from curve fitting Eq. (4.3). The coefficients S_1 and S_2 define the static stall characteristic, while α_1 defines the break point corresponding to $f = 0.7$, which is very near to the value of the angle of attack for static stall onset. S_1, S_2, and α_1 can easily be determined from wind tunnel static lift data.

It follows that, forward of the 70% chord location, for $\alpha > \alpha_1$

$$\frac{\mathrm{d}f}{\mathrm{d}\alpha} = -{S_2}^{-1} K_2 \exp\left[\frac{\alpha_1 - \alpha}{S_2}\right] = -{S_2}^{-1} (f - f_{min}) \tag{4.4}$$

Using an unsteady boundary layer model, Scruggs *et al.* (1974) demonstrated that there was a high degree of correlation between the incidence at which computed flow reversal reached the 50% chord location, and the experimentally-assessed incidence of dynamic stall. It was also note that this flow reversal was delayed with increased pitch rate. Eq. (4.4) indicates that the rate of change of separation point with incidence at the 50% of chord location , $f = 0.5$, is approximately proportional

to $S_2{}^{-1}$. On this basis, Gracey *et al.* (1996) suggested that S_2 may be a suitable parameter to link static trailing edge separation and vortex inception.

The Correlation

The correlation is based on wind tunnel data obtained by Galbraith *et al.* (1992) for seven smooth clean aerofoils. These tests, conducted at a Reynolds number of 1.5 x 10^6 with natural boundary layer transition, were for ramp motions covering a reduced pitch rate range $0.0001 \leq \alpha^+ \leq 0.037$, and for oscillatory tests over a reduced frequency range of $0.01 \leq k \leq 0.2$.

In the fully dynamic stall regime, the incidence of stall onset varies linearly with reduced pitch rate. By consideration of this behaviour and the assumption that the incidence of static stall, α_{ss}, corresponds to a limiting case which can be regarded as a ramp at zero pitch rate, it was possible to develop an effective stall onset correlation based on S_2. This correlation was extended down into the quasi-steady stall regime by switching the indicator from vortex inception to peak suction collapse. This is possible because of an apparent convergence of vortex inception and suction collapse on the upper boundary of the quasi-steady regime as seen in by Gracey *et al.* (1996) The final form of the correlation is

$$\alpha_{ds} = -5.428 + 1.379\,\alpha_{ss} + 111.677 {S_2}^{1/4}\alpha^+ + 42.723({S_2}^{1/4}\alpha^+)^{1/2} \qquad (4.5)$$

where α_{ds} is the resulting incidence angle for dynamic stall onset, α_{ss} is the incidence of static stall, S_2 is related to the slope of the static separation point curve as seen in Eq. (4.4) and α^+ is the non-dimensional rate of change of angle of attack, reduced pitch rate, represented in the form

$$\alpha^+ = \frac{\frac{\mathrm{d}\alpha}{\mathrm{d}t}c}{2W} \qquad (4.6)$$

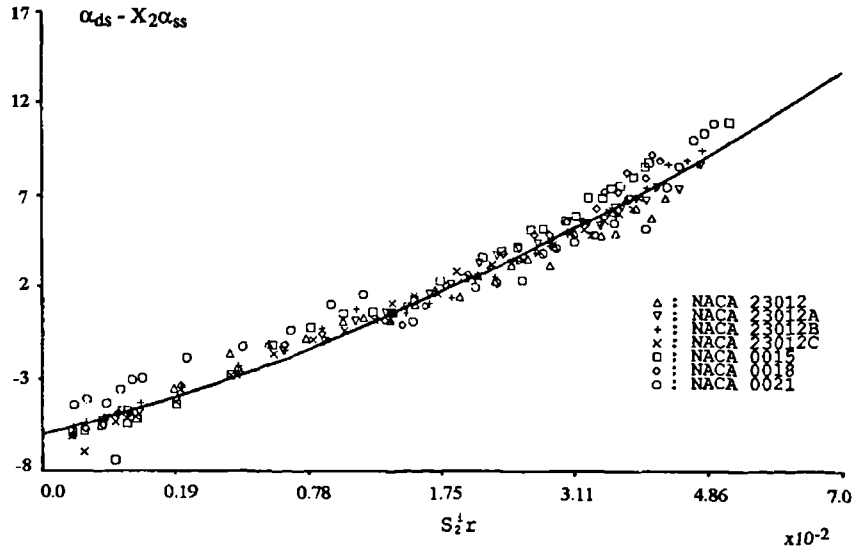

Figure 4.1: *Correlation of C_p deviation incidences, (source: Gracey et al. 1986)*

Gracey *et al.* (1996) demonstrated the effectiveness of the correlation for constant pitch rate ramp motions. In particular, Figure 4.1 illustrates the level of correspondence between the correlation and measured stall onset from wind tunnel tests on seven aerofoils tested by Galbraith *et al.* (1992). The formulation $\alpha_{ds} - 1.379\,\alpha_{ss}$ is plotted against ${S_2}^{1/4}\alpha^+$ over the entire range of reduced pitch rate displaying a good agreement. Particularly interesting to note is the narrow scatter in the experimental data. This is evidence of the suitability of S_2 as an appropriate parameter.

In the case of a yawing wind turbine, the pitch rate experienced by the blades is not constant and so application of the correlation is more problematic. Gracey *et al.* (1996) proposed the following solution for oscillatory cases: "If the mean incidence of the oscillatory cycle is such that the pitch rate through the incidence at which onset is deemed to have occurred is still greater than zero but not significantly lower than the maximum pitch rate in the cycle, then the maximum reduced pitch rate which the aerofoil experiences in the cycle should be used as the representative parameter".

Whilst this may be possible when considering the incidence variation produced by yawed onset flow, it is unlikely to be practical when considering the rapid incidence variations in the tower shadow domain. For this reason, it was decided to apply the correlation directly at each calculation point using the reduced pitch rate and incidence at that point. Whilst this may produce some errors in pinpointing the absolute location of stall onset, the general regions of dynamic stall on the rotor should still be identified. Using the correlation in this way, dynamic stall would be expected if the instantaneous local angle of attack α, predicted by the BEM routine is greater than the dynamic stall angle α_{ds}, given by the correlation, Eq. (4.5).

4.4.2 Results

In this section, the model will be applied to the NREL Phase II and Phase IV wind turbines. The NREL Phase II machine is a downwind, three-bladed, stall regulated wind turbine. The rotor diameter is 10.06 m. operating at 72 rpm and it rotates clockwise, viewed from downwind. The three blades are untwisted, untapered and have an NREL S809 aerofoil section with a 0.457 constant chord. The blades were set at a constant +12° pitch angle.

The Phase IV turbine has highly twisted blades, set at a constant +3° pitch angle, the rest of the configuration is the same as the Phase II machine. Both turbines are supported on a 0.4064 meter diameter cylindrical tower.

4.4.3 Regions of Dynamic Stall: NREL UAE Phase II

At azimuth angle $\psi = 0°$, the turbine blade is pointing straight up (12 o'clock), and at $\psi = 180°$ the turbine blade is aligned with the cylindrical tower. It should be noted that the results plotted here correspond to an observer located downwind, facing the wind, who will see the rotor in front of the support tower. Thus, the direction of rotation is clockwise for the reader and observer.

The onset of dynamic stall depends to some extent on the rate of change of incidence of the blade. As discussed previously, this is represented in the dynamic stall onset correlation by the reduced pitch rate parameter α^+. The variation of this parameter on the rotor disc for the zero yaw case is presented in Figure 4.2(a). As may be expected, the only region of the disc where there is any temporal rate of change of incidence is in the tower shadow. It should be noted that in the first half of the tower shadow the incidence is decreasing before increasing in the second half. Because of this, the only region of the disc susceptible to dynamic stall is the region of exit from the second half of the tower shadow domain and,

as may be observed in Figure 4.2(b), dynamic stall onset, identified by the contoured region, is predicted there on inboard blade sections. It should be noted that the contoured region indicates a region where the instantaneous blade incidence is higher than the predicted dynamic stall angle. Dynamic stall onset is possible anywhere within this region but, at a given radius, and considering the direction of rotation, clockwise for the reader/observer, the most likely location of dynamic stall onset is the point where the blade first penetrates the region.

Effect of Changes in Yaw

If the turbine operates in a yawed flow, the blades are then subject to a cyclic variation in incidence. If this variation is severe enough, in terms of incidence and pitch rate, then dynamic stall can be induced. Figure 4.2(e) shows the variation in reduced pitch rate on the rotor disc for a yaw angle of +30°. It is immediately apparent that much more of the disc is potentially vulnerable to dynamic stall than in the previous case. The region of tower shadow has moved ahead of the 180° location because of the fact that the tower is separated by a finite distance from the rotor plane. In addition to this region, however, there is also an area of high positive reduced pitch rate on the left-hand side of the disc, which arises from the yawed

onset flow. Application of the dynamic stall onset correlation to this case yields Figure 4.2(f) which shows that dynamic stall would indeed be manifest over a large region of the disc. It is interesting to note here that dynamic stall onset appears to be triggered by both the tower shadow and the basic cyclic variation in incidence resulting from yawed flow operation. It appears, from these results, that the latter may be the most significant influence. Once again, it should be noted that the most likely location of dynamic stall onset is the point where the blade first penetrates the contoured region. On this basis, and considering the direction of rotation, clockwise for the reader, it would appear that dynamic stall will be initiated first on inboard sections and then spread progressively outboard from 47% to almost 90% of the rotor radius.

When the dynamic stall correlation is applied to the +15° of yaw case, Figure 4.2(d), the region of predicted stall onset is apparently decreased from the +30° of yaw case. In fact, the actual boundary of the onset region does not extend as close to the blade tip, reaching only 70% of the blade radius. The result indicates that dynamic stall would be likely to be more confined to a specific azimuth range. One possible explanation for this is forthcoming from examination of Figure 4.2(c), which shows the contours of reduced pitch rate for the +15° of yaw case. Here, on the left half of the rotor, the boundary contour of reduced pitch rate which delimits the possibility of vortex onset is more confined in azimuth making this case less susceptible to dynamic stall. Once again, it is interesting to note that stall appears to be initiated on inboard sections of the rotor before progressing out. In addition, the stall onset boundary associated with the exit from tower shadow becomes more defined as the yaw angle decreases.

Effect of Changes in Wind Velocity

The effect of changing wind velocity at a fixed yaw angle may be observed in Fig-

ure 4.3 for a yaw angle of +30°. In this case, the stall onset boundary extends progressively towards the outer edge of the rotor disc as the wind velocity increases. It is also interesting to note that this is true for both the section of the boundary associated with the exit from tower shadow, just before $\psi = 180°$, and that resulting from the cyclic variation in incidence. The reason for this lies in the increase in local angle of attack when the wind velocity augments. In Figure 4.4, the angle of attack distribution over the rotor disc is shown for the three cases presented in Figure 4.3.

It may be observed that the angle of attack contours are slightly asymmetric due to the constant yaw angle of +30° in all the three plots. As the wind velocity increases the local angle of attack increases at all azimuth and span locations. Thus, the stall threshold is more severely penetrated at high wind speeds thus increasing the possibility of dynamic stall occurrence.

A previous study by Huyer *et al.* (1996) identified dynamic stall onset by analysis of experimental measurements from the NREL Unsteady Aerodynamics Experiment, UAE Phase II untwisted blade tests. The azimuth angles at which dynamic stall was identified are compared with the code prediction in Figure 4.5 for a yaw angle of +30° and a wind velocity of 15 m/s. The measured dynamic stall onset locations are plotted at three radial locations along the rotor: 30%, 47% and 63% of span. At 30% of span, the prediction agrees very well with the field measurements. Further outboard the prediction progressively lags the field data. It is interesting to note that no dynamic stall was identified outboard of the 80% of span location. This is consistent with the prediction from the model. There are several possible reasons for the differences between the predicted and measured onset locations. In all the cases previously studied, it is interesting to note that the regions of dynamic stall are predominantly located on inboard blade sections where three-dimensional stall delay would be expected. It is likely that three-dimensional effects will influence the dynamic stall process but not necessarily in the way they influence static stall.

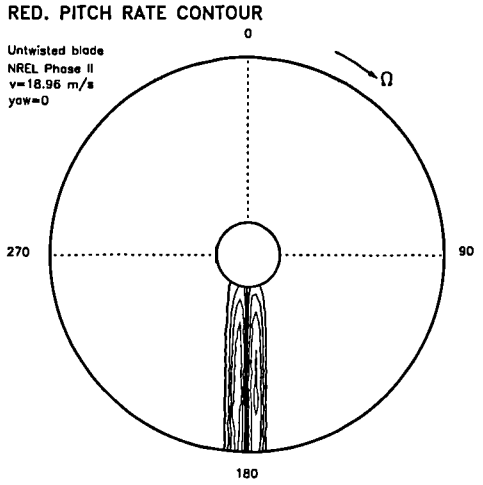

(a) α^+ Reduced Pitch Rate, yaw=0°

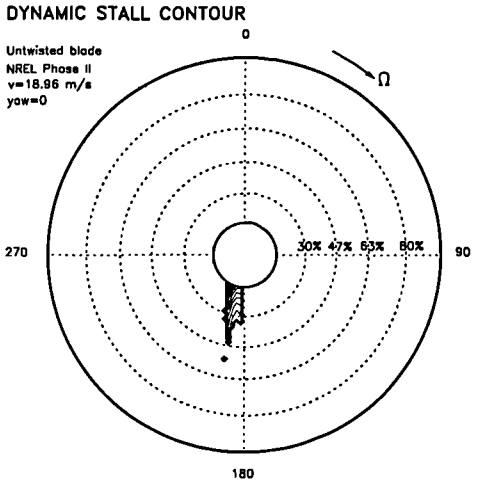

(b) Dynamic Stall, yaw= 0°

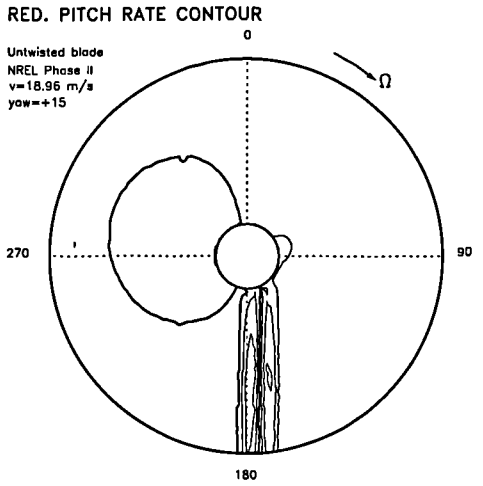

(c) α^+ Reduced Pitch Rate, yaw=+15°

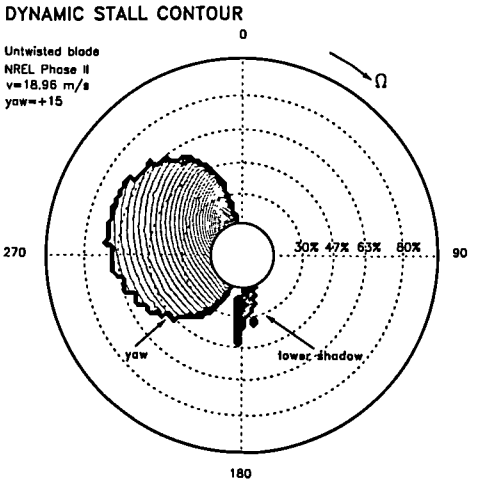

(d) Dynamic Stall, yaw=+15°

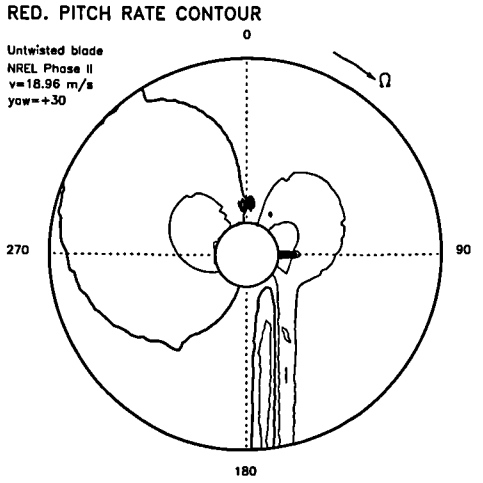

(e) α^+ Reduced Pitch Rate, yaw=+30°

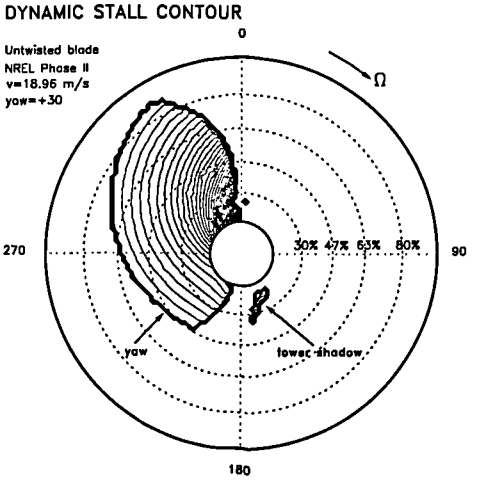

(f) Dynamic Stall, yaw=+30°

Figure 4.2: *Dynamic Stall, wind velocity=18.96 m/s, NREL Phase II*

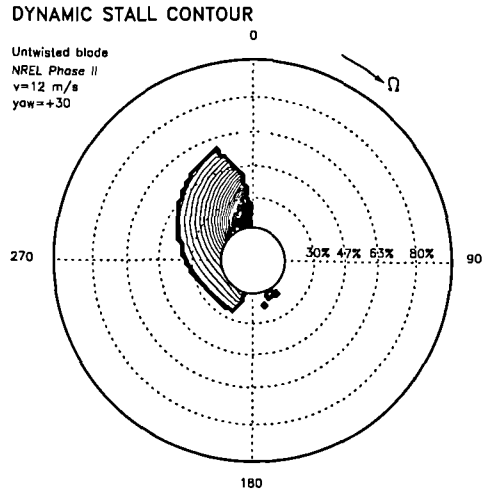

(a) wind velocity=12 m/s

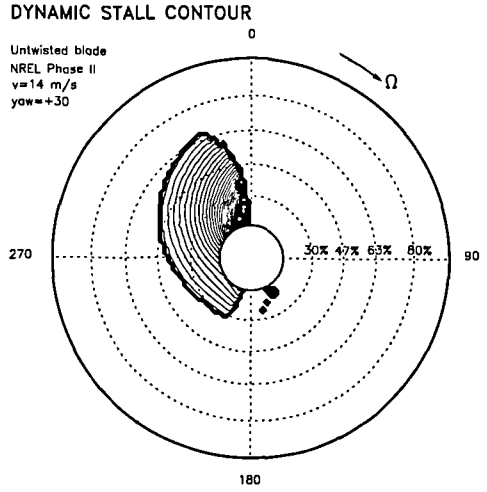

(b) wind velocity=14 m/s

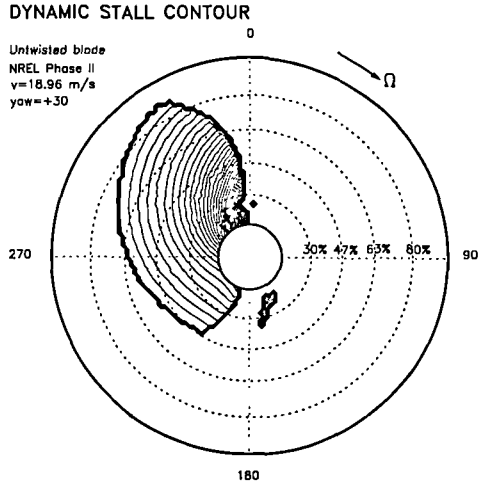

(c) wind velocity=18.96 m/s

Figure 4.3: *Effect of wind velocity at yaw=+30°, NREL Phase II*

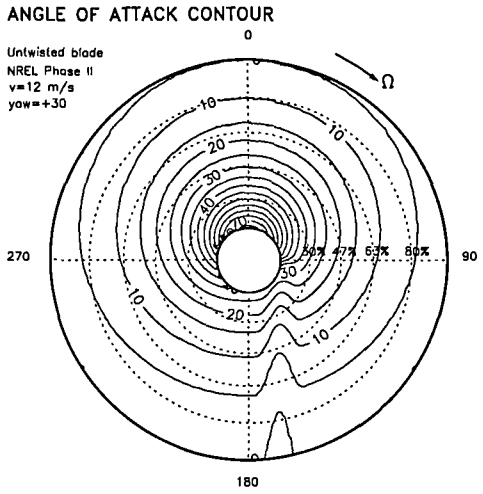

(a) wind velocity=12 m/s

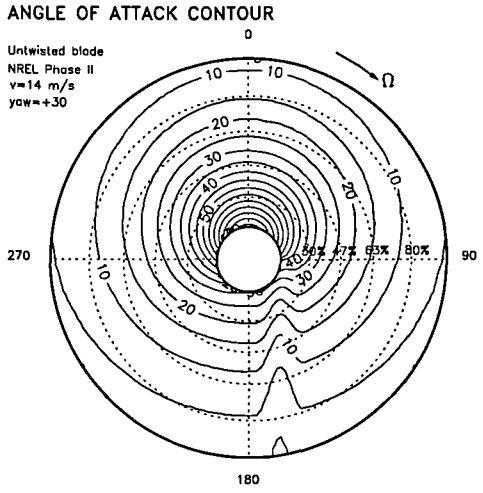

(b) wind velocity=14 m/s

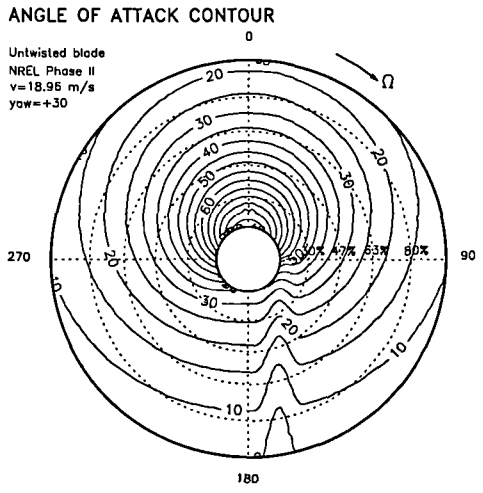

(c) wind velocity=18.96 m/s

Figure 4.4: *Angle of Attack for Fig 4.3, NREL Phase II*

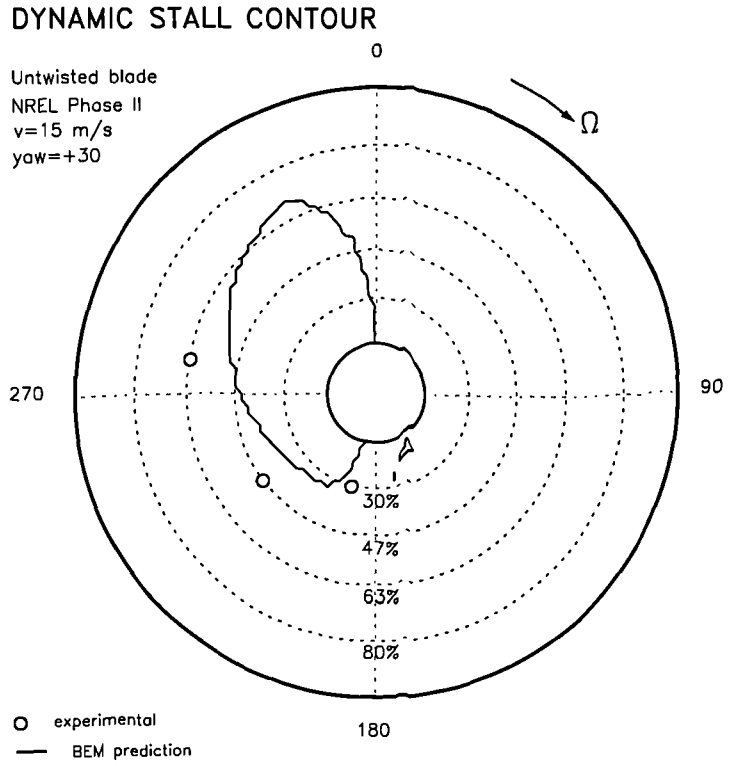

wind velocity=15 m/s, yaw=+30°

Figure 4.5: *Dynamic Stall prediction compared to measurements, NREL Phase II*

Recently Coton and Galbraith (1999) demonstrated that dynamic stall onset on a finite wing was a strongly three-dimensional phenomena. They observed that, during pitching motion, dynamic stall was initiated at the mid-span of the wing. This then triggered dynamic stall on outboard sections earlier than would have otherwise been expected. This may explain the apparent lag in the prediction when compared with the test data in the present case. Following a similar argument, it is also possible that on a wind turbine, where strong spanwise flows develop once flow separation has been initiated, that the simplistic nature of the present 2–D correlation may be somewhat compromised if the movement of the separation point is influenced by 3–D flows. In the actual correlation, the separation process is founded on the parameter S_2 and the static stall angle based on 2–D aerofoil data. On the other hand it is possible that the tuning of the constants in the present correlation, will

allow a closer agreement with the experiment to be obtained.

4.4.4 Regions of Dynamic Stall: NREL UAE Phase IV

The method was applied to the NREL UAE Phase IV turbine to illustrate the effect of blade twist on the occurrence of dynamic stall.

On the Phase IV machine, the blade twist distribution, Figure 4.6, was optimised to yield an angle of attack of 15° along the entire blade at a pitch angle of +3° and a wind speed of 8 m/s. Designers hoped to maintain a constant angle of attack along the entire blade span in order to have a progressive stall over the blade span. On the other hand, this may have the undesirable effect of causing the entire blade to stall dynamically instead of just over a limited section. If this is correct, it could be argued that, when a particular twist distribution is being implemented on the blade the dynamic stall onset should be considered in the design process.

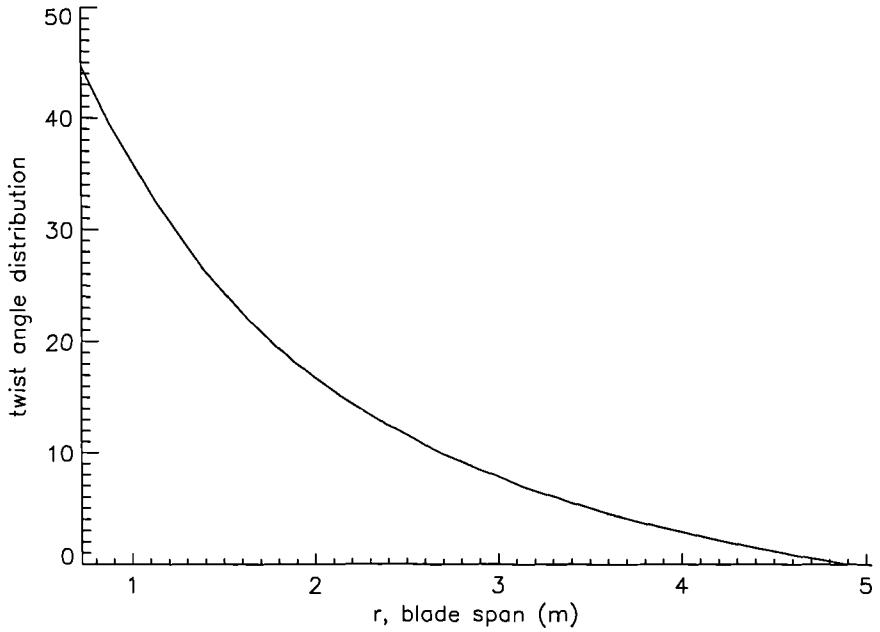

Figure 4.6: *Twist angle distribution for NREL Phase IV wind turbine*

The angle of attack distribution for three wind velocities, 12, 14 and 18.96 m/s

at +30° yaw angle on the Phase IV twisted blade, may be seen in Figure 4.7. This figure can be directly compared to the Phase II untwisted blade cases presented in Figure 4.4. Some significant differences may be observed. On the Phase II untwisted blade Figure 4.4 the angle of attack contours follow a concentric pattern around the hub with a small eccentricity about the 0° azimuthal axis, due to the yaw error. However, in Figure 4.7, for the Phase IV turbine, the overall angle of attack map differs considerably. The concentric incidence contours are localised at the top half of the rotor, and have a higher eccentricity. As a result, in the 45 to 315° azimuthal region, the contours are more radially aligned. This effect is very marked in the tower shadow region. The magnitude of the angle of attack values are also significantly different. For example, at $\psi = 0°$ the untwisted Phase II blade in Figure 4.4 exhibits a maximum angle of attack range of approximately 50° to 70° at the 30% of span location. The twisted Phase IV blade, however, has maximum angle of attack values of approximately 32° to 55° at the same azimuth and span. In the tower shadow region the incidence distribution has change dramatically. For the untwisted blade, the angle of attack can reach 30 ° on the most inboard sections, while for the twisted blade the angle of attack values are lower than 15 °.

Effect of Changes in Yaw

In Figure 4.8 the predicted regions of dynamic stall onset are presented for a fixed wind velocity of 14 m/s at three different yaw angles. At zero yaw, there is no indication of dynamic stall onset, even at the exit from tower shadow. The effect of yaw angle on the location and shape of the regions of stall onset is reflected in the +15 and +30° yaw cases. In general, the region of stall onset is much more localised than on the Phase II turbine and there is no evidence of dynamic stall induced by the tower. Comparison of Figure 4.8(c) with Figure 4.3(b) illustrates this effect clearly. It is, however, interesting to note that the radial extent of dynamic stall in this

particular case is greater on the Phase IV machine than on the Phase II turbine. In fact, over a much wider range of cases, it can be demonstrated that the likelihood of dynamic stall on the Phase IV turbine is much less than on the Phase II machine. This agrees well with the observations of Acker and Hand (1999) from field data.

Effect of Changes in Wind Velocity

The effect of increasing wind velocity on the occurrence of dynamic stall on this turbine is shown in Figure 4.9 for a yaw angle of +30°. This figure can be compared directly with Figure 4.3 for the Phase II turbine and shows one particularly interesting result. Whilst the Phase IV machine is generally less susceptible to dynamic stall, this is not the case at high wind velocities. It appears that the entire rotor blade may experience dynamic stall at wind velocity 18.96 m/s. In this case, Figure 4.9(c), stall is being initiated on outboard sections first, at around 63% of span, progressing very quickly along the blade span. Eventually, except for the most outer portion of the tip, the stall covers the entire span of the blade.

An interesting case of dynamic stall initiation along the blade, at wind speed 18.96 m/s, is shown for a yaw angle of +15° in Figure 4.10. With the blade rotating clockwise, the first stall event occurs on the lower half of the rotor just after 180° azimuth. The dynamic stall for this cycle initially occurs inboard, at around 30% of span, and then moves in both directions outboard towards the tip, and inwards towards the hub. This figure can be directly compared to the dynamic stall onset for the untwisted blade at the same inflow conditions presented in Figure 4.2(d). In Figure 4.10, the twisted configuration presents no signs of dynamic stall due to the blade passing the tower shadow region. However, in Figure 4.2(d) dynamic stall induced by the tower, can be clearly identify at 180° azimuth and almost reaches 47% of span for the untwisted blade. In addition, it can be observed that the yaw induced dynamic stall onset on the left hand side of the rotor occupies, in

both cases, a similar portion of the blade span and a similar azimuthal location in the rotational cycle. However, the progression of stall is significantly different. In contrast to Figure 4.2(d) where the untwisted blade stall onset is triggered at the most inboard radial positions, near the root hub, and progresses outwards towards the tip, the dynamic stall for the twisted blade planform moves in both directions towards the tip and towards the root hub. This behaviour is particularly interesting and suggests that the flow field structure on the twisted blade differs substantially from the untwisted planform.

The dynamic stall occurrence for wind velocity 18.96 m/s, corresponding to a tip speed ratio of $\lambda = 2$, and yaw angle of 5°, is presented in Figure 4.11. The motivation for such a yaw error calculation was the possibility of identifying tower shadow induced dynamic stall which, has not been observed in any of the previous Phase IV calculations. In fact, in Figure 4.11 it may be observed that, just after $\psi = 180°$, a very narrow region of dynamic stall appears near the hub as the blade leaves the tower shadow. At around $\psi = 270°$ another region of dynamic stall can be seen, this time due to the yawed inflow condition.

In addition to examining the effect of twist, the effect of varying the tip pitch angle has been calculated for wind velocity=18.96 m/s and yaw angle=+30° . It is shown in Figure 4.12 that a decrease from pitch=+3° (solid line) to pitch=+2.3° (dashed line), does not, in this particular case, alter the radial extent of dynamic stall. It does, however, appear that a smaller tip pitch angle provokes dynamic stall to occur at later times in the rotor cycle.

This tip pitch angle deviation appears to happen under normal operating conditions during the life of the turbine, as well as during data collection experiments like on the NREL Phases II to IV, which suffer from non-desirable variations of the fixed blade pitch angle over a range of ±1°, (Simms *et al.* 1999).

The effect of blade parameters on the extent of dynamic stall occurrence on a

wind turbine blade has been examined. It has been shown that the extent of dynamic stall onset, both in terms of azimuthal location and span position, is dependent of the inflow conditions and the blade planform, twist and pitch angle. The strong dependence on blade planform shape is particularly interesting and the identification of this behaviour demonstrates the capability of the present model to provide input to the design process.

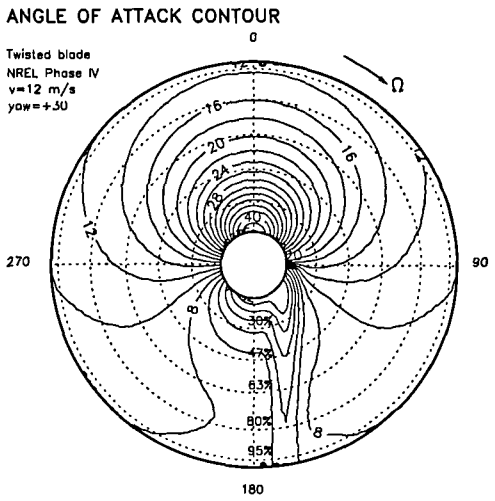

(a) wind velocity=12 m/s

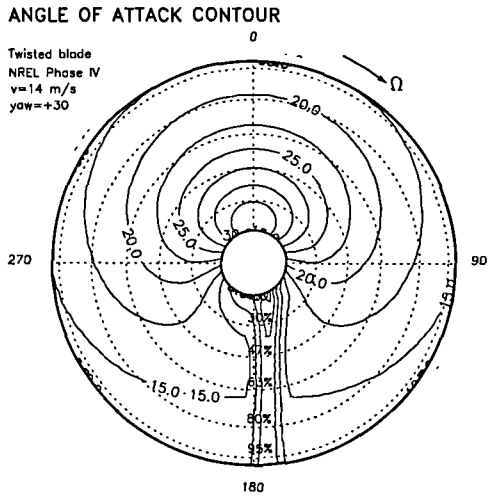

(b) wind velocity=14 m/s

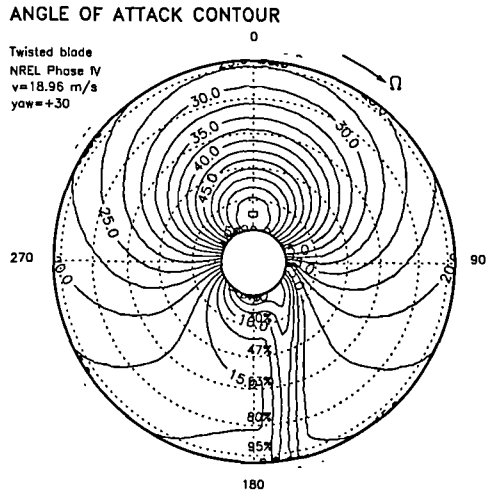

(c) wind velocity=18.96 m/s

Figure 4.7: *Effect of Twist distribution on incidence, NREL Phase IV*

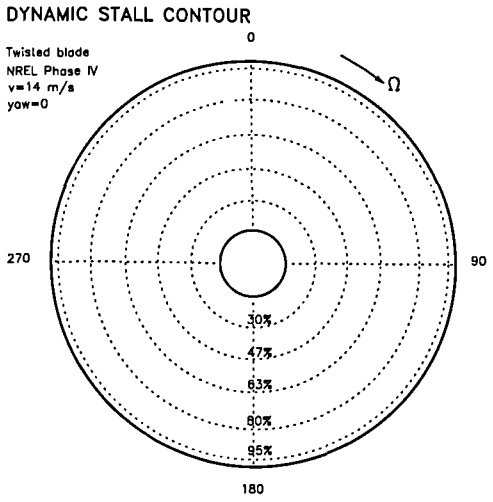

(a) yaw=0°

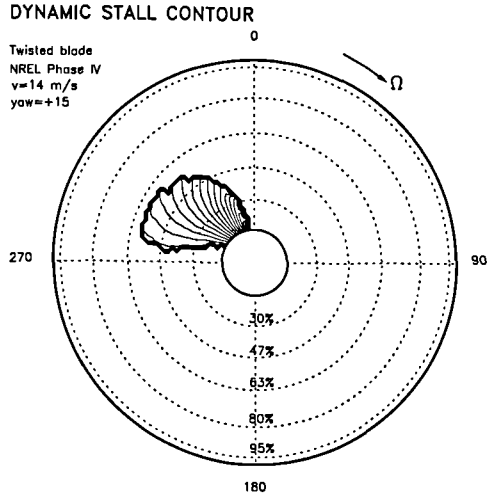

(b) yaw=+15°

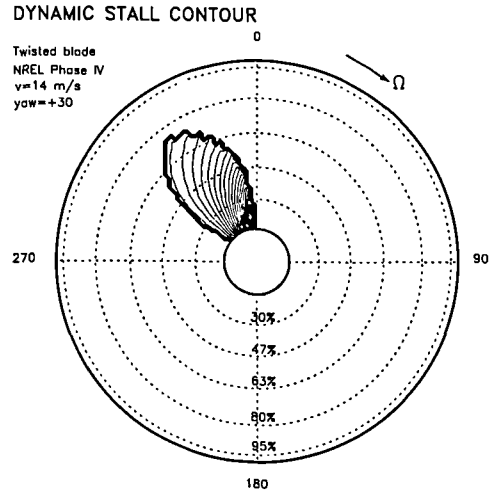

(c) yaw=+30°

Figure 4.8: *Effect of yaw at wind velocity=14 m/s, NREL Phase IV*

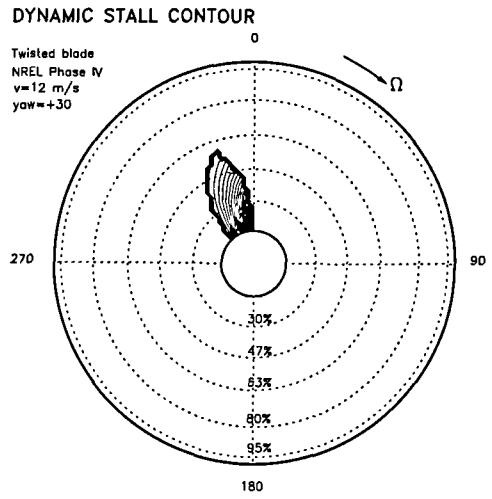

(a) wind velocity=12 m/s

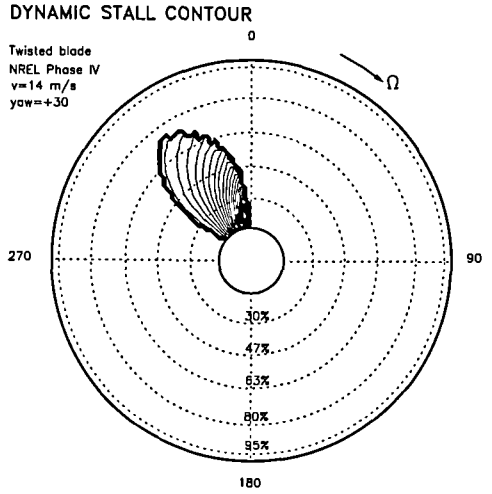

(b) wind velocity=14 m/s

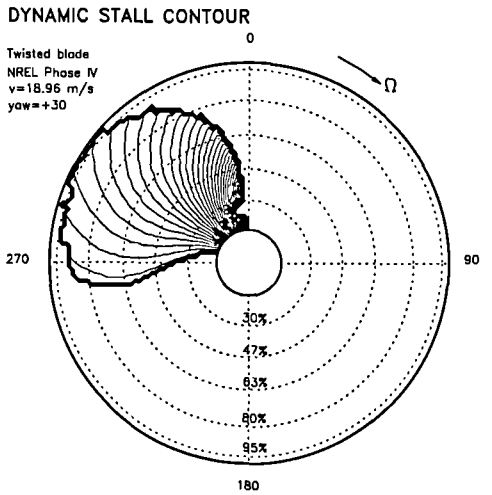

(c) wind velocity=18.96 m/s

Figure 4.9: *Effect of wind velocity at yaw=+30° , NREL Phase IV*

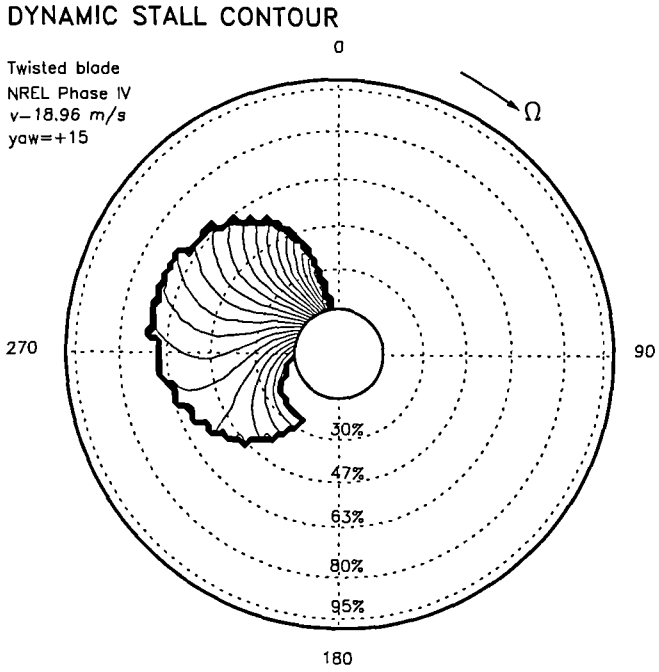

wind velocity=18.96 m/s

Figure 4.10: *Effect of wind velocity at yaw=+15°, NREL Phase IV*

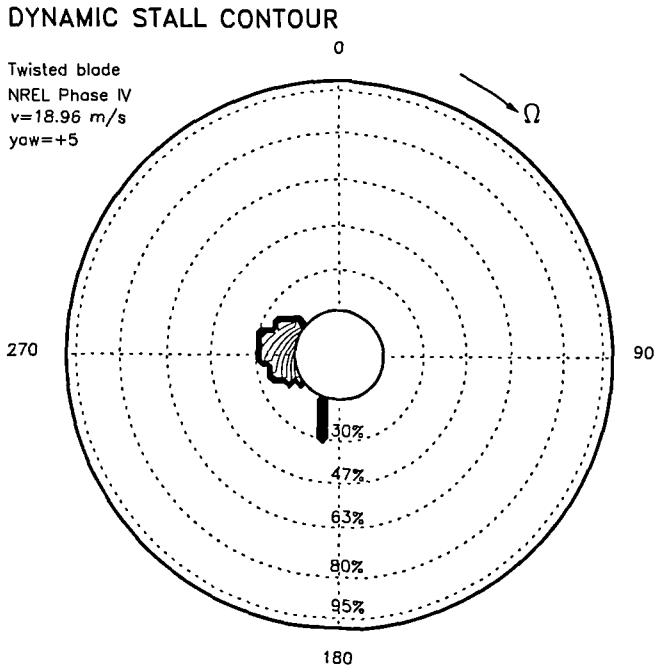

wind velocity=18.96 m/s

Figure 4.11: *Effect of wind velocity at yaw=+5° , NREL Phase IV*

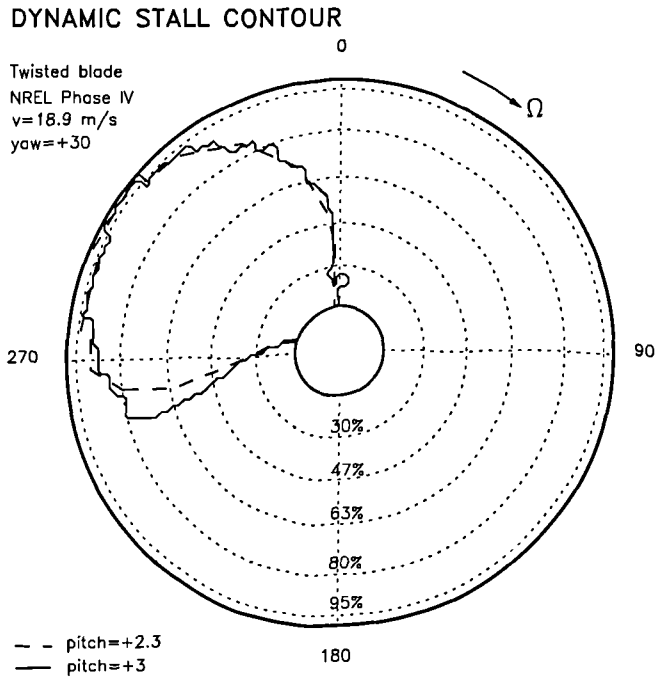

wind velocity=18.96 m/s, yaw angle=+30°

Figure 4.12: *Effect of pitch angle, NREL Phase IV*

Prediction Compared to NREL Phase IV Measurements

Schreck *et al.* (2000) identified dynamic stall onset on the Phase IV turbine by analysis of experimental measurements. This work provided an opportunity to validate the present technique against field data. The entirety of Phase IV data comprises 75 campaigns, each of 10 minutes of recorded samples. The results documented herein were derived entirely from campaign d403022, which NREL judged to be typical of Phase IV data in terms of mean wind velocity, 10.1 m/s and mean yaw error, −11.5°. The average pitch angle during campaign d403022 is +2.3°; note that average pitch angle during all 75 campaigns of Phase IV was +3°.

Campaign d403022 contained 720 cycles of data. One cycle was equivalent to one rotor revolution, and contained measurements of the hub height wind velocity, yaw error, azimuth position, angle of attack and blade surface pressures. The normal force, C_n was calculated by integration of the surface pressure coefficient values, C_p.

Cycles in which the maximum C_n reached or exceeded 1.3 at the 30% span station were identified by NREL as probably containing a stall event. Using the criterion of minimum fluctuation around the cycle averaged yaw error, cycles were selected for yaw angles between -45 and +45 °. This process identified 21 isolated cycles that were then analysed by NREL to provide C_p, C_n, and α histories and from these, the occurrence of peak C_n was defined. From this subset of 21 cycles, 9 cycles are presented here, which cover the entire pre and post-static stall regime. It should be noted that, in the experimental measurements presented here, peak C_n is identified. This may be associated with *static or dynamic* stall depending on the value of the angle of attack and the severity of the pitch rate in each particular cycle.

The predicted dynamic stall onset locations for a range of wind velocities and yaw angles, are presented in Figures 4.13 through 4.19. The azimuth angles and the radial positions at which peak C_n was identified by NREL (plotted as open circles) are compared with the BEM code prediction (marked by solid squares) for dynamic stall onset. All sets of data are plotted at five radial locations along the rotor: 30%, 47%, 63%, 80%, and 95% of span. (Note that the real positions of the transducers in the experiment were located on the instrumented blade at: 30%, 46.6%, 63.3%, 80%, and 95% of span.)

Angle of attack contourlines are also plotted, to give an indication of whether the experimental values of peak C_n exceed the static stall angle, 16°; a necessary condition for dynamic stall vortex formation. Note that the blade rotates clockwise for a viewer located downwind, and for the reader. The azimuthal position of the blade $\psi = 0$ is at 12 o'clock. At each radial position, the rotating blade encounters a sinusoidal variation in α for every rotation, due to the yawed inflow. This cyclic variation in α depends on the magnitude of the wind velocity, yaw angle, rotational frequency, and blade twist architecture.

Post-Stall Region

The results presented in Figure 4.13 correspond to positive yaw angles, while Figure 4.14 is for negative yaw angles; in both cases greater than 15° . As can be observed in Figure 4.13(a), for a wind velocity of 11.6 m/s and a yaw angle of +17.03°, dynamic stall is both measured and predicted at the two inner most locations, 30% and 47% span, where the rate of increase in angle of attack is noticeably rapid. For example, at 30% span, the angle of attack is 16° just before the $\psi = 270°$ azimuth location but increases to a maximum of 27.5° at azimuth $\psi = 360°$. The 47% span location exhibits a similar trend, albeit at a reduced level. At both of these span positions, the dynamic stall onset predictions (solid squares) show good agreement with the measured stall locations (open circles), although the prediction noticeably lags the measured stall location at 47% of span. At the third radial location, 63% of span, the blade angle of attack variation is quite different. Here the blade exceeds the static stall angle of 16° at around $\psi = 285°$ and gradually reaches a maximum α of 18.5° at $\psi = 360°$. The small amplitude of the oscillation and the slow effective pitching do not trigger dynamic stall. Further outboard, blade angles of attack are always below the static stall value.

In the next case, a moderate increase in yaw angle can be observed in Figure 4.13(b), for an almost equivalent wind velocity of 11.5 m/s.

At both 30% and 47% of span, the rate of increase in blade incidence in the fourth quadrant, the 270 to 360° of azimuth region, is greater than in the previous case. The predicted locations of dynamic stall, at 30% and 47% of span considerably lead the measured data, with the code predicting earlier azimuthal dynamic stall. Outboard of 47% of span, the effective pitching is too mild to produce dynamic stall. Further outboard, at 63% of span, the angle of attack is always below the static stall value.

In Figure 4.14(a), a negative yaw case is presented for a wind velocity of 12 m/s

and a yaw angle of $-15.56°$. In this case, the right half of the rotor encounters the wind before the left half. For this reason, dynamic stall is more likely to occur in the 90 to 180° of azimuth region. At 30% and 47% of span the rate of increase in angle of attack there is considerable. For 30% span, α is above 18° at azimuth $\psi = 90°$ and reaches a maximum of $\alpha = 28°$ at azimuth $\psi = 180°$. At 47% of span, the trend is once again similar but the magnitude of the incidence change, is reduced. At these two radial stations, the predicted locations of dynamic stall show good general agreement with the measured stall locations, although, the prediction is slightly early at 30% of span and late at 47% span. The rest of the rotor disc is not prone to dynamic stall due to the low amplitudes of the oscillations and the slow effective pitching rates.

In Figure 4.14(b), the inflow velocity has increased to 14.7 m/s and the yaw angle to $-23.92°$. In this case, large and rapid variations in angle of attack can be identified at the first four radial locations, 30%, 47%,63% and 80% span. However, near the tip at 95% span, the maximum angle of attack is found to be around 19°, with only a very gentle incursion into the post-static stall region. As a result, dynamic stall has penetrated further outboard, being identified by the correlation at four different span locations, but there are still no signs of dynamic stall onset at 95% of span.

Pre-Stall Region

A case in which there is a low wind velocity and a small yaw angle is presented in Figure 4.15(a). As may be observed in the figure, there is no predicted dynamic stall onset for this wind velocity, 9.4 m/s, and yaw angle, $-5.42°$. At 30% of span, the maximum angle of attack is 14.5°. This decreases further outboard until at 95% span, the maximum angle of attack is only 9.5°. Because the static stall boundary was not exceeded, dynamic stall would not be expected and the model confirms

this expectation. Therefore, the experimental locations of peak C_n, plotted as open circles, may simply correspond to the locations where the maximum angle of attack at a particular radial position is reached. In order to verify this, the maximum C_l at each radial position was calculated using the BEM code and then contours of these C_l values were plotted in Figure 4.15(b). As may be seen from this figure, the predicted azimuth angles at which the maximum C_l contours intercept the radial stations generally agree well with the measured static stall data.

Stall Region

Figure 4.16, presents results for a wind velocity of 11.6 m/s and a yaw angle of +8.3°. As mentioned earlier, the onset of dynamic stall depends on α^+ , the rate of change of the angle of attack, as well as angle of attack itself. Table 4.1, presents the calculated mean values and amplitude of the periodic variation in angle of attack at three of the span locations for this case. Clearly, angle of attack variations are greatest at the inner radial location, 30% span, and progressively smaller at 47% and 63% of span. The non-dimensional pitch rates, α^+, at the experimentally derived locations of peak C_n were also computed to estimate if the effective pitching was high enough to allow dynamic stall vortex initiation.

Seto and Galbraith (1985) detected two divisible stall regimes around $\alpha^+ = 0.01$. At low values, $\alpha^+ < 0.01$, the regime is labelled quasi-static: the pressure profiles are similar to those in steady conditions, no vortex is formed, but the lift coefficient value shows an overshoot. At higher non-dimensional pitch rates, "a dynamic stall vortex is clearly defined and is manifest as a suction bulge (bump)". Examination of Figure 4.16 and Table 4.1 shows that the computed α^+ values at the experimental peak C_n locations (open circles), α^+ =0.0005, 0.0002, 0.0007, fall into the quasi-static regime. Therefore, a very weak dynamic overshoot might be expected, but no dynamic stall vortex formation. However at 30% span, the α^+ value at the predicted

location of dynamic stall is about ten times larger, equal to 0.009, which is on the threshold of the fully dynamic regime and may be sufficient to allow dynamic stall to occur.

Large Yaw Angles

As mentioned earlier in Chapter 2, the applicability of the model may be limited at higher yaw angles. To examine this potential limitation, the computed dynamic stall onset locations at three high yaw angles are compared with experimental observations in Figures 4.17 through 4.19. Also in the figures are both, quasi-steady and unsteady predictions from the more complex prescribed wake code of (Coton and Wang 1999) (open squares).

Figure 4.17(a) presents results for a wind velocity of 9.6 m/s and yaw angle of $-26.02°$. Dynamic stall onset is only predicted by the BEM model at the inner most section, 30% of span at $\psi = 165°$. This is in good agreement with the open square at $\psi = 162°$ which corresponds to the quasi-steady calculation from the vortex wake code. The open circles, as before, are the experimentally determined locations of peak C_n which apparently occur near the maximum angle of attack which is approximately 12°. As may be seen from the figure, the predictions from the two schemes lead the field data.

Figure 4.17(b), is the same case but this time with the unsteady calculation from the vortex wake code along with the previously presented BEM prediction and the field data. In this case the unsteady vortex method predicts dynamic stall at a radial position of 20% of span at $\psi = 174°$.

The effect of increasing the yaw angle to $-30.7°$ for a wind velocity of 12.3 m/s is shown in Figure 4.18(a). For this case the BEM model predicts dynamic stall initiation at three radial locations: 30%, 47% and just less than 67% of span. The prescribed wake prediction follows a similar trend, and the two predictions

agree particularly well at 30% of span. Further outboard, dynamic stall is predicted slightly earlier in azimuth angle by the vortex model compared to the BEM model. The field measurements at 30% span are consistent with the predictions. At 47%, 67%, 80% and 95% span, the peak C_n events occur below stall, since the maximum angle of attack is only 14°. In Figure 4.18(b) the unsteady wake code computation is presented. Although slightly delayed compared to the BEM prediction, the two predictions follow each other quite closely.

The final figure in the sequence, Figure 4.19 presents an extremely yawed turbine, yaw angle $-40.46°$ and wind velocity 10.8 m/s. In Figure 4.19(a) the field data (open circles) at 95%, 80%, 63%, and 47% do not exceed the static stall boundary, since the maximum angle of attack corresponding to the measured peak C_n is only 14°. Therefore, there is no stall onset at these four span sections. However, at 30% span, the static stall angle of attack is exceeded and a maximum instantaneous value of 34° is achieved at $\psi = 162°$, at a reduced pitch rate sufficient for dynamic stall. On the other hand, both the prescribed wake and BEM models, predict dynamic stall locations at 30%, and 47% of span in regions of high blade incidence. Here, the difference between the quasi-steady computation and the unsteady computation, Figure 4.19(b) from the prescribed wake model is quite small.

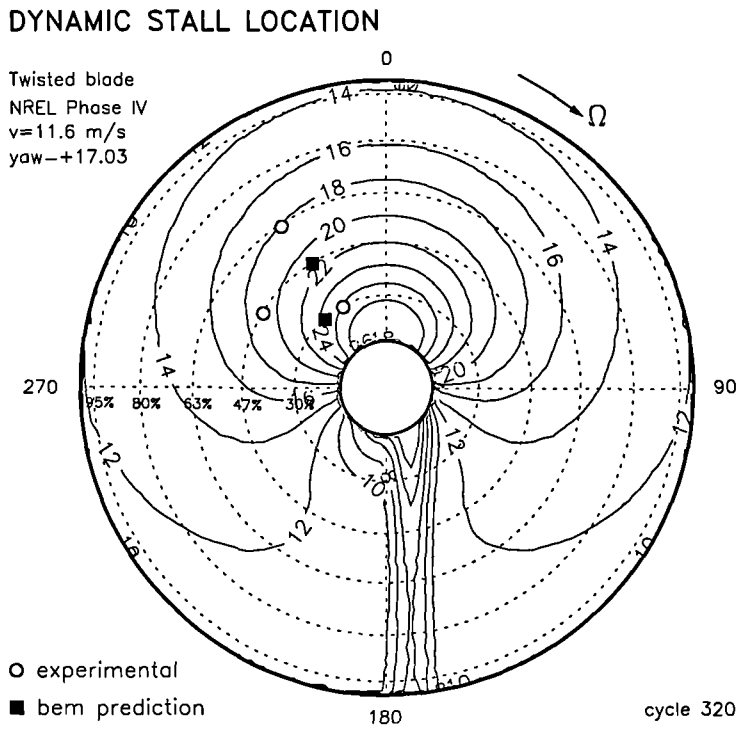

(a) wind velocity=11.6 m/s, yaw=+17.03°

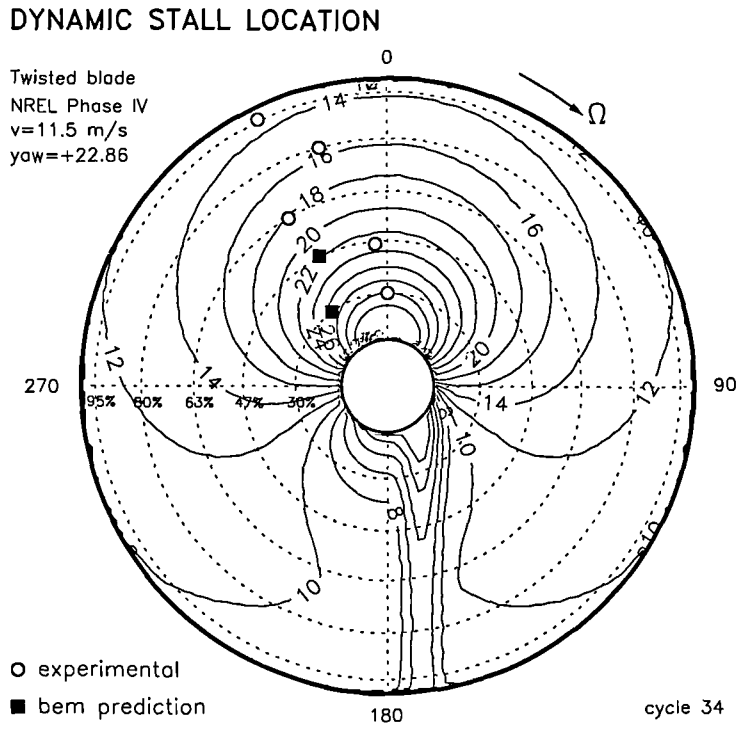

(b) wind velocity=11.5 m/s, yaw=+22.86°

Figure 4.13: *Dynamic Stall prediction compared to NREL Phase IV measurements*

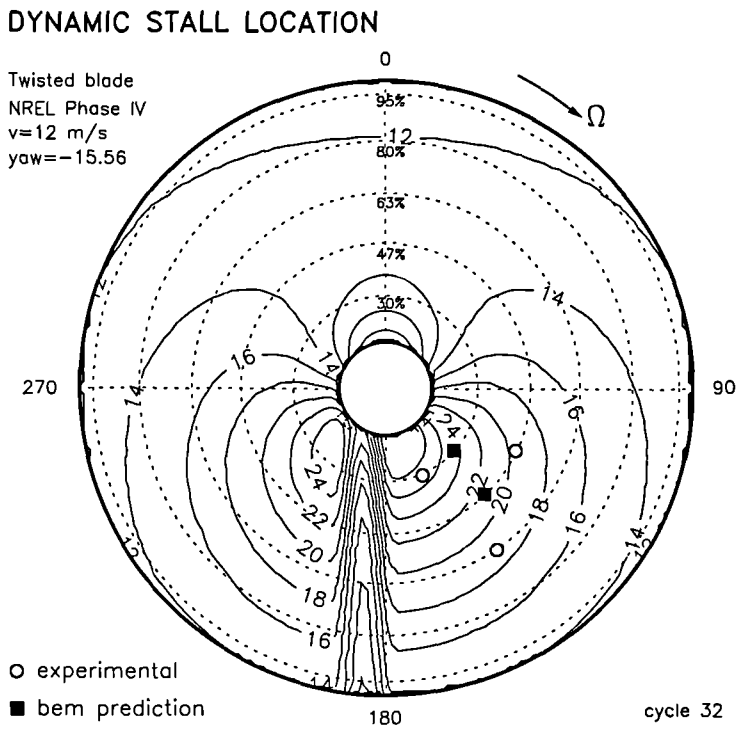

(a) wind velocity=12 m/s, yaw=−15.56°

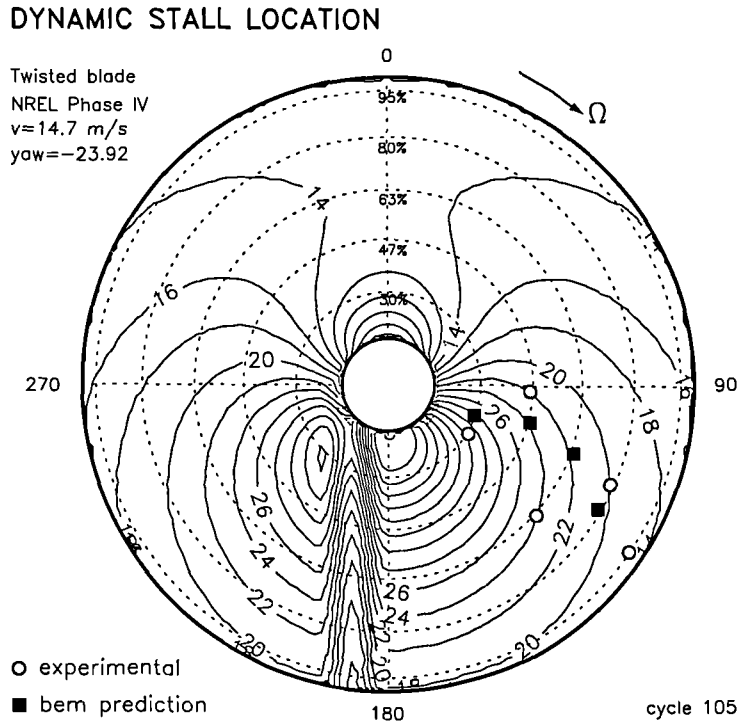

(b) wind velocity=14.7 m/s, yaw=−23.92°

Figure 4.14: *Dynamic Stall prediction compared to NREL Phase IV measurements*

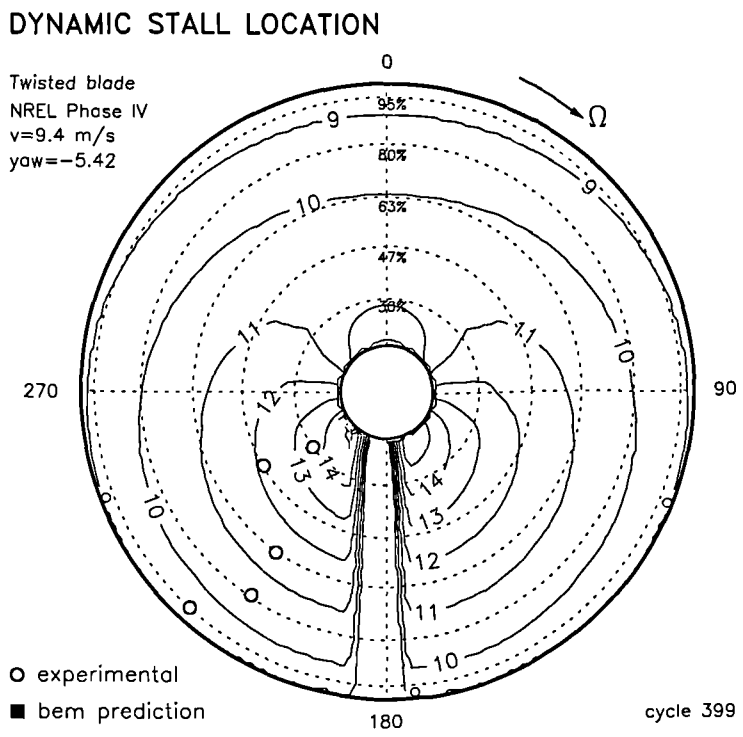

(a) wind velocity=9.4 m/s, yaw=−5.42°

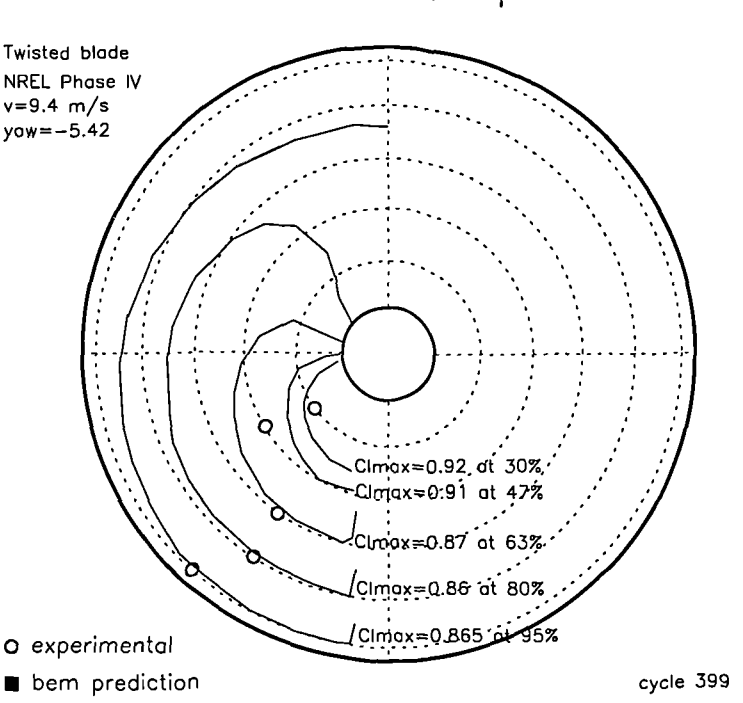

(b) C_lmax Contours for Fig(a)

Figure 4.15: *Dynamic Stall prediction compared to NREL Phase IV measurements*

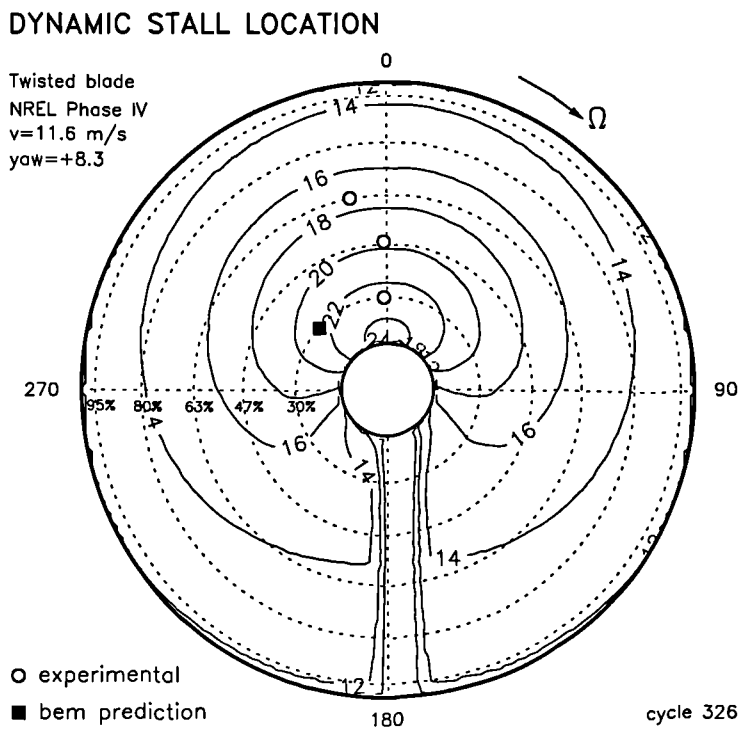

wind velocity=11.6 m/s, yaw=+8.3°

Figure 4.16: *Dynamic Stall prediction compared to NREL Phase IV measurements*

Table 4.1: *Pitching characteristics for Figure 4.16*

r radius	mean angle of attack	Amplitude of oscillation	K red. freq.	α^+ at experimental peak C_n red. pitch rate
30%	17.5	5.5	0.115	0.0007
47%	16	4	0.090	0.0002
63%	14.75	2.75	0.070	0.0005
%	degrees	degrees	-	-

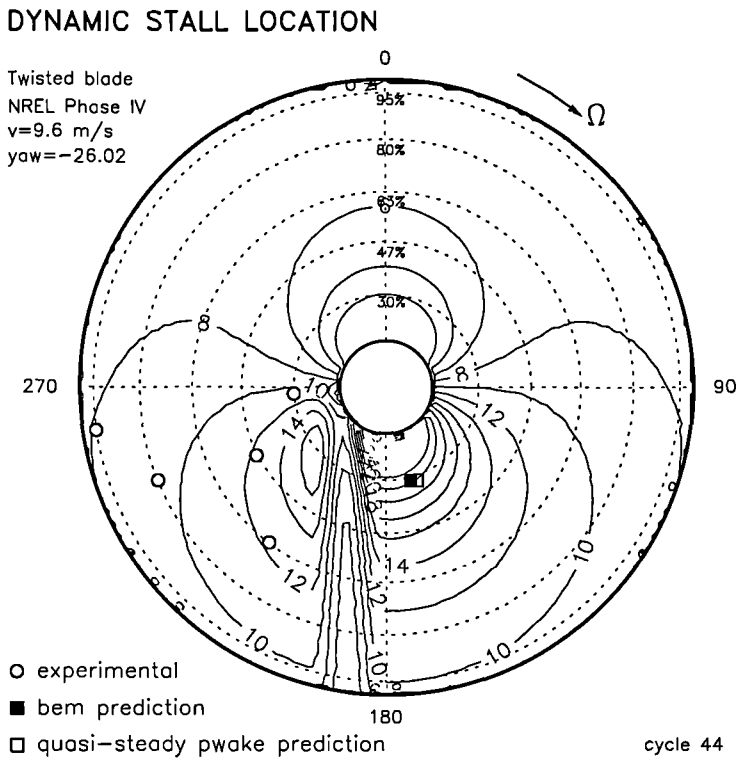

(a) Quasi-steady Prescribed Wake, wind velocity=9.6 m/s yaw=−26.02°

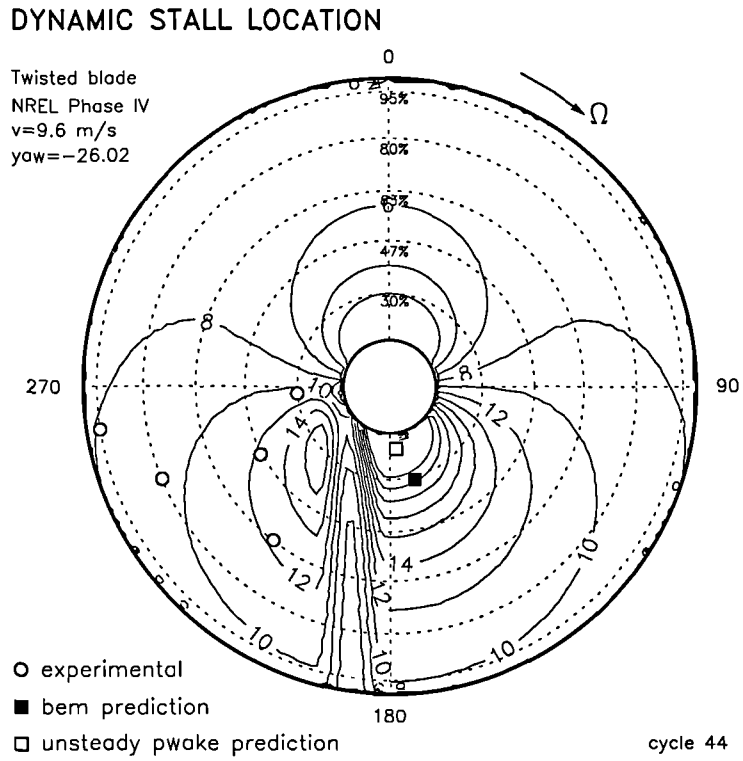

(b) Unsteady Prescribed Wake, wind velocity=9.6 m/s yaw=−26.02°

Figure 4.17: *BEM and PWake Dynamic Stall prediction compared to Phase IV*

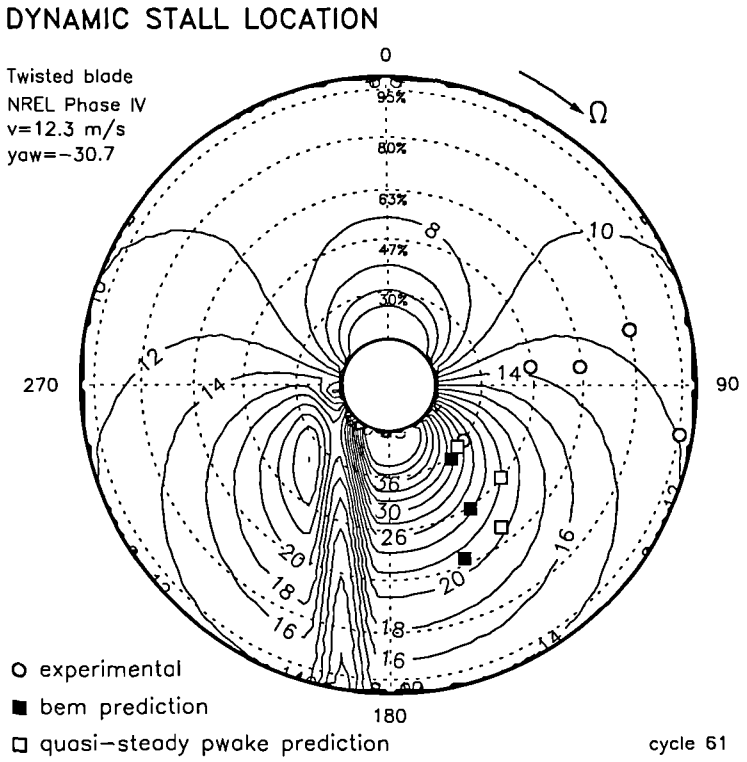

(a) Quasi-steady Prescribed Wake, wind velocity=12.3 m/s yaw=−30.7°

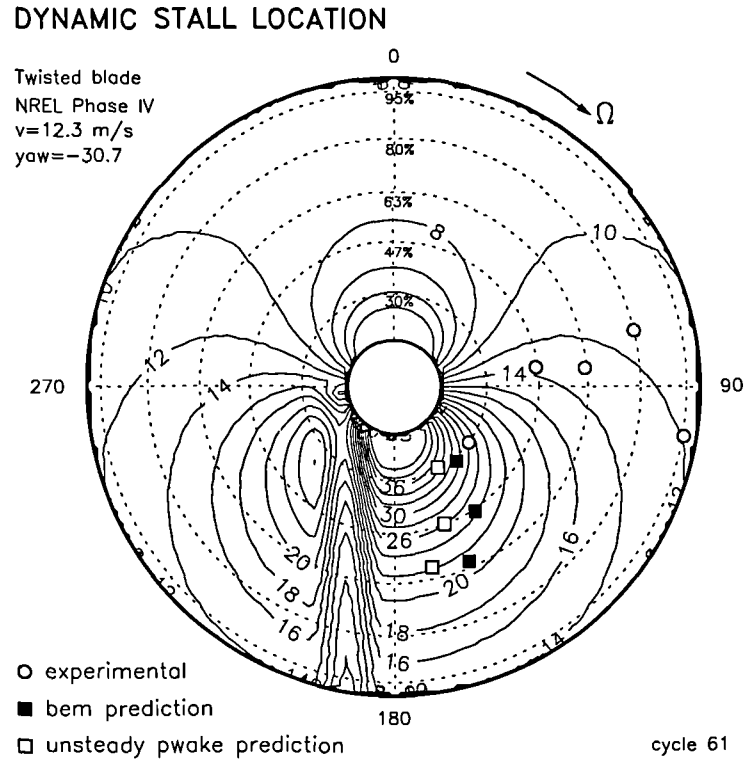

(b) Unsteady Prescribed Wake, wind velocity=12.3 m/s yaw=−30.7°

Figure 4.18: *BEM and PWake Dynamic Stall prediction compared to Phase IV*

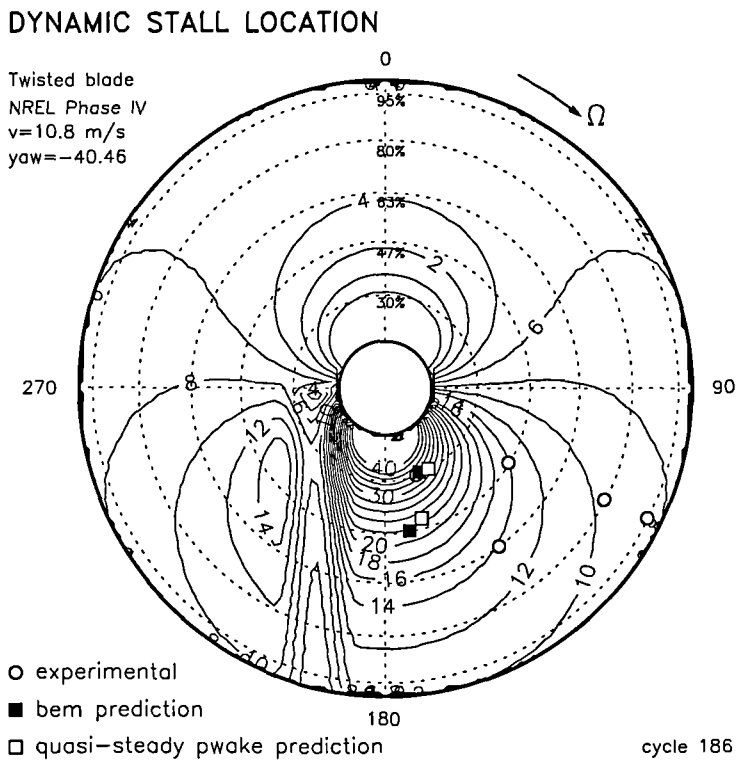

(a) Quasi-steady Prescribed Wake, wind velocity=10.8 m/s yaw=−40.46°

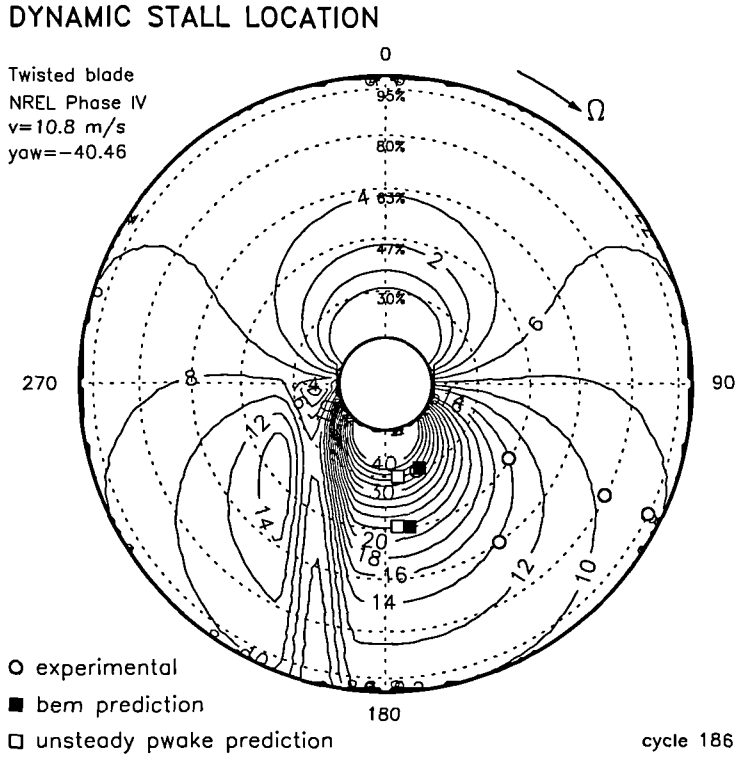

(b) Unsteady Prescribed Wake, wind velocity=10.8 m/s yaw=−40.46°

Figure 4.19: *BEM and PWake Dynamic Stall prediction compared to Phase IV*

4.4.5 Discussion

The general level of prediction obtained from the BEM scheme is comparable with predictions from the more sophisticated prescribed wake code, as shown in Figures 4.17 through 4.19. The BEM prediction compares well to the unsteady and very well to the quasi-steady solution from the vortex wake code. This suggests that blade element/momentum theory is able to provide a good estimate of angles of attack, even at the high yaw angles tested here.

Generally, a slight phase difference in azimuthal position is detected between the quasi-steady vortex wake and BEM predictions. The reason for this may lie in the level of accuracy employed in the solution. The prescribed wake calculation is made at relatively low azimuthal resolution to ensure an acceptable computation time. For instance, the azimuthal interval for global calculations of turbine performance is normally $\Delta\psi = 20°$ for the vortex code. In the wake vortex calculations which provided the results for Figure 4.17 to Figure 4.19, the azimuthal interval was reduced to $\Delta\psi = 10°$. This resulted in a six-fold increase in the required computational time. By contrast, since BEM calculations are not too computationally demanding, the azimuthal resolution employed through out all the calculations has been 1°. This high resolution would also increase the resolution of the input to the dynamic stall model.

The difference between the $\Delta\psi = 10°$ resolution for the prescribed wake code and the $\Delta\psi = 1°$ used in the BEM model can more clearly been seen in Figure 4.20 where the calculated blade incidence variations corresponding to Figure 4.18(a) are presented.

The blade incidence variations predicted by the prescribed wake scheme in Figure. 4.20(a), can be compared with those from the BEM model in Figure. 4.20(b). The curves of angle of attack calculated by the BEM code (1° azimuth step) are smooth. In contrast, the results from the vortex wake code (10° azimuth step) are

rather jagged. Looking carefully at the contours, it can be observed that there appears to be a slight azimuthal offset in the general incidence pattern in the two figures. This arises, primarily, from the discretisation step used in the prescribed wake model. This may explain the offset in the dynamic stall locations predicted by the prescribed wake code and the BEM model, and observed in Figures 4.17 through 4.19.

The radial step size used in the BEM model may also have an effect on the results, and this effect is briefly evaluated next. The influence of the radial resolution on the dynamic stall contourlines predicted by the BEM model is demonstrated by comparison of a prediction with 19 radial stations with one using 25 radial stations. The region of dynamic stall shown in Figure 4.21(a) (19 radial elements) never reaches 47% span, whereas in Figure 4.21(b) (25 radial elements) it penetrates just outboard of the 47% span location. The calculations presented in this work have all been carried out with 25 spanwise blade elements.

The previous discussion serves to highlight the problems that may arise if a low resolution modelling approach is used. The unsteady model seems to exhibit a high sensitivity to the radial and azimuthal step size, especially for large pitch rates, where the angle of attack variation is large and rapid. BEM calculations are less time consuming than other techniques and hence, increased resolution is possible whilst keeping the computing time relatively low (acceptable for the design process). This enhances the accuracy of the required input to the dynamic stall model. Furthermore, it is straight forward and easy to implement this demand. In the present BEM scheme no requirement to smooth the input for the stall onset model has been identified.

The predicted locations of dynamic stall compare well with the experimental measurements, especially when the field data exhibit low variations in mean yaw. It should be noted that the measured wind velocities and yaw directions vary during

a single cycle. Also, the values of wind velocity and yaw angle are not constant (unique) over the entire blade span at any given azimuth position. Whereas the previous calculations have all been computed for a fixed mean velocity and yaw angle on the rotor disc, a single case where velocities and yaw angles are azimuth averaged at each radial station is presented in Figure 4.22(b). Comparison of this calculation with the equivalent simulation in which the values are averaged over the rotor disc, Figure 4.22(a), shows that the use of local averaged values as input for the BEM prediction may provide an improvement in the predicted locations of dynamic stall onset.

It should also be noted that the predicted dynamic stall locations, via the C_p deviation criterion, should appear earlier than the experimental peak C_n. It is interesting to observe that this is, in fact, the case at the most inboard locations for most of the cases presented here.

With this in mind the locations of dynamic stall are correctly characterised. For the Phase II configuration, the largest differences can be seen to occur at the outboard sections of the blade (low pitch rates), although predictions fall within the scatter of the field data, Figure 4.5. For the Phase IV turbine, a marked feature in the difference in azimuthal phase may be observed at the inboard sections by looking carefully at Figures 4.13 through 4.19. The BEM predicted locations at 30% of span, are generally, as expected, at an earlier azimuthal angle than the measured locations, whereas at 47% of span the opposite behaviour is consistently observed.

The disagreement between the locations predicted by the dynamic stall correlation and the data collected in the NREL experiment may come from either the correlation itself or from the field data. This is now examined in more detail.

The Correlation

The dynamic stall correlation was developed from ramp motion (constant rate) pitching. Its application to sinusoidal pitching oscillations, as on wind turbines blades, has only been validated, Gracey *et al.* (1996), for reduced frequencies, greater than 0.01 and not in the quasi-steady region at low α^+. As already indicated, Gracey *et al.* (1996), suggested that the highest pitch rate in the oscillatory cycle should be used in the correlation rather than the instantaneous value used herein. To investigate the sensitivity of the correlation to the slight changes in the pitch rate, two cases in which the pitch rate is averaged over 5 and 10 azimuthal step times, are shown in Figure. 4.23. This figure shows that the extent of the dynamic stall region increases slightly in the radial direction when the averaged values are used. However, the relatively low sensitivity to the change in the reduced pitch rate from instantaneous to averaged values, suggests that the use of the instantaneous value of α^+ will provide a reliable estimate of the stall onset boundary. Nevertheless, a more thorough analysis of the effect of the history of the reduced pitch rate, would be required before this could be stated with complete confidence.

Some of the discrepancies could also be related to the Reynolds number influence on aerofoil characteristics, (Galbraith *et al.* 1987), such as the incidence of static stall, which is required as an input data to the correlation. The test conditions used to develop the correlation were, a Reynolds number of 1.5 x 10^6, which is more common number for large scale wind turbines. The NREL turbine operates at less than half this Reynolds number, around 5 x 10^5. Coton *et al.* (2002) in an examination of key aerodynamic issues raised by the NREL blind comparison, suggest that the predicted characteristics of a similar machine, are sensitive to the choice of input aerofoil data in the Reynolds number range Re=5 x 10^5 to 1 x 10^6 . In that case the higher Reynolds number data, gave a better match to the NREL-NASA Phase VI test, for quasi-steady calculations, especially on outboard blade sections. The influence of Reynolds number on the dynamic stall onset correlation

has been studied to an extent by Gracey (1991) who suggested a possible adjustment of the correlation. The data used to derive this adjustment were, however, not comprehensive enough to fully validate it.

The computed results generally seem to be on the conservative side. A possible reason for this may be the high static stall angle, α_{ss}=16°, chosen for the S809 aerofoil as an input for the dynamic stall correlation. It is possible that a smaller value of α_{ss}, may produce better agreement between the correlation and the field data. The peculiar aerodynamic characteristics of the S809 aerofoil in the pre and post-static stall region, make the accurate specification of α_{ss} difficult.

Gracey *et al.* (1996) suggested that the correlation produced better agreement with experiment, if α_{ss} was regarded as the incidence of pitching moment break in steady conditions. The incidence of the pitching moment break in steady conditions for the $S809$ aerofoil is around 16° , (reference Ohio). Therefore, substitution of α_{ss} as the pitching moment break angle will not affect the results, since the static stall angle is also 16°.

The Dynamic Stall Field Data

The prediction scheme used here assumes locally two-dimensional flow. This may not actually be the case in reality and it is possible that the field data may be exhibiting dynamic stall triggered by the spanwise influences in a highly three-dimensional dynamic stall process.

The experimental study of Coton and Galbraith (1999) on a finite wing showed, that once the stall vortex was initiated at the mid span location it triggered dynamic stall on outboard sections earlier than would have otherwise been expected. As may be observed in Figure 4.5 the earliest signs of dynamic stall which in this case appear on inboard blade sections are generally well predicted. As the blade moves around the azimuth, the stall progresses outboard, where the predicted locations are delayed

compared to the field data. The three-dimensionality of the dynamic stall process may be the main reason why this effect is particularly pronounced on outboard blade sections.

On the other hand, improved experimental measurements of the azimuthal position of the blade, will be of benefit when phenomena occurring in a relatively small azimuthal range are of interest. A slight phase difference between the measured and actual azimuthal position may be present in the experimental measurements as cited by Simms *et al.* (1999). in relation to the NREL UAE, Phases II and IV. An NREL analysis of Phase II data, Huyer *et al.* (1996), showed that the uncertainty in measuring blade azimuth angle amounts to a full scale error of 2.8%. In addition, measurements suffer from non-desirable total uncertainty in the fixed blade pitch angle of $\pm 1°$. In reality, the major cause of the discrepancies is likely to be the variations in onset flow conditions experienced by the turbine during the field tests. This would account for the apparent mis-match between the experimentally determined peak C_n values and the mean incidence distributions observed in Figures 4.18 and 4.19. In fact, even in moderately benign field conditions, the variations in instantaneous onset flow velocity and direction can be severe enough to make comparison with predicted average values problematic.

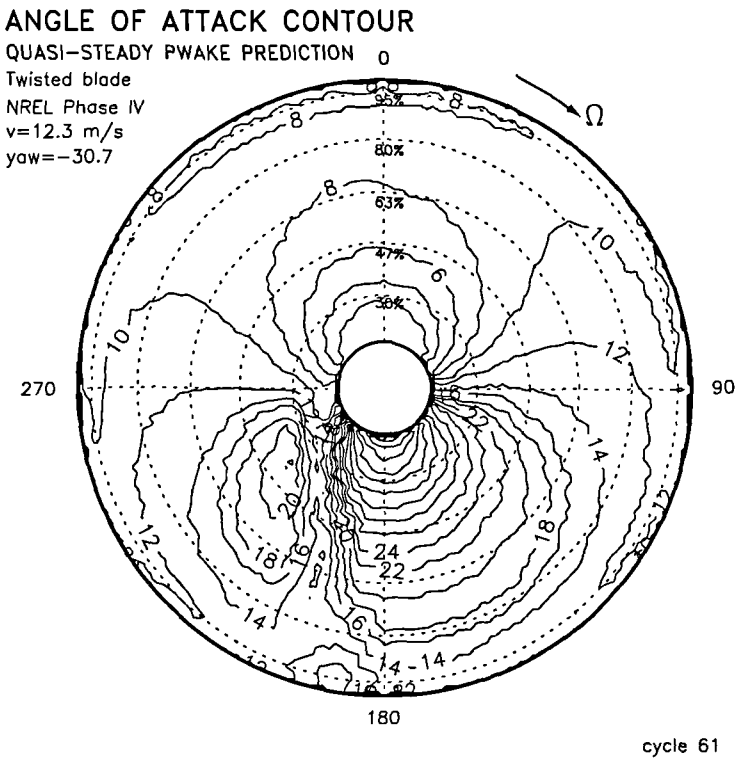

(a) Quasi-steady Prescribed Wake for $\Delta\psi = 10°$

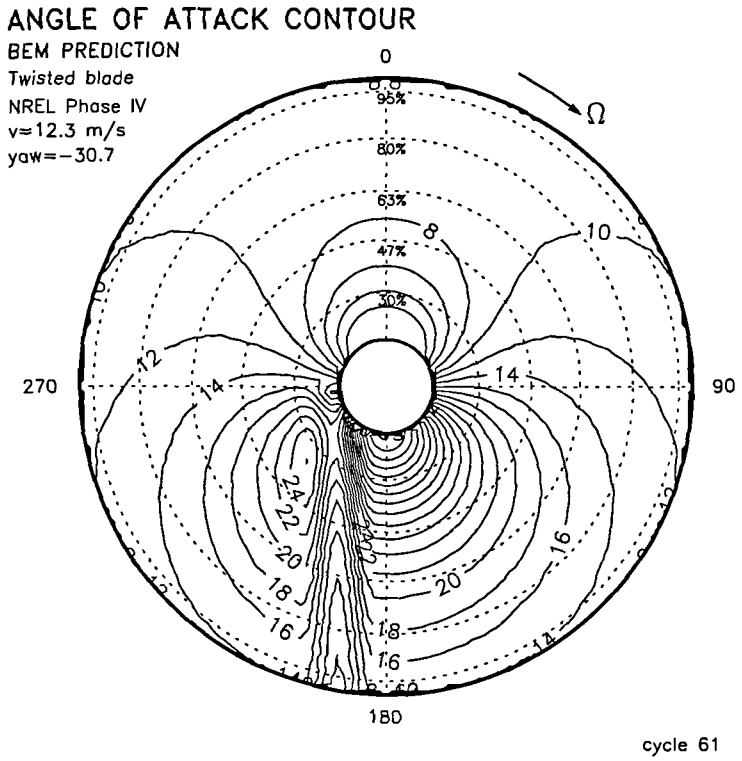

(b) BEM prediction for $\Delta\psi = 1°$

Figure 4.20: *Azimuthal step size influence on PWake and BEM angle of attack*

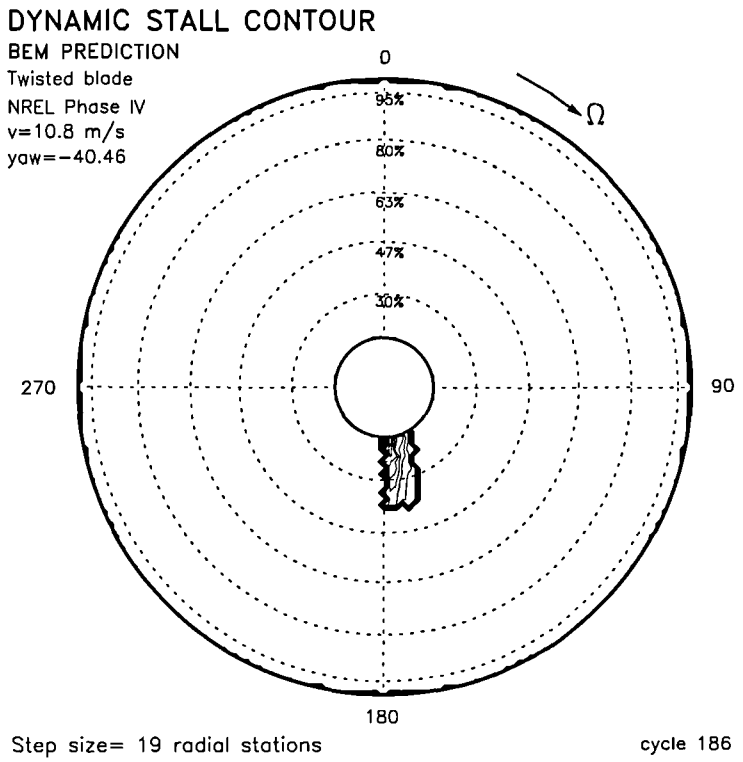

(a) BEM prediction, 19 blade elements, wind velocity=10.8 m/s, yaw=−40.46°

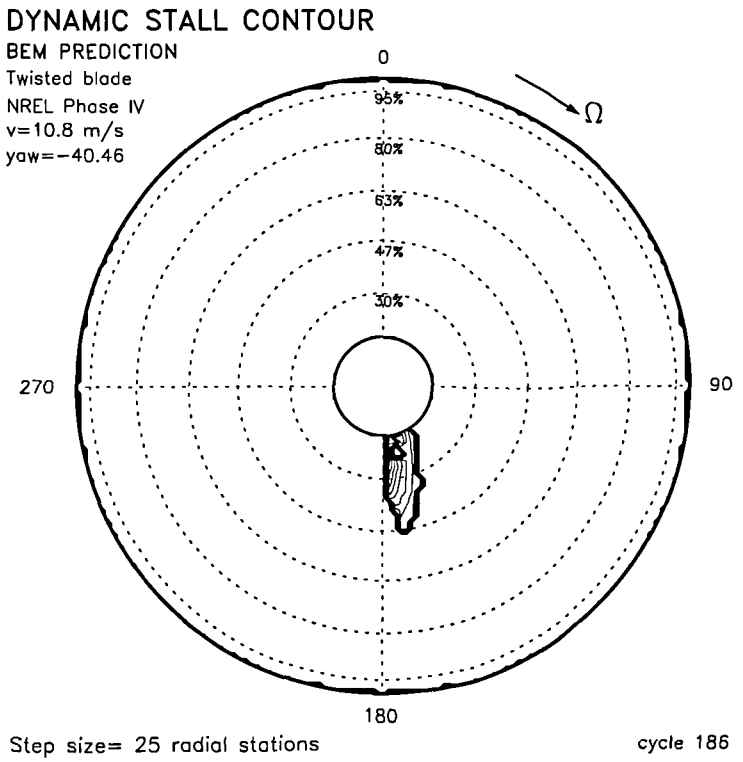

(b) BEM prediction, 25 blade elements, wind velocity=10.8 m/s, yaw=−40.46°

Figure 4.21: *Radial Step size influence on BEM Dynamic Stall prediction*

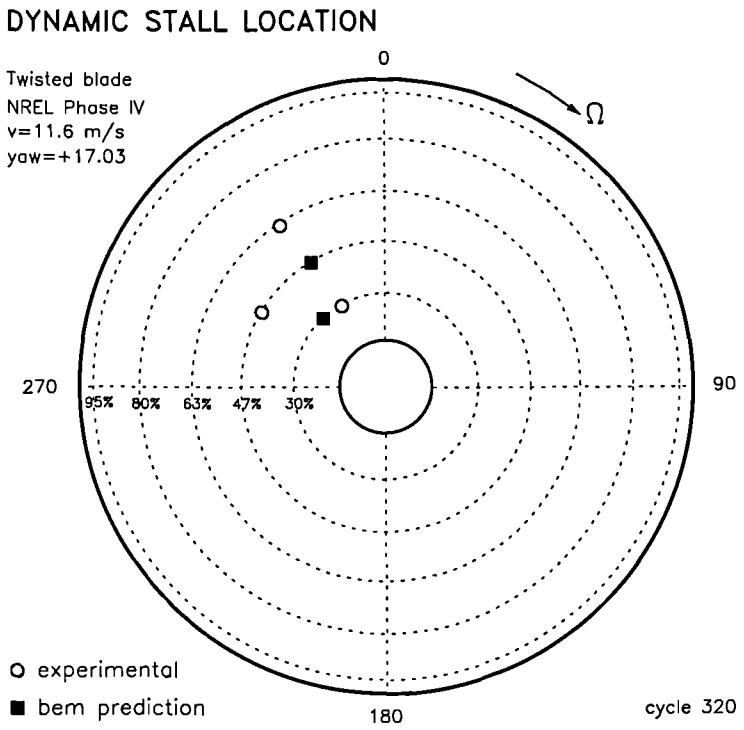

(a) Fixed inflow values, wind velocity=11.6 m/s yaw=+17.03°

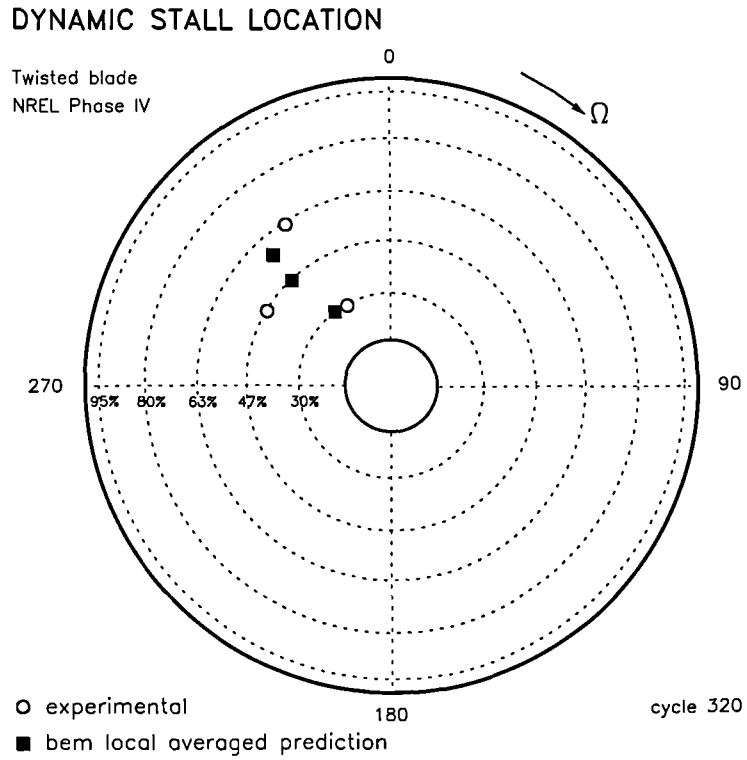

(b) Local averaged inflow values varying at each span location.

Figure 4.22: *Effect of local averaged inflow values in BEM, NREL Phase IV*

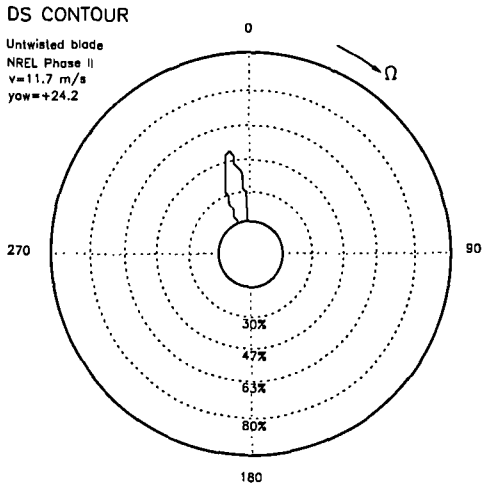

(a) instantaneous $\alpha+$

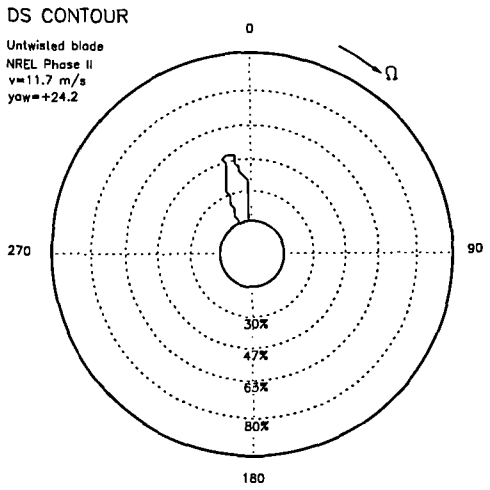

(b) $\alpha+$ =mean of the 5 previous values

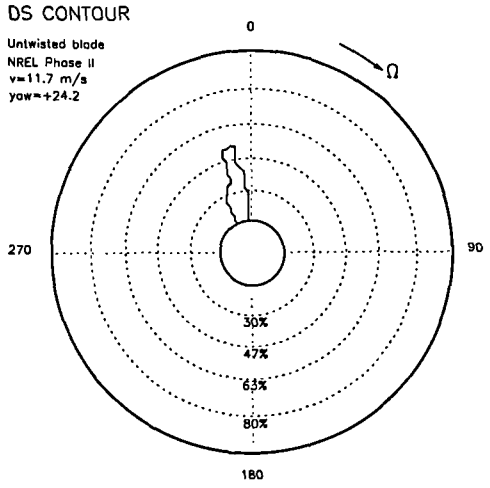

(c) $\alpha+$ =mean of the 10 previous values

Figure 4.23: *Effect of history of the reduced pitch rate, NREL Phase IV*

4.4.6 2–D Conclusions

Application of the method to the downwind configured NREL Unsteady Aerodynamics Experiment turbine Phases II and IV identifies regions of dynamic stall which are broadly in line with field observations. It is shown that the location and severity of dynamic stall on the rotor disc is, as may be expected, very sensitive to the onset flow conditions, blade planform, twist and tip pitch angle. It is also shown that dynamic stall can be produced by two different mechanisms. The first is associated with the exit of the blade from the tower shadow region and is, thus, particular to downwind machines. The second mechanism is simply the effective temporal variation in incidence experienced by the blades when the turbine operates in yawed flow. It is also clear, at this stage, that the yaw and tower shadow induced dynamic stall regions, given their proximity, are likely to interact.

The potential effect of blade design on the extent and location of dynamic stall has been illustrated by comparison of the predictions for the untwisted Phase II and the twisted Phase IV rotor configurations. For example, dynamic stall may be first triggered either at the outboard sections, as may be observed in Figure 4.9(c) for the Phase IV twisted blade, or at the most inboard radial positions, as has been shown for both the Phase II and Phase IV wind turbine configurations.

There is obviously room to improve the quasi-steady 2–D dynamic stall predictor. At this stage, only the onset of dynamic stall has been considered and even this has been dealt with in a fairly crude manner. Once dynamic stall has been initiated, the subsequent process involves a complex series of events which take around three to four chord lengths of blade travel to be completed. Even after this, depending on the subsequent variation of blade incidence, secondary vortex shedding can produce large fluctuating loads. This effectively means that large portions of the disc are likely to be affected by dynamic stall if the turbine operates in a significantly yawed flow.

In all the cases studied, it is interesting to note that there is some overlap between the regions of dynamic stall and three-dimensional stall delay. It is possible that three-dimensional effects may, in fact, delay the onset of dynamic stall in a manner similar to the delay in static stall. Such an effect, however, will inevitably be restricted to inboard blade sections. The extent to which three-dimensional stall delay interacts with the regions of unsteadiness will be considered next.

4.5 3–D Dynamic Stall Onset Predictor

Although contemporary aerodynamic models (Rawlinson-Smith 1996) reflect more of the flow physics than was previously possible, a key aerodynamic issue remaining to be addressed is the manner in which unsteady three dimensional flow develops and subsequently influences the loading distribution on the blades.

In order to assess the severity of the interaction of three dimensional stall delay with regions of unsteadiness, a simple method is presented below.

4.5.1 Three Dimensional Unsteady Stall Model

The inclusion of three-dimensional effects in the dynamic stall model described previously, has been attempted by combining it with a 3–D stall delay lift correction to the static Kirchhoff model for separated flow. Two parameters from the dynamic stall correlation, Eq. (4.5), have been used to model the effects of 3–D flow separation in the unsteady stall model. These two variables are: S_2, the rate of change of separation point with incidence and α_{ss}, the incidence of static stall. This technique is briefly described next.

3–D Stall Delay Lift Correction to 2–D Aerofoil Data

As has been seen in Chapter 3, strong spanwise separated flow on a rotating blade

can produce a delay in the stalling process compared to static aerofoil data. As a result, the aerodynamic force coefficients can be altered resulting in an increase in lift and a reduction in drag. The 3–D lift and drag coefficients, C_{l3D}, C_{d3D} can be calculated from

$$C_{l3D} = C_{l2D} + \Delta C_l \tag{4.7}$$

$$C_{d3D} = C_{d2D} - \Delta C_d \tag{4.8}$$

where C_{l2D} and C_{d2D} are the 2–D aerofoil lift and drag coefficients. Based on the stall delay correlation, the increment in the lift coefficient ΔC_l and decrement in the drag coefficient ΔC_d are modelled as

$$\Delta C_l = f_l \left(C_{lp} - C_{l2D}\right) \tag{4.9}$$

$$\Delta C_d = f_d \left(C_{d2D} - C_{d\alpha=0}\right) \tag{4.10}$$

where $C_{d\alpha=0}$ is the 2–D aerofoil drag coefficient at zero incidence, and the potential lift coefficient C_{lp} is given by

$$C_{lp} = 2\,\pi \left(\alpha - \alpha_0\right)$$

with α_0 being the angle of attack at which $C_{l2D} = 0$. The correction factors for lift and drag, f_l and f_d are obtained from Eq. 3.7, the empirical separation point correlation as

$$f_l = \frac{1}{2\pi}\left[\frac{1.6(c/r)}{0.1267}.\frac{C_1 - (c/r)^{\frac{C_3}{\Lambda}\frac{R}{r}}}{C_2 + (c/r)^{\frac{C_3}{\Lambda}\frac{R}{r}}} - 1\right] \tag{4.11}$$

$$f_d = \frac{1}{2\pi}\left[\frac{1.6(c/r)}{0.1267}.\frac{C_1 - (c/r)^{\frac{C_3}{2\Lambda}\frac{R}{r}}}{C_2 + (c/r)^{\frac{C_3}{2\Lambda}\frac{R}{r}}} - 1\right] \tag{4.12}$$

Thus, the stall delay model has been used to derive a 3–D lift coefficient C_{l3D}. The new set of curves obtained for C_{l3D} are presented in Figure 4.24. The lowest curve represents the static C_{l2D} lift coefficient versus angle of attack, which corresponds to the behaviour at the tip of the blade, where there are no 3–D stall delay effects. The rest of the curves correspond to radial positions progressively closer to the root of the blade, where 3–D stall might delay separation and increase lift. The upper curve corresponds to the inboard section at 32% of span. As may be seen from the figure, the modelling assumes 3–D post-stall characteristics similar to the static behaviour.

3–D Lift Correction in the Unsteady Model

Once the 3–D lift coefficient is obtained, the three-dimensional values for the normal force coefficient C_{n3D}, and the chordwise force coefficient, C_{t3D} are given by

$$C_{n3D} = C_{l3D}\ \cos\alpha + C_{d3D}\ \sin\alpha \tag{4.13}$$

$$C_{t3D} = C_{l3D}\ \sin\alpha - C_{d3D}\ \cos\alpha \tag{4.14}$$

Assuming that the Kirchhoff flow separation model Eq. (4.1) can be applied to 3–D flows, then the movement of the 3–D trailing edge separation point can be expressed in terms of C_{n3D} by rearranging Eq. (4.2) as

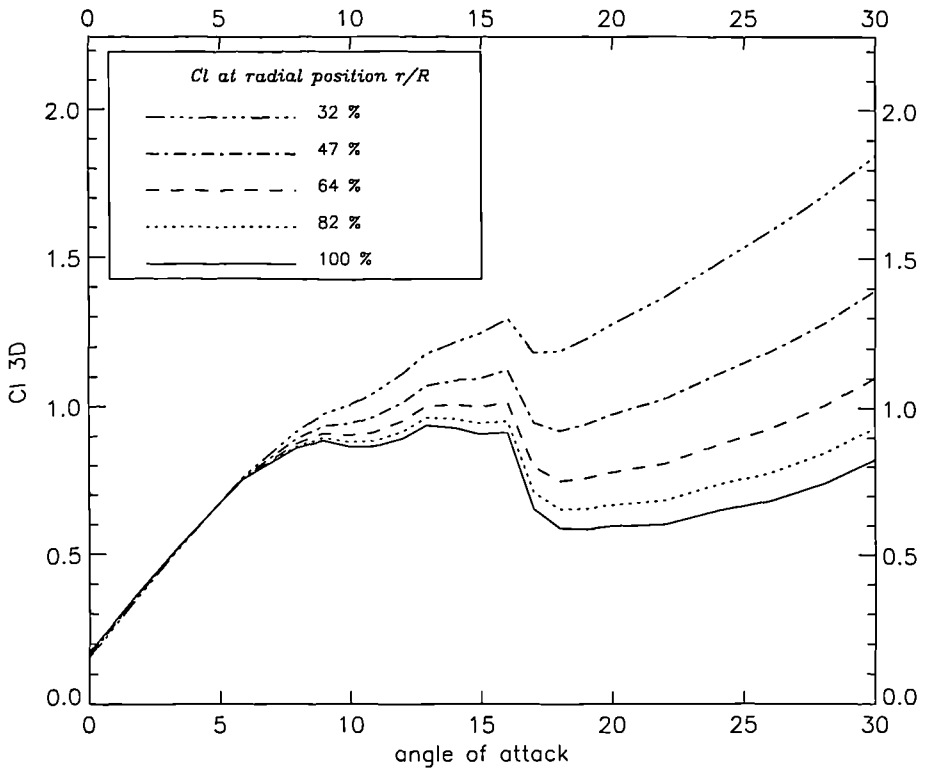

Figure 4.24: *Calculated lift coefficient incorporating 3–D stall delay*

$$f_{3D} = 4\left[\sqrt{\frac{C_{n3D}}{C_{n_\alpha}(\alpha - \alpha_0)}} - \frac{1}{2}\right]^2 \tag{4.15}$$

where f_{3D} represents the chordwise location of flow separation in the 3–D flow.

For a fixed tip speed ratio, f_{3D} is a function not only of angle of attack, as in the 2–D case, but also of the local radius r, thus $f_{3D} = g(\alpha, r)$. On this basis a new set of curves can be obtained and are presented in Figure 4.25

As in the previous figure, the lowest curve represents the static separation point versus angle of attack, which corresponds to the behaviour at the tip of the blade, where there are no 3–D stall delay effects. The rest of the curves correspond to

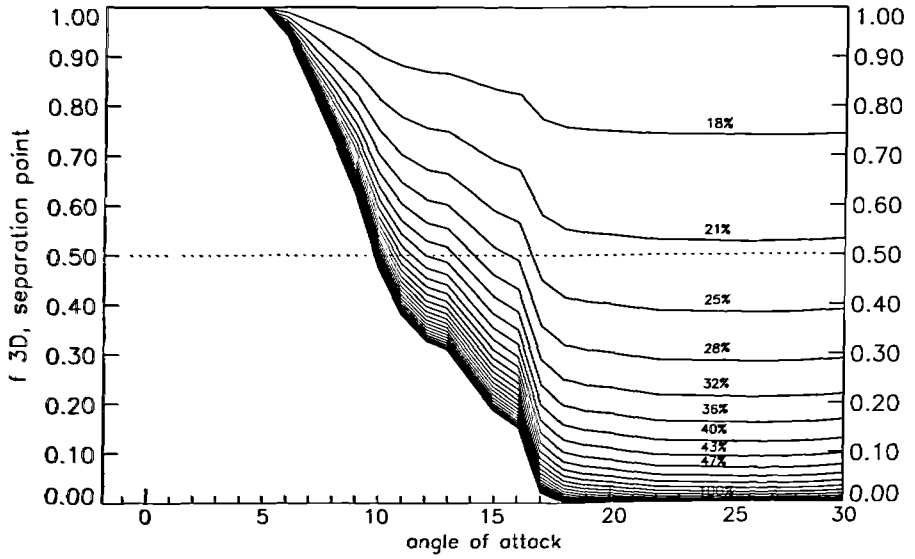

Figure 4.25: *Calculated flow separation incorporating 3–D stall delay*

radial sections progressively closer to the root of the blade, where 3–D stall might delay separation. The upper curve corresponds to the most inboard section at 18% of span.

Thus, the relationship between the separation point f and the angle of attack α, is no longer an unique (static) curve. Instead, a set of f-α curves has been obtained; one curve for each radial station. This, in turn, changes both the parameter S_2, which is related to the slope of the f-α curve through the relationship shown in Eq. (4.4), and α_{ss}, the incidence of static stall, as can be seen in Figure 4.25. It should be appreciated that for a fixed value of α along the blade span, moving from the tip inwards towards the root, the separation point moves backwards, towards the trailing edge ($f = 1$). Another feature is that, in order to obtain a fixed chordal separation point across the whole blade span, the sectional angle of attack needs to increase towards the blade root.

In the present work, the values of the two parameters, S_2 and α_{ss}, are stored

in a lookup table as a function of radial position for input into the dynamic stall onset correlation. Results obtained from the 3–D dynamic stall predictor using these values are presented in the next section.

4.5.2 Results and Discussion

The regions of dynamic stall and stall delay due to rotation have been previously shown to overlap. In this section, the capability of the modelling strategy to monitor how three-dimensional stall delay interacts with the regions of unsteadiness will be evaluated and compared to the NREL UAE Phase II wind turbine data, for a wind velocity of 15 m/s and yaw angle of +30°. The open circles represent the experimentally assessed locations of dynamic stall onset, while the predicted region of dynamic stall is plotted as a contour line.

Effect of S_2

The parameter S_2 is related to the position and rapidity of movement of the steady separation point. From Eq. (4.4), this relationship is approximately

$$S_2 \simeq \frac{-f}{\frac{df}{d\alpha}} \tag{4.16}$$

So, the higher the value of S_2 at a particular chord location, the slower the steady separation point moves with increasing incidence . Higher values of S_2 in the correlation are, therefore, expected to have the effect of reducing the dynamic stall onset boundary.

The basic effect of S_2 on the extent of the dynamic stall region predicted by the correlation is examined in Figures 4.26(a) through 4.26(f), which have been obtained for values of S_2 equal to 0.8, 1.2, 1.6, 1.8, 3.2 and 4 respectively. The nominally 2–D static S_2, equal to 1.6, is shown in Figure 4.26(c) to facilitate comparison.

From the preceding analysis, Figure 4.25, this may be a representative range of S_2 for the S809 aerofoil, when 3–D effects are considered. Interestingly, the predicted dynamic stall contours show little sensitivity to variations in the parameter. Even the highest value of $S_2 = 4$, Figure 4.26(f), produces a similar region of predicted dynamic stall to the 2–D static case. Closer examination of this case does, however reveal a slightly inboard movement of the contour between 30% and 63% of span, delaying the dynamic stall onset at these inboard stations.

To examine how S_2 may influence the onset of 3–D dynamic stall in a more realistic scenario, a case is presented in Figure 4.27 in which, α_{ss} has been kept constant and equal to 16°, whereas S_2, changes at each radial position, according to the slope of the f_{3D}-α curves at $f = 0.5$, in Figure 4.25.

Comparison of this case with the 2–D case presented in Figure 4.26(c) shows that the predicted location of 3–D dynamic stall has not significantly changed, except between 30% to 63% of span, where a very marginal inboard movement of the dynamic stall contour may be observed. For example, by looking carefully at 47% of span, just after 270° , a delay in the azimuthal location of dynamic stall initiation can be detected in the 3–D case.

In reality, if the blade incidence is constant along the span, a situation will exist in which, if the 3–D effects are considered, the separation point will be near the leading edge at the blade root and near the trailing edge at the blade tip. As may be observed from Figure 4.25, f will increase at the most inboard locations, but the slope of the f-α curve does not change for a fixed value of α. Therefore the S_2 variation, which is a function of both f and the slope of the f-α curve, Eq. (4.16) is less severe than in the previous case, where the slope changes. Thus, the general shape of the dynamic stall contour will not change significantly, and a more 2–D like prediction may be expected.

Effect of α_{ss} at $f = 0.5$

In addition to S_2, the other principle parameter in the dynamic stall onset correlation is the static stall angle. The effect of accounting for 3–D stall delay through this parameter is examined in Figure 4.29 where S_2 is kept constant while α_{ss} changes for each radial location according to the f_{3D}-α curve at $f = 0.5$. Although α_{ss} has been described as the static stall angle, it has been suggested that a more appropriate physical interpretation for α_{ss} is the incidence at which flow reversal from the trailing edge has reached the mid-chord. The effect of changing α_{ss} according to Figure 4.25, in comparison with the 2–D case presented again in Figure 4.28, is that the predicted location of 3–D dynamic stall extends further outboard, reaching 80% of span. Also at 63% and 47% of span, it is identified at an earlier azimuthal angle. At span sections where $r \leq 21\%$, dynamic stall is not detected at all.

This behaviour can be related to Figure 4.25. The range of α_{ss} values at $f = 0.5$, starts at around 10° at 100% of span and increases steadily until the separation point *does not* actually reach $f = 0.5$ at the most inboard sections, $r \leq 21\%$. This effectively means that dynamic stall would not be predicted by the correlation. For the more outboard sections, dynamic stall is predicted in accordance with the reduction in α_{ss}, which represents the boundary which must be exceeded for dynamic stall to happen.

In order to avoid the problem at inboard sections a cut-off strategy was implemented. This was done by limiting the range of α_{ss} from around 10° at the 100% of span location, to an upper limit of 16° at approximately 28% of span. This inner value was then maintained constant for locations further inboard. Doing this, whilst keeping S_2 constant, produces the result shown in Figure 4.30, where dynamic stall onset is predicted now at the most inboard locations. The implications of this result are discussed in more detail later.

Effect of α_{ss} and S_2 at $f = 0.5$

The effects of simultaneous changes in S_2 and α_{ss} at $f = 0.5$ are presented in Figure 4.31. In this case, α_{ss} is allowed to vary in the manner described above, and S_2 increases, according to the f_{3D}-α curve at $f = 0.5$, from the tip of the blade to the 28% of span location. Further inboard, S_2 remains constant to retain consistency with the α_{ss} cut-off strategy. The resulting predicted locations of 3–D dynamic stall are shown in Figure 4.31

Most of the characteristics apparent in Figure 4.31, are quite similar to those in Figure 4.30. At 30% of span the prediction has remain unchanged. At 47% and 63% of span, the predicted contour of dynamic stall has in both cases, again moved outboard, in comparison with the 2–D case. Furthermore, the 3–D dynamic stall prediction now reaches 80% of span.

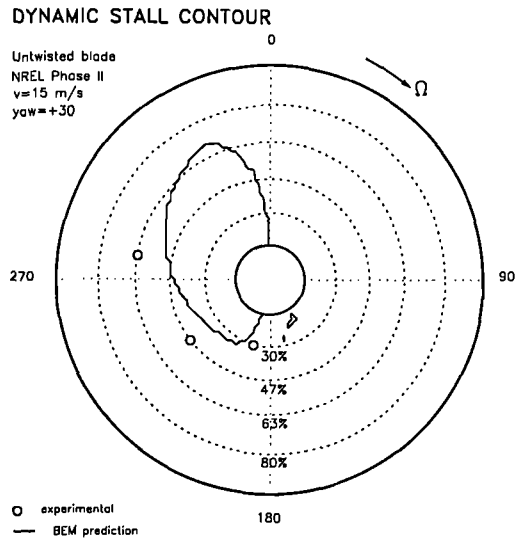

(a) $S_2 = 0.8$

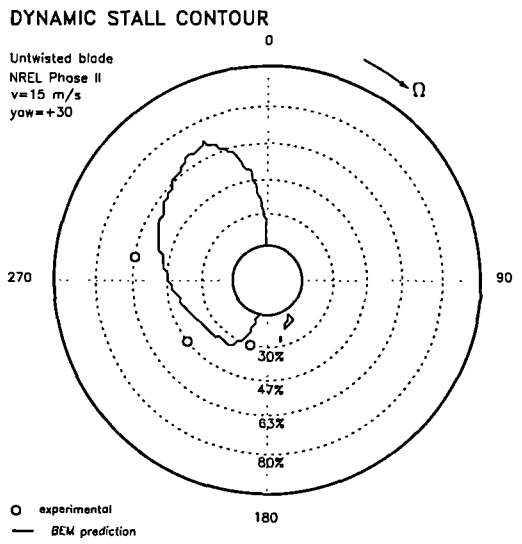

(b) $S_2 = 1.2$

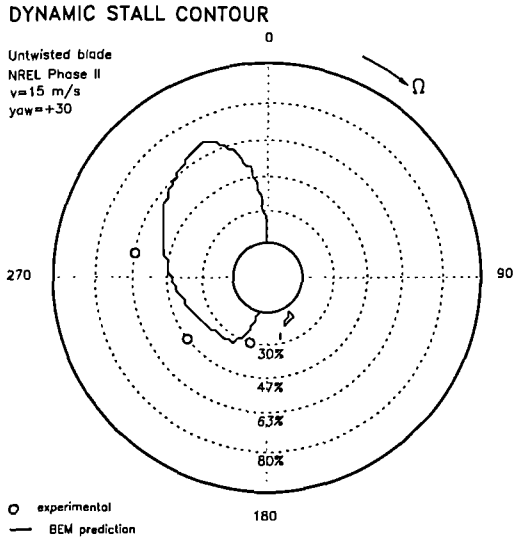

(c) $S_2 = 1.6$

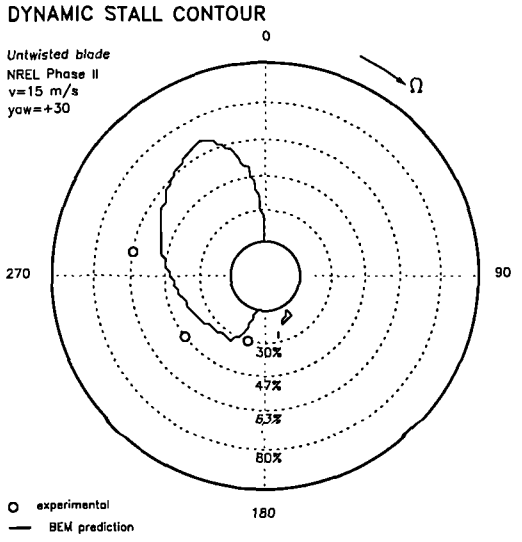

(d) $S_2 = 1.8$

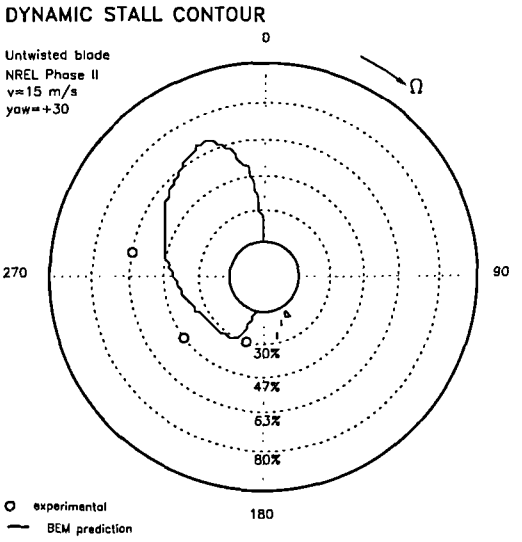

(e) $S_2 = 3.2$

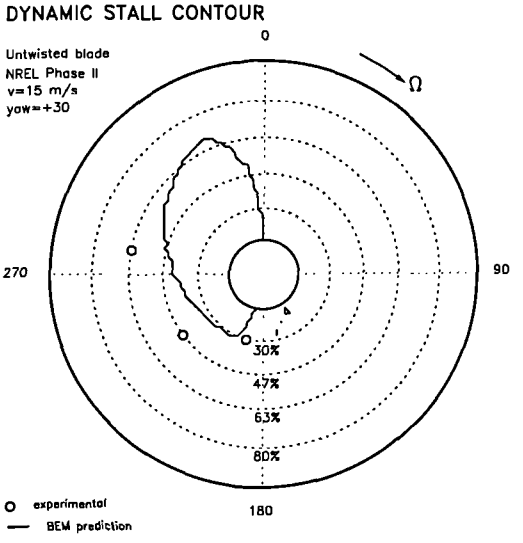

(f) $S_2 = 4$

Figure 4.26: *Dynamic Stall prediction, α_{ss} fixed from 2–D static test, NREL Phase II*

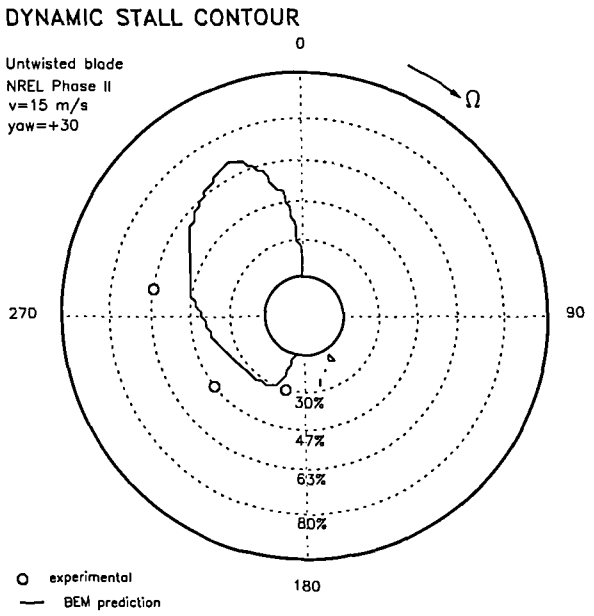

S_2 variable at $f = 0.5$, α_{ss} fixed from 2–D static test

Figure 4.27: *3–D Dynamic Stall prediction, compared to NREL Phase II*

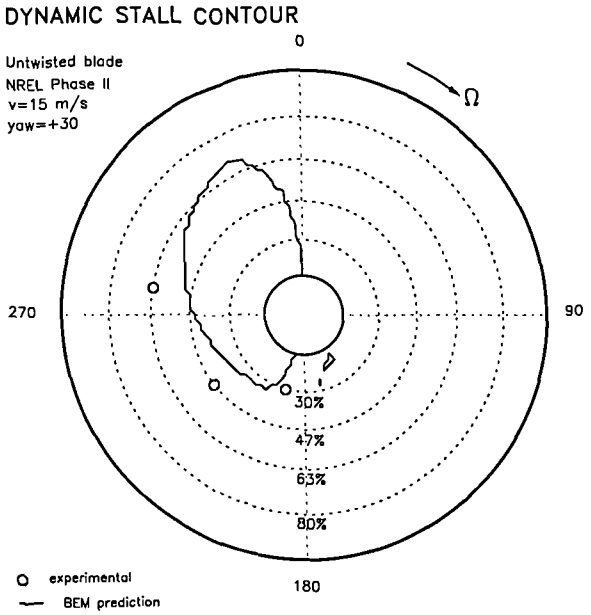

S_2 and α_{ss} fixed from 2–D static test

Figure 4.28: *Dynamic Stall prediction compared to NREL Phase II measurements*

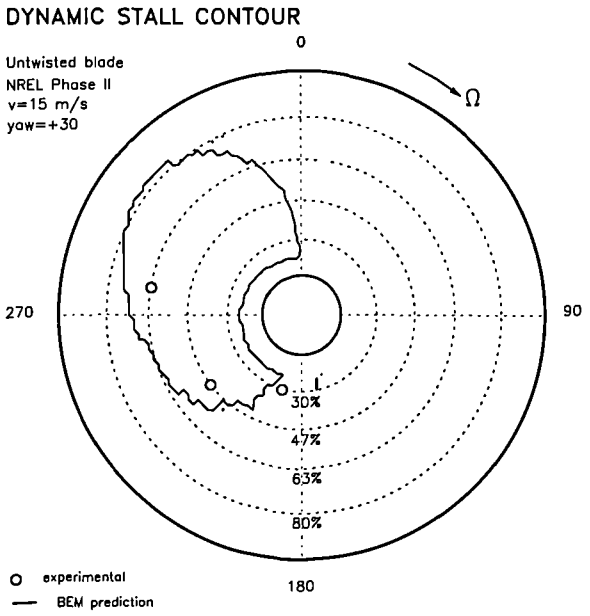

α_{ss} variable at $f = 0.5$ and S_2 fixed from 2–D static test

Figure 4.29: *3–D Dynamic Stall prediction compared to NREL Phase II*

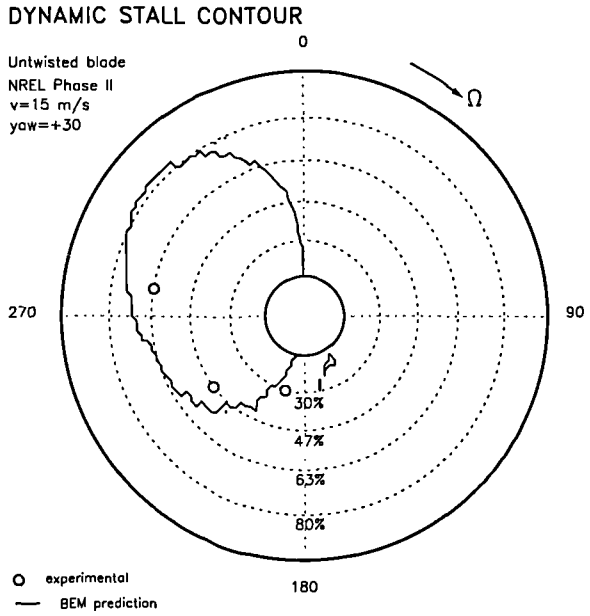

α_{ss} variable at $f = 0.5$ and S_2 fixed from 2–D static test

Figure 4.30: *3–D Dynamic Stall prediction compared to NREL Phase II*

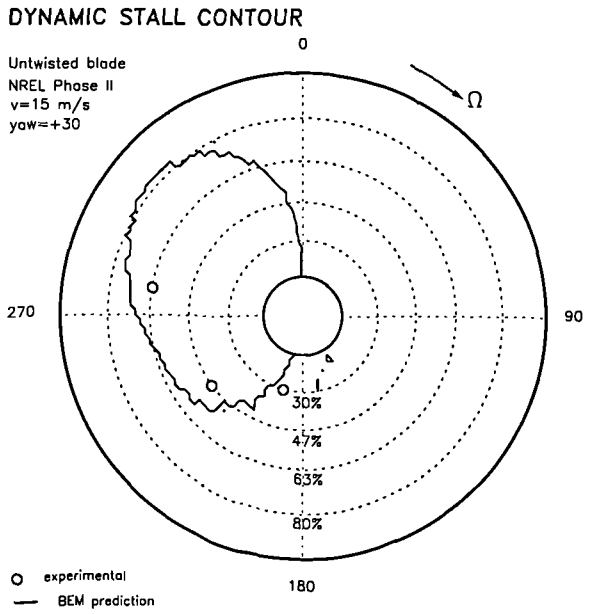

α_{ss} and S_2 variable at f=0.5

Figure 4.31: *3–D Dynamic Stall prediction compared to NREL Phase II*

Discussion

It has been shown that consideration of the position and rapidity of the movement of the separation point along the blade surface, through changes in α_{ss} and S_2 respectively, can affect the onset of the dynamic stall process considerably. The stall boundary is particularly sensitive to the choice of α_{ss}.

This attempt to simulate the three dimensionality of the dynamic stall process through rotational stall delay, has highlighted a serious limitation of the modelling strategy at the most inboard sections of the blade. The drawback can be explained with reference to Figure 4.25, which relies on the Kirchhoff formulation and in addition assumes that 3–D post-stall aerodynamic characteristics exhibit the same behaviour as their quasi-steady counterparts. In Figure 4.25, for blade radius $r \leq$ 21%, the separation point does not show any symptoms of moving forward of the mid-chord, as the angle of attack is increased. In the same manner, for blade radius

$r \leq 25\%$ the separation point does not reach 0.38 of the chord. This behaviour would suggest that the suction pressure will theoretically keep increasing in an unrealistic manner with incidence, without any sign of stalling. Therefore, dynamic stall would not be predicted by the correlation at the inboard sections of the blade, Figure 4.29. This raises the question as to whether 3–D rotating effects affect dynamic stall in a different manner to the way they influence the delay of the static stall. Indeed, the experimentally measured locations of dynamic stall onset are closely characterised by the 2–D correlation, for both the Phase II and Phase IV configurations, especially when the onset occurs at inboard locations on the blade.

The main discrepancies between dynamic stall in 2–D flow and on the turbine blade may occur after stall has been initiated and a dynamic stall vortex has been formed. For example, experiments on a three-dimensional pitching wing, Coton *et al.* (2001), have shown that initiation of dynamic stall at one location on the wing can promote early stall on adjacent sections of the wing.

Given this discussion, the potential to develop a 3–D dynamic stall predictor as an extension of the present 2–D module is severely limited. The main considerations would be:

- the location of dynamic stall onset is predicted using the assumption of 2–D flow reversal from the trailing edge prior to unsteady flow separation at the leading edge. The particular criterion adopted needs more careful consideration and should be representative of distinct aerofoil profile characteristics. This is examined in more detail in the following section.

- based on consideration of the duration of dynamic stall from Galbraith *et al.* (1986), it may be possible not only to identify stall onset but also to identify the azimuthal extent of the dynamic stall process. Galbraith *et al.* (1986) suggested that dynamic stall can endure for about eight semi-chords duration,

with a vortex convection speed independent of the reduced pitch rate or the frequency. The maximum azimuthal extent of dynamic stall can be calculated for the NREL machine on this basis, and is about 20°. It is interesting to note that this may be in conflict with other experimental studies. In a experimental analysis of a rotating wind turbine blade, Schreck *et al.* (2000) concludes that the kinematics of the vortex convection speed, at low wind velocities and small angles, vary in a near linear fashion with the reduced frequency, whereas at moderate to high wind velocities and intermediate to large yaw angles, the convection speed varies in a highly non-monotonic fashion with reduced frequency.

- developing a simple model of how the dynamic stall vortex evolves and convects in a 3–D highly separated environment may be a more challenging task. Understanding the manner in which the dynamic stall vortex affects and interacts with other portions of the blade is still the focus of experiment and analysis Coton *et al.* (2001), Schreck *et al.* (2001).

Possibly the most significant outcome of the analysis conducted in this section is the beneficial effect of reducing α_{ss} on outboard blade sections. This cannot be considered as a 3–D stall delay effect since the lower limit of α_{ss} in the 3–D case should be the static stall angle. Instead, the result brings into question the definition of α_{ss}. It is also interesting to note that, on outboard blade sections, the reduced pitch rate can be close to the quasi-steady boundary. Both of these issues are now considered in more detail.

2–D Correction

As observed in Figure 4.30, at low pitch rates on outboard portions of the blade, low values of α_{ss}, compared with the static stall angle, which gradually increase until

approximately the stall angle at inboard locations, appear to give better agreement with the 3–D dynamic stall locations measured in the experiment. The manner in which this reduction in the incidence of α_{ss} can be justified is discussed below.

The angle at which the flow reversal reaches a particular chordal position in the steady f-α curve, has, in previous studies, been found to provide a good correlation with the angle at which dynamic stall onset is triggered at different pitch rates. The appropriate angle and chordal position, in the case of the S809 aerofoil, have never been properly established. Previous studies on other aerofoil sections illustrate the wide range of possibilities.

McCroskey *et al.* (1976), suggested from experimental results that dynamic stall onset is dependent on the abruptness of the aerofoil's steady trailing edge separation characteristics. Prior to vortex initiation, a gradual forward movement of flow reversal in a thin layer was observed at the bottom of the boundary layer.

Scruggs *et al.* (1974) found good correlation between the predicted angle of attack at which the flow reversal point reached the $f = 0.5$ chordal position, and dynamic stall onset for the NACA 0012 aerofoil in low Mach number tests.

Experimental investigations by Seto (1988) on the NACA 23012 indicated that flow reversal may have reached the $f = 0.30$ chord location prior to the detection of the nascent dynamic stall vortex.

Niven and Galbraith (1997) found for the case of the NACA 23012A, which to an extent resembles the S809 aerofoil, that a good correlation existed between the angle of attack at which C_p deviation predicted dynamic stall onset and the angle at which the separation point reached $f = 0.34$ chord. They noted that, when a C_p divergence criterion was used to indicate dynamic stall vortex inception, the aerofoil shape had little influence (apart from aerofoil thickness, and especially leading edge thickness) if the movement of the trailing edge separation point with incidence under steady conditions, was similar for the aerofoils considered.

In the correlation due to Gracey *et al.* (1996) the onset of dynamic stall is predicted on the basis of slope of the $f - \alpha$ curve and the incidence of static stall. The use of the static stall incidence is, however, problematic. Wilby (1980), Wilby (2001), in his review of rotor aerofoil testing in the U.K., suggested that, " steady state wind tunnel tests do not provide a means of assessing the relative merits of aerofoils operating under dynamic conditions." He did, however, note that some successful semi-empirical dynamic stall models use the angle of attack at which static stall occurs within their formulation, but qualified this by stating that it is by no means clear how this angle should be identified. Indeed, Gracey *et al.* (1996) suggested that the angle of moment stall may be more appropriate than the angle of lift stall in his correlation.

It is clear from the preceding discussion that the use of the static angle of attack in the correlation of (Gracey *et al.* 1996) is, somewhat, arbitrary. It clearly provided Gracey *et al.* (1996) with a good fit to the data on which they based their correlation. It may, however, not be appropriate for all aerofoils. The S809 has particularly unusual stalling characteristics and so may be one such aerofoil. A possible substitute for the static stall angle would be some angle based on the characteristics of the $f - \alpha$ curve. In particular, aerofoils exhibit a marked change in the rate of forward movement of the separation point around stall. The angle at which this change occurs may be appropriate to use, as it may mark a distinct change in the boundary layer dynamics in a pitching case. It may also represent a boundary below which dynamic stall cannot be forced. This is important since the measured data suggest vortex onset even at pitch rates which are firmly in the quasi-steady regime.

For rapidly trailing edge stalling aerofoils under steady conditions, the first divergence of the $f - \alpha$ slope to a lower gradient, occurs at an incidence coincident with the static stall angle. Contrary to this, in the case of aerofoils which have been designed to stall gradually, the slope of the $f - \alpha$ curve is less severe and the curve

tends to flatten out as the static stall incidence is approached. Such aerofoils, may exhibit the first divergence of the $f - \alpha$ slope to a lower gradient, well before the incidence has reached the static stall angle. It may be possible to replace α_{ss} in the correlation with this angle, α_f.

The way in which the incidence α_f can be deduced from the steady $f - \alpha$ curve, for the $S809$ aerofoil is explained next.

The $S809$ aerofoil stalls between 15.2 and 16°, as the Reynolds number is increased from 3 x 10^5 to 5 x 10^5, Huyer *et al.* (1996). In the present work a static stall angle of 16° has always been considered. Figure 4.25 shows the static trailing edge separation point movement from ($f = 1$) *trailing edge, towards* ($f = 0$) *the* leading edge. From around $f = 0.95$ to $f = 0.60$, $\alpha = 6°$ to 9°, the slope of the f-α curve is constant. Beyond $f = 0.60$ the slope slightly decreases before increasing again until approximately $f = 0.38$, which may be regarded as the point where the reversing flow particles, first start experiencing a slow down in their forward progression. At any point between $f = 0.38$ and $f = 0.32$, $\alpha = 11°$ to 12°, the slope remains constant. Forward of $f = 0.32$ there is an irregular increase of f with α until the trailing edge separation point reaches 0.15 chord where the aerofoil stalls at approximately 16°.

The $f = 0.38$ chord location may be considered as the first divergence of the $f - \alpha$ slope to a lower gradient. The incidence α_f at this point is equal to 11°. Because however, of the approximate nature of the assumption, any point between $f = 0.38$ to $f = 0.32$, $\alpha = 11°$ to 12°, may be a fair approximation to α_f.

Using the incidence $\alpha_f = 11°$ at the 38% chord position, as the lower limit to be input to the correlation, the locations of dynamic stall for the Phase II untwisted wind turbine at wind velocity 15 m/s and yaw angle +30° are presented in Figure 4.32(a). In this case S_2 is kept constant, while $\alpha_{ss}(\alpha_f)$ is allowed to change according to the f_{3D}-α curve, at the $f = 0.38$ chordal position, starting at 11° for

the most outboard blade station until reaches the static stall angle of 16° on the inboard parts of the blade.

As a result, comparison with the 2–D case presented in Figure 4.28 shows that the predicted locations of 3–D dynamic stall, Figure 4.32(a), extend further outboard, reaching 80% of span. Also at 47% and 63% of span, it is identified at an earlier azimuthal angle, whereas, at 30% of span, dynamic stall is predicted at the same location. Thus the predictions using the correction are more in line with the experimentally identified locations. It is worthy of note that the reduced pitch rates encountered in this case were: α^+ =0.0070 at 30%, α^+ =0.0085 at 47% and α^+ =0.0012 at 60% of the span. Thus, dynamic stall would not be expected as far outboard as 60% of the span in this case. The possibility that it is triggered there by the formation of the vortex further inboard cannot be ruled out.

Application of the same correction, to the Phase IV configuration is presented in Figure 4.32(b). It may be observed that, at around 47% of span, and more clearly at 63% of span, dynamic stall is detected now just after the static stall threshold of 16°. The pitch rates encountered at the predicted locations of dynamic stall were: $\alpha^+ = 0.015$ at 30% $\alpha^+ = 0.0084$ at 47% and $\alpha^+ = 0.0065$ at 60% of the span

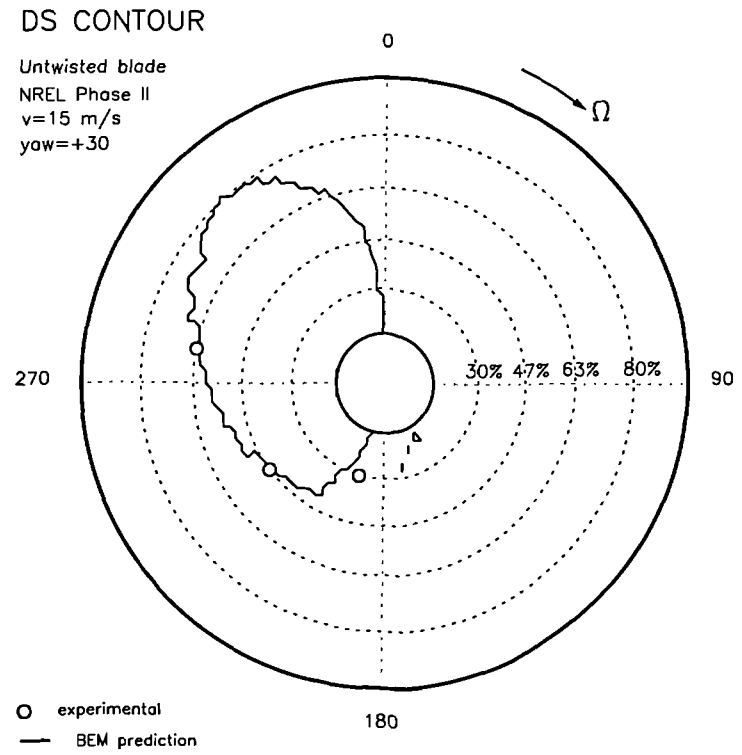

(a) α_f prediction, NREL Phase II

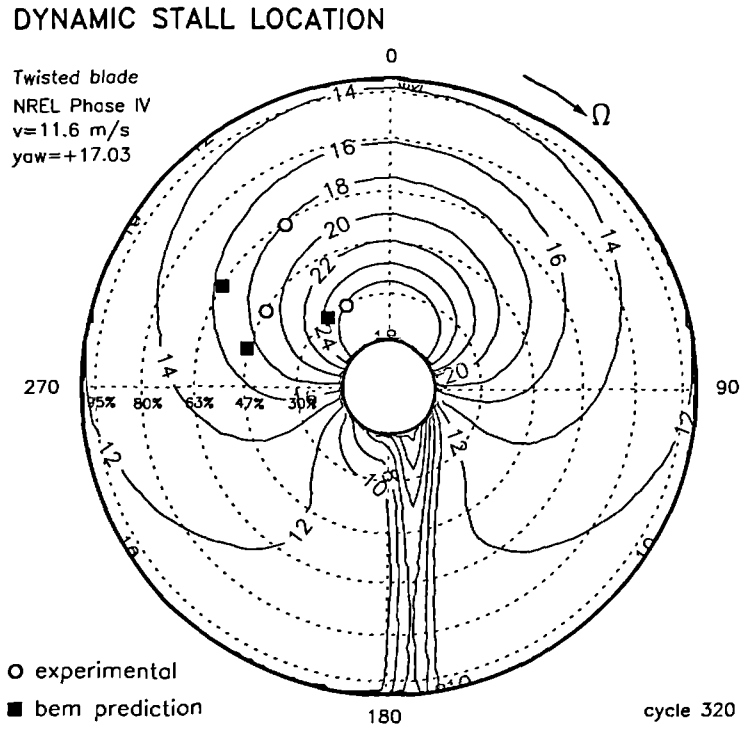

(b) α_f prediction, NREL Phase IV

Figure 4.32: *Dynamic Stall prediction with α_{ss} variable at f=0.38 and S_2 fixed from the 2–D static test*

4.5.3 3–D Conclusions

BEM predictions based on a 2–D correlation of vortex stall onset provide a fair representation of the actual dynamic stall onset experienced by the rotating wind turbine blade over the entire range of operating conditions, that have been analysed.

It has been shown that rotational stall delay does not affect dynamic stall as it does static stall. Examination of the three-dimensionality of the dynamic stall process has revealed that, its initial onset is correctly characterised by the BEM 2–D correlation but that after its local inception, earlier dynamic stall appears to be triggered in adjacent stations.

The influence of the wind turbine blade planform and aerofoil section on dynamic stall onset has been examined using two parameters related to the steady stall characteristics. The first, S_2 represents the abruptness of the steady trailing edge separation and the second, α_{ss}, is the static stall angle. The incidence α_f, at which the first divergence of the $f-\alpha$ slope to a lower gradient is detected from the steady characteristics, has been introduced as a possible replacement for α_{ss}. It appears to provide a possible mechanism to improve the prediction from the correlation for the particular aerofoil used on the NREL turbine. Further work is, however, required to fully consider the impact of three-dimensional effects on the dynamic stalling process. Theoretical and experimental studies, such as flow visualisation of a rotating wind turbine blade, will be of help in addressing the complicated physics of both, attached and separated unsteady three dimensional rotating flows.

The applicability of the correlation of Gracey *et al.* (1996) to the S809 aerofoil is also a major question that needs to be considered. Ideally, this aerofoil should be tested under dynamic conditions and the results compared to the correlation. This would help to resolve the question of the suitability of α_f or α_{ss}.

Chapter 5

Tower Shadow

This section presents detailed experimental measurements of blade surface pressures obtained during the interaction of a wind turbine blade with the tower wake. The blade pressure distributions, were also integrated around the chord to yield transient normal force and quarter chord pitching moment coefficients which are also presented to illustrate the salient features of the aerodynamic response. In examining the effect that the tower wake has on the blade, special attention will be given to the behaviour of C_n, the normal force coefficient and C_m, the pitching moment coefficient. Finally, comment will be made on the suitability of specific tower shadow modelling strategies with emphasis on how improvements could be made.

A explanation of tower shadow effects is given next, together with a brief review of relevant experimental and numerical efforts.

5.1 Tower Shadow Effects

The blades of a horizontal axis wind turbine, HAWT, are connected through the hub and shaft to the rest of the components which are ultimately supported by a cylindrical tower. During the rotational cycle, the blade encounters a region of disturbed inflow when it passes near the azimuthal position coincident with the

tower. For upwind rotor configurations this effect is mainly caused by the slow down and deflection of the flow due to the presence of the tower and only extends a short distance upstream. In the case of a downwind turbine, i.e. when the rotor is downwind of the tower, the blades interact with the wake of the tower which extends some distance downstream. The tower wake or shadow is a region of reduced wind velocity and turbulence produced, as the name suggests, by the wake of the turbine tower. For this reason, it has a significant effect on turbines which operate in a downwind configuration. Upwind machines often experience fluctuations in blade loads as the blades pass in front of the tower but these proximity effects are not considered in the present work.

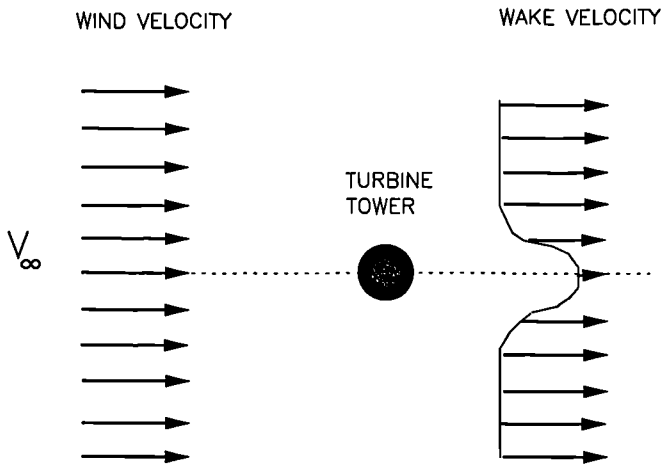

Figure 5.1: *Sketch of tower shadow velocity deficit, plant view*

On a downwind turbine, the tower wake has a severe effect on the blade inflow conditions. Tower shadow will produce a rapid decrement of the inflow velocity followed by an increment as the blade passes through the wake, Figure 5.1, which will

vary the angle of attack in an oscillatory and impulsive manner. As explained in Chapter 4 rapid variations of the blade incidence may cause stall to occur dynamically. In addition, concentrated vorticity shed from both sides of the tower could produce a blade vortex interaction BVI like effect.

All these perturbations contribute to the unsteady loads suffered by the blade as it passes the tower. These dynamic loads can induce blade stall vibrations which will either mitigate (damp) or amplify, the natural frequency oscillations of the tower, with serious structural dynamics implications for the turbine. The blade deflection around the rotor cycle may also be accentuated in the tower wake region. As a result, flap bending moments on the blade can reach their maximum values at azimuthal positions coincident with the tower shadow. This has been seen in experiments (Thresher *et al.* 1986). The yawing moment will, therefore, be very much dependent on the damping of the blade oscillations produced in the tower wake (Petersen 1984). In addition to these problems, the oscillations in the loading of the blades, may introduce fluctuations in the generated electric signal, damaging the quality of the power output and compromising the stability of the grid connection.

Some early downwind turbine designs also developed a distinction for generating noise as the blades passed through the tower shadow. Downwind turbines operating today generally have lower tip speeds which result in negligible infrasound emissions (Kelley and McKenna 1985). Because the blade spends such a brief period of time in the tower shadow, one may incorrectly conclude that the primary tower shadow effects are on the fatigue life and on noise, other than mean power performance. The tower shadow not only alters the local angle of attack, but can also significantly influence the onset of dynamic stall. Even under unyawed conditions, tower shadow can trigger dynamic stall, which lasts a significant duration before the blade recovers from stall. This may contribute to a persistent loss of power for a prolonged period of time. The location and severity of dynamic stall on the rotor disk, is very sensitive

to the onset flow conditions. Given the rapid incidence variations within the tower shadow domain, any aerodynamic design code needs to cope with tower shadow in order to correctly identify dynamic stall.

5.2 Tower Shadow Experiments and Modelling

Experiments

In addition to producing a velocity deficit, the shadow region may contain sources of unsteadiness resulting from vortex shedding from the tower itself, making the local aerodynamic response of the blade highly unsteady (Robinson *et al.* 1995). Although some experimental testing into the problem has been undertaken, few detailed analyses of the measurements are available in the open literature at the time of writing this chapter.

Some early wind tunnel experiments (Savino and Wagner 1976, Burley *et al.* 1976, Snyder and Wentz 1981, Powles 1983) measured the wind velocity profile in the wake of tower models to determine the magnitude of the velocity reduction. Subsequently studies of tower shadow effects were conducted via wind tunnel pressure measurements and open field collected data, (Petersen 1984, Wilmshurst *et al.* 1985, Shipley *et al.* 1995*b*, Graham and Brown 1999). For example, the NREL Unsteady Aerodynamics Experiment has collected field data which comprises pressure distributions on different blade sections, integrated blade loads (normal force, tangential force, and pitching moment coefficients), information about the angle of attack at various wind speeds and yaw angles, on a downwind turbine, thus providing unique aerodynamic data for model validation and development. More recently, this turbine was used in the NREL/NASA Ames wind tunnel experiment to provide high quality clean data for a downwind turbine, without the uncertainties of open field measurements.

European laboratories have also conducted a unified study of the rotor tower interaction problem, (Rotow 2000). Wind tunnel and field data, together with numerical simulations have been contributed to this E.U. Joule project. The final report from this project has not been made available, to date.

Independently, Glasgow University conducted a wind tunnel test in February 1998, the results of which are presented later in this chapter.

Modelling

Studies have been initiated to examine how the induced unsteadiness produced by the tower shadow on the rotor aerodynamics could be modelled.

By close examination of experimental pressure differences and wind velocity contours in the tower wake, Powles (1983) proposed a model for the tower shadow velocity deficit as a cosine fall-off from the free stream velocity, with width and depth variation of this cosine function varying with the distance from the tower. When Thresher *et al.* (1986) used a computer code to analyse blade dynamic loads, the tower shadow effects were not the main concern; instead, the velocity deficit in the tower shadow was included in passing only as a deterministic excitation. The model of Thresher *et al.* (1986), employed a pi-shaped tower shadow representation of the velocity deficit, which was assumed to be approximately 0.25 to 0.30 of the free stream wind velocity, based on the experimental work of Snyder and Wentz (1981).

Hansen (1992) studied the free-yaw mechanics of downwind turbines and developed engineering design tools which included tower shadow modelling. His structural response code named *YawDyn*, developed by the University of Utah for NREL, makes use of the *AeroDyn* aerodynamics subroutine which is based on BEM theory and with a cosine-shaped wake representing the tower shadow.

A similar approach has been followed in the commercial aeroelastic code, *Bladed*, version 3.2 (Bossanyi 1997). Originally, this structural code, developed and owned

by Garrad Hassan and Partners Limited, utilised a cosine function to represent the tower shadow. This was based on the experimental work of Powles (1983), with a fixed user-specified width and depth intensity. But, in a later version, the width and intensity of the tower wake vary with the square root and inverse square root of the distance from the tower, respectively. This is also the case in the *YawDyn* code.

Wang *et al.* (1998) presented a tower shadow modelling strategy for downwind wind turbines. The scheme is also based on a cosine pi-shaped function that accounts for yawed flow and the corresponding skew of the tower wake. Application of this model within a vortex wake code has been reported in several papers, with encouraging results (Coton and Wang 1999, Wang and Coton 2001).

Duque *et al.* (1999), used an Navier–Stokes solver to examine rotor tower interaction but, in comparison to experiment, the computed results are still not quite satisfactory, mainly due to grid density mismatches in the analysis. Xu and Sankar (2000) used a hybrid Navier–Stokes / potential flow solver developed at Georgia Institute of Technology in which spanwise and azimuthal variations of circulation are captured using vortex filaments, freely convected by the local flow. In a progress report to NREL, Sankar (2001) states that the hybrid Navier–Stokes / potential code predicted the loss in dynamic pressure due to the tower shadow, but the vortex shedding from the tower was not captured because of the sparse grid employed there.

Recently, within the Rotow Joule project, two and three-dimensional simulations of the rotor blade aerodynamic interaction with the tower wake and its impact on the wind turbine design were conducted. Commercial packages such as *Fluent* and *Star-Cd* were tested together with in-house solvers and engineering codes. It was suggested by Johansen and Bak (2000) that wind tunnel experimental conditions could be the reason for the bad comparison with their numerical results for a downwind rotor. In particular the low Reynolds number of 7.2×10^4, large centrifugal

forces, the coarse distribution of pressure taps on the measured blade and tunnel blockage were cited as contributing factors.

Some approaches in the form of simple engineering models have also recently appeared in the literature. Three models are described and tested by Madsen (2000), who prefers a model, called *model 3* for the downwind configuration. In this model the flow around the tower is represented by a potential flow but with the tower radius and the tower drag included in the formulation. Another method proposed to model the response of the blade to the tower wake, paying special attention to the unsteady conditions in attached flow, has been described by Leishman (2002). He proposes the use of the Küssner function in order to simulate the response of the blade to the change in the velocity field during its passage through tower shadow. This approach is examined in more detail later in this chapter.

5.3 Wind Tunnel Experiment

The objective of the present work is the study and analysis of wind tunnel experimental data to enhance understanding of the aerodynamic effect that the tower has on the passage of the blades, and if possible, from this understanding to outline ways to improve its modelling. Descriptions of the experimental test setup, data processing and results are presented next.

5.3.1 Description of the Wind Tunnel Experiment

A series of tests were previously conducted in the closed circuit "Handley Page" wind tunnel at the University of Glasgow on a small wind turbine using laser sheet visualisation (LSV) and particle image velocimetry (PIV) to study the rotor wake structure (Grant *et al.* 1998, Grant *et al.* 2000). This wind turbine also provided the opportunity to carry out an additional experiment to examine tower shadow

interference with the blades.

This section presents results from the experimental study of tower shadow on the small scale wind turbine in the controlled environment of the wind tunnel. The test programme was conducted in the "Handley Page", University of Glasgow, 2.13 m x 1.61 m low speed wind tunnel. The turbine model, which was a two bladed upwind design, had a rotor diameter of 1 m, and a nacelle specifically designed to maximise the available internal space for instrumentation. The NACA 4415 section blades were manufactured from carbon fiber composite and had a chord length of 0.1 m. The stiff blades were set at a fixed $-12°$ pitch angle, having no twist and no taper. One blade was instrumented with sixteen miniature pressure transducers positioned at the 75% of chord location, eleven on the upper surface and five on the lower side of the aerofoil. The internal structure of the nacelle was constructed from aluminium and housed the rotating shaft of the turbine. On this shaft were located the necessary electronics to condition the signals from the pressure transducers prior to passing the signals through slip-rings located at the rear of the nacelle. The signals were then passed to a high speed data acquisition system capable of sampling at up to 50kHz per channel. The speed of rotation was controlled by an electronic braking system, similar to that used in the PIV proving tests, located below the wind tunnel floor and connected to the turbine shaft by a belt and pulley system. In this manner, a fixed tip speed ratio of 5 was achieved throughout the measurement process. The entire turbine arrangement could be rotated about the support shaft and locked at any required yaw angle. Most of the measurements were made for the head-on flow case although some were made at yaw angles up to $+20°$.

To simulate tower shadow, a dummy, tunnel-spanning tower was placed ahead of the turbine. This additional tower was mounted vertically in a direct line with the actual turbine support strut. As a consequence, the turbine blades experienced a double tower shadow as they passed the dummy tower both above and below

the nacelle. The lower tower passage was contaminated by the proximity of the turbine support strut and so only the tower shadow above the nacelle is considered here. A schematic of the experimental arrangement is illustrated in Fig. 5.2. The cylindrical tower had a 70 mm diameter and the distance between the rear edge of the tower and the rotational plane of the blade was set equal to 140 mm, i.e. two tower diameters. Because of the low Reynolds numbers, test were conducted with both a clean smooth tower, and a roughened tower surface.

5.3.2 Pre and Post-Processing of Data

A fully automated data acquisition system was used for the measurement of the unsteady blade pressures. This system has two-hundred channels, each of which is capable of sampling to a maximum rate of 50kHz. For the tests reported here, the wind tunnel velocity ranged from 9 m/s to 11.7 m/s and the turbine rotational speed from 15.3 Hz to 19.9 Hz.

During testing, the pressure data were sampled at a frequency of 50kHz per channel, giving approximately 2500 to 3200 samples per revolution. The pressure transducer signals were corrected for the effects of rotation by subtracting the signals measured during a test in which all the transducers were covered by tape.

No wall or tunnel blockage corrections were applied to the data. Normal force, pitching moment and tangential force coefficients, were calculated as a function of time by integration of the chordal pressure distributions using the trapezoidal rule.

A summary of the experimental test conditions is presented in Table 5.1.

5.3.3 Results of the Wind Tunnel Experiment

As a basis for comparison, and also as a measure of the quality of the data, a steady case with no tower is presented in Figure 5.3 for zero yaw error and 11 m/s wind velocity. The bottom plot in the figure, shows the locations of the transducers on

Table 5.1: *Experimental conditions of tower shadow tests*

yaw angle	wind velocity	rotational speed	Tip Speed Ratio	Reynolds number at the blade	type of tower
0	9	15.3	5.34	2.5 x10^5	smooth tower
0	11	18.7	5.33	3.0 x10^5	smooth tower
0	11	18.7	5.33	3.0 x10^5	rough tower
0	11	18.8	5.35	3.1 x10^5	no tower
0	11.7	19.8	5.31	3.2 x10^5	smooth tower
0	11.7	19.9	5.34	3.2 x10^5	no tower
+20	9	15.3	$\simeq$ 5	2.5 x10^5	smooth tower
+20	11	18.7	$\simeq$ 5	3.0 x10^5	smooth tower
+20	11	18.7	$\simeq$ 5	3.0 x10^5	rough tower
+20	11	18.7	$\simeq$ 5	3.0 x10^5	no tower
+20	11.7	19.9	$\simeq$ 5	3.2 x10^5	smooth tower
+20	11.7	19.7	$\simeq$ 5	3.2 x10^5	no tower
degrees	m/s	Hz	-	-	-

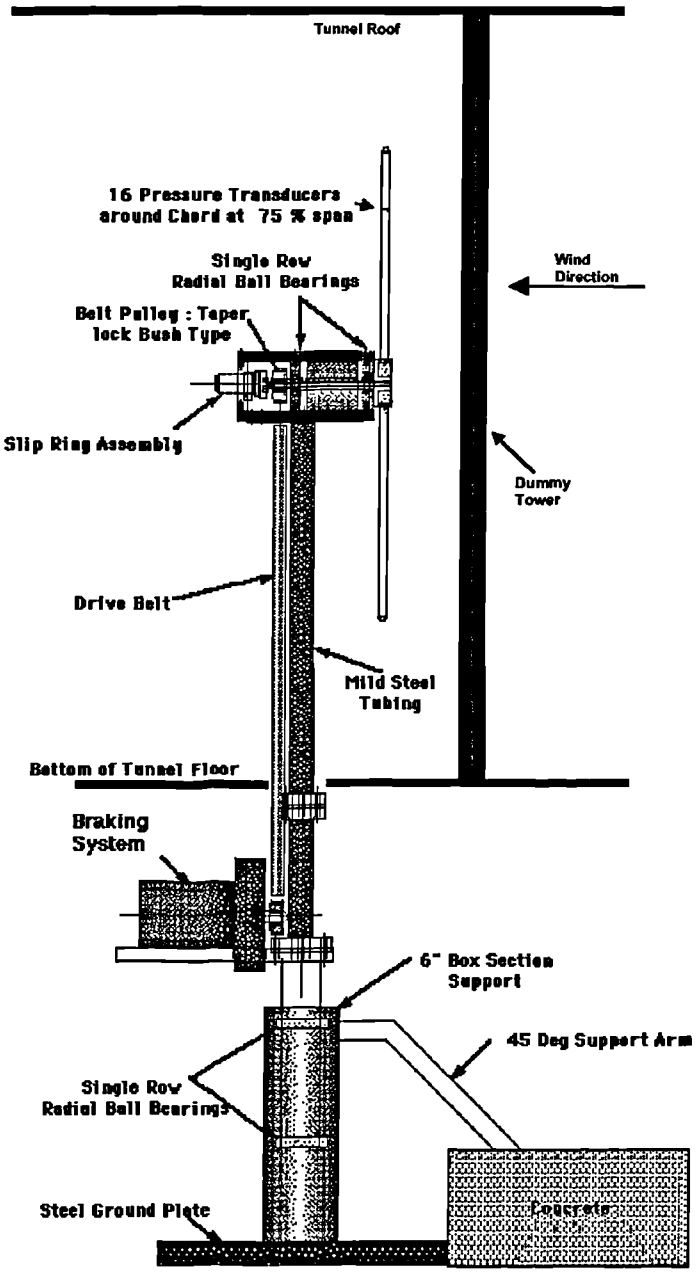

Figure 5.2: *Schematic of the wind turbine model for tower shadow experiment*

the upper and lower surfaces of the NACA 4415 aerofoil. The top plot shows the chordal pressure distribution measured during one rotational cycle of the blade. All 2500 samples measured over the entire 360° rotational cycle are plotted at each transducer location in this figure. As expected, with the turbine set at zero yaw error and no tower present, the pressure coefficients remain almost constant over the complete cycle.

In Figure 5.4, the calculated pressure distribution from a panel method (triangle symbols) for an angle of attack equal to 1°, is compared to the experimental pressure distribution (diamond symbols). This angle provided the best fit between the panel method and the measured data. Despite this, substantial disagreement exits between the two distributions. For example the measured pressure at the stagnation point, is not correctly evaluated; instead of the theoretical $-C_p = -1$ obtained from the panel method at $x/c = 0$, the experimental data give a $-C_p = -1.2$ at the leading edge. This could be due to the difficulty in determining the true value of the dynamic pressure in the rotating environment but this would not explain the more significant differences elsewhere on the chord. No clear explanation for this has been found by the author. For the calculated geometric angle of attack, about 0.9° including the local negative aerofoil pitch, the flow conditions are attached and the blades are not stalled. However, the centrifugal effect due to rotation is of such a magnitude that the steady 2–D panel method approach may be questionable. A more likely reason for the difference relates to the manner in which the centrifugal offsets were taken. It is possible that covering the blades with tape may introduce some difficulties. For example, the tape may trap air above the transducer at a pressure above ambient. Alternatively, the tape itself may act like a diaphragm which deforms under the action of the flow. In both cases, the offset reading would be compromised. Regardless of the cause of the difference, it is likely that the effect that the tower has on the response of each individual pressure signal will still be

correctly characterised by the measured data.

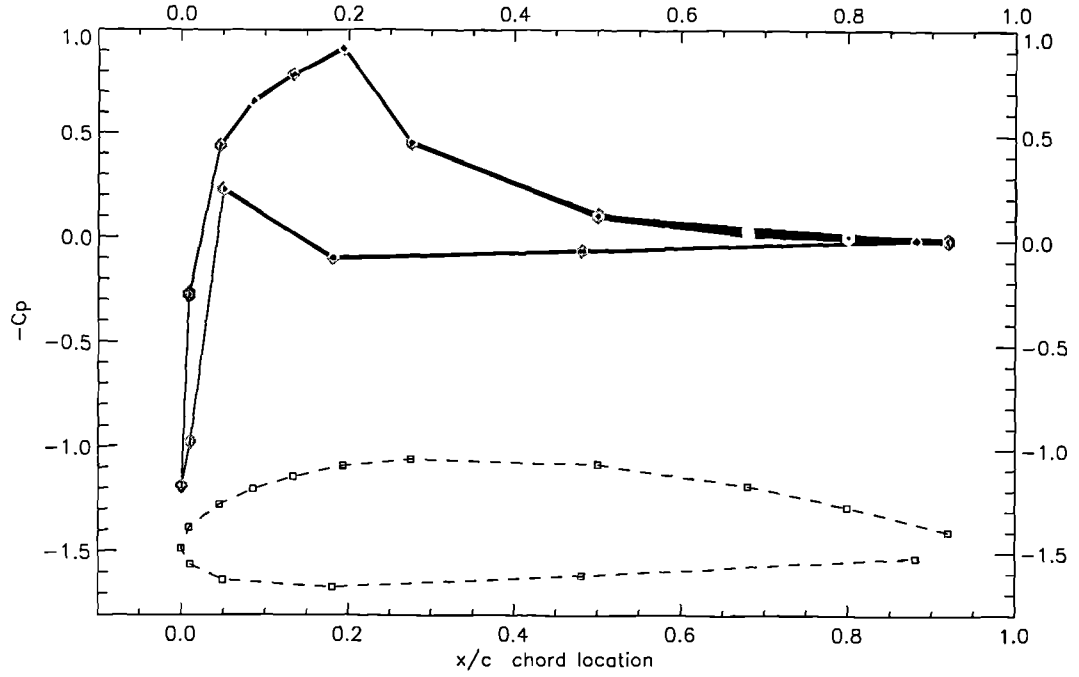

Figure 5.3: *Pressure distribution on the aerofoil for one cycle, no tower, wind velocity=11 m/s, yaw=0°*

The results presented herein are instantaneous unaveraged data, and so exhibit some degree of noise. Generally, however, the quality of the pressure signals are such that they permit an assessment of the force and moment coefficients without filtering or averaging. In addition, clear correspondence between detailed time histories in each cycle can be observed.

In order to understand the basic response to tower shadow, head-on flow cases are examined first. At 75% of the blade span, the tower shadow is the only source of unsteadiness in head-on flow and hence any variations in the blade loads are caused by tower shadow effects. Figures 5.5 through 5.9 illustrate measured pressure, normal force and quarter chord pitching moment coefficients at three wind velocities: 9 m/s, 11 m/s and 11.7 m/s for nominally unyawed cases.

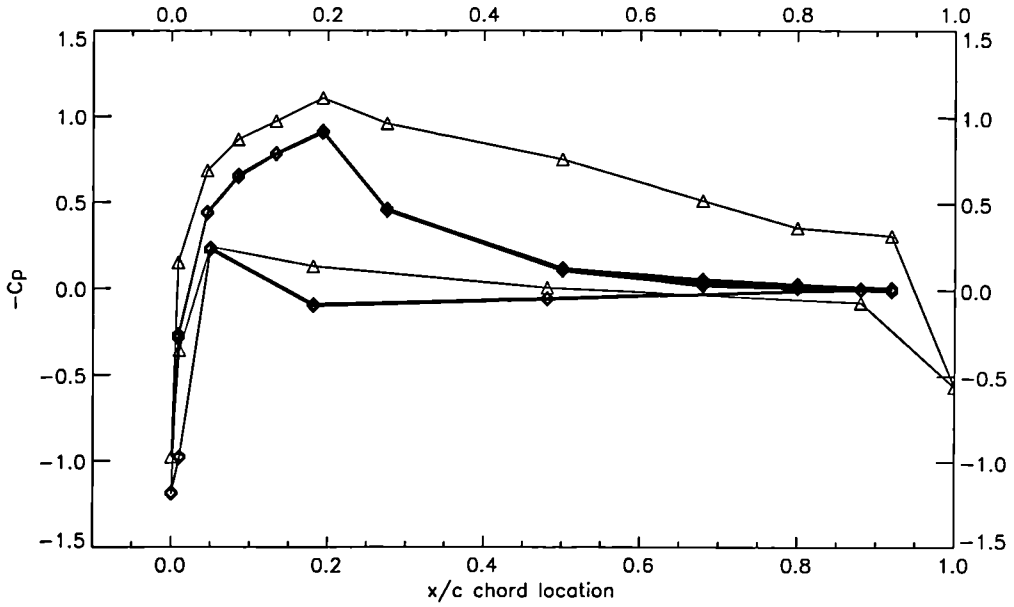

Figure 5.4: *Comparison of measured pressure (diamonds) and calculated via panel method (triangles), no tower, wind velocity=11 m/s, yaw=0°*

Head-on Flow Cases

Figure 5.5 shows the azimuthal pressure coefficient time histories recorded for transducers on the upper and lower surface of the blade section (top left and right plots of the figure respectively) and the corresponding chordal force and moment time histories (bottom plot) for a test case in which the wind velocity was set at 9 m/s and the turbine was set at zero yaw error.

In both of the pressure coefficient plots, the bottom trace represents the measurement from the transducer closest to the leading edge and the top trace is from the transducer closest to the trailing edge. The intermediate traces show the progression from leading edge to the trailing edge. The pressure traces themselves, are plotted such that a drop indicates a decrease in suction and a rise an increase in suction. The tower shadow region, which is clearly identifiable in the figure, around the 90° azimuth angle, exhibits a number of interesting features. For example the response at the leading edge is quite different from elsewhere on the blade and is closely linked

to the movement of the stagnation point during the passage of the blade through the tower wake. Generally, however, the data show a progressive trend in which the severity of the response reduces as the trailing edge is approached. In fact, the transducers near the trailing edge show almost no response until later stages of the tower shadow passage when a slight rise in suction can be observed. Another significant feature of the figure is the slight rise in suction experienced by some forward transducers on the upper surface, just prior to the tower shadow entry, as can be seen on the second transducer from the leading edge at approximately 85° azimuth. This is accompanied, on the lower surface, by a slight drop in suction observed just before entering the tower shadow region, as may be seen on the third transducer from the leading edge at around 85° azimuth angle. This effect is significant and, as may be observed in the corresponding plot of normal force and pitching moment versus azimuthal angle (bottom plot), sustains the normal force and causes a progressive increase in pitching moment prior to a sharp drop in C_n and C_m, at points 1 and A respectively. Within the tower shadow region, approximately 80° through 130° azimuth, points 1-2-3; the normal force drops considerably from about 0.30 to 0.05 and then it recovers as the blade leaves the tower shadow region. This dramatic change in normal force is mainly associated with the velocity deficit encountered by the blade behind the cylindrical tower.

The quarter chord pitching moment remains roughly constant up to about an azimuthal position of 70°. Beyond this azimuthal value, the pitching moment increases until it reaches a local maximum, point A, just before the 90° azimuth position. After that, within the tower shadow region, the blade initially experiences a drop in pitching moment, A-B as the blade enters the tower wake. This is followed by a recovery of the pitching moment between B' and C, reaching a second local maximum peak, C just before the 120° azimuthal position. Following this, C_m drops sharply, C-D, the pitching moment then gradually returns to the undisturbed value. Coin-

cident in azimuth with the local maximum at point C, is a small localised decrease in C_n just before the 120° azimuth angle. This reflects a minor loss of suction as the blade trailing edge passes out of the tower shadow. The relatively slow recovery in C_n from the tower shadow, points 2-3, is also an interesting feature of this plot.

Increasing the wind tunnel velocity yields the case presented in Figure 5.6, in which the wind velocity was set at 11 m/s and the turbine was set at zero yaw error. Most of the features observed previously (Figure 5.5) apply to this case, although they may not appear as clearly as in the previous case. An interesting difference in Figure 5.6 is that there is no strong evidence of a rise in suction at any of the forward transducers on the upper surface just before the tower shadow entry. Similarly, none of the lower surface pressure coefficients show any symptoms of a drop in suction just before entering the tower shadow region. As a consequence, the normal force begins to drop earlier and more gradually than in the previous case, although the pitching moment shows some indication of a slow increase between 70° and 90° azimuth angle, before collapsing. Once more, as the blade leaves the tower shadow, the recovery of the normal force from the minimum value of 0.07, points 2-3, is less rapid than the drop in C_n when the blade enters the tower shadow region.

In Figure 5.7, the wind velocity is again set at 11 m/s and the turbine at zero yaw error, but this time, the tower surface is not smooth. The roughness was increased by means of a strip of sand-paper stuck to the tower surface. Increasing the tower roughness, for this particular case, does not significantly change the blade load variation compared with the smooth tower at the same flow conditions. However, a feature which distinguishes the rough tower case is the absence of clear local C_m peaks, at entry and exit from the tower shadow region; points A and C respectively. Once again the C_n recovery is more gradual than the initial drop.

A steady case with no tower presence was also measured. Figure 5.8 presents, the data measured for this case in which the wind velocity was set at 11 m/s and the

turbine set at zero yaw error. In this case the pressure coefficient traces are almost horizontal but not quite. This and the undulation in the C_n curve indicates that there was a small yaw error during the experiment, possibly due to slightly skewed flow in the wind tunnel. The higher level of noise on the C_m plot is an artifact of the integration process.

The final zero yaw case is presented in Figure 5.9 for a wind velocity of 11.7 m/s, with a smooth tower. This case has some interesting features. Some of the forward transducers on the upper surface, experience a slight rise in suction, just prior to the tower shadow entry at approximately 85° azimuth. This is accompanied by a slight pressure rise at the corresponding lower surface transducers. As may be observed in the corresponding plots of normal force and pitching moment, this manifests itself as a progressive increase in the normal force and pitching moment prior to a sharp and severe drop in C_n and C_m, points 1 and A respectively. The effective lift decreases from points 1-2 and the normal force reaches a minimum value of 0.04. The pitching moment recovery, points B'-C, is much more gradual than the drop as the blade enters the tower shadow, points A-B. When the blade is leaving the shadow region, the force data show a perturbation just before the 130° azimuth angle. Here, an upward spike in the positive C_n direction is detected. The reason for this is not obvious from the individual pressure traces. Once more the pressure signals and normal force recover more gradually as the blade leaves the shadow region.

Yawed Flow Cases

On a yawed wind turbine, the incoming flow and the tower wake are not perpendicular to the rotor plane anymore. Thus, for a +20° yaw angle, the blade is encountering the wake at a slightly later azimuth. The blade does not cut the tower wake in a perpendicular fashion, but rather on a skewed basis instead. In addition, there is a cross-flow component of the inflow, on the rotor plane, which causes the blade angle

of attack to vary with azimuth in a sinusoidal fashion.

Figures 5.10 through 5.14 show the azimuthal pressure coefficient time histories recorded on the upper and lower surface of the blade section (top left and right plots respectively) and the force and moment time histories (bottom plot), for cases in which the turbine was set at +20° yaw error. The wind velocities and remaining test conditions are the same as in the head-on flow configuration, that is: smooth tower at 9 m/s, smooth tower at 11 m/s, rough tower at 11 m/s, no tower at 11 m/s and smooth tower at 11.7 m/s.

From the pressure histories (top plots), it can be seen again that the first trace corresponding to the leading edge pressure transducer exhibits a different signal than the rest of the traces. This can be related, as previously mentioned, to the movement of the stagnation point when entering the tower shadow region. The rest of the transducers exhibit a similar behaviour to the unyawed case. As mentioned above, the tower shadow region has shifted about 5° to a higher azimuth angle, because of the yawed position of the tower wake.

The normal force and pitching moment coefficients are presented in the bottom plots of Figures 5.10 to 5.14. Within the region of the tower wake influence, points 1-2-3, a drop in suction followed by a slow recovery as the blade is leaving the tower shadow region can be observed in all the figures, in a manner similar to the head-on flow test cases. Outside the tower shadow region, a persistent increase in C_n and C_m can be observed before entering the tower shadow, prior to point 1, followed by a decrease in both coefficients after leaving the region, beyond point 3. This is caused by the cross-flow on the rotor which produces the azimuthal variation in the angle of attack. This can be clearly observed in the yawed case presented in Figure 5.13 without the tower presence, where the force and moment values vary in response to the yawed inflow.

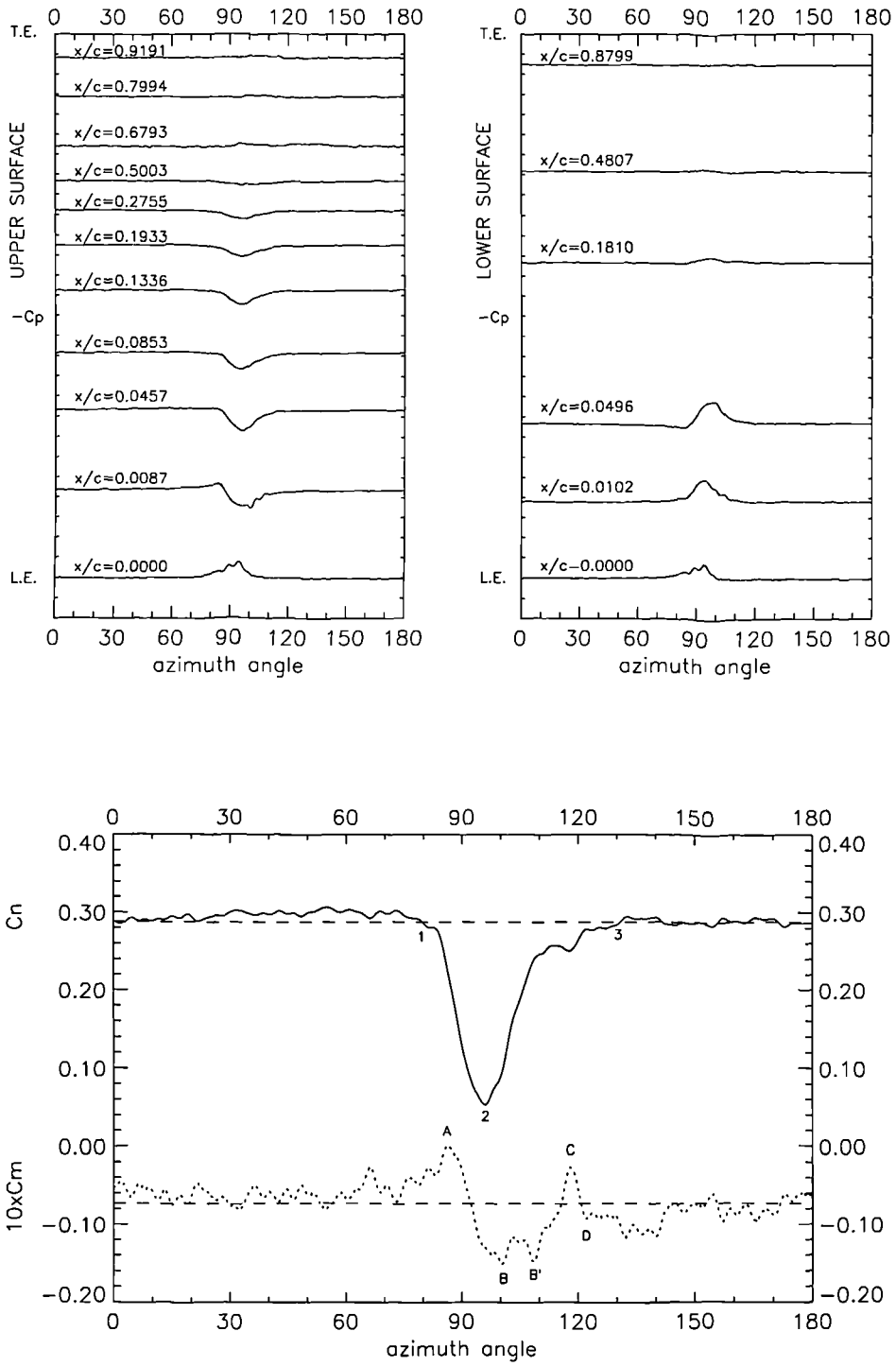

Figure 5.5: *Upper and lower surface pressure measurements, normal force and pitching moment coefficients, smooth tower, yaw=0°, wind velocity=9 m/s*

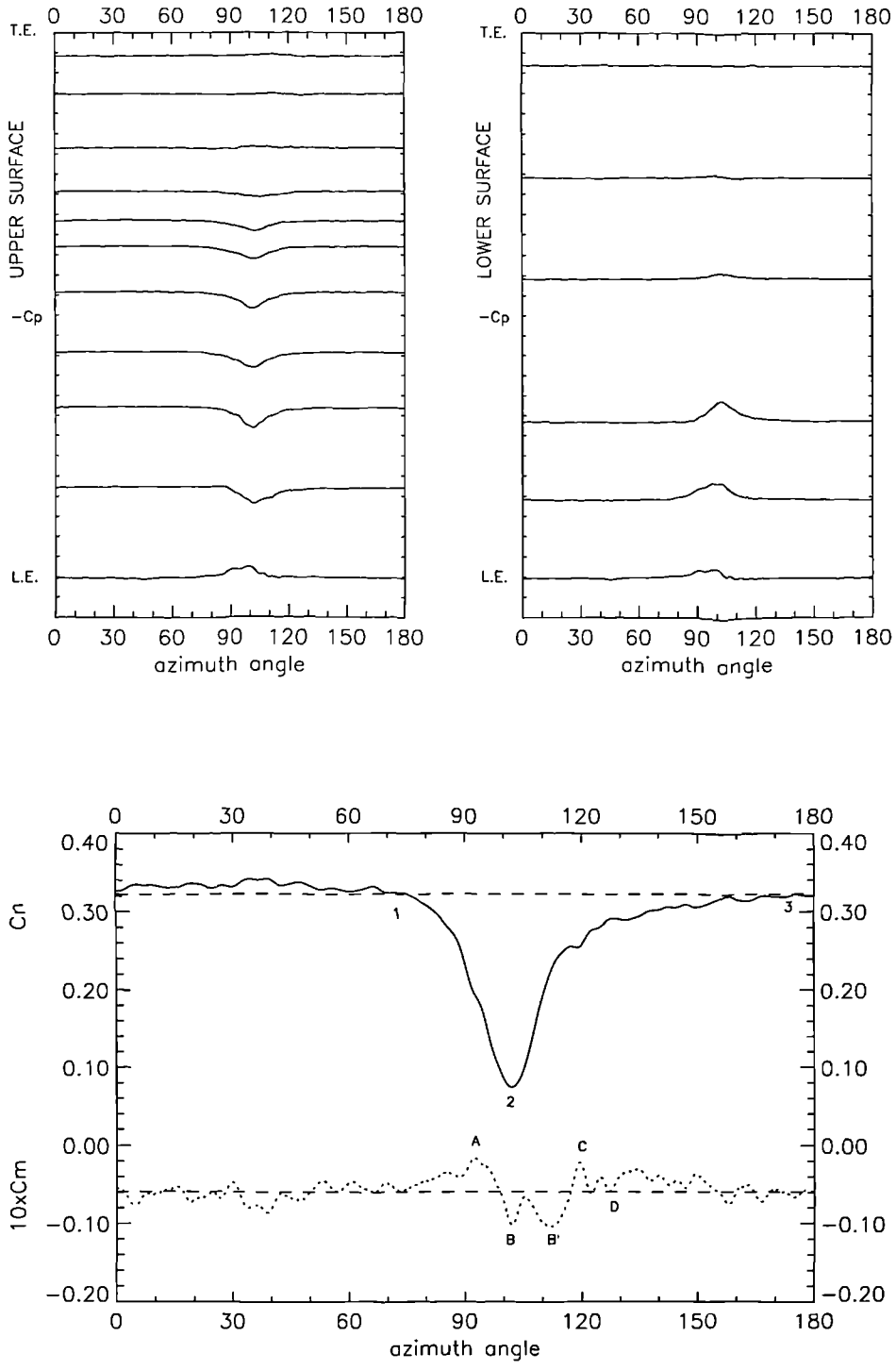

Figure 5.6: *Upper and lower surface pressure measurements, normal force and pitching moment coefficients, smooth tower, yaw=0°, wind velocity=11 m/s*

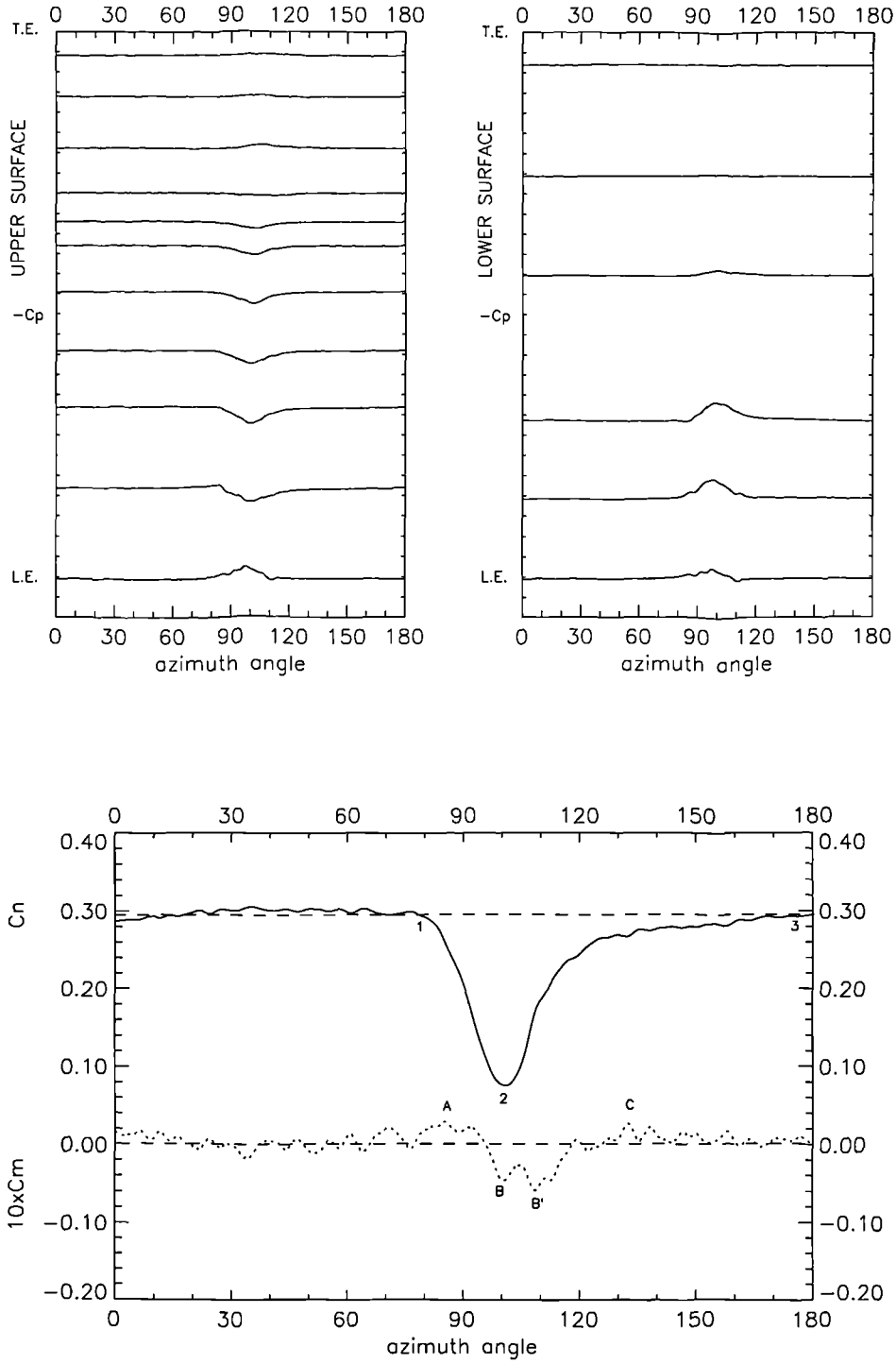

Figure 5.7: *Upper and lower surface pressure measurements, normal force and pitching moment coefficients, rough tower, yaw=0°, wind velocity=11 m/s*

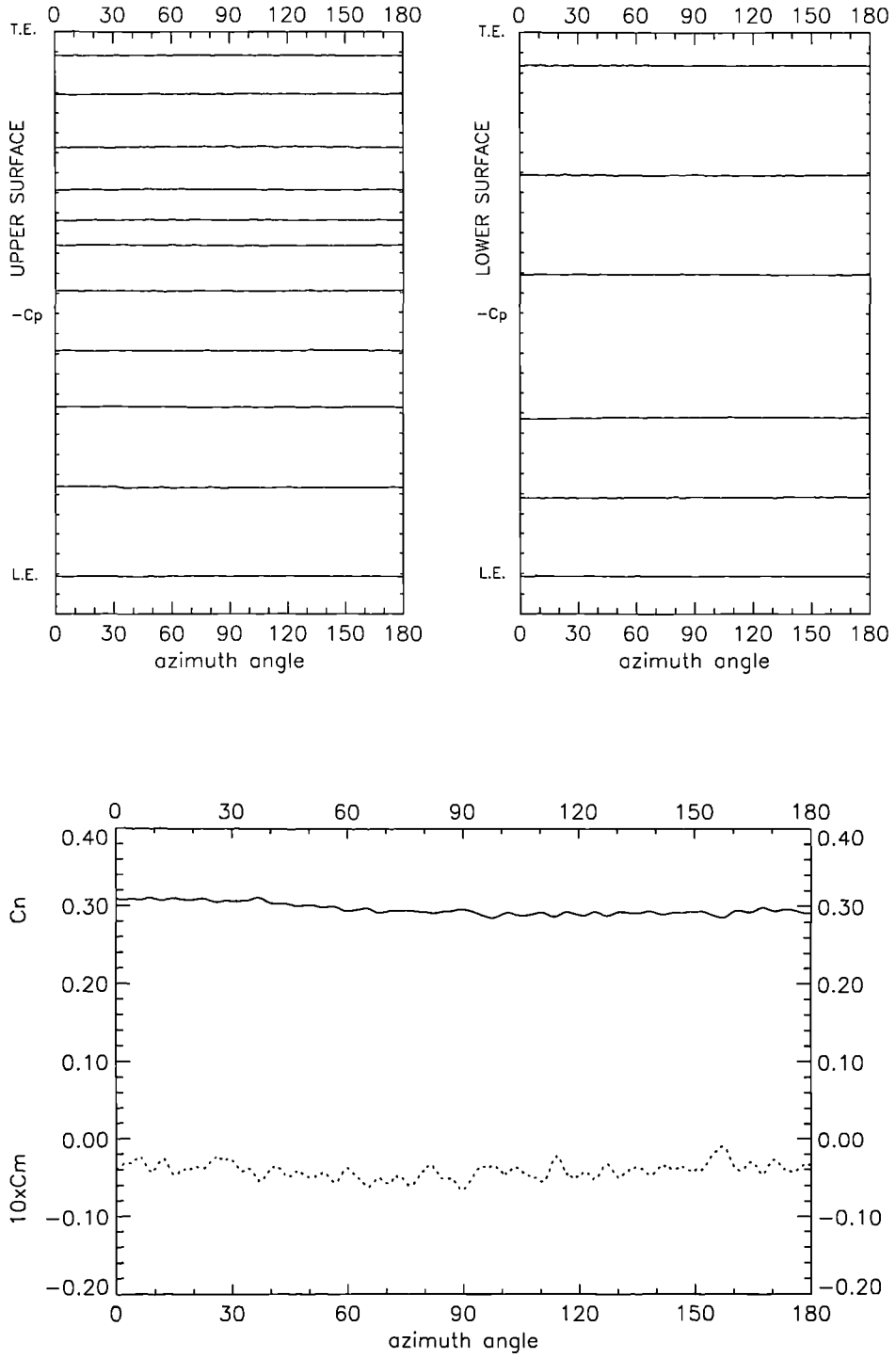

Figure 5.8: *Upper and lower surface pressure measurements, normal force and pitching moment coefficients, no tower, yaw=0°, wind velocity=11 m/s*

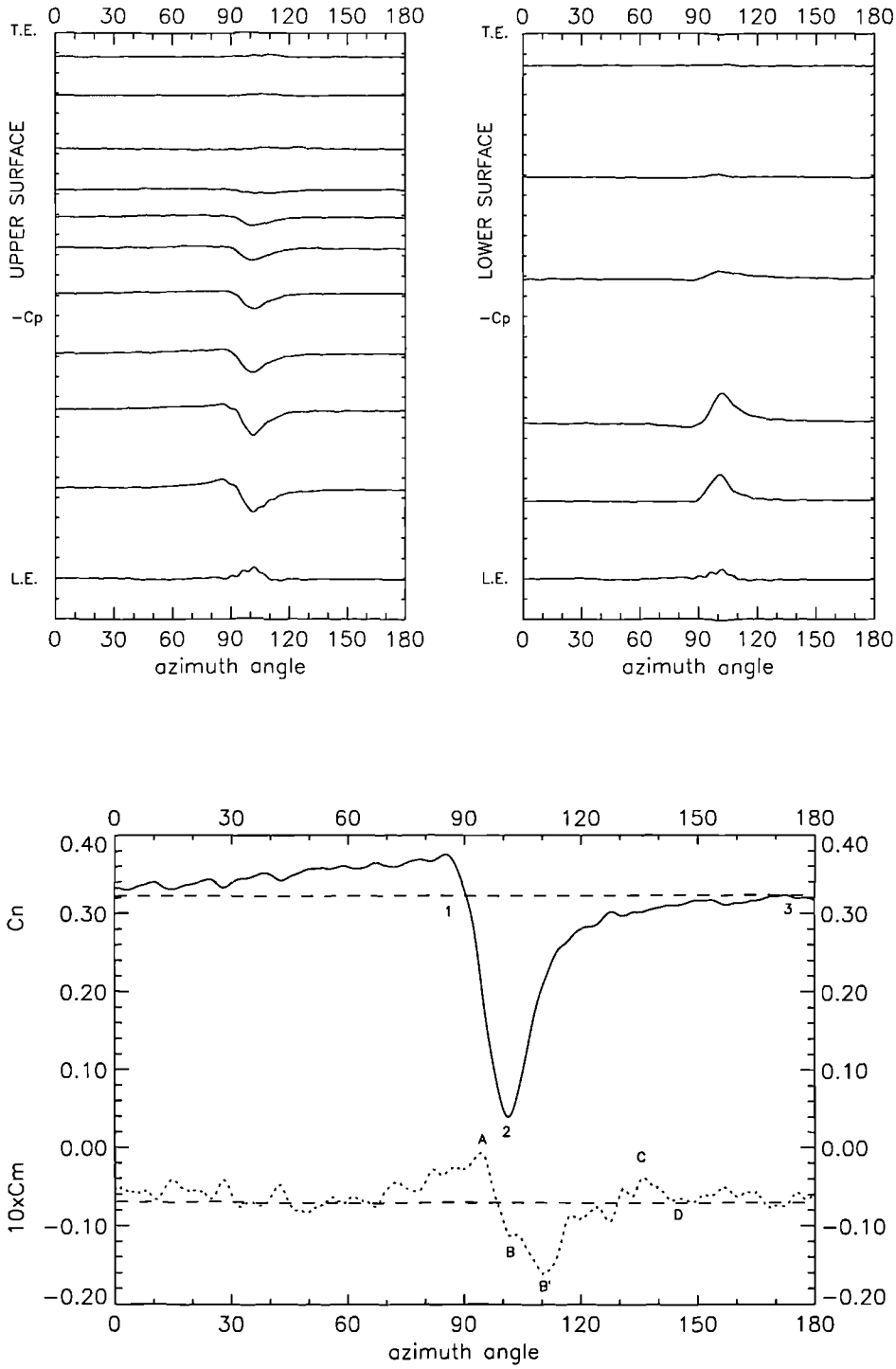

Figure 5.9: *Upper and lower surface pressure measurements, normal force and pitching moment coefficients, smooth tower, yaw=0°, wind velocity=11.7 m/s*

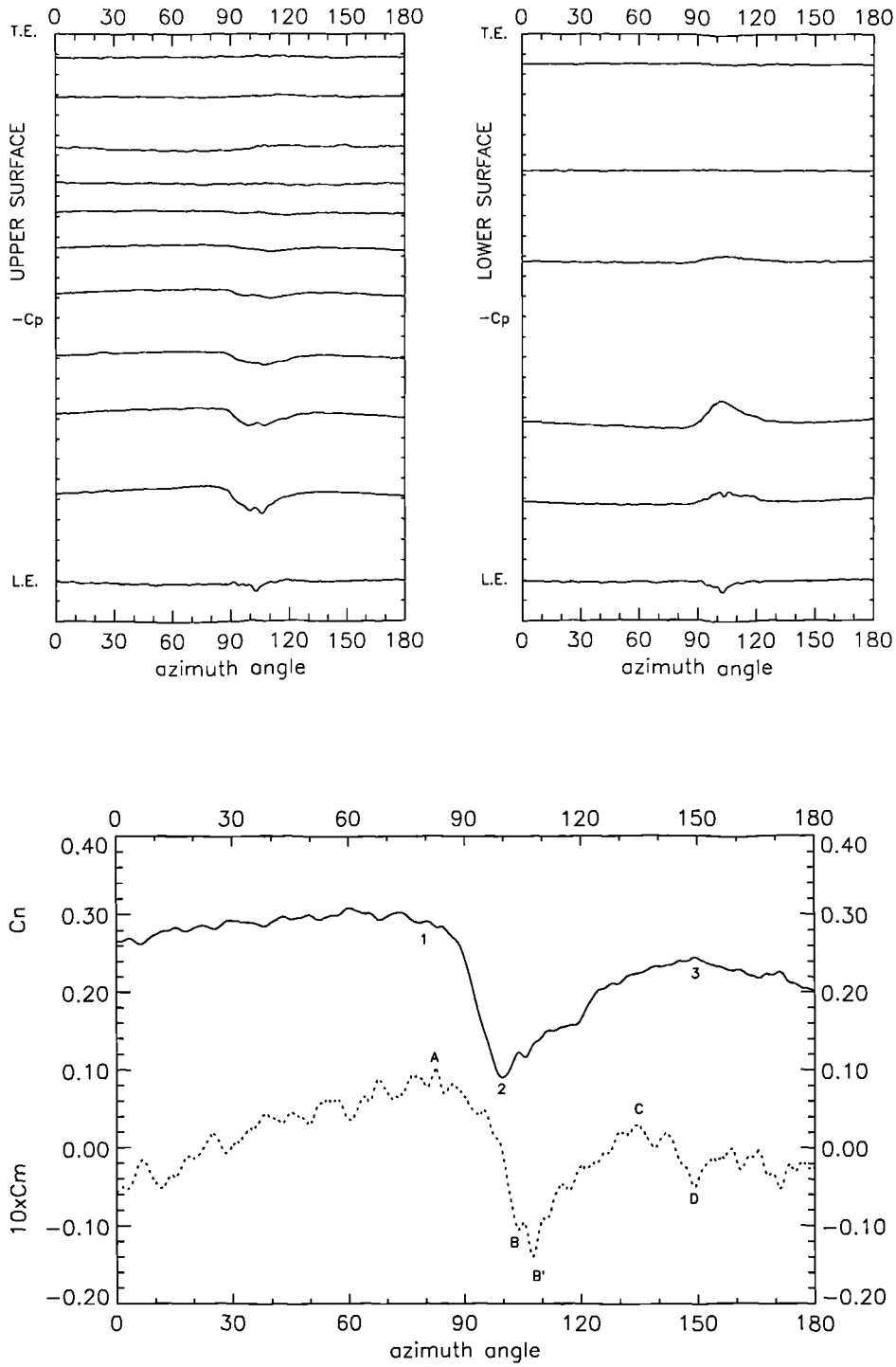

Figure 5.10: *Upper and lower surface pressure measurements, normal force and pitching moment coefficients, smooth tower, yaw=+20°, wind velocity=9 m/s*

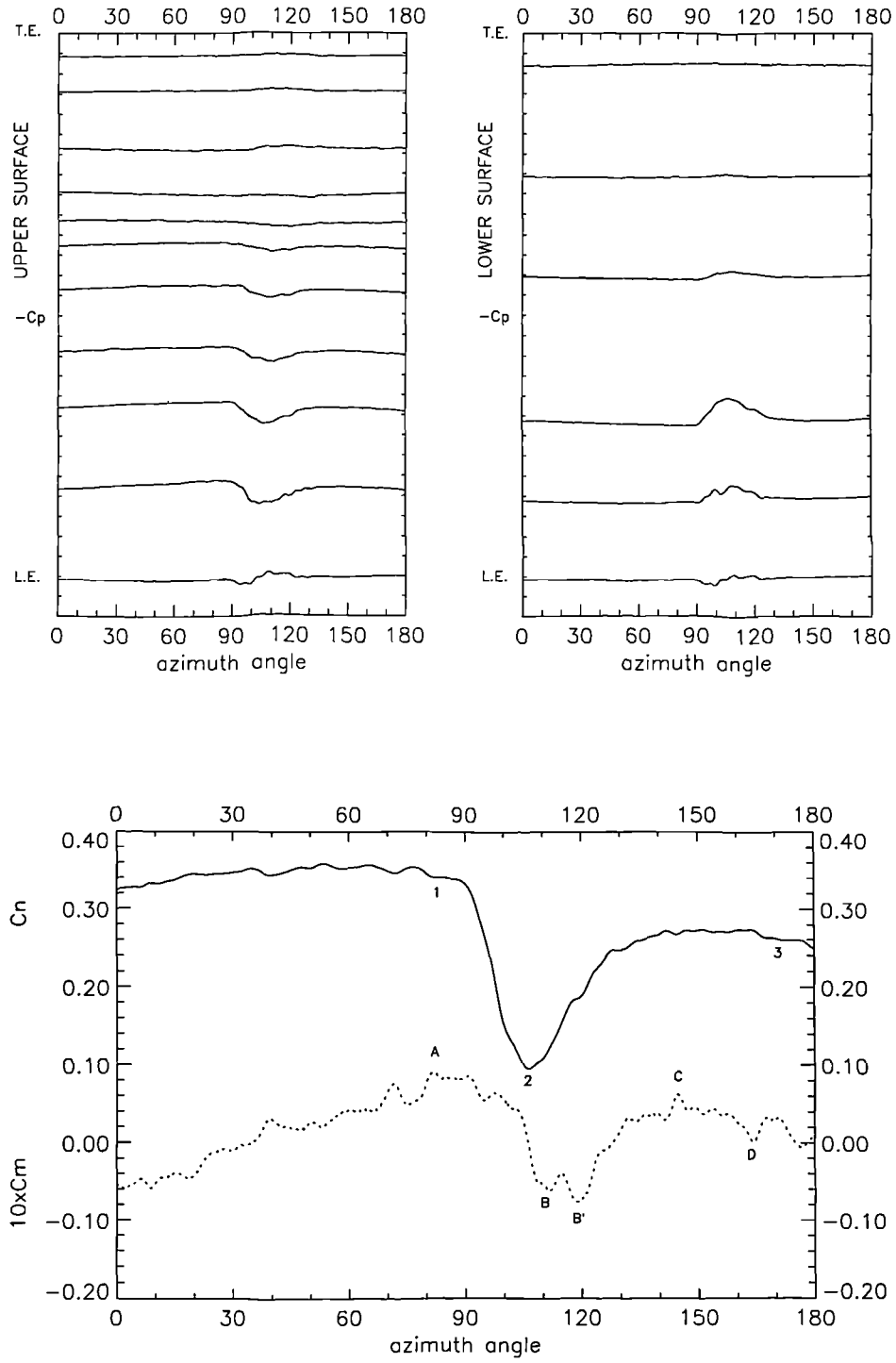

Figure 5.11: *Upper and lower surface pressure measurements, normal force and pitching moment coefficients, smooth tower, yaw=+20°, wind velocity=11 m/s*

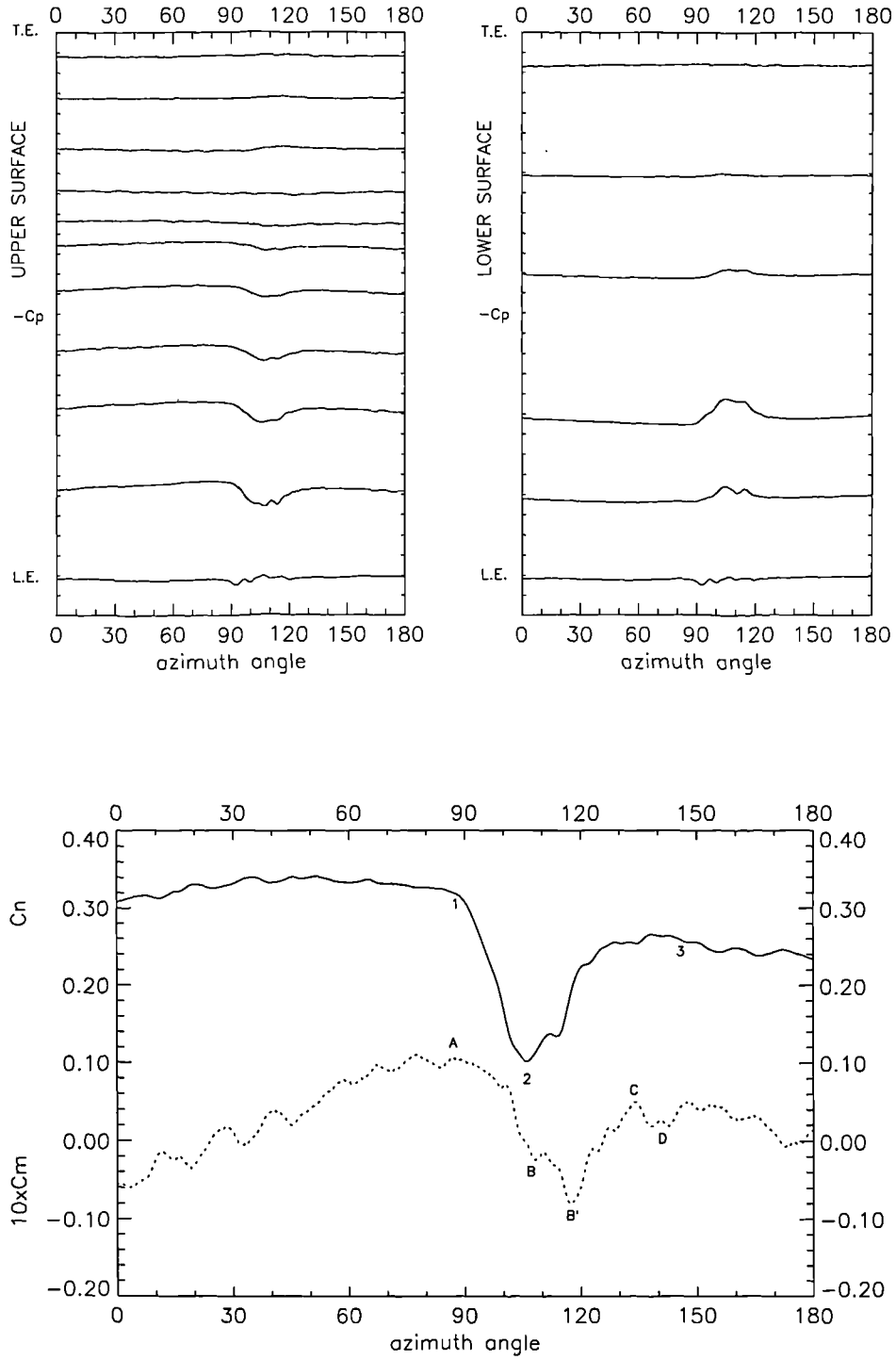

Figure 5.12: *Upper and lower surface pressure measurements, normal force and pitching moment coefficients, rough tower, yaw=+20°, wind velocity=11 m/s*

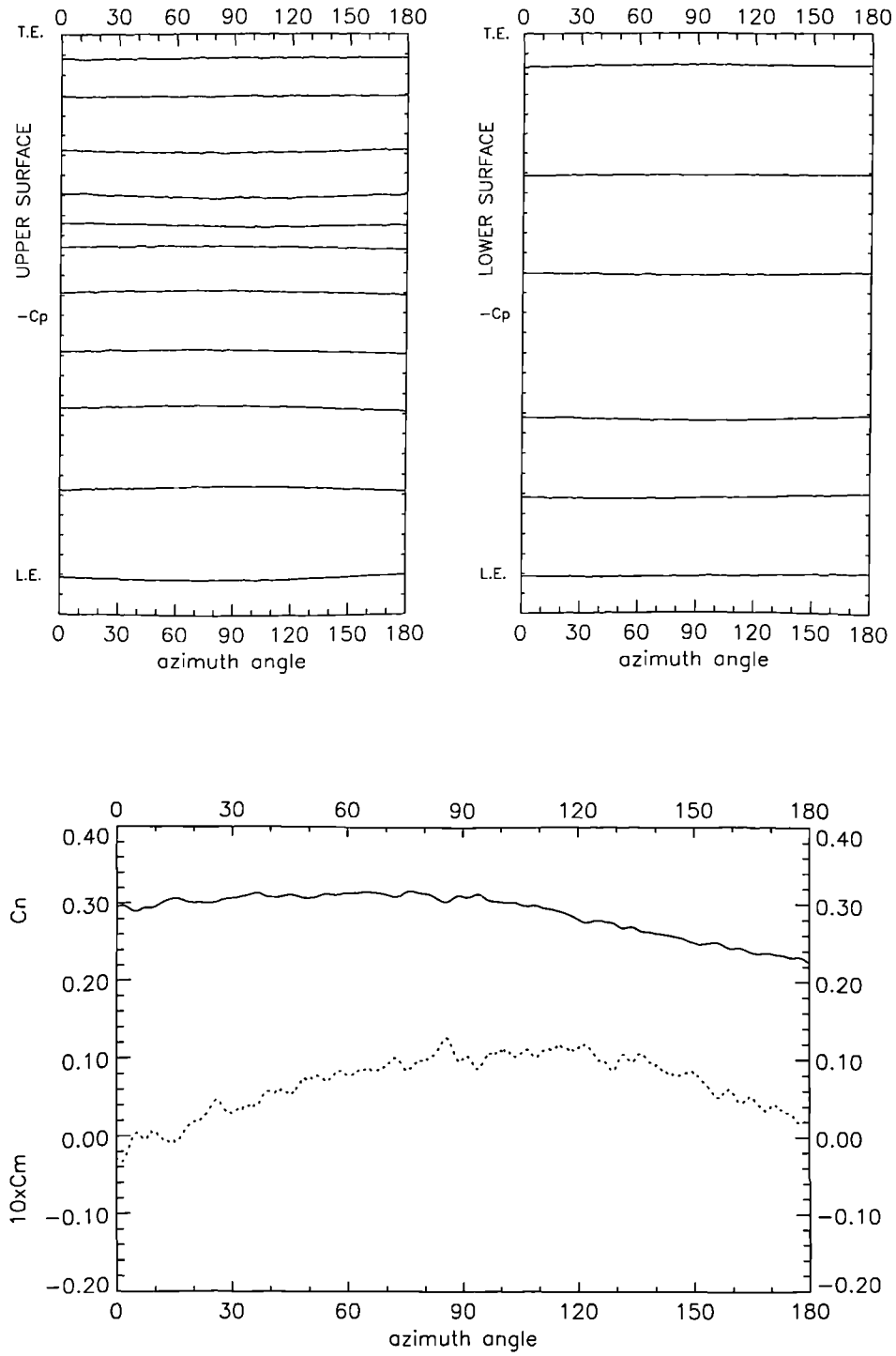

Figure 5.13: *Upper and lower surface pressure measurements, normal force and pitching moment coefficients, no tower, yaw=+20°, wind velocity=11 m/s*

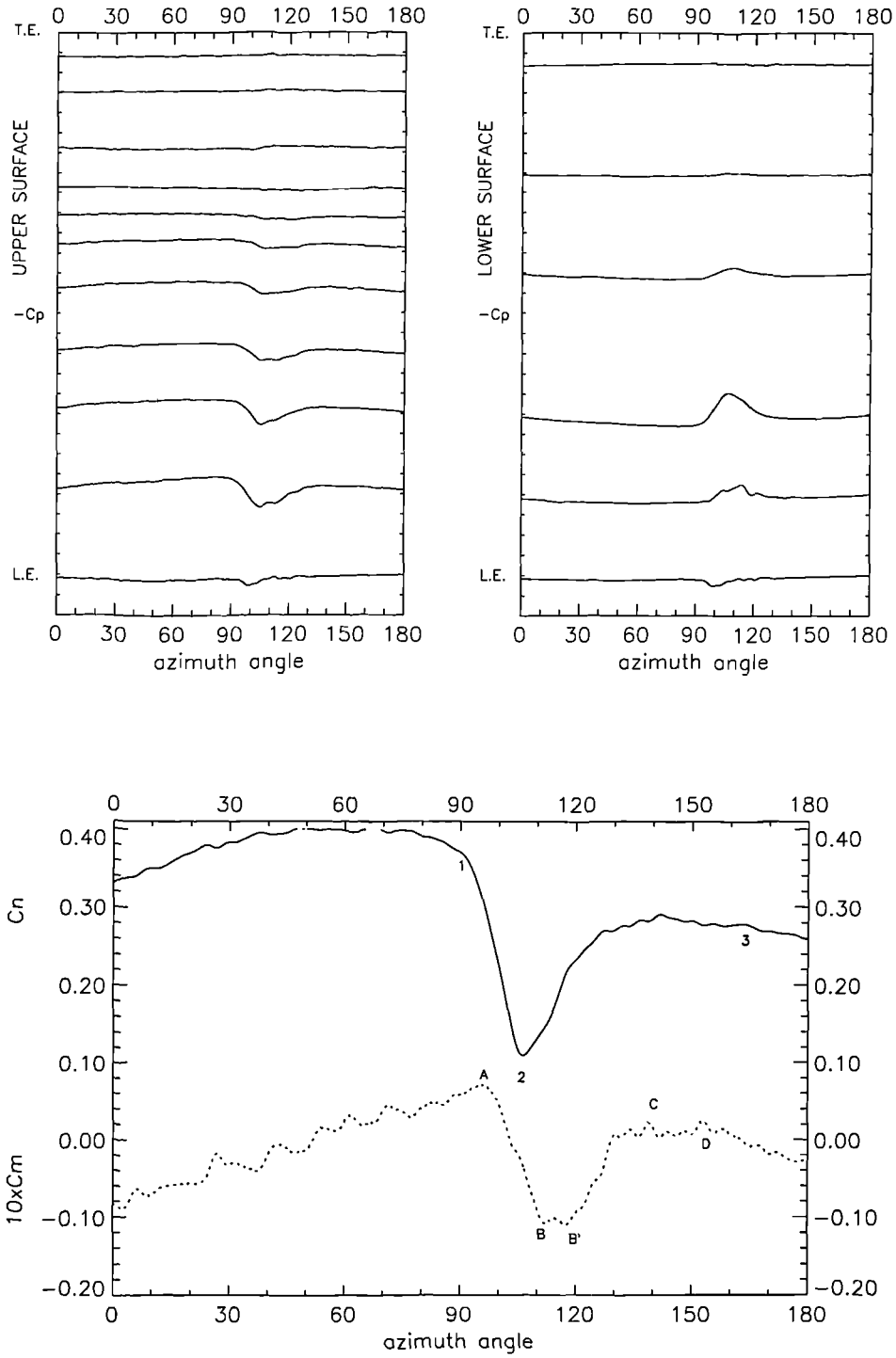

Figure 5.14: *Upper and lower surface pressure measurements, normal force and pitching moment coefficients, smooth tower, yaw=+20°, wind velocity=11.7 m/s*

5.3.4 Discussion

The basic features of the effect that the support tower has on the aerodynamic response of the blade have been presented. To gain a better understanding of the physical mechanisms associated with the tower shadow interaction, it is appropriate to take a closer look to the measurements.

A closer examination of the upper surface pressure response near the leading edge is presented in Figure 5.15 for the head-on flow cases with a smooth tower at 9 m/s, 11 m/s and 11.7 m/s wind velocities, and a rough tower at 11 m/s wind velocity. The data for the 9 m/s case, Figure 5.15(a), all exhibit a drop in suction during the interaction but the transducer closest to the leading edge (the bottom trace) initially experiences a rise in suction when the blade first encounters the wake. There are two possible explanations for this behaviour. It may be indicative of a vortex interacting with the blade Horner *et al.* (1995). It is possible that the vorticity shed from the support tower is convected along the edge of the wake in discrete structures that are encountered first by the blade. This vorticity will, inevitably be quite weak. The vorticity would only be encountered by transducers near the leading edge before being convected downstream and so its effect is diminished at the other transducers. Similar behaviour, although with different intensity is found at 11 m/s wind velocity for the smooth and the rough tower cases presented in Figures 5.15(b) and (c), respectively. For the higher wind velocity case of 11.7 m/s in Figure 5.15(d), the suction rise prior to the dramatic decrease in pressure, appears more clearly defined and affects more of the surface of the blade.

Another possible reason for the slight increase in suction before the blade enters the tower shadow, may be an increase in the wind velocity field at each edge of the tower shadow area as the flow separates from the cylindrical tower. This has been predicted numerically (Sorensen and W.Z.Shen 1999) and observed in experiment (Powles 1983).

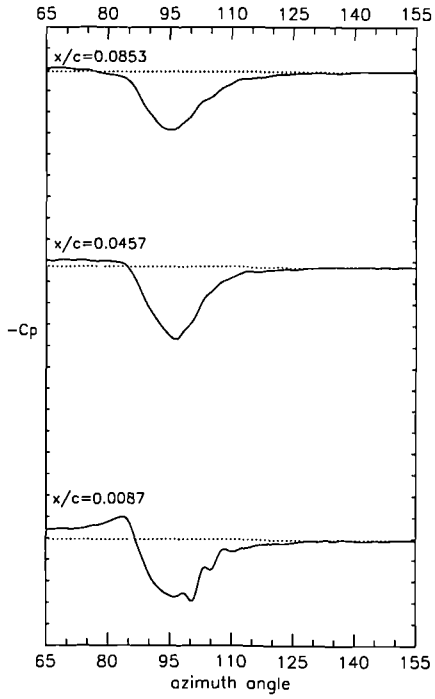

(a) wind velocity=9 m/s, smooth tower

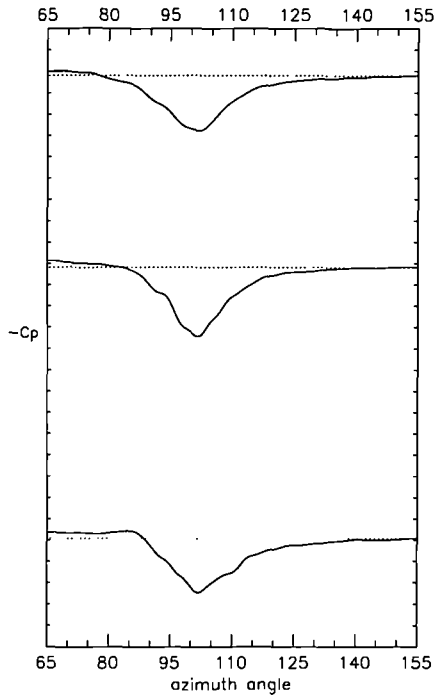

(b) wind velocity=11 m/s, smooth tower

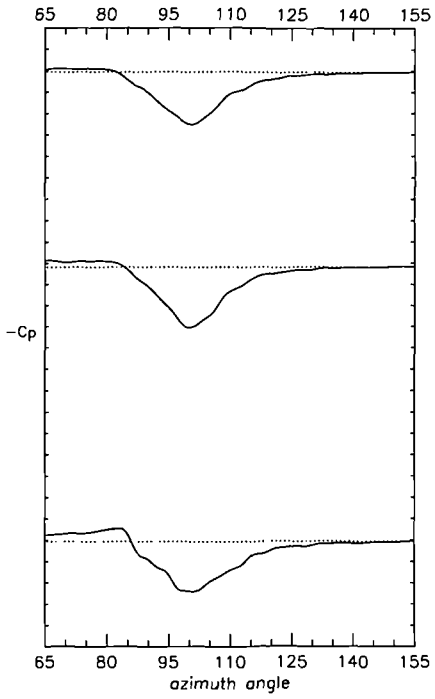

(c) wind velocity=11 m/s, rough tower

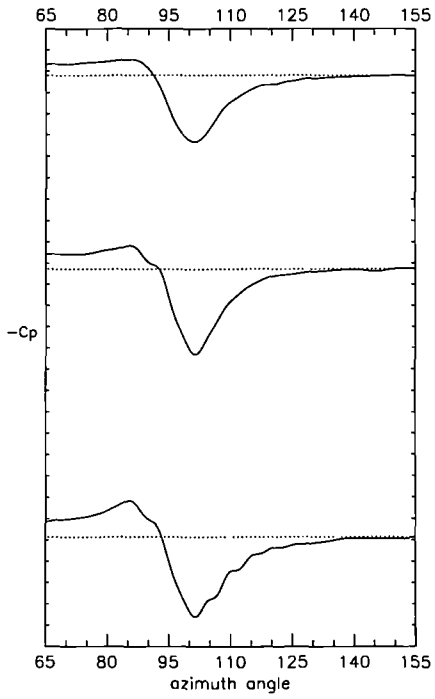

(d) wind velocity=11.7 m/s, smooth tower

Figure 5.15: *Detail of Upper surface -Cp measurements near the L.E., yaw=0*

The different intensity of this pressure rise in each of the figures does not have a straightforward explanation. Reynolds number variations around a critical value, can produce either laminar or turbulent separation on a cylindrical surface, with resulting changes in wake structure. The flow over a circular cylinder has been the subject of extensive study (Schlichting 1979). It has been established that, at Reynolds numbers less than $5x10^4$ the flow is expected to be characterised by asymmetric vortex formation in a broad wake, with asymmetrically disposed laminar boundary layer separation points on the cylinder surface. For $Re > 5x10^5$ a turbulent symmetric flow, with symmetrically placed turbulent boundary separation points may appear, producing a narrower wake than in the laminar case. This Reynolds number dependency it is obviously influenced by the turbulence intensity of the flow and the roughness of the tower surface.

At 9 m/s, 11 m/s and 11.7 m/s the corresponding Reynolds numbers at the tower are $Re = 4.3x10^4$, $Re = 5.2x10^4$ and $Re = 5.6x10^4$. At 9 m/s laminar separation would be expected. The 11 m/s and 11.7 m/s cases fall within the transitional Reynolds number range and so it is not clear if turbulent separation will occur. The strongest rises in suction have been observed at the lowest and highest Reynolds numbers and not at the intermediate value. This would suggest that the test Reynolds number cannot be used to account for the changes in severity of the suction rise prior to tower shadow.

To provide some insight, the three sets of results for the smooth tower at 9m/s, 11 m/s and 11.7 m/s wind velocity have been over-plotted in Figure 5.16. In this figure, the variations in the upper surface pressure coefficient, for the 9m/s case (dotted line), appear to be shifted by approximately 5° azimuth when compared to both, the 11 m/s (dashed line) and 11.7 m/s (solid line) cases.

This azimuthal difference could be attributed to a broader wake in the 9 m/s case typical of that associated with laminar separation. Despite apparently being

in phase, the pressure variations on the 11 m/s and 11.7 m/s cases exhibit different shapes within the tower shadow. Between 90° and 100° azimuth angle the slope of the 11.7 m/s response is much steeper than the other case.

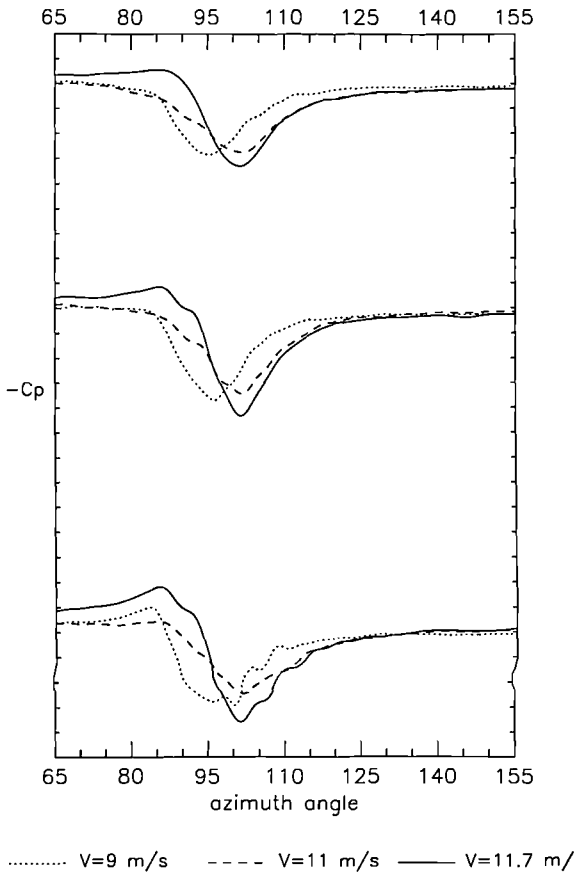

Figure 5.16: *Comparison of Upper surface -Cp measurements near the L.E. at three wind velocities, yaw=0°*

The reason for this is not clear but will inevitably be linked to the state of the tower wake. Indeed the difference between the two cases may be indicative of the passage of discrete vortical structures of different strength that have been shed from the tower. As the blade leaves the tower shadow region, the response of the transducers is quite similar, showing a comparable rate of recovery in each of the cases. This is a particularly interesting result, which appears to be independent of

the wind velocity.

The same three pressure responses for the smooth tower at 9m/s, 11 m/s and 11.7 m/s wind velocities are presented in Figure 5.17 for the +20° yaw case.

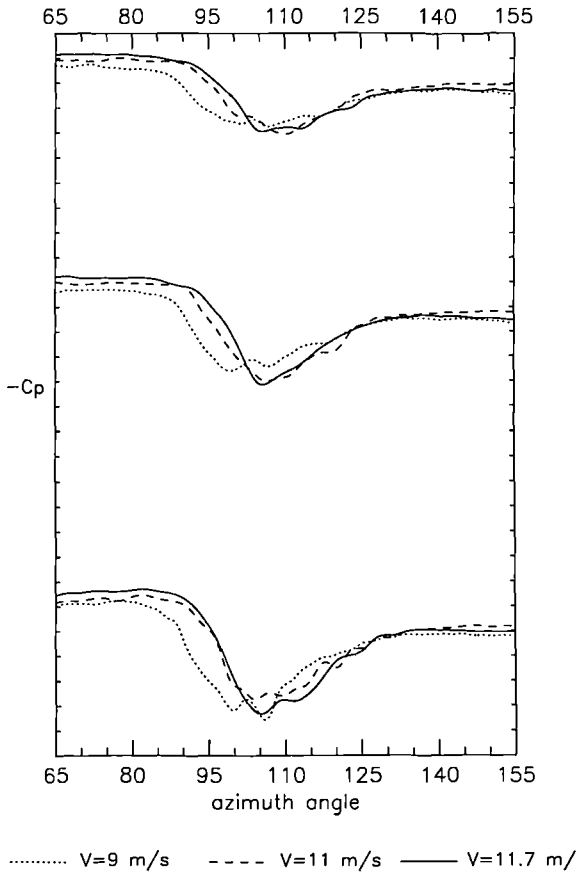

Figure 5.17: *Comparison of Upper surface -Cp measurements near the L.E. at three wind velocities, yaw=+20°*

Once again the 9m/s case, appears to be out of phase with the other two cases. Compared to the head-on case (Figure 5.16), all the responses in the yawed configuration show an azimuthal delay of 5°. It is also interesting to note that the azimuthal range of the pressure rise is greater than in the head-on flow cases.

In the head-on and the yawed flow figures, a common feature of the pressure profile at 9 m/s can be observed when comparison is made with, the 11m/s and

11.7 m/s responses. The azimuthal response at 9 m/s occurs earlier and is wider than for the other two velocities. This is in consistent with the wider wake produced behind a cylinder in laminar flow. Increasing the Reynolds number, has the effect of narrowing the wake, which could explain the dephase and azimuthal range change at the 11m/s and 11.7 m/s cases.

Given the degree of similarity, and the observed differences, between the 11 m/s and 11.7 m/s cases, it is interesting to examine these cases further by looking in more detail at the normal force and pitching moment coefficients.

Figure 5.18 illustrates the effects of the tower shadow region at wind velocities of 11 m/s and 11.7 m/s, for the turbine set at zero yaw error. Figure 5.18(a) shows a comparison between the measured C_n histories with and without the tower, at a wind velocity of 11 m/s. As may be seen from this plot, the response of the normal force with no tower, represented as a dashed line, is almost horizontal, with a mean C_n value of 0.33. The variation that the normal force suffers when the tower is present can be seen from the solid line; it exhibits a drop in the force as the blade enters the tower wake followed by an a slow recovery, until the normal force reaches the undisturbed inflow matching the no tower case. Here it is interesting to note that, prior to the drop in suction, the value of the normal force is almost constant, there is no sign at all of a rise in C_n. Figure 5.18(b) shows the measured C_n history with and without the tower at a wind velocity of 11.7 m/s. The dashed line, represents the normal force for the no tower configuration, and has a mean value of 0.32. The solid line represents the normal force when the tower is present, and shows a consistent and progressive increase in the normal force up to a value of 0.375 prior to the blade entrance into the tower shadow region. Furthermore, a dramatic drop in the normal force is observed as the blade enters the tower wake and the subsequent recovery is slow as it leaves the tower wake region.

Figure 5.18(c) provides comparison of the measured normal force and pitching

moment coefficients for the two wind velocities presented in plots (a) and (b). It can be seen that there are significant differences between the measured aerodynamic coefficients in the two cases. For example, while the measured normal force C_n, coincides well when the blade is leaving the tower shadow, there are obvious discrepancies between the C_n values at entry to the tower shadow region. This is consistent with the pressure transducer response presented in Figure 5.16. In particular, the drop in C_n begins much later and is much steeper in the high velocity case. The level of agreement in the pitching moment coefficients in the two cases is considerable. There is, however, an obvious difference in the strength of the pitching moment between 95° and 110° azimuth. This may be related not only to differences in the velocity deficit in the tower shadow but also to the blade encountering shed vorticity during its passage out of the wake.

Figure 5.19 illustrates the aerodynamic response in the tower shadow region at wind velocities of 11 m/s and 11.7 m/s, for the turbine set at +20° yaw error. When the turbine is yawed, the features of the tower shadow response are qualitatively similar to that observed in head-on flow. The two cases presented do, however, exhibit some interesting features. It is noticeable that the data from the two wind velocities exhibit a similar response but with an almost constant offset in both, C_n and C_m. It is possible that the offsets between the curves have arisen from experimental error. In fact, the relatively small number of chordal pressure measurement locations make the force integration sensitive to small errors in individual pressures. It is interesting to note, in this respect, that the corresponding cases with no tower present, also exhibit the offset. Despite the offset, it is clear that the correspondence between the two cases is better than in the head-on flow case.

In order to clarify the effects of tower shadow for different tower roughness, a comparison at 11 m/s wind velocity is presented next for two roughness levels at zero yaw error angle. The solid line in Figure 5.20 represents the smooth tower

measurements of C_n and C_m, while the dotted line represents the C_n and C_m data for a rough surfaced tower. The results for the rough tower reflect most of the features observed for the smooth tower. There is, however, a constant offset between the two sets of results. This may, again, be due to an experimental error. If the offset were to be removed, the drop in C_n due to the passage of the blade through the rough tower, would be smaller than for the smooth tower. The difference would, however, be too small to be significant. Figure 5.21 shows the effect of the rough and smooth tower at +20° yaw error. Once again, the only discernible difference in the curves is a slight offset between the cases.

The data presented so far in this chapter have been extracted from individual rotor cycles at each wind velocity. These data are, therefore, unaveraged, and may include instantaneous variations that are not presented in the mean cycle response. In order to verify the repeatability of the aerodynamic features discussed previously, a comparison is now made between two consecutive cycles. This comparison is shown in Figures 5.22 and 5.23 at 11 m/s and 11.7 m/s wind velocity respectively. It should be noted that, only two consecutive tower shadow responses were measured for each case. In both figures an obvious azimuthal shift of 3° to 4° can be observed. This is probably due to the experimental uncertainty in the measurement of the azimuth angle. Slight differences in rotational speed impact significantly on the calculation of azimuth position.

Despite this, the distinct response at entry to the tower shadow and the recovery phase on the way out, remain qualitatively the same for the two consecutive cycles at each of the velocities. They, therefore, demonstrate the repeatable nature of the interaction measurements.

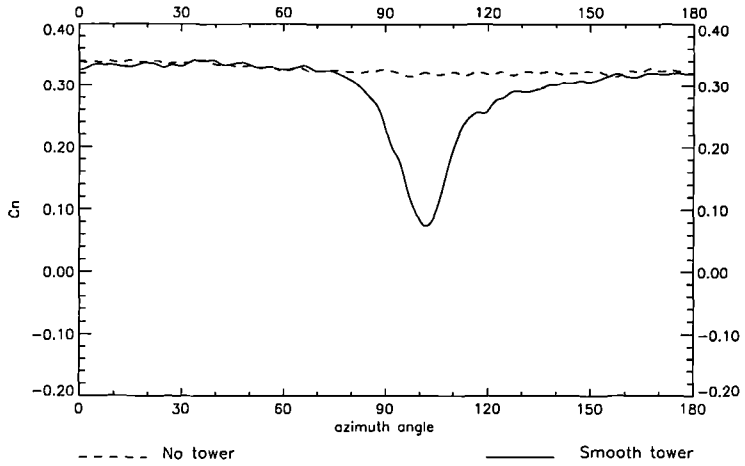

(a) Effect of tower presence on Cn at wind velocity=11 m/s

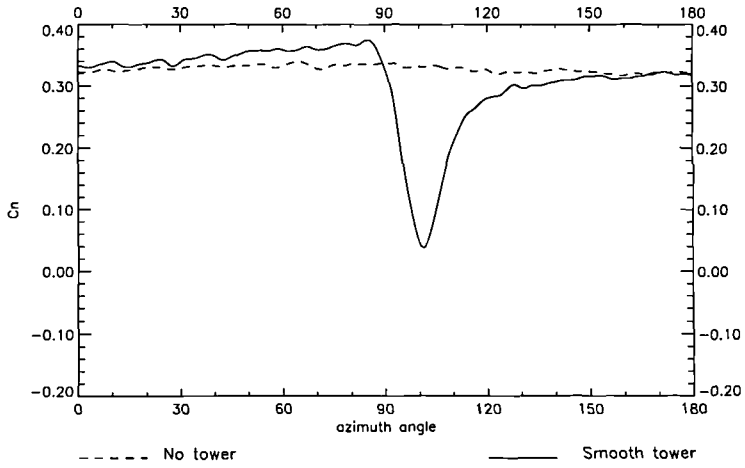

(b) Effect of tower presence on Cn at wind velocity=11.7 m/s

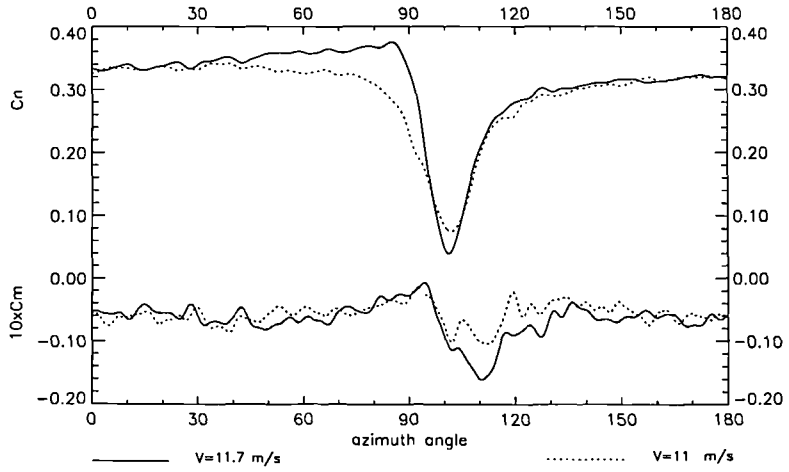

(c) Effect of wind velocity on Cn and Cm

Figure 5.18: *Effect of tower shadow at two wind velocities, 11 m/s and 11.7 m/s, yaw=0°*

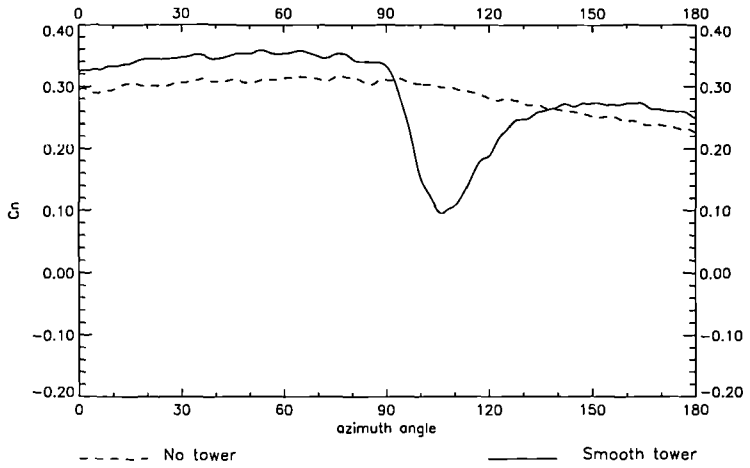

(a) Effect of tower presence on Cn at wind velocity=11 m/s

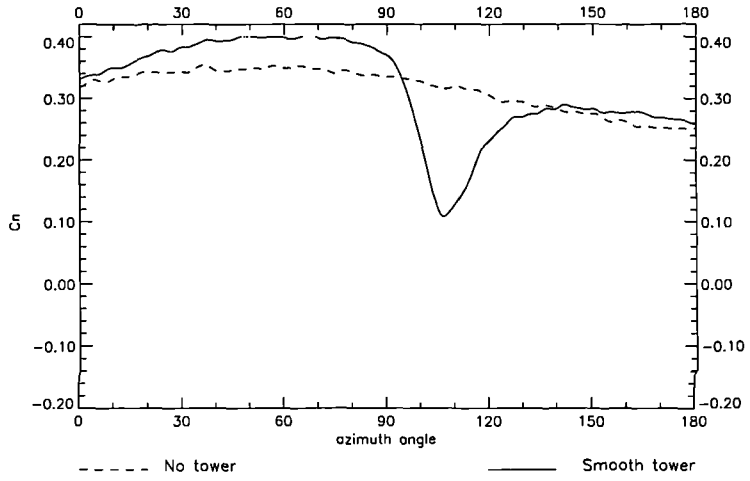

(b) Effect of tower presence on Cn at wind velocity=11.7 m/s

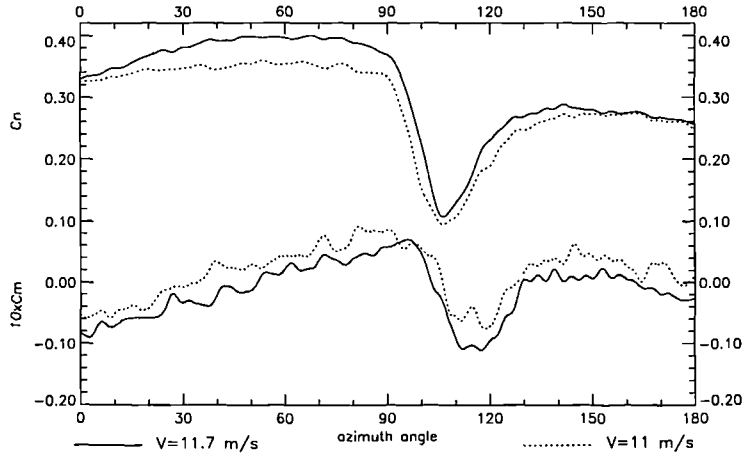

(c) Effect of wind velocity on Cn and Cm

Figure 5.19: *Effect of tower shadow at two wind velocities, 11 m/s and 11.7 m/s, yaw=+20°*

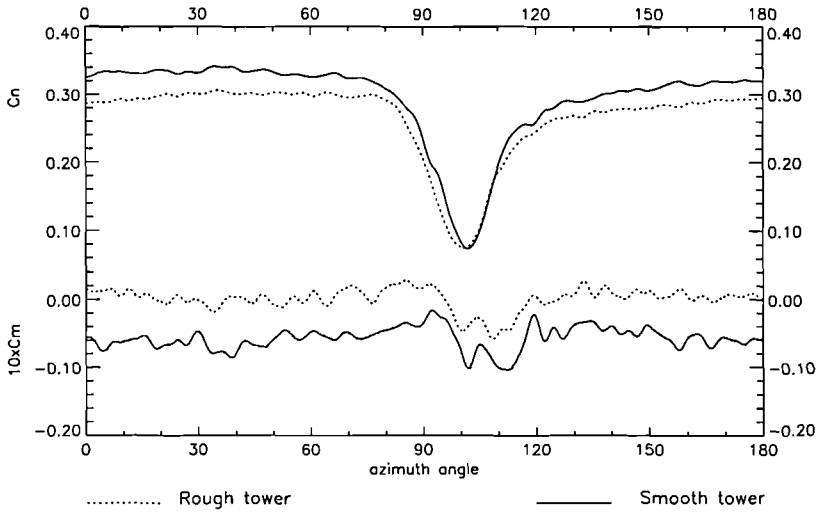

Figure 5.20: *Effect of tower roughness on Cn, Cm, wind velocity=11 m/s, yaw=0°*

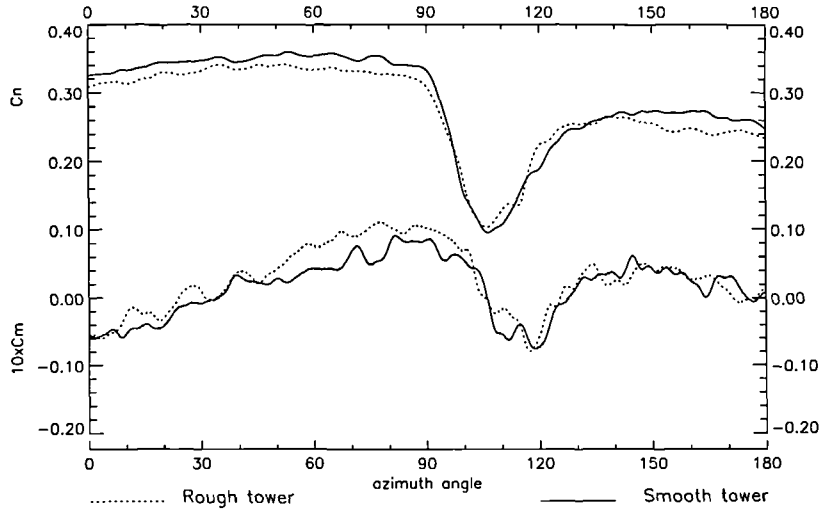

Figure 5.21: *Effect of tower roughness on Cn, Cm, wind velocity=11 m/s, yaw=+20°*

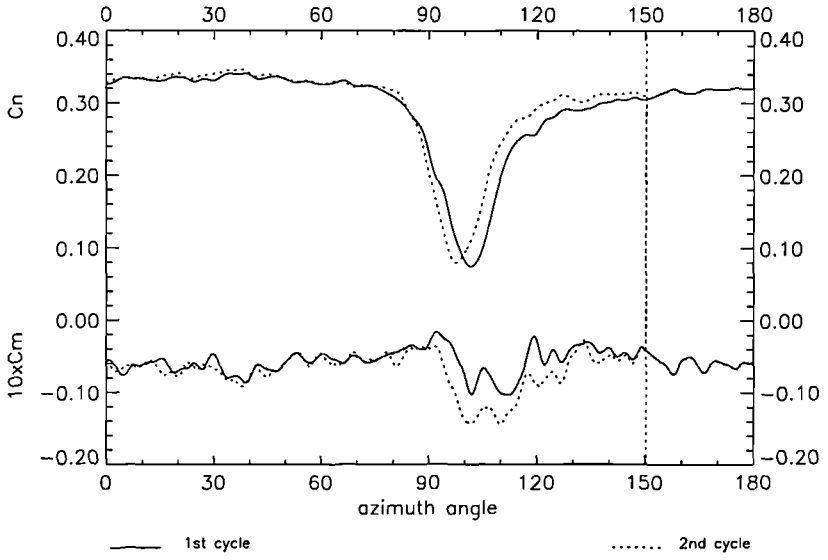

Figure 5.22: *Experimental comparison of two consecutive cycles, yaw=0° at wind velocity=11 m/s*

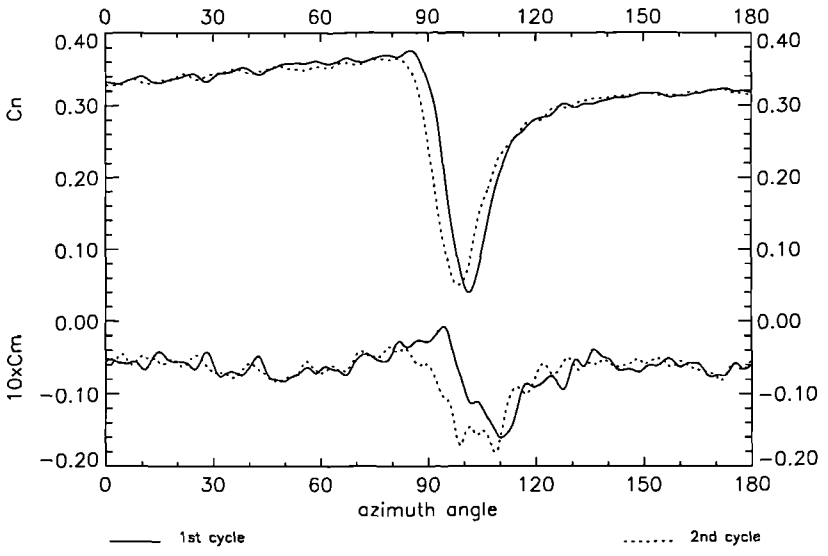

Figure 5.23: *Experimental comparison of two consecutive cycles, yaw=0° at wind velocity=11.7 m/s*

5.3.5 Conclusions

Pressure measurements and integrated values of normal force and quarter chord pitching moment have been presented in order to analyse the impact of the blade interaction with the tower wake on a downwind turbine.

Prior to the blade entering the tower shadow, deviations in $-C_p$, C_n and C_m from the undisturbed flow values have been observed. This is not the case for all flow speeds but is repeatable from cycle to cycle. It is, as yet, unclear why this should be so.

Over a circular cylinder, the boundary layer can separate under laminar or turbulent flow conditions, depending on Reynolds number, surface roughness, and turbulence intensity. Laminar or turbulent separation will produce quite different wake formations behind the cylinder. This will influence the phase and extent of the blade interaction with the wake behind the cylindrical tower and may provide the key to understanding the behaviour described above. Indeed the measurements were all taken around a transitional Reynolds number range where variations in the wake geometry may be significant for even small changes in velocity. Clearly, however, these changes are not progressive as the anomalous behaviour at 11 m/s illustrates.

It is interesting to note that for head-on flow, the wind tunnel measurements of the tower shadow are not centred around the 90 ° azimuth position. Instead the minimum normal force peak has been measured at 95° and 100°. This may be due to inaccuracies in measuring the blade azimuth or interaction of the tower wake with the rotor inflow. It may also, however, be a feature of the dynamic response of the blade as it passes through the tower shadow.

The pressure recovery as the blade leaves the tower wake is much slower than the response at the entrance to tower shadow region. This behaviour is consistent regardless of possible vortex collisions, and wind velocity (Reynolds number) as may be seen in Figures 5.16, 5.17, 5.18(c) and 5.19(c). This behaviour is most likely

a feature of the dynamic response of the normal force to the velocity deficit as the blade progresses through tower wake. The delay in recovery of C_n could be explained in terms of the induced velocity due to the vorticity shed from the aerofoil as its circulation changes.

For all the cases presented here, the tower roughness had a negligible effect on the blade response.

5.4 Modelling of Tower Shadow Effects

The blade element method described previously has been extended to include a representation of the blade/tower interaction. The effect that this has on the onset of dynamic stall has been previously analysed in Chapter 4. In this section, two different tower shadow strategies are analysed. In the first, only the steady aerodynamic response due to the velocity deficit has been taken into account. In the second, an enhancement of the physical interaction between the tower wake and the aerofoil has been implemented by including the unsteady aerodynamic effects resulting from the aerofoil wake induced effects. In this section, the calculated aerodynamic forcing deriving from the two strategies, are shown and analysed.

5.4.1 Formulation and Implementation of the Steady Model

The steady tower shadow model and the equations used to describe the velocity deficit in the wake are detailed next.

For downwind machines, the tower wake has been modelled as a velocity deficit in the form of a cosine function; according to Wang *et al.* (1998) represented by:

$$\frac{V}{V_\infty} = 1 - \frac{D_V}{2}\left[1 + \cos\frac{2\pi\left(\psi_t - \frac{\pi}{2}\right)}{2\psi_0}\right] \tag{5.1}$$

where V, the velocity within the tower shadow is expressed as a function of the freestream velocity V_∞, the maximum velocity deficit D_V, the half angle of the tower shadow sector ψ_0 and the shadow azimuth angle ψ_t corresponding to a blade section r at the azimuth ψ (see Fig. 5.24)

Generally,

$$\psi_0 = \arctan \frac{B_t}{2r \sin \psi_1} \tag{5.2}$$

$$\psi_t = \frac{\pi}{2} - \arctan \frac{r \cos\gamma \sin\psi - Z_t \sin\gamma}{r \sin\psi_1} \tag{5.3}$$

where B_t is the tower shadow width and Z_t the distance from the yaw axis to the blade rotation plane. The tower shadow width B_t and maximum value of velocity deficit D_V mainly depend on the streamwise distance downstream and Reynolds number. For a yawed rotor, the tower shadow region will not centre around the 180° azimuth position. Thus, because the wake as seen by the blade is not symmetric about its centerline, it is necessary to account for the skew of the tower wake by means of ψ_1 and ψ_2. These azimuth angles, ψ_1 and ψ_2 at which the blade enters and leaves the shadow respectively, vary with the spanwise location r, and can be formulated thus (see Fig. 5.24)

$$\psi_1 = \arccos \frac{Z_t \sin\gamma + \frac{1}{2} B_t}{r \cos\gamma} \tag{5.4}$$

$$\psi_2 = \arccos \frac{Z_t \sin\gamma - \frac{1}{2} B_t}{r \cos\gamma} \tag{5.5}$$

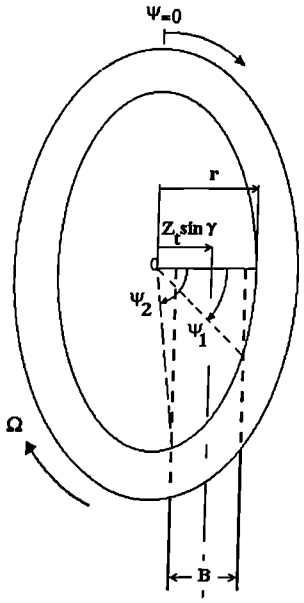

(a) Blade enters at ψ_1 and leaves at ψ_2 the tower shadow

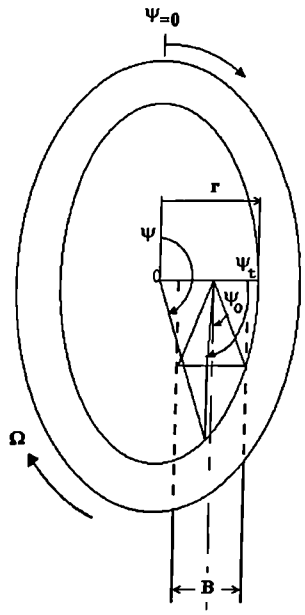

(b) Tower shadow additional parameters

Figure 5.24: *Definition of the tower shadow modelling parameters*

This tower shadow model has been introduced into the BEM scheme by representing the incoming wind velocity in the tower shadow domain by the velocity V, from Eq. (5.1). Outside the range of influence of the wake, the incoming wind velocity remains unaltered according to the free stream, V_∞. Then, the induced velocities at the blades can be calculated using the BEM method (Chapter 2). The aerodynamic information obtained from the extended BEM model, such as angle of attack transients due to the inflow alteration by the tower wake, are then input to the 3–D stall delay model (Chapter 3) and to the dynamic stall onset correlation (Chapter 4).

5.4.2 Results and Discussion

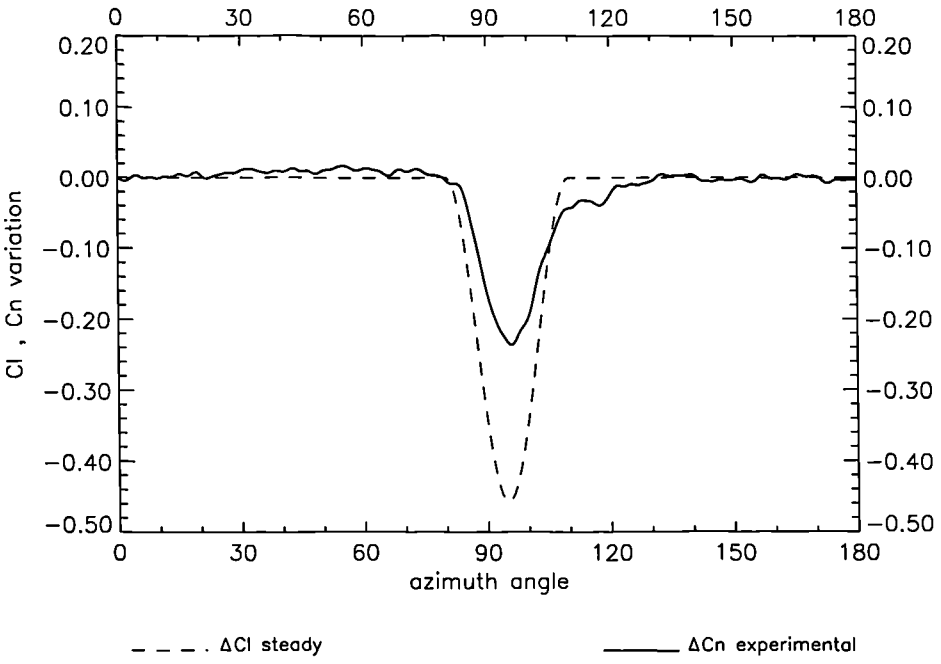

Figure 5.25: *Steady prediction ($D_V = 0.30, B_t = 2.75$) compared to measurements, yaw=0°, wind velocity=9 m/s*

Here, the focus is on the tower shadow response, and its modelling accuracy will

be contrasted with the wind tunnel measurements. At a wind velocity of 9 m/s in head-on flow, Figure 5.25 shows the force variation encountered by the blade during its passage through the tower wake. The experimental and predicted force coefficients have been normalised by subtracting the force response outside the tower shadow region. Thus, only the force variation due to the tower wake contribution is illustrated.

The tower shadow width has been modelled as 2.75 tower diameters, and the maximum velocity deficit is 0.30. On the basis of these parameters, the suitability of which are discussed later, the intensity of the prediction is not well characterised by the model when compared to the wind tunnel measurements. In addition, the trend, particularly on the way out of the tower shadow region, is not correctly captured by the steady model. The model prediction follows the symmetric profile of the velocity deficit, while the measurements show asymmetry with a slow recovery as the blade leaves the tower wake.

The reason for this disagreement, could be a change in the blade wake induced velocity caused by its passage through the tower shadow velocity deficit. At this stage, only the velocity deficit has been considered in the tower shadow modelling and even this has been dealt with in a crude manner. Once the blade encounters the tower wake, the subsequent process involves a complex series of events in which the unsteady response of the blade may be a significant factor.

5.4.3 Enhancement of the Tower Shadow Modelling

Intrinsic to the BEM scheme is the idealization of the physical blade as a one-dimensional lifting line. Thus, the steady aerodynamic information corresponding to a blade element is evaluated and considered exclusively at a single point, usually the quarter chord location is used as a control point. This treatment of the aerodynamics, which produces acceptable results under steady inflow conditions, may have

a serious disadvantage when the aerofoil encounters a nonuniform velocity inflow over its chordal extension. This is the situation in the tower shadow case. The short duration of the tower shadow passage also means that, even at low angles of attack, unsteady effects may be significant.

A new tower shadow model is proposed based on the Küssner function, as described by Leishman (2002). The Küssner function responds to the problem of obtaining the transient lift response to a sharp change in the nonuniform velocity normal to the blade chord for unsteady attached flow. This indicial method is an appropriate way of simulating the response of the blade during its passage through tower shadow. The formulation of the model, as implemented here, is explained next.

5.4.4 The Küssner Function

For attached flow, the unsteady lift produced on a thin aerofoil entering a sharp change in velocity normal to the chord was considered by Küssner and solved by von Kármán and Sears. This classical theory, among others, can be found in *e.g.* Bisplinghoff *et al.* (1996).

The physical mechanism underlying the method is that an aerofoil moving through a varying velocity normal to the chord, in addition to a change in angle of attack, experiences a nonuniform angle of attack over the entire aerofoil chord.

Indicial Response

An indicial function is by definition the response to a disturbance which is applied instantaneously at time zero and held constant thereafter; i.e. a response given by a step change in forcing. The unsteady loads due to arbitrary step changes (e.g. in angle of attack or in induced velocity) can be obtained by superposition of indicial aerodynamic responses, using Duhamel's integral. In addition, the total indicial

response can be split into two components; one for the circulatory loading which builds up quickly and asymptotes to the appropriate steady state loading, and the other for the initial loading which is impulsive (noncirculatory) and decays rapidly with time. Thus, for the head-on tower shadow case the total indicial lift force coefficient, C_l due to a change in inflow velocity (deficit) over the blade chord can be written using Duhamel's superposition integral of the velocity deficit, $w_{ge}(S)$ as

$$C_l(S) = \frac{2\pi}{W}\left[w_{ge}(S)\right] = \frac{2\pi}{W}\left[w_g(0)\,\psi(S) + \int_0^S \frac{\mathrm{d}w_g(\sigma)}{\mathrm{d}\sigma}\,\psi(S-\sigma)\,\mathrm{d}\sigma\right] \tag{5.6}$$

where W is the relative velocity of the aerofoil, $w_g(0)$ is the initial value of the velocity deficit, σ is a representative time variable, S is the reduced time in terms of the distance travelled by the aerofoil in semi-chords at a constant velocity W given by

$$S = \frac{Wt}{c/2}$$

and $\psi(S)$, is the indicial response function; in this case the Küssner function. Although the Küssner function is known, it is not in a convenient analytical form. Therefore, for practical calculations it is usually replaced by an exponential approximation given by Sears and Sparks (1941) as

$$\psi(S) = 1 - A_1\,\exp(-b_1 S) - A_2\,\exp(-b_2 S)$$

where the coefficients

$$A_1 = A_2 = 0.5,\;\; b_1 = 0.13,\;\; b_2 = 1.0$$

The Duhamel's integral above, $w_{ge}(S)$ then becomes

$$w_{ge}(S) = w_g(0)\ [1 - A_1\ \exp(-b_1 S) - A_2\ \exp(-b_2 S)] +$$

$$+ \int_0^S \frac{\mathrm{d}w_g(\sigma)}{\mathrm{d}\sigma}\ [(1 - A_1\ \exp(-b_1(S-\sigma)) - A_2\ \exp(-b_2(S-\sigma))]\ \mathrm{d}\sigma$$

The expression in Eq. (5.6) is usually solved numerically for discrete values of time, (S). If the indicial function $\psi(S)$ is written in exponential form as above and the terms representative of short term transients are neglected, the evaluation of the velocity response $w_{ge}(S)$ can be conducted in a simple recursive manner. This leads to Duhamel's integral of the velocity deficit, $w_{ge}(S)$ being written as

$$w_{ge}(S) = w_g(S)\ - X(S) - Y(S) \tag{5.7}$$

were the resultant inflow velocity is expressed by subtracting from the original steady velocity deficit $w_g(S)$ the deficiency functions $X(S)$ and $Y(S)$. These represent the time history effect due to the aerofoil's shed wake and are given in terms of the Küssner indicial approximation as

$$X(S) = X(S - \Delta S)\ \exp(-b_1 \Delta S) + A_1/6 \Delta w_g(S)\ [1 + 4\exp(-b_1 \Delta S/2) + \exp(-b_1 \Delta S)]$$

$$Y(S) = Y(S - \Delta S)\ \exp(-b_1 \Delta S) + A_2/6 \Delta w_g(S)\ [1 + 4\exp(-b_2 \Delta S/2) + \exp(-b_2 \Delta S)]$$

This approach assumes continuity between samples and a time step ΔS, which can be nonuniform, where

$$\Delta S = \frac{W\ \Delta t}{c/2}$$

The method works by evaluating the velocity deficit at each time step and subtracting from it the history effects of the unsteady aerodynamics contained in the functions $X(S)$ and $Y(S)$. These history functions are then updated and the calculation steps forward in time to the next sample.

5.4.5 Implementation of the Unsteady Tower Shadow Model

In the present model, the nonuniform velocity has been implemented only for the head-on flow case, where the relative velocity of the aerofoil W is considered as a constant.

Instead of using the steady velocity deficit prescribed in the form of a cosine function to predict the tower shadow aerodynamic response, the cosine velocity deficit V from Eq. (5.1) is introduced into Eq. (5.7) as the $w_g(S)$ term. This velocity deficit is progressively modified by the unsteady aerodynamic history effects and, the resulting unsteady lift is calculated by means of Eq. (5.6).

5.4.6 Results and Discussion

The results in Figures 5.26 to 5.28 show the normalised experimental and predicted force coefficient variations due to the tower wake interaction for head-on flow cases.

The normal force coefficient variation obtained from the wind tunnel experiments is compared to the lift variation from both, the previous steady tower model and the enhanced unsteady tower shadow scheme. Normal force and lift coefficients are not strictly comparable. However, due to the small blade incidence angle, of approximately 1°, a comparison between the experimental C_n and the predicted C_l is not inappropriate.

The tower shadow geometry settings that have been used for the prediction are the same as before. These settings, maximum velocity deficit D_V of 0.30 of the freestream velocity and tower shadow width, B_t, of 2.75 tower diameters, have been

determined from observation of the blade response and are in line with other wind tunnel studies (Schlichting 1979, Snyder and Wentz 1981) and field observations of the tower shadow geometry for wind turbines (Shipley *et al.* 1995*b*).

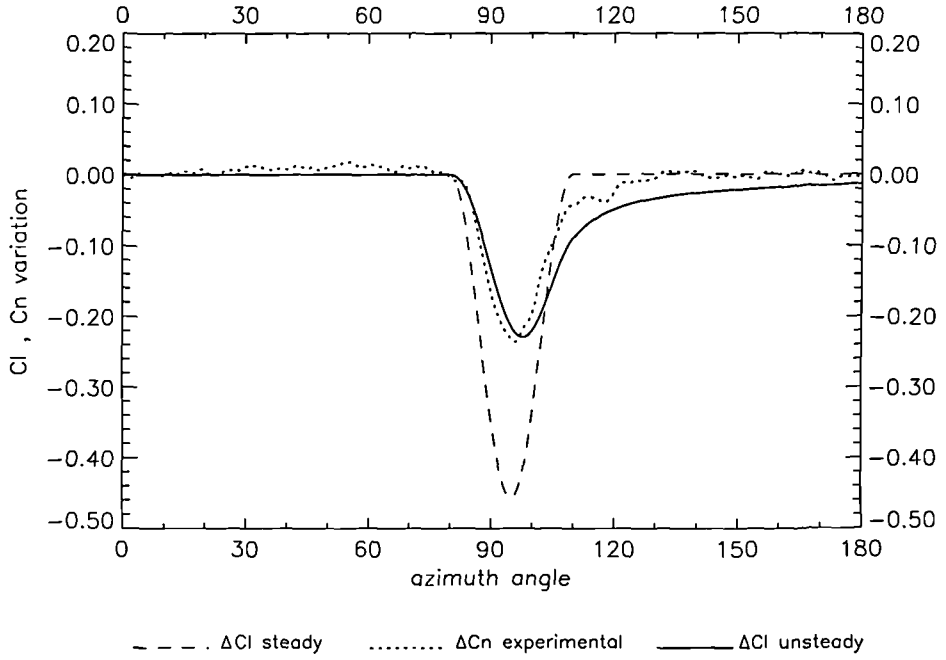

Figure 5.26: *Tower shadow prediction* ($D_V = 0.30, B_t = 2.75$) *and measurement at yaw*=0°, *wind velocity*=*9 m/s*

At a wind velocity of 9 m/s and zero yaw angle, in addition to the steady model prediction (dashed line), Figure 5.26 shows a quite remarkable improvement of the predicted lift using the unsteady model (solid line) compared to the measurements (dotted line). Both, the phase and intensity of the unsteady prediction show a good agreement with the experimental measurements. It is worthy of note that the slow recovery from the tower shadow is now captured by the unsteady model.

At a wind velocity of 11 m/s and zero yaw error, Figure 5.27 illustrates again the improvement of the unsteady solution compared to the steady prediction. Although a slight intensity difference and phase lag is evident between the experimental normal

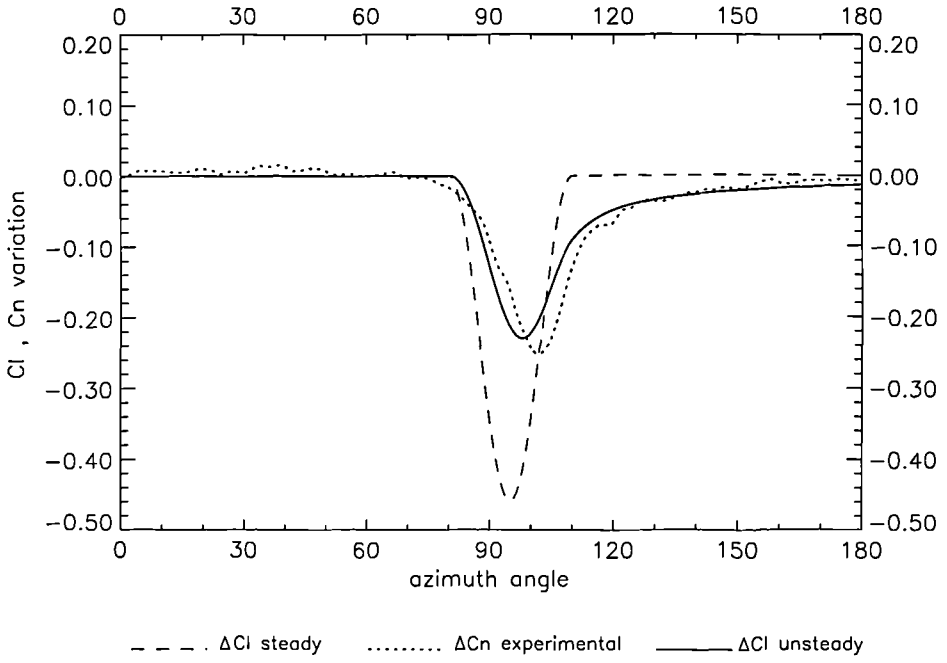

Figure 5.27: *Tower shadow prediction ($D_V = 0.30, B_t = 2.75$) and measurement at yaw=0°, wind velocity=11 m/s*

force coefficient and the predicted unsteady lift, the general trend is well captured. In particular, the force recovery at the blade exit from the tower shadow region is well represented.

Figure 5.28 shows the normal force and lift coefficient variations for a wind velocity of 11.7 m/s at zero yaw error. In this figure the measured data differ considerably from the unsteady prediction. It appears, that the blade encounters the tower wake at a later azimuthal position and is affected by a more intense velocity deficit than the unsteady prediction suggests. The reason for this disagreement is not straightforward. Possibly this behaviour could have been attributed to the instantaneous unaveraged nature of the experimental data, were only a single rotation to have been presented. However, verification of the response in a second consecutive cycle, as previously shown in Figure 5.23, confirms the repeatability of the

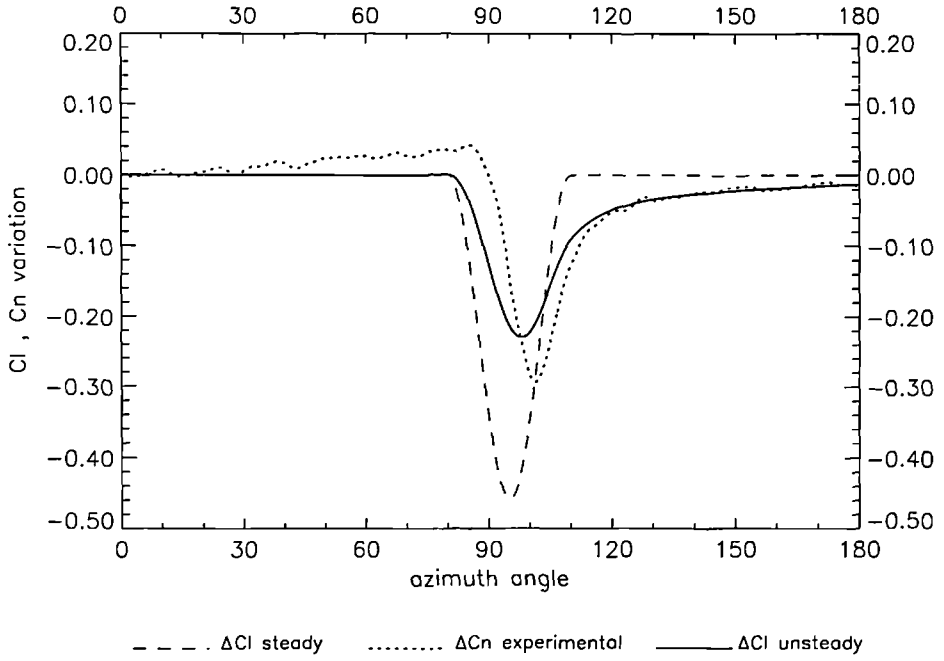

Figure 5.28: *Tower shadow prediction ($D_V = 0.30, B_t = 2.75$) and measurement at yaw=0°, wind velocity=11.7 m/s*

measured aerodynamic normal force. It was previously noted that this particular case was measured at a Reynolds number, based on the tower diameter, of 5.6x10^4 where transition from laminar to turbulent boundary layer separation could appear. In previous experiments, Snyder and Wentz (1981) showed that the tower shadow width depends strongly on the type of boundary layer; as the Reynolds number increases the tower shadow width decreases. This could be the reason for the narrower width of the tower wake encounter in this case. The more energetic deficit in the wake may also be explained in this way.

Sensitivity of the Unsteady Model to the Tower Shadow Geometry

It is worthy of note, from all the previous figures, that there is almost no appreciable change in the force predictions at 9 m/s 11 m/s and 11.7 m/s. The reason for the

similarity can be explain by the sensitivity of the model to the tip speed ratio and the tower shadow parameters. It should be noted that the experimental measurements were collected at an almost constant tip speed ratio by means of increasing the rotational speed as the free stream was increased for the three wind velocities tested. As may been seen in Table 5.1, the tip speed ratio does not change dramatically; 5.34, 5.33 and 5.31 at 9 m/s 11 m/s and 11.7 m/s respectively. In addition the tower shadow settings are fixed in the numerical model. Therefore the model, correctly, does not show any appreciable change when predicting the unsteady lift in the three cases.

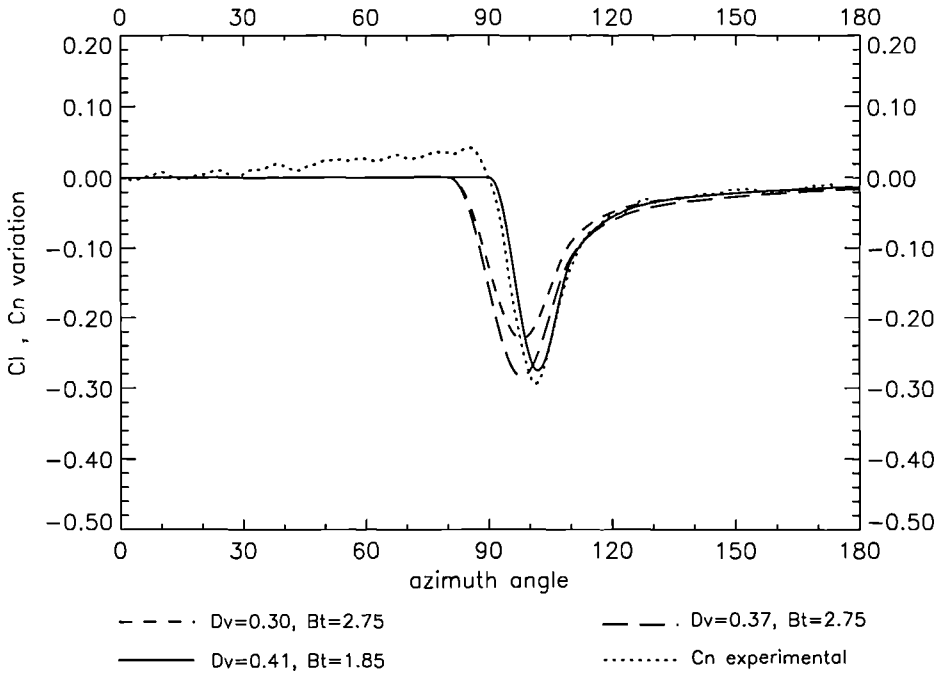

Figure 5.29: *Effects of tower shadow geometry, D_V and B_t on the unsteady prediction at yaw=0°, wind velocity=11.7 m/s*

The sensitivity of the unsteady model prediction to the tower shadow width and the velocity deficit is illustrated in Figure 5.29 at 11.7 m/s wind velocity and zero yaw error. The differences in the predicted lift variation produced by the different

settings of the tower shadow geometry can be observed in terms of both the severity and extent of the unsteady response. An increase in the maximum velocity deficit D_V from 0.30 to 0.37, while maintaining a constant width, B_t, of 2.75 tower diameters, has the effect of producing a more severe variation of the lift intensity while keeping the same phase. On the other hand, a simultaneous reduction in the tower shadow width from 2.75 to 1.85 tower diameters, together with an increase in the velocity deficit to 0.41 (solid line) reduces the extent and changes the phase of the response. The intensity is also increased, obtaining a closer agreement with the experiment (dotted line). Thus, for this particular case, reduction in the tower shadow width and an increase of the maximum velocity deficit seems to be responsible for the different response in the test. It is possible that the marginal change in Reynolds number between the different cases produces this effect. Indeed, this behaviour was observed by Snyder and Wentz (1981) at higher Reynolds number but in a different test facility with a different turbulence environment.

5.4.7 Conclusions

Two different models of the aerodynamic response of a wind turbine blade, due to the velocity deficit produced by the wind turbine support tower, have been presented. In the first model, the velocity deficit is simply applied to the onset flow as a cosine function. This substantially modifies the blade incidence and velocity variations through the tower shadow region. Unfortunately, this approach does not adequately represent the response of the blade in the tower shadow region.

An alternative model has been developed which involves the use of the Küssner function for the velocity deficit. This model includes the contribution of the attached flow unsteadiness in terms of the attenuation in unsteady lift response and a phase lag compared to the steady lift values. This considerably improves the tower shadow modelling.

The effect that the tower shadow has on the chordal variation in angle of attack persists until the aerofoil is far away from the source of the velocity distortion. This has been seen from the wind tunnel measurements and the new model captures this effect very well. This will inevitably influence dynamic stall onset due to tower shadow and, with appropriate extension, the new model may provide a means to predict this more accurately.

It should be noted that the azimuthal interval used within the shadow region was 0.5° but, despite this, the computational cost introduced by the unsteady model is almost negligible.

Further Improvements

In the light of the results presented here, a further validation and extension to the yawed case seems reasonable. This could provide a focus for future work. In this case however it would also be necessary to account for the unsteady effects produced by the yawed flow.

The flow over bluff bodies is still an open challenge for modelling; even the simplest case of a cylinder. If unsteady vortex shedding effects could be included in a tower shadow model, it would be possible to examine cycle by cycle loads to identify peak unsteady loadings. This, however, will require a model of some complexity.

Another area of interest is the sensitivity of the tower shadow response to the distance between the blade and the tower. The velocity deficit of the wake decays quite gradually in the axial direction of the wake. From an aerodynamic point of view, a large distance between the tower and the rotor will be beneficial by producing a less energetic response. Obviously from the structural point of view, it is desirable to have the tower axis as close as possible to the rotor hub. The design trend for new downwind turbines is to have greater tower clearances. A novel prototype,

the *MS4* constructed by the Wind Energy Group, has highly flexible blades which move by coning in strong winds. The Scottish Provengen manufacturer of small sized turbines, uses a simple and similar power regulating system. Coning can be introduced to decrease mean blade loads by balancing aerodynamic loads with centrifugal loads for downwind turbines. In addition coning means that the blades pass through the tower wake at a greater distance from the tower. For machines that are designed to cone under the action of the wind, the coning angle, and hence the tower/blade separation distance will change with the turbine operating conditions. It would, therefore, be desirable to extend the tower shadow model to account for the axial decay of the tower wake with increased distance from the tower.

Chapter 6

Conclusions and Recommendations

The main conclusions of this investigation are summarised next and further work is suggested at the end of this chapter. In addition to the concluding remarks, more detailed and partial conclusions are given at the end of every chapter.

6.1 Final Conclusions

A code to assist in the preliminary stages of wind turbine blade aerodynamic design has been developed at Glasgow University, which embodies the methods applied and the results obtained during this investigation. This engineering tool, based on a classic BEM solver, can provide valuable information on three-dimensional stall delay, dynamic stall onset and tower shadow effects.

The basic model still exhibits the classical limitations of the BEM theory; blade incidence will be prone to error at low wind speed or high yaw angles. Although the predicted unsteady response, such as the locations of dynamic stall are sensitive to this effect, the general level of prediction obtained from the scheme is acceptable. This has been illustrated by comparing the BEM predicted spanwise variation in

blade incidence at low wind speeds (Chapter 2) and the dynamic stall locations at high yaw angles (Chapter 4), with predictions from the more sophisticated prescribed wake scheme of Coton and Wang (1999).

In line with previous work, it has been shown that three-dimensional stall delay is restricted to inboard blade sections regardless of the onset flow conditions. The present results showed an acceptable sensitivity to the blade chord to radius parameter, c/r, but almost no dependency to changes in wind velocity and rotational speed for the normal operational conditions of the NREL Phase II untwisted wind turbine. The stall delay model is based on a laminar separation analysis, which does not take into consideration the turbulent boundary layer. Previous flow visualisation studies have indicated that the strongest effects appear to be confined to turbulent regions of separated flow on the blades. Therefore, consideration must be made of the turbulent radial flow ahead of the massive separations occurring on wind turbine blades, if development of better 3–D stall delay algorithms are to be achieved.

Despite some differences in the measured and predicted results, the BEM predictions based on a 2–D correlation of dynamic stall vortex onset provide a fair representation of the actual dynamic stall onset experienced by the untwisted and the twisted rotor configurations of the NREL Unsteady Aerodynamics Experiment turbine Phases II and IV. The location and severity of dynamic stall on the rotor disc has been shown to be very sensitive to onset flow conditions and blade geometry. The results show that dynamic stall can be produced by two different mechanisms; the tower shadow region and the turbine operating in yawed flow.

It has been shown that 3–D stall delay does not affect dynamic stall in the same way as it does static stall. Examination of the three-dimensionality of the dynamic stall field measurements has revealed that, the initial stall onset is correctly characterised by the 2–D correlation. After its local inception, however earlier dynamic

stall appears to be triggered in adjacent stations. This is a significant result and suggests that the first signs of dynamic stall on a wind turbine blade can be correctly determined on the basis of the prediction scheme assuming locally two-dimensional flow. Despite this, there is obviously room to improve the 2–D dynamic stall predictor. In particular, it has been shown that basing the dynamic stall prediction on the static stall angle may be inappropriate in some cases and so an alternative formulation has been explored. It has been shown that the use of the angle, α_f, at which the first divergence of the $f - \alpha$ curve to a lower gradient occurs in steady flow, may be a more appropriate parameter for the S809 aerofoil, which has unusual static stalling characteristics.

Finally, the work has considered the aerodynamic response to tower shadow. A wind tunnel experiment was conducted and results from the analysis of pressure measurements and integrated force coefficients have been presented. The impact that the tower wake on a downwind turbine has on the blade for both, head-on flow and a fixed yaw error has been examined. It has been observed that for head-on flow, the wind tunnel measurements of the tower shadow are not centred around the 90 ° azimuth position, the minimum normal force peak has been measured between 95° and 100°. This may be partially due to inaccuracies in measuring the blade azimuth but it is also a feature of the dynamic response of the blade as it passes through the tower shadow.

The pressure recovery as the blade leaves the tower wake is much slower than the response at the entrance to the tower shadow region. This observation is important and suggests that the effective variation in angle of attack persists until the aerofoil is far away from the source of the velocity distortion. This behaviour is consistent regardless of possible vortex collisions and Reynolds number. This delay in the recovery of the normal force could be explained in terms of the induced velocity due to the vorticity shed from the aerofoil as its circulation changes during the passage

through the tower wake. The implications of this for dynamic stall modelling may be significant since it is the effective variation in angle of attack on the way out of the tower wake that determines the onset of dynamic stall in this region.

In parallel to the experimental data analysis, the blade element method was extended to include the blade/tower interaction using two different tower shadow modelling strategies. These were evaluated by comparison with the wind tunnel measurements.

In the first model, only the steady aerodynamic response due to the wake velocity deficit described by a cosine function was taken into account. Unfortunately, this approach did not adequately represent the response of the blade in the tower shadow region. In the second model, an enhancement of the physical interaction between the tower wake and the aerofoil was implemented for unyawed flow by including unsteady aerodynamic effects. This considerably improved the tower shadow modelling. It was shown that the phase, extent and intensity of the tower shadow effects were modelled well. In addition, the predicted recovery as the blade leaves the tower wake was almost identical to the measured data.

It should be noted that the design tools developed during this study contribute to enhanced rotor design capability. In particular, the methods should allow more comprehensive evaluation of new blade designs at an early stage of the design process. This should, in turn, reduce the risk of bringing entirely new blade geometries into operational service.

6.2 Further Work

In addition to local flow unsteady aerodynamics, the global unsteadiness inherent in the wake due to the various flow states that a wind turbine encounters in its

operational envelop, needs further research. For most normal operating conditions a wind turbine is operating in the windmill brake state, where BEM methods have proved to provide accurate results. However, turbulent wake and vortex ring states may occur, for example, during start-up at low wind speeds. New trends are pointing towards wind turbines operating even at lower wind speed regimes, where cut-in velocities are lower and the probability of general operation at low winds speed is increased. The basic BEM theory has a number of limitations when predicting these flow conditions, as do the more complex codes. If BEM methods are to be used to provide input into aeroelastic calculations or control strategies, extension into these regimes will be necessary.

In order to improve stall delay calculations, a better physical understanding of the flow under rotational conditions is needed. Full numerical calculations together with experimental flow measurements and visualization on wind turbines may throw some new light into the physics of 3–D stall delay. This, in turn, may provide the basis for obtaining new practical semi-empirical models that capture and embody the effects of separated flows around the rotating wind turbine blades. It should be noted that 3–D effects and the corresponding semi-empirical models have their origin in propeller and helicopter studies. There are important differences between these and wind turbines. The helicopter flow field is dominated by compressibility effects, and the rotor blades have very low solidity. A relevant characteristic of helicopters, as Wood (1991) stated, is that " the most rapid change in bound circulation occurs near the tip of the rotor, so the hub vortex is relatively unimportant. For the turbine considered here, and probably for most turbines, the hub trailing vortex contributes significantly to the downstream circulation and hence to the power extracted from the wind ". Insight into the hub vortex effect could help to clarify the stall delay phenomenon. In addition consideration of 3–D blade geometry such as taper, aspect ratio and sweep effects may also provide more insight.

The applicability of the dynamic stall correlation to the S809 aerofoil is also a major question that needs to be considered. Ideally, this aerofoil should be tested under dynamic conditions and the results compared to the correlation. This would help to resolve the question of the suitability of α_f or α_{ss} within the correlation. The response at reduced pitch rates close to the quasi-steady boundary also requires further investigation. Developing a simple model of how the dynamic stall vortex evolves and convects in a highly separated 3–D environment may be a more challenging task. Understanding the manner in which the dynamic stall vortex affects and interacts with other portions of the blade is still the focus of ongoing experimental effort. Further work is, however, required to fully consider the impact of three-dimensional effects on the dynamic stalling process. Theoretical and experimental studies, such as flow visualisation of a rotating wind turbine blade, will be of help in addressing the complicated physics of both, attached and separated unsteady three dimensional rotating flows.

In the light of the tower shadow predictions obtained here, further validation and extension to the yawed case seems reasonable. The unsteady tower shadow model captures very well the response as the blade leaves the tower wake. This will inevitably influence dynamic stall onset due to tower shadow and, with appropriate extension, the new model may provide a means to predict this more accurately.

Another area of interest is the sensitivity of the tower shadow response to the distance between the blade and the tower. For machines that are designed to cone under the action of the wind, the coning angle, and hence the tower/blade separation distance will change with the turbine operating conditions. It would, therefore, be desirable to extend the tower shadow model to account for the axial decay of the tower wake with increased distance from the tower. This could provide a focus for future work.

Throughout the progress of this work it has become clear to the author that

much of the physics undergoing the aerodynamics of wind turbines is still lacking in even the most elaborate design tools. There is a need to address these deficiencies if more efficient, cost-effective designs are to be realised in the future.

Bibliography

Abbott, I. H. and A. E. von Doenhoff (1959). *Theory of wing sections.* Dover Publications, Inc.. New York.

Acker, T. L. and M. M. Hand (1999). Aerodynamic performance of theNREL Unsteady Aerodynamics Experiment Phase IV twisted rotor. In: *A Coll. 1999 ASME Wind Energy Symp. Tech. Papers Presented 37th AIAA Aerospace Sci. Meeting and Exh., Reno, USA, AIAA-99-0045.*

Anderson, M. B., D. J. Milborrow and J. N. Ross (1982). Performance and wake measurements on a 3 m diameter horizontal axis wind turbine rotor. In: *Proc. 4th Int. Symp. on Wind Energy Systems, Stockholm.*

Banks, W. H. H. and G. E. Gadd (1963). Delaying effect of rotation on laminar separation. *AIAA J.* **1**(4), 941–942.

Bareiß, R., G. Guidati and S. Wagner (1996). Wake simulation for wind turbines with free, prescribed and hybrid wake method. In: *10th IEA Symp. on the Aerodynamics of Wind Turbines: Advanced Rotor Performance Methods, Edinburgh.*

Beddoes, T. S. (1976). A synthesis of unsteady aerodynamic effects including stall hysteresis. *Vertica* **1**, 113–123.

Beddoes, T. S. (1983). Representation of airfoil behaviour. *Vertica* **7**(2), 183–197.

Beddoes, T. S. (1991). A 3–d separation model for arbitrary planforms. In: *Proc. 47th Ann. Forum - Am. Helicopter Soc.*. pp. 451–460.

Bisplinghoff, R. L., H. Ashley and R. L. Halfman (1996). *Aeroelasticity*. Dover Publications, Inc.. New York.

Bjorck, A. (1995). Dynamic stall and three-dimensional effects. final report for the Joule II Project. FFA–TN–1995–31. The Aeronautical Research Institute of Sweden.

Bossanyi, E. A. (1997). BLADED for windows theory manual. Technical report. Garrad Hassan and Partners Limited.

Buhl, M. L., A. D Wright and J. L. Tangler (1997). Wind turbine design codes: A preliminary comparison of the aerodynamics. NREL/CP–500–23975. Nat. Renewable Energy Lab.

Burley, R.R, J. M. Savino, L. H. Wagner and J.H. Diedrich (1976). Some techniques for reducing the tower shadow of the DOE/NASA Mod-0 wind turbine tower. NASA TM–79202.

Bussel, G. J. W. (1996). The application of advanced rotor (performance) methods for design calculations. In: *Proc. 10th IEA Symposium on the Aerodynamics of Wind Turbines, Edinburgh, Scotland.* pp. 141–158.

Butterfield, C. P. (1989*a*). Aerodynamic pressure and flow-visualization measurement from a rotating wind turbine blade. In: *8th ASME Wind Energy Symp. Houston, TX, USA.*

Butterfield, C. P. (1989*b*). Three-dimensional airfoil performance measurements on a rotating wind turbine wing. In: *Proc. Eur. Wind Energy Conf. '89, Glasgow, Scotland.*

Butterfield, C. P., G. Scott and W. Musial (1992*a*). Comparison of wind tunnel airfoil performance data with wind turbine blade data. *ASME J. Solar Energy Eng.* **114**(2), 119–124.

Butterfield, C. P., W. P. Musial, G. N. Scott and D. A. Simms (1992*b*). NREL Combined Experiment final report Phase II: draft. NREL/TP–442–4807. Nat. Renewable Energy Lab.

Cardona, J. L. (1984). Flow curvature and dynamic stall simulated with an aerodynamic free-vortex model for VAWT. *Wind Eng.* **18**(3), 135–143.

Carr, L. W. (1977). Analysis of the development of dynamic stall based on oscillating airfoil experiments. NASA TN D–8382.

Carr, L. W. (1988). Progress in analysis and prediction of dynamic stall. *J. Aircraft* **25**(1), 6–17.

Carr, L. W. and M. S. Chandrasekhara (1996). Compressibility effects on dynamic stall. *Prog. Aerospace Sci.* **32**, 523–573.

Carta, F. O. (1974). Analysis of oscillatory pressure data including dynamic stall effects. NASA CR–2394.

Chaviaropoulos, P. K. (1996). Investigating dynamic stall, 3–D and rotational effects on wind turbine blades by means of an unsteady quasi 3–D Navier–Stokes solver. In: *10th IEA Symp. on the Aerodynamics of Wind Turbines: Advanced Rotor Performance Methods, Edinburgh.* pp. 175–181.

Chaviaropoulos, P. K. and M. O. L. Hansen (2000). Investigating three-dimensional and rotational effects on wind turbine blades by means of a quasi 3–D Navier–Stokes solver. *ASME J. Fluids Eng.* **122**(2), 330–336.

Clausen, P. D. and D. H. Wood (1988). An experimental investigation of blade element theory for wind turbines. part2. phase-locked averaged results. *J. Wind Eng. and Ind. Aerodyn.* **31**(2–3), 305–322.

Clausen, P. D., D. M. Piddington and D. H. Wood (1987). An experimental investigation of blade element theory for wind turbines. part1. mean flow results. *J. Wind Eng. and Ind. Aerodyn.* **25**(2), 189–206.

Conlisk, A. T. (1997). Modern helicopter aerodynamics. *Ann. Rev. Fluid Mech.* **29**, 515–567.

Corrigan, J. J. and J. J. Schillings (1994). Empirical model for stall delay due to rotation. In: *Proc. Am. Helicopter Soc. Aerodyn. Specialists Conf., San Francisco, CA, Jan. 1994.* pp. 1–16 (8.4).

Coton, F. N. and R. A. McD. Galbraith (1999). An experimental study of dynamic stall on a finite wing. *Aeronaut. J.* **103**(1015), 229–236.

Coton, F. N. and T. Wang (1999). The prediction of horizontal axis wind turbine performance in yawed flow using an unsteady prescribed wake model. *Journal of Power and Energy* **213**, 33–43.

Coton, F. N., D. Jiang and R. A. McD. Galbraith (1994). Unsteady prescribed wake model for vertical axis wind turbines. *Proc. I.Mech.E., Part A: J. Power and Energy* **208**(1), 13–16.

Coton, F. N., R. A. McD. Galbraith and R. B. Green (2001). The effect of wing planform shape on dynamic stall. *Aeronaut. J.* **105**(1045), 151–159.

Coton, F. N., T. Wang and R. A. McD. Galbraith (2002). An examination of key aerodynamic modelling issues raised by the NREL blind comparison. In: *A Coll.*

2002 ASME Wind Energy Symp. Tech. Papers Presented 40th AIAA Aerospace Sci. Meeting and Exh., Reno, USA, AIAA-2000-0038.

de Vries, O. (1979). Wind tunnel tests on a model of a two bladed horizontal axis wind turbine. NLR–TR–79071L. Nat. Aerospace Lab., Amsterdam.

de Vries, O. and M. den Blanken (1981). Second series of wind tunnel tests on a model of a two bladed horizontal axis wind turbine. NLR-TR–81069. Nat. Aerospace Lab., Amsterdam.

Du, Z. and M. S. Selig (1998). A 3-D stall-delay model for horizontal axis wind turbine performance prediction. In: *A Coll. 1998 ASME Wind Energy Symp. Tech. Papers Presented 36th AIAA Aerospace Sci. Meeting and Exh., Reno, USA, AIAA-98-0021.*

Duque, E. P. N. (2001). Web page available through:. http://quest.arc.nasa.gov/aero/team/fjournals/duque/inthebeg.html.

Duque, E. P. N., C. P. van Dam and S. C. Hughes (1999). Navier–Stokes simulations of the NREL Combined Experiment Phase II rotor. In: *A Coll. 1999 ASME Wind Energy Symp. Tech. Papers Presented 37th AIAA Aerospace Sci. Meeting and Exh., Reno, USA, AIAA-99-0037.*

Dwyer, H. and W. J. McCroskey (1970). Crossflow and unsteady boundary layer effects on rotating blades. AIAA–70–50.

Eggers, A. J. Jr. and R. V. Digumarthi (1992). Approximate scaling of rotational effects of mean aerodynamic moments and power generated by the Combined Experiment rotor blades operating in deep-stalled flow. In: *11th ASME Wind Energy Symp.*. pp. 33–43. ASME Solar Eng. Div., Vol.12.

Eggleston, D. M. (1990). New results in flow visualization for wind turbines. In: *Windpower '90.* American Wind Energy Association.

Eggleston, D. M. and F. S. Stoddard (1987). *Wind Turbine Engineering Design.* Van Nostrand Reinhold. New York.

Ekaterinaris, J. A. and M. F. Platzer (1997). Computational prediction of airfoil dynamic stall. *Prog. Aerospace Sci.* **33**(11–12), 759–846.

Ekaterinaris, J. A., N. N. Sorensen and F. Rasmussen (1998). Numerical investigation of airfoil dynamic stall in simultaneous harmonic oscillatory and translatory motion. *ASME J. Solar Energy Eng.* **120**(1), 75–83.

Fogarty, L. E. (1951). The laminar boundary layer on a rotating blade. *J. Aeronaut. Sci.* **18**(4), 247–252.

Fogarty, L. E. and W. R. Sears (1950). Potential flow around a rotating, advancing cylindrical blade. *J. Aeronaut. Sci.* **17**(9), 599.

Froude, R. E. (1889). On the part played in propulsion by differences of fluid pressure. *Trans. Inst. Naval Arch.* **30**, p. 390.

Galbraith, R. A. McD., A. J. Niven and F. N. Coton (1990). Aspects of unsteady aerodynamics in wind turbines. *Wind Eng.* **14**(5), 286–299.

Galbraith, R. A. McD., A. J. Niven and L. Y. Seto (1986). On the duration of dynamic stall. In: *1th ICAS Congress. London.* number ICAS-86-2.4.3.

Galbraith, R. A. McD., F. N. Coton, E. Saliveros and G. Kokkodis (1987). Aerofoil scale effects and the relevance to wind turbines. In: *Proc. 9th BWEA Wind Energy Conf., , England.* pp. 268–278.

Galbraith, R. A. McD., M. W. Gracey and E. Leitch (1992). Summary of pressure data for thirteen aerofoils on the university of glasgow's aerofoil database. GU AERO Report–9221. University of Glasgow.

Ganander, H. and R. Lindstrom (2001). Short term power variations in the output of wind turbines. *DEWI Magazine* (19), 27–30.

Gessow, A. and G. C. Myers (1952). Aerodynamics of the helicopter. Technical report. Frederick Ungar Publishing.

Giguere, P., M. S. Selig and J. L. Tangler (1999). Blade design trade-offs using low-lift airfoils for stall-regulated hawts. NREL/CP–500–26091. Nat. Renewable Energy Lab.

Glauert, H. (1935). Airplane propellers. In: *Aerodynamic Theory* (W. F. Durand, Ed.). Vol. IV, Div.L. Springer. Berlin.

Glauert, H. (1948). *The Elements of Aero Foil and Airscrew Theory.* Cambridge Univ. Press. Cambridge.

Gormont, R. E. (1973). A mathematical model of unsteady aerodynamics and radial flow for application to helicopter rotors. US Army AMRDL Eustis Directorate Report TR–72–67. US Army Air Mobility Res. Dev. Lab.

Gould, J. and S. P. Fiddes (1992). Computational methods for the performance of hawts. *J. Wind Eng. and Ind. Aerodyn.* **39**(1–3), 61–72.

Gracey, M. W. (1991). The design and low Mach number wind tunnel performance of a modified NACA 23012 aerofoil, with an investigation of dynamic stall onset. PhD thesis GU AERO Report–9108. Univ. of Glasgow.

Gracey, M. W., A. J. Niven and R. A. McD. Galbraith (1989). A consideration of low-speed dynamic stall onset. In: *15th European Rotorcraft Forum.* number paper no.: 11. Amsterdam.

Gracey, M. W., A. J. Niven, F. N. Coton and R. A. McD. Galbraith (1996). A correlation indicating incipient dynamic stall. *Aeronaut. J.* **100**(997), 305–311.

Gracey, M. W., F. N. Coton and R. A. McD. Galbraith (1997). On the prediction of aerofoil unsteady stall critically. *Aeronaut. J.* (2223), 331–334.

Graham, J. M. R. and C. J. Brown (1999). Aerodynamics of horizontal axis rotor interacting with the tower. In: *Proc. Eur. Wind Energy Conf. '99, Nice, France.*

Grant, I., M. Mo, X. Pan, P. Parkin, J. Powell, H. Reineche, K. Shuang, F.N. Coton and D. Lee (1998). Optical evaluation of the wake characteristics of a wind turbine and a prescribed wake model. In: *8th Int. Symp. on Flow Visualization.*

Grant, I., M. Mo, X. Pan, P. Parkin, J. Powell, H. Reineche, K. Shuang, F.N. Coton and D. Lee (2000). An experimental and numerical study of the vortex filaments in the wake of an operational, horizontal-axis, wind turbine. *J. Wind Eng. and Ind. Aerodyn.* **85**(2), 177–189.

Griffiths, R. T. (1977). Effect of aerofoil characteristics on windmill performance. *Aeronaut. J.* **81**(799), 322–326.

Griffiths, R. T. and M. G. Woollard (1978). Performance of the optimal wind turbine. *Applied Energy* **4**(4), 261–272.

Hand, M. M., D. A. Simms, L. J. Fingersh, D. W. Jager and J. R. Cotrell (2001*a*). Unsteady Aerodynamics Experiment Phase V: Test configuration and available data campaigns. NREL/TP–500–29491. Nat. Renewable Energy Lab.

Hand, M. M., D. A. Simms, L. J. Fingersh, D. W. Jager, J. R. Cotrell, S. Schreck and S. M. Larwood (2001*b*). Unsteady Aerodynamics Experiment Phase VI: Wind tunnel test configurations and available data campaigns. NREL/TP–500–29955. Nat. Renewable Energy Lab.

Hansen, A. C. (1992). Yaw dynamics of horizontal axis wind turbines. NREL/TP–442–4822. Nat. Renewable Energy Lab.

Hansen, A. C. (1995). Aerodynamic damping of blade flap motions at high angles of attack. *ASME J. Solar Energy Eng.* **117**(3), 194–199.

Hansen, A. C. and C. P. Butterfield (1993). Aerodynamics of horizontal-axis wind turbines. *Ann. Rev. Fluid Mech.* **25**, 115–149.

Hansen, A. C., C. P. Butterfield and X. Cui (1990). Yaw loads and motions of a horizontal axis wind turbine. *ASME J. Solar Energy Eng.* **112**(4), 310–314.

Harris, F. D. (1966). Preliminary study of radial flow effects on rotor blades. *J. Am. Helicopter Soc.* **11**(3), 1–21.

Harris, F. D., F. J. Tarzanin and R. K. Jr. Fisher (1970). Rotor high-speed performance; theory vs. test. *J. Am. Helicopter Soc.* **15**(3), 35–44.

Himmelskamp, H. (1947). Profile investigations on a rotating airscrew. MAP-VG–177-t. MAP Volkenrode Reports and Translations.

Horner, M. B., R.A.McD. Galbraith, F. N. Coton, I. Grant, J. N. Stewart and F. de la Iglesia Moreno (1995). A descriptive model of the flows underlaying the impulsive loading produced by blade-vortex interaction. In: *Wind Energy 1995 – Proc. Energy-Source Technology Conf. and Exh., Houston, TX, USA* (W. D. Musial, S. M. Hock and D. E. Berg, Eds.). pp. 175–184. ASME Solar Eng. Div., Vol.16.

Huyer, S. A., D. Simms and M. C. Robinson (1996). Unsteady aerodynamics associated with a horizontal-axis wind turbine. *AIAA J.* **34**(7), 1410–1419.

Johansen, J. (1999). Unsteady airfoil flow with application to aeroelastic stability. Risø–R–1116–(en). Risø National Laboratory.

Johansen, J. and C. Bak (2000). Investigation of the aerodynamic interaction between wind turbine rotor blades and the tower and its impact on wind turbine design (ROTOW). Work package 2 report. Risø contribution to Rotow.

Jones, B. M. (1933). An experimental study of the stalling of wings. RM–1588. British ARC.

Jones, B. M. (1934). Stalling. *Aeronaut. J.* **38**(285), 753–770.

Kelley, N. D. and H. E. McKenna (1985). Acoustic noise associated with the MOD–1 wind turbine: its source, impact and control. SERI/TP–635–116. Sol. Energy Res. Inst.

Kuchemann, D. (1978). *The aerodynamic design of aircraft.* Pergamon Press.

Leishman, J. G. (1987*a*). Practical modeling of unsteady airfoil behaviour in nominally attached two-dimensional compressible flow. UM–AERO–87–6. University of Maryland.

Leishman, J. G. (1987*b*). A semi-empirical model for dynamic stall. UM–AERO–87–24. University of Maryland.

Leishman, J. G. (1988). Validation of approximate indicial aerodynamic functions for two-dimensional subsonic flow. *J. Aircraft* **25**(10), 914–922.

Leishman, J. G. (2002). Challenges in modeling the unsteady aerodynamics of wind turbines. In: *A Coll. 2002 ASME Wind Energy Symp. Tech. Papers Presented 40th AIAA Aerospace Sci. Meeting and Exh., Reno, USA, AIAA–2000–0040.*

Leishman, J. G. and T. S. Beddoes (1989). A semi-empirical model for dynamic stall. *J. Am. Helicopter Soc.* **34**(3), 3–17.

Lorber, P. F. and F. O. Carta (1987). Airfoil dynamic stall at constant pitch rate and high reynolds number. In: *Paper Presented at AIAA 19th Fluid Dynamics, Plasma Dynamics and Laser Conf., Hawaii, AIAA–87–1329.*

Madsen, H. A. (1991). Aerodynamics of a horizontal axis wind turbine in natural conditions. Risø–m–2903. Risø National Laboratory.

Madsen, H. A. (1996). A cfd analysis of the actuator disc flow compared with momentum theory results. In: *Proc. 10th IEA Symposium on the Aerodynamics of Wind Turbines, Edinburgh, Scotland.* pp. 109–124.

Madsen, H. A. (2000). Modelling tower influence in aeroelastic calculations. Risø–R–1214–(en). Risø National Laboratory.

Madsen, H. A. and F. Rasmussen (1988). Derivation of three dimensional airfoil data on the basis of experiment and theory. In: *Proc. Windpower'88 Conf., Honolulu, Hawaii.*

Madsen, H. A. and H. F. Christensen (1990). On the relative importance of rotational, unsteady and three dimensional effects on the hawt rotor aerodynamics. *Wind Engineering* **14**(6), 405–415.

Masson, C. (1997). Performance and wake predictions of hawts in wind farms. In: *Windpower 97 Conf., Austin, Texas, USA.*

McCroskey, W. J. (1971). Measurements of boundary layer transition, separation and streamline direction on rotating blades. NASA TN–d-6321.

McCroskey, W. J. (1981). The phenomenon of dynamic stall. NASA TM–81264.

McCroskey, W. J. and P. F. Yaggy (1968). Laminar boundary layers on helicopter rotors in forward flight. *AIAA J.* **6**(10), 1919–1926.

McCroskey, W. J., L. W. Carr and K. W. McAlister (1976). Dynamic stall experiments on oscillating airfoils. *AIAA J.* **14**(1), 57–63.

McCullough, G. B. and D. E. Gault (1951). Examples of three representative types of airfoil-section stall at low speed. NACA TN–2502. Nasa Ames Aeronautical Laboratory.

Milborrow, D. J. (1985). Changes in aerofoil characteristics due to radial flow on rotating blades. In: *Proc. 7th BWEA Wind Energy Conf., Oxford, England.*

Miles, J. W. (1956). The aerodynamic force on an airfoil in a moving gust. *J. Aeronaut. Sci.* **23**(11), 1044–1050.

Miller, R. H., J. Dugundji, M. Martinez-Sanchez, J. Gohard, S. Y. Chung and T. Humes (1978). Aerodynamics of horizontal axis wind turbines. In: *Wind Energy Conversion.* Vol. II. U. S. Dept of Energy, COO 3141–T1/MIT, ASRL TR–184–8.

Moir, S. and F. N. Coton (1995). An examination of the dynamic stalling of two wing planforms. GU AERO Report–9526. University of Glasgow.

Molenaar, D. P. and Sj. Dijkstra (1999). State-of-the-art of wind turbine design codes: main features overview for cost-effective generation. *Wind Engineering* **23**(5), 295–311.

Munduate, X. and F. N. Coton (2000*a*). An aerodynamic method for the preliminary design of horizontal axis wind turbines. *Acta Politecnica - The Journal of Advanced Engineering Design* **40**(1), 59–65.

Munduate, X. and F. N. Coton (2000*b*). Identification of dynamic stall regions on horizontal axis wind turbines. In: *A Coll. 2000 ASME Wind Energy Symp. Tech. Papers Presented 38th AIAA Aerospace Sci. Meeting and Exh., Reno, USA, AIAA-2000-0039.*

Musial, W. D., C. P. Butterfield and M. D. Jenks (1990). A comparison of two- and three-dimensional S809 airfoil property for rough and smooth HAWT rotor operation. In: *9th ASME Wind Energy Symp. New Orleans, USA.* pp. 63–70. ASME Solar Eng. Div., Vol.9.

Narramore, J. C. and R. Vermeland (1992). Navier–Stokes calculations of inboard stall delay due to rotation. *J. Aircraft* **29**(1), 73–78.

Niven, A. J. (1988). An experimental investigation into the influence of trailing edge separation on an aerofoil's dynamic stall performance. PhD thesis. Univ. of Glasgow.

Niven, A. J. and R. A. McD. Galbraith (1990). Experiments on the establishment of fully attached aerofoil flow from the fully stalled condition during ramp-down motions. In: *17th ICAS Congress. Sweden.*

Niven, A. J. and R. A. McD. Galbraith (1997). Modelling dynamic stall vortex inception at low match numbers. *Aeronaut. J.* (2163), 67–76.

Oye, S. (1991). Dynamic stall simulated as a time lag of separation. In: *Proc. 4th IEA Symposium on the Aerodynamics of Wind Turbines, Rome, Italy.*

Peters, D. A. (1985). Toward a unified lift model for use in rotor blade stability analysis. *J. American Helicopter Society* **30**(3), 32–42.

Petersen, Helge (1984). Calculations on the DWT wind turbine. In: *Proc. 6th BWEA Wind Energy Conf., Reading, England.*

Pierce, K. and A. C. Hansen (1995). Prediction of wind turbine rotor loads using the Beddoes–Leishman model for dynamic stall. *ASME J. Solar Energy Eng.* **117**(3), 200–204.

Powles, S. J. R. (1983). Effects of tower shadow on the dynamics of a horizontal-axis wind turbine. *Wind Eng.* **7**(1), 26–42.

Prandtl, L. (1904). Uber flussigkeitsbewegung bei sehr kleiner reibung. International Mathematical Congress, Heidelberg, Germany. pp. 484–491.

Prandtl, L. and O. Tietjens (1957). *Fundamentals of Hydro and Aeromechanics.* Dover. New York.

Rankine, W. J. (1865). On the mechanical principles of the action of ship propellers. *Trans. Inst. Naval Arch.* **6**, 13–39.

Rasmussen, F. (1995). Engineering model for dynamic stall. Risø–M–854. Risø National Laboratory.

Rasmussen, F., S. M. Petersen, G. Larsen, A. Kretz and P. D. Andersen (1988). Investigations of aerodynamics, structural dynamics and fatigue on danwin 180 kw. Risø–m–2727. Risø National Laboratory.

Rawlinson-Smith, R. I. (1996). Development of a three dimensional model of dynamic stall. In: *Proc. Eur. Wind Energy Conf. '96, Gothenberg, Sweden.*

Rawlinson-Smith, R. I. and R. L. Hales (1990). Computational study of stalled rotor performance. In: *Proc. British Wind Energy Conf. '1990.*

Riziotis, V. A., P. K. Chaviaropoulos and S. G. Voutsinas (1996). Development of a state-of-the-art aeroelastic simulator for horizontal axis wind turbines. Part 2. Aerodynamic aspects and application. *Wind Eng.* **20**(6), 423–440.

Robinson, M. C., R. A. McD. Galbraith, D. E. Shipley and M. S. Miller (1995). Unsteady aerodynamics of wind turbines. In: *33rd AIAA Aerospace Sci. Meeting and Exh., Reno, USA, AIAA-95-0526.*

Robison, D. J., F. N. Coton, R. A. McD. Galbraith and M. Vezza (1994). The development of a prescribed wake model for the prediction of the aerodynamic performance of horizontal axis wind turbines in steady axial flow. GU AERO Report–9403. University of Glasgow.

Robison, D. J., F. N. Coton, R. A. McD. Galbraith and M. Vezza (1995). Application of a prescribed wake aerodynamic prediction scheme to horizontal axis wind turbines in axial flow. *Wind Eng.* **19**(1), 41–51.

Ronsten, G. (1992). Static pressure measurements on a rotating and a non-rotating 2.375m wind turbine blade – comparison with 2D calculations. *J. Wind Eng. and Ind. Aerodyn.* **39**(1–3), 105–118.

Rotow (2000). ROTOW-investigation of the aerodynamic interaction between wind turbine rotor blades and the tower and its impact on wind turbine design. JOR3-CT98-0273-1998-2000.

Sankar, L. N. (2001). Computational studies of horizontal axis wind turbines. XCX–7–442–7393. School of Aerospace Eng., Georgia Institute of Tech.

Savino, J. M. and L. H. Wagner (1976). Wind tunnel measurements of the tower shadow on models of the ERDA/NASA 100 kw wind turbine tower. NASA TM X–73548.

Savino, J. M. and T. W. Nyland (1983). Wind turbine flow visualization studies: tip and root vortices and wind stream pattern at low power. Wind Energy Project Office PIR–241. NASA Lewis Research Center.

Schepers, J. G., A. J. Brand, A. Bruining, J. M. R. Graham, M. M. Hand, D. G. Infield, H. A. Madsen, R. J. H. Paynter and D. A. Simms (1997). Final report of IEA Annex XIV: Field Rotor Aerodynamics. ECN–C–97–027. Netherlands Energy Research Foundation ECN.

Schlichting, H. (1979). *Boundary layer theory.* McGraw-Hill. New York.

Schreck, S. J., M. C. Robinson, M. M. Hand and D. A. Simms (2001). Blade dynamic stall vortex kinematics for a horizontal axis wind turbine in yawed conditions. *ASME J. Solar Energy Eng.* **123**, 272–281.

Schreck, S., M. Robinson, M. Hand and D. Simms (2000). Hawt dynamic stall response asymmetries under yawed flow conditions. In: *A Coll. 2000 ASME Wind Energy Symp. Tech. Papers Presented 38th AIAA Aerospace Sci. Meeting and Exh., Reno, USA, AIAA–2000–0040.*

Scruggs, R. M., J. F. Nash and R. E. Singleton (1974). Analysis of dynamic stall using unsteady boundary layer theory. NASA CR–2462.

Sears, W. R. (1950). Potential flow around a rotating cylindrical blade. *J. Aeronaut. Sci.* **17**(3), 183–184.

Sears, W. R. and B. O. Sparks (1941). On the reaction of an elastic wing to vertical gusts. *J. Aeronaut. Sci.* **9**(2), 64–51.

Selig, M. S. (1998). Private communication.

Seto, L. Y. (1988). An experimental investigation of low speed dynamic stall and reattachment of the naca 23012 aerofoil under constant pitch motion. GU AERO Report–8829. University of Glasgow.

Seto, L. Y. and R. A. McD. Galbraith (1985). The effect of pitch rate on the dynamic stall of a naca 23012 aerofoil. In: *11th European Rotorcraft Forum.* number paper no.: 34. London.

Shipley, D. E., M. S. Miller and M. C. Robinson (1995*a*). Dynamic stall occurrence on a horizontal axis wind turbine. In: *Wind Energy 1995 - Proc. Energy-Source Technology Conf. and Exh., Houston, TX, USA* (W. D. Musial, S. M. Hock and D. E. Berg, Eds.). pp. 167–173. ASME Solar Eng. Div., Vol.16.

Shipley, D. E., M. S. Miller, M. C. Robinson, M. W. Luttges and D. A. Simms (1995*b*). Techniques for the determination of local dynamic pressure and angle of attack on a horizontal axis wind turbine. NREL/TP–442–7393. Nat. Renewable Energy Lab.

Simms, D. A., M. M. Hand, L. J. Fingersh and D. W. Jager (1999). Unsteady Aerodynamics Experiment Phases II-IV: Test configurations and available data campaigns. NREL/TP–500–25950. Nat. Renewable Energy Lab.

Simms, D., S. Schreck, M. Hand and L. J. Fingersh (2001). NREL Unsteady Aerodynamics Experiment in the nasa-ames wind tunnel: a comparison of predictions to measurements. NREL/TP–500–29494. Nat. Renewable Energy Lab.

Simoes, F. J. and J. M. R. Graham (2001). Application of a free vortex wake model to a horizontal axis wind turbine. In: *Proc. Eur. Wind Energy Conf. '91, Amsterdam, The Netherlands.* pp. 46–50.

Snel, H. (1998). Review of the present status of rotor aerodynamics. *Wind Energy* **1**(S1), 46–69.

Snel, H. (2001). Survey of induction dynamics modelling within BEM–like codes: Dynamic inflow and yawed flow modelling revisited. In: *A Coll. 2001 ASME*

Wind Energy Symp. Tech. Papers Presented 39th AIAA Aerospace Sci. Meeting and Exh., Reno, USA, AIAA-2001-0027.

Snel, H. and J. G. Schepers (1994). Joint investigation of dynamic inflow effects and implementation of an engineering method. ECN–C–94–107. Netherlands Energy Research Foundation ECN.

Snel, H., R. Houwink and J. Bosschers (1994). Sectional prediction of lift coefficients on rotating wind turbine blades in stall. ECN–C–93–052. Netherlands Energy Research Foundation ECN.

Snel, H., R. Houwink, J. Bosschers, W. J. Piers, G. J. W. van Bussel and A. Bruining (1993). Sectional prediction of 3-D effects for stalled flow on rotating blades and comparison with measurements. In: *Proc. Eur. Community Wind Energy Conf., Germany.* pp. 395–399.

Snyder, M. H. and W. H. Jr. Wentz (1981). Dynamics of wakes downstream of wind turbine towers. NASA–CP–2185.

Sorensen, J. N. (1986). Prediction of three dimensional stall on wind turbine blade using three level, viscous inviscid interaction model. In: *Proc. Eur. Wind Energy Conf. '86, Italy.*

Sorensen, J. N. (1999). Viscwind. Viscous effects on wind turbine blades, final report for the Joule III Project. ET–AFN–9902. Department of Energy Engineering, Technical University of Denmark.

Sorensen, J. N., W. Z. Shen and X. Munduate (1996). Vortex ring state by a full-field actuator disc model. In: *Proc. 10th IEA Symposium on the Aerodynamics of Wind Turbines, Edinburgh, Scotland.*

Sorensen, J. N., W. Z. Shen and X. Munduate (1998). Analysis of wake states by a full-field actuator disc model. *Wind Energy* **1**(2), 73–88.

Sorensen, J.N. and R. Mikkelsen (2001). On the validity of the blade element momentum method. In: *Proc. Eur. Wind Energy Conf. 2001, Copenhagen, Denmark.*

Sorensen, J.N. and W.Z.Shen (1999). Computation of wind turbine wakes using combined Navier–Stokes/Actuator-line methodology. In: *Proc. Eur. Wind Energy Conf. '99, Nice, France.* pp. 156–159.

Stoddard, F. S. (1977). Momentum theory and flow states for windmill. *Wind Technology* **1**, 3–9.

Tan, C. M. and L. W. Carr (1996). The AFDD international dynamic stall workshop on correlation of dynamic stall models with 3–d dynamic stall data. NASA TM–110375.

Tangler, J. L. (1983). Assessment of blade -element/momentum analysis for horizontal axis wind turbines. In: *Proc. 6th Biennial Wind Energy Conf. and Workshop, Minneapolis and St. Paul, MN, USA.*

Tangler, J. L. (1996). Influence of pitch, twist, and taper on a blade's performance loss due to roughness. In: *Proc. 10th IEA Symposium on the Aerodynamics of Wind Turbines, Edinburgh, Scotland.* pp. 159–167.

Tangler, J. L. and M. S. Selig (1997). An evaluation of an empirical model for stall delay due to rotation for hawts. In: *Proc. Windpower'97 Conf., Texas.* pp. 87–96.

Thresher, R. W., A. D. Wright and E. L. Hershberg (1986). A computer analysis of wind turbine blade dynamic loads. *ASME J. Solar Energy Eng.* **108**(1), 17–25.

Thwaites, B. (1960). *Incompressible aerodynamics.* Oxford University Press.

Viterna, L. A. and D. C. Janetzke (1982). Theoretical and experimental power from large horizontal-axis wind turbines. NASA TM–82944.

Viterna, L. A. and R. D. Corrigan (1981). Fixed pitch rotor performance of large horizontal axis wind turbines. In: *Proc. Workshop on Large Horizontal-Axis Wind Turbines.* DOE/NASA.

Voutsinas, S. (1995). *Joule Project Dynamic Stall and 3-D effects, NTUA contribution, Available through http://www.fluid.mech.ntua.gr/~renesunet/English/Projects/Wind/Project1.html.*

Voutsinas, S. and V. Riziotis (1995). Vortex particle modelling of stall IEA Annex XIV: Field Rotor Aerodynamics. NTUA–FS–W–8–95. Nat. Tech. University of Athens.

Voutsinas, S. G. and V. A. Riziotis (1996). Vortex particle modelling of stall on rotors. Application to wind turbines. *Proc. 1996 ASME Fluids Eng. Div. Summer Meeting, San Diego, CA, USA, ASME Fluids Eng. Div.* **238**(3), 25–32.

Wang, T. and F. N. Coton (1999). An unsteady aerodynamic model for HAWT performance including tower shadow effects. *Wind Eng.* **23**(5), 255–268.

Wang, T. and F. N. Coton (2001). A high resolution tower shadow model for downwind turbines. *J. Wind Eng. and Ind. Aerodyn.* **89**, 873–892.

Wang, T., F. N. Coton and R. A. McD. Galbraith (1998). An examination of two tower shadow modelling strategies for downwind wind turbines. In: *A Coll. 1998 ASME Wind Energy Symp. Tech. Papers Presented 36th AIAA Aerospace Sci. Meeting and Exh., Reno, USA, AIAA–98–0022.*

Wentz, W. H. Jr. and J. T. Calhoun (1981). Analytical studies of new airfoils for wind turbines. In: *NASA Conference Publication 2184.*

Wilby, P. G. (1980). The aerodynamic characteristics of some new rae blade sections, and their potential influence on rotor performance. *Vertica* **4**, 121–133.

Wilby, P. G. (1984). An experimental investigation on the influence of a range of airfoil design features on dynamic stall onset. In: *10th European Rotorcraft Forum.* The Hague.

Wilby, P. G. (2001). The development of rotor airfoil testing in the UK. *J. Am. Helicopter Soc.* (July), 210–220.

Wilmshurst, S., A. J. F. Metherell, D. M. A. Wilson, D. J. Milborrow and J. N. Ross (1984). Wind turbine rotor performance in the high thrust region. In: *Proc. 6th BWEA Wind Energy Conf., Reading, England.* pp. 268–278.

Wilmshurst, S. M. B., S. J. R. Powles and D. M. A. Wilson (1985). The problem of tower shadow. In: *Proc. 7th BWEA Wind Energy Conf., Oxford, England.*

Wilson, R. E. (1981). Aerodynamic potpourri. In: *Proc. Wind Turbine Dynamics Conf., Cleveland, Ohio, NASA Conf-2185.*

Wilson, R. E. and P. B. S. Lissaman (1974). Applied aerodynamics of wind power machines. Oregon State Univ. Report NSF/RA/N–7413. NTIS PB 238594.

Wood, D. H. (1991). A three-dimensional analysis of stall-delay on a horizontal-axis wind turbine. *J. Wind Eng. and Ind. Aerodyn.* **37**(1), 1–14.

Xu, G. and L. N. Sankar (2000). Computational study of horizontal axis wind turbines. *ASME J. Solar Energy Eng.* **122**, 35–39.

Young, W. H. (1984). Fluid mechanics mechanisms in the stall process for helicopters. NASA TM–81956.

Young, W. H. and J. C. Williams (1972). Boundary-layer separation on rotating blades in forward flight. *AIAA J.* **10**(12), 1613–1619.